Collective behavior in biophysical systems

From patterns in non-equilibrium protein systems to growth dynamics of cell populations

Jonas Sebastian Denk

Munich 2018

Collective behavior in biophysical systems

From patterns in non-equilibrium protein systems to growth dynamics of cell populations

Jonas Sebastian Denk

A dissertation submitted

to the Faculty of Physics at the

Ludwig–Maximilians–Universität München

for the degree of

Doctor rerum naturalium

Munich, 8th September 2018

First referee: Prof. Dr. Erwin Frey

Second referee: Prof. Dr. Ulrich Gerland

Day of the oral examination: 22nd October 2018

Zusammenfassung (Summary in German)

Meine Doktorarbeit behandelt kollektive Phänomene in drei unterschiedlichen Bereichen der Nichtgleichgewichts-Biophysik. Diese Bereiche sind Reaktions-Diffusions Systeme, Aktive Systeme und bakterielle Ökosysteme. Durch eine ständige Energiezufuhr in Form von ATP, GTP oder Nährstoffen sind die Bestandteile der jeweiligen Systeme dauerhaft im Nichtgleichgewicht. Durch diese Energiezufuhr können die Bestandteile molekulare Reaktionen ausführen, sich gerichtet bewegen oder wachsen. Außerdem unterscheiden sich die behandelten Systeme durch die Art und Längenskalen der auftretenden Interaktionen. Dies führt zu einem breiten Spektrum kollektiver Phänomene, welche auf unterschiedlichen Mechanismen basieren.

I Musterbildung in Reaktions-Diffusions-Systemen
mit *Jacob Halatek, Simon Kretschmer, Fridtjof Brauns, Caroline Hartl, Korbinian Pöppel, Petra Schwille und Erwin Frey.*
Der erste Teil meiner Arbeit befasst sich mit Musterbildung der sogenannten Min Proteine. Das Min System ist maßgebend beteiligt an der Positionierung des kontraktilen Ringes in Bakterien und ist beispielhaft für musterbildende Reaktions-Diffusions-Systeme in der Zelle. Es umfasst die Proteine MinC, MinD und MinE, welche im Zytosol diffundieren, oder an die Membran binden und dort molekulare Reaktionen ausführen können. Im ersten Projekt kollaborierten wir mit Simon Kretschmer und Petra Schwille des MPI für Biochemie (Martinsried) und zeigten, dass ein gegenseitiger 'Switch' molekularer Konformationen in Proteinen essentiell ist für die robuste Bildung von Proteinmustern. Die Ergebnisse dieser Studie wurden veröffentlicht in "MinE conformational switching confers robustness on self-organized Min protein patterns", Proc. Natl. Acad. Sci. (2018), (abgedruckt im Unterkapitel I.2). In einem weiteren Projekt untersuchten wir Musterselektion in einem räumlich reduzierten mathematischen Modell des Min Systems. Hier identifizierten wir einen Übergang von regelmäßigen zu turbulenten Mustern basierend auf einer Ein-Moden-Instabilität (Unterkapitel I.3).

II Selbstorganisation in aktiven Systemen
mit *Lorenz Huber, Emanuel Reithmann, Timo Krüger und Erwin Frey.*
Im zweiten Teil meiner Doktorarbeit liegt der Fokus auf kollektivem Verhalten in Systemen aktiver Teilchen, d.h. Teilchen, welche interne Energie oder Energie aus ihrer Umgebung in gerichtete Bewegung umwandeln. Das erste Projekt dieses Kapitels ist motiviert durch beobachtete Ringmuster in Rekonstitutionsexperimenten mit FtsZ-Polymeren. FtsZ Polymere sind Hauptbestandteile des kontraktilen Ringes

in Bakterien und damit zentral für die Zellteilung. Wir untersuchten das kollektive Verhalten von aktiven, gekrümmten Polymeren mathematisch und identifizierten eine Phase von Vortexmustern für mittlere Polymerdichten. Die Ergebnisse dieser Studie wurden veröffentlicht in "Active Curved Polymers Form Vortex Patterns on Membranes", Phys. Rev. Lett. 116, 178301 (2016), (abgedruckt im Unterkapitel II.2). In einem weiteren Projekt (Unterkapitel II.3), entwickelten wir eine allgemeinere Beschreibung aktiver Systeme mit gemischter Interaktionssymmetrie. Hier fanden wir eine interessante Rückkopplung zwischen Musterbildung und Symmetriebrechung, welche zur Koexistenz verschiedener Symmetrien führen kann.

III Ökologischer Selbstmord in Mikroben

mit *Christoph Ratzke und Jeff Gore.*

Das letzte Projekt meiner Doktorarbeit behandelt kollektive Phänomene in bakteriellen Ökosystemen. Diese Studie begann während meines dreimonatigen Forschungsaufenthaltes in der Gruppe von Jeff Gore am MIT (Cambridge, USA), wo ich hauptsächlich Experimente an räumlich gemischten Kulturen von Bodenbakterien durchführte. Wir fanden, dass manche Bakterienpopulation während ihres Wachstums den pH-Wert ihrer Umgebung so verändern, dass es nachteilig für sie ist und sogar zum Aussterben der Population führen kann. Wir zeigten weiter, dass dieses selbst-verschuldete Aussterben zu einigen interessanten und auch überraschenden kollektiven Effekten führt. Zum Beispiel fanden wir Oszillationen in der Populationsgröße und einen Rettungsmechanismus von bakteriellen Populationen durch für Bakterien schädliche Substanzen wie s.B. Antibiotika. Die Ergebnisse dieser Studie wurden veröffentlicht in "Ecological suicide in microbes", Nat. Ecol. Evol., 2(2018) 867, (abgedruckt im Unterkapitel III.2)

Overview of the thesis

My thesis deals with collective behavior in three prototypic fields of nonequilibrium biophysics. These are reaction-diffusion systems, active matter systems and ecological networks. All of the studied systems are driven out of equilibrium due to a constant energy supply in the form of ATP, GTP, or nutrients. This energy supply enables the constituents of the studied systems to undergo molecular reactions, propel themselves, or grow, respectively. Furthermore, interactions in these systems differ and act on different lengthscales. This leads to a wide range of collective phenonema that base on different interesting mechanisms.

I Pattern formation in reaction-diffusion systems
with *Jacob Halatek, Simon Kretschmer, Fridtjof Brauns, Caroline Hartl, Korbinian Pöppel, Petra Schwille, and Erwin Frey.*
The first part of my thesis is concerned with pattern formation in the Min protein system. The Min system is central for positioning of the bacterial contractile ring during cell division and constitutes a stereotypical example for pattern forming reaction-diffusion systems in the cell. Here, the proteins MinC, MinD and MinE diffuse in the cytosol and attach to the membrane, where they undergo molecular reactions. In the first project, together with our experimental collaborators Simon Kretschmer and Petra Schwille from the MPI of Biochemistry (Martinsried), we showed that a mutual switch of the proteins MinD and MinE is essential for robust protein pattern formation. The results of this study are published in "MinE conformational switching confers robustness on self-organized Min protein patterns", Proc. Natl. Acad. Sci. (2018), (reprinted in section I.2). In another project (section I.3), we investigated pattern selection in a spatially-reduced mathematical model for the Min system. Here, we identified a transition from regular to turbulent protein patterns based on a single-mode instability.

II Self-organization in active matter systems
with *Lorenz Huber, Emanuel Reithmann, Timo Krüger, and Erwin Frey.*
In the second part of my thesis, the focus will be on collective behavior in systems of active entities, i.e. entities that can transduce internal or ambient energy into directed motion. The first project was motivated by ring patterns in reconstitution experiments of the bacterial FtsZ-polymers, which are key constituents of the bacterial contractile ring and thus central for cell division. We theoretically studied the collective behavior of active curved polymers and identified a phase of vortex patterns for intermediate polymer densities. The results of this work are published

in "Active Curved Polymers Form Vortex Patterns on Membranes", Phys. Rev. Lett. 116, 178301 (2016), (reprinted in section II.2). In another project (section II.3), we developed a more general theoretical description of active systems with mixed interaction symmetry. Here, we found an interesting feedback mechanism between pattern formation and symmetry breaking which can lead to coexisting symmetries.

III Ecological suicide in microbes

with *Christoph Ratzke and Jeff Gore.*

The last project of my thesis deals with collective phenomena in bacterial ecosystems. This work was initiated during my three-month research stay in the group of Jeff Gore at MIT (Cambridge, USA), where I mostly performed growth experiments on well-mixed cultures of soil bacteria in the laboratory. When growing certain soil bacteria in a nutrient rich environment, we found that some bacteria alter their ambient pH in a way that is detrimental for them and that can even lead to extinction of the whole population. We showed that this self-inflicted death lead to several interesting and possibly counter-intuitive collective effects. For instance, our results indicate oscillatory dynamics of the population size and reveal a rescue mechanism of bacterial populations by substances usually considered harmful for bacteria, such as antibiotics. The results of this study are published in "Ecological suicide in microbes", Nat. Ecol. Evol., 2(2018) 867, (reprinted in section III.2).

Abstracts of the projects

Collective (or emergent) behavior is widespread in physics and often appears in the context of large-scale phenomena such as phase transitions or condensation effects. The term is used whenever interactions between individual entities lead to large-scale properties and dynamics of their collective, which fundamentally differ from the behavior of the isolated constituents. Collective behavior is not restricted to physical phenomena but can be found in various fields of daily life including information spread in social networks, the dynamics of financial markets or herding of animals. In particular, biological systems provide prime examples that show collective behavior on vastly different lengthscales.

During my doctoral studies, I worked on collective behavior of three different bacterial systems on respectively different lengthscales. In particular, I investigated protein pattern formation in reaction-diffusion networks, self-organization of active entities such as active polymers, and collective growth dynamics of well-mixed bacterial populations. Based on the different interactions in each system, I identified different collective phenomena and investigated their underlying mechanisms.

In my first project (section I.2), we worked on a mathematical description of the Min protein system. The Min system is critical for proper cell division in the bacterium *Escherichia coli* and forms a prototypical example of protein pattern formation [1]. To investigate the underlying mechanisms for pattern formation, Jacob Halatek, Erwin Frey and I studied theoretical models based on reaction-diffusion networks for the involved proteins MinD and MinE. In close collaboration, Simon Kretschmer and Petra Schwille from the Max Planck Institute for Biochemistry in Martinsried, Germany, performed *in vitro* experiments using various MinE mutants. Our combined research showed that a mutual switch between MinD and MinE is essential for the formation of protein patterns in a wide range of protein concentrations including the physiological range.

The experiments performed by Simon Kretschmer and Petra Schwille as well as previous theoretical studies by Jacob Halatek suggest the emergence of turbulent dynamics at the onset of pattern formation. To focus on this phenomenon, we developed a spatially-reduced mathematical model for the Min system, which preserves the pattern phenomenology of previous, less accessible models (section I.3). On the basis of this model, we pinpoint and investigate a novel mechanism for turbulence induced by a single-mode instability.

The second part of my doctoral studies was concerned with pattern formation in systems of self-propelled entities. Motivated by experimentally observed ring

patterns of the bacterial FtsZ polymers [2], we studied the collective behavior of self-propelled, curved polymers on a flat membrane (section II.2). We found that propulsion on circular tracks in combination with steric repulsion between polymers lead to pattern formation at intermediate polymer densities. Here, polymers assemble into dynamic vortex patterns reminiscent to the experimentally observed structures.
In this system, the polar symmetry of polymer interactions is directly translated to the formation of macroscopic polar order. In contrast, recent observations in active polymer systems [3] give hint to emergent macroscopic symmetries that are not obvious from the microscopic interactions of its constituents. To investigate the collective behavior of active entities with more general interaction symmetry, we studied a system with mixed polar and nematic particle alignment (section II.3). For a moderate bias of polar alignment, we found a novel type of dynamic pattern transition where nematic bands can induce polar traveling wave patterns.
In my last project, I worked on collective behavior of bacterial populations in the group of Jeff Gore at MIT in Cambridge, USA (section III.2). Whereas in the previous projects I employed theoretical approaches, here I mostly performed experiments and complemented these studies by mathematical modeling. In particular, we revealed a negative feedback between population growth and a change in the environmental pH which can lead to a self-inflicted death of the bacterial population. Our experiments show interesting non-monotonous growth dynamics and several, possibly counter-intuitive phenomena such as the rescue of bacteria by substances that are usually considered harmful for them.

I MinE conformational switching confers robustness on self-organized Min protein patterns

with *Jacob Halatek, Simon Kretschmer, Caroline Hartl, Petra Schwille, and Erwin Frey.*

Summary

In the first project of my doctoral studies, I investigated the reaction-diffusion network that underlies protein pattern formation in the bacterial Min system. Whereas previous mathematical models [4, 5] were able to reproduce the experimentally observed pattern phenomenology, the concentration range of patterns in experiments is significantly larger than predicted by these theories. In particular, previous theory predicted that pattern formation is only possible when MinD exceeds MinE in concentration; however, this is in stark contrast to experimentally observed Min patterns also for MinE being much more abundant than MinD [6].

Based on recent experimental evidence [7], we extended a previous mathematical model [4, 5] by a fast molecular switch of MinE. More specifically, in the extended model MinE undergoes a MinD-induced conformational switch from a state of low

to a state of high MinD binding affinity. By combining linear stability analyses and numerical simulations, we theoretically studied the concentration regime compatible with pattern formation. Our analyses suggest that the included switch of MinE dramatically increases the MinE concentration range of pattern formation. Especially, it also enables patterns when MinE is much more abundant than MinD.

Our collaborators Simon Kretschmer and Petra Schwille from the Max-Planck institute for biochemistry in Martinsried were able to test our theoretical predictions in reconstitution experiments with MinE mutants. In agreement with our theory, they find that when disabling MinE's conformational switch, the MinE concentration range in which patterns form is drastically reduced and falls to values much lower than the MinD concentration.

Given the ubiquity of molecular switches in protein networks [8, 9], our study suggests that mutual switching between proteins constitutes a common design principle to ensure robustness of patterns with vital function in the cell.

Background

Bacterial cell division is coordinated by a large set of proteins. The tubulin homologue FtsZ plays a prominent role, as it forms the Z-ring at the future division site [10, 11]. The Z-ring recruits further cell division proteins and thereby initiates the formation of a division septum and facilitates cell constriction. Placement of the Z-ring at midcell is important for cell division into two equally sized daughter cells. While the proteins of the cell division machinery are largely conserved across various bacteria, the proteins that are involved in the positioning of the Z-ring are not [12, 13]. In *Escherichia coli*, placement of the Z-ring is coordinated by the Min system which consists of the proteins MinC, MinD, and MinE [1]. Here, MinD and MinE self-organize into pole-to-pole oscillations that establish a time-averaged concentration minimum of MinC at midcell. Since MinC acts as an inhibitor of FtsZ, the Min system thereby confines the division machinery to mid-cell. The self-organization of MinD and MinE into protein patterns has not only been observed in the cell, but could also be reconstituted on flat supported lipid bilayers [6].

Experimental as well as theoretical studies have helped to gain insights into the reaction network underlying this self-organization process [1]. MinD is an ATPase that dimerizes in the presence of ATP and then binds to the plasma membrane where it can recruit further MinD. Membrane-bound MinD also recruits its ATPase-activating protein MinE, which then form membrane-bound MinDE complexes. In the complex, MinE induces ATP hydrolysis by MinD followed by desintegration of the MinDE complex and release of MinE and ADP-bound MinD into the bulk. There, MinD exchanges ADP for ATP before it can rebind to the membrane. Mathematical models centered around this reaction network [4, 5, 14], which we will refer to as

skeleton network, were capable of reproducing the pattern phenomenology observed *in vivo* as well as *in vitro*. However, whereas theoretical studies allow patterns only if MinE is less abundant than MinD, *in vitro* experiments show patterns for MinE/MinD ratios ranging between 0.125 and 5 [6, 15, 16]. This contradiction prompts a shortcoming of the above simplified view on the Min system.

Furthermore, recent experiments suggest an extension of the skeleton reaction network in terms of a revised MinE dynamics. More specifically, structural biological experiments [7, 17, 18] indicate that upon interaction with membrane-bound MinD, MinE changes from a six to a four-stranded β sheet structure. The remaining two sheets are tranformed into MinD interaction helices which enable strong MinD binding. In addition, experiments [7, 18] indicate direct membrane interactions of MinE through its membrane targeting sequences.

Motivation and research question

The first goal of this project was to find a simple and meaningful extension of the previously studied skeleton network that can resolve the discrepancy in pattern robustness between this network and experiments. Given the experimental evidence of a conformational switch in MinE, we further wanted to elucidate the role of mutual switches in spatially extended protein networks. Eventually, the theoretical predictions of our extended network should be testable by controlled experiments. Here, we strongly profitted from a close collaboration with Simon Kretschmer and Petra Schwille.

Summary of results

A MinD-induced switch in MinE's binding affinity to MinD enables pattern formation in a broad and physiological range of concentration ratios. First, we developed a mathematical reaction-diffusion network that accounts for a conformational switch in MinE as revealed in recent structural biology experiments. Here, MinE can be present in two different modes of action. In its native, cytosolic form, MinE has a very low binding affinity to membrane-bound MinD. However, upon interaction with membrane-bound MinD, MinE switches to a reactive form, which then strongly binds to MinD and forms a MinDE complex on the membrane. After MinE-induced desintegration of the MinDE complex into the bulk, we assume that relaxation of reactive to latent MinE happens fast but not instantaneously. Thus, there is a finite (albeit very short) time after desintegration in which MinE stays in its reactive form with a high binding affinity to membrane-bound MinD. The rapid decay of reactive MinE into its latent form creates a spatial gradient with predominantly reactive MinE at the membrane and predominantly latent MinE further away from the membrane. This spatial separation of MinE's two modes of action leads to an

interesting mechanism for pattern robustness: In membrane regions depleted of Min proteins, cooperative binding of MinD first facilitates accumulation of MinD on the membrane (formation of a MinD zone). Importantly, a MinD zone can also form when MinE exceeds MinD in concentration, since recruitment of latent MinE is very weak. If MinE was only present in its latent conformation, MinD accumulation would always dominate and the dynamics would cease. However, after desintegration of MinDE complexes, MinE remains in its reactive form for a finite time. Since reactive MinE binds stronger to membrane-bound MinD than MinD itself, recruitment of reactive MinE is prefered over recruitment of MinD. As MinE's reactive state is short-lived, it is effectively restricted to a thin boundary layer close to the MinD zone. This thin layer of reactive MinE can then successively deplete the MinD zone on the membrane while a new MinD zone can build up at a distant region on the membrane where reactive MinE is absent. In a model with only one (reactive) MinE conformation, such as the original skeleton model, initial accumulation of MinD on the membrane is only possible when MinD is more abundant than MinE.

Employing linear stabilty analyses and finite element simulations of reaction networks with and without MinE's conformational switch, we could confirm this intuitive picture. We find that the regime of MinE/MinD concentration ratios compatible with pattern formation can be increased by about two orders of magnitude when including a conformational switch of MinE. In particular, patterns also form when MinE exceeds MinD in its overall concentration. Interestingly, depending on the recruitment rates of MinE, this is also true when the switch of MinE is so rapid that the cytosol layer of reactive MinE appears negligibly small as compared to the total extension of the cytosol. Thus, even very rapid conformational switches can be important for pattern forming systems since they spatially separate different modes of action.

To test our theoretical predictions, we collaborated with Simon Kretschmer and Petra Schwille, who were able to reconstitute various MinE variants on lipid bilayer assays. More specifically, they inserted point muations L3E, I24N as well as the double mutation L3E/I24N into wildtype (WT) MinE and studied the ability of these variants to form patterns together with MinD. Comparing, variants which feature a conformational switch (WT & MinE L3E) to mutants where this switch is disabled (MinE I24N & MinE L3E/I24N), we found excellent agreement with our theoretical predictions: whereas WT MinE and MinE L3E show patterns for a wide range of MinE/MinD concentration ratios, this range is dramatically decreased for MinE I24N and MinE L3E/I24N and falls to values much lower than one. Remarkably, the range of MinE/MinD concentration ratios compatible with pattern formation for MinE I24N and MinE L3E/I24N is below the physiological range. This suggests a critical role of MinE's conformational switch even in the cell.

Direct MinE membrane interactions do not markedly affect the concentration range of pattern formation. Recent studies suggest that even in the absence of MinD, MinE can directly bind to the membrane through its membrane targeting sequences. While the relation between MinE-membrane interactions and MinE's conformational switch is unclear, MinE-membrane interactions could in principle also affect the robustness of patterns. Therefore, we also studied direct MinE-membrane interactions in our theoretical reaction-network as well as in suitable reconstitution experiments. Our theoretical approach shows that, in principle, direct membrane interactions of MinE could de- or increase the range of MinE/MinD concentration ratios compatible with pattern formation, depending on the choice of reaction rates. *In vitro* experiments by Simon Kretschmer and Petra Schwille eventually showed, that membrane interactions do not markedly affect this concentration range: MinE variants with possible direct membrane interactions (WT & MinE I24N) displayed patterns in the same range of MinE/MinD concentration ratios as their respective counterparts with disabled membrane interactions (MinE L3E & MinE L3E/I24N). In terms of our mathematical models, this suggests that direct MinE-membrane interactions do not have to be taken into account to observe pattern formation in a broad range of protein concentrations.

The skeleton network serves as useful basis for studying pattern formation in the Min system. In the MinE L3E/I24N double mutant, both, membrane interactions and the MinE-MinD interaction switch, are disabled. This variant thus closely emulates the MinE dynamics in the original skeleton network. This mutant still self-organizes into dynamic protein patterns, albeit only in a narrow range of MinE/MinD ratios. In particular, we observe patterns only when MinD exceeds MinE in concentration, confirming previous theoretical predictions based on the skeleton network [5]. This agreement between theory and experiment, consolidates the skeleton network as suitable and useful basis to theoretically study Min pattern formation at least for a suitable choice of low MinE/MinD concentration ratios.

Relevance and outlook

The Min protein system forms a prototypical example of intracellular pattern formation [13]. While previous studies mostly focused on the switch of MinD's nucleotide state, our work emphasizes the critical role of MinE's functional switch for pattern robustness. In fact, functional switches are ubiquitous in pattern forming protein networks. They appear in the form of nucleoside triphosphatases (NTPases) [8, 19], which are involved in flagellar patterning, chemotaxis arrays or even in eukaryotic cells in the polarization of budding yeast. But they have also gained recent attention in the form of metamorphic proteins [9], which can reversibly switch between alternative conformations with distinct functions. Prominent examples for metamorphic proteins include KaiB, which plays an important role in

the KaiABC system, a prominent protein oscillator that serves as a circadian clock in cyanobacteria [20].

Our work suggests, that mutual switching of proteins is critical to enable pattern formation in a wide range of protein concentrations. A large concentration regime of patterns could allow the system to adjust certain features of patterns such as the wavelength or period by changing protein concentrations respectively. Furthermore, in the course of evolution the ability to form patterns in a large range of protein concentrations is essential to allow for protein mutations while the key functions of the organism, such as protein patterning, remain intact.

While our work identified the critical role of the MinE dynamics, a better understanding of the MinD dynamics based on controlled (reconstitution) experiments remains a major challenge for future research. Furthermore, a quantitative comparison of *in vitro* and *in silico* pattern phenomenology including standing waves, traveling waves or also more irregular patterns would yield insights into the key mechanisms that underly pattern selection.

The results from this project were published in "MinE conformational switching confers robustness on self-organized Min protein patterns", Proc. Natl. Acad. Sci. (2018), and are reprinted in section I.2.

II Single-mode turbulence and a spatially-reduced model for intracellular pattern formation

with *Jacob Halatek, Fridtjof Brauns, Korbinian Pöppel and Erwin Frey.*

Summary

The second project of my doctoral studies deals with pattern selection in the *in vitro* Min system. Here, we developed a spatially simplified reaction-diffusion model of the above-mentioned skeleton network. In this model, the complete vertical bulk extension is reduced to a bulk layer further away from the membrane coupled to a bulk-membrane layer close to the membrane. This *two-layer model* represents a dramatic reduction of the original skeleton model in terms of complexity and numerical effort; nevertheless, it reproduces the full pattern phenomenology of the original skeleton model. On the basis of this simplified model, we focused on the onset of pattern formation, i.e. on protein densities close to their threshold value beyond which proteins self-organize into patterns. Combining linear stability analyses with finite element simulations, we find that close above the onset of pattern formation the system approaches a turbulent state induced by a *'single-mode instability'*. By varying the system length, we identify a transition between regular standing wave patterns and turbulent dynamics. Finally, we explore a further reduced model with discretized lateral extension and show that the signature of this transition is retained even for a very coarse discretizaton.

Background

Previous experimental [21, 22] as well as theoretical [23] studies on the Min system in *in vitro* geometry observed a rich pattern phenomenology when varying parameters such as protein densities or the system height. Especially, at the onset of pattern formation, the Min system displays irregular protein patterns on the membrane, which are replaced by more regular patterns further away from the onset [22, 23]. This is in contrast to the conventional notion of pattern formation, where irregular patterns are explained on the basis of a nonlinear coupling of many unstable modes far beyond the onset of patterns [24, 25]. While irregular protein patterns in the Min system have been repeatedly reported in theory and experiments, their underlying mechanism is largely elusive.

Motivation and research question

In this project we asked what mechanisms determine protein pattern formation and selection in the Min system, especially at the onset of pattern formation. More specifically, we wanted to understand how complex patterns such as turbulence emerge and if they can be related to analytically accessible properties of the system such as dispersion relations.

Summary of results

The spatially extended Min skeleton model can be reduced to a two-layer model. Experimental and theoretical studies suggest that the relevant protein dynamics in the bulk happens within a layer very close to the membrane; however, neglecting the bulk extension does not provide a meaningful description of the membrane-bulk flux [26]. In this project, we showed that the protein flux between a reactive membrane and an extended bulk can be reduced to a single bulk layer further away from the membrane, coupled to a bulk-membrane layer close to the membrane. For a suitable choice of the thicknesses of the these two layers, we identify regimes of different patterns as a function of protein concentrations. In detail, we find regimes of standing wave patterns, traveling wave patterns, homogeneous oscillations, as well as more irregular, turbulent dynamics in very well agreement with the original, spatially extended Min skeleton model.

A single-mode instability can induce chemical turbulence and explain a transition between regular and turbulent patterns. In agreement with previous experimental observations as well as theoretical studies, our spatially-reduced two-layer model displays turbulent protein patterns close to the onset of pattern formation. By linear stability analyses, we show that the emergence of turbulent dynamics is induced by a single-mode instability on the largest lengthscale of the (periodic) system. In other words, only the first mode of a wave-like perturbation in the

membrane protein density has a positive growth rate. A systematic variation of this lengthscale by varying the system's lateral extension reveals a transition between regular standing wave patterns and turbulence. We find turbulence whenever the wavelength with the largest (positive) growth rate is smaller than the length of the system. Otherwise, i.e. when this wavelength is larger than the system length, the protein densities on the membrane assume regular standing wave patterns. The transition between regular and turbulent patterns thus critically depends on the wavelength with the maximal growth rate, albeit this wavelength might not obey the (periodic) boundary conditions of the system. To investigate the role of the lateral extension in the two-layer model, we also employed a lateral discretization. Our results suggest that while a coarse discretization may not be able to resolve the resulting regular or turbulent patterns, the transition between different lengthscales of patterns based on a single-mode instability is preserved even for a very coarse discretization.

Relevance and outlook

The spatial reduction of the Min skeleton network provides a numerically feasible and meaningful basis to study pattern formation in systems where a reactive surface is coupled to a diffusive bulk. Such systems are not only ubiquitous in intracellular pattern forming systems [8, 13], but can also be found in more general model networks such as in the catalytic carbon monoxide oxidation on platinum [27, 28].

Our observation of turbulence at a single-mode instability hints towards a necessary rethinking of conventional theories of nonlinear systems where turbulence typically involves the coupling of multiple unstable modes on various lengthscales. Furthermore, our work sheds new light on the important role of the dispersion relation for pattern selection.

III Active polymers form vortex patterns on membranes

with *Lorenz Huber, Emanuel Reithmann, and Erwin Frey.*

Summary

In the next project of my doctoral studies, I theoretically investigated the collective motion and pattern forming behavior of curved, self-propelled polymers on a flat membrane. This project was largely motivated by recent *in vitro* experiments where Loose and Mitchison found dynamic ring patterns of treadmilling FtsZ polymers on a supported lipid bilayer [2].

We addressed the dynamics of curved, active polymers on microscopic and mesoscopic length scales by employing Brownian dynamics simulations and a kinetic Boltzmann approach, respectively. In our Brownian dynamics simulations, we

assumed elastic polymers with fixed intrinsic curvature that move with a constant tangential velocity. The polymers are assumed to interact only through steric repulsion. We complemented this microscopic analysis with a kinetic approach, in which the we treated point-like particles that move clockwise on circular paths and undergo diffusion and binary collisions. Here, collisions were assumed to have polar symmetry, i.e. two interacting particles fully line up along their average propulsion direction (half-angle alignment). In both approaches, we identified different regimes of collective behavior depending on the particle density and noise level. In particular, we find a regime of dynamic vortex patterns for intermediate density and noise values. In this regime, our Brownian dynamics simulations display rotating ring patterns reminiscent to the experimentally observed ring patterns of FtsZ polymers. In addition to our Brownian dynamics and kinetic approaches, we derived a hydrodynamic theory for the density and the polar order field. Interestingly, the equation for the polar order constitutes a generalization of the complex Ginzburg-Landau equation, which is prominent for its rich pattern phenomenology.

Background

As mentioned in the context of my first project, intracellular pattern formation of the Min proteins is important to guide the Z-ring and the cell division machinery to midcell. Yet, Z-ring formation and cell constriction are poorly understood, especially since no FtsZ-associated motor proteins are known [29] and lateral interactions are weak [30]. Experiments have shown that FtsZ polymerizes into filaments whose intrinsic curvature may depend on FtsZ's nucleotide state [31]; moreover, FtsZ polymers exhibit treadmilling dynamics upon ATP consumption [2, 32]. To gain insight into the formation of the Z-ring, Loose and Mitchison [2] recently investigated a reconstituted *in vitro* model system. Here, FtsA and ZipA, the key anchor proteins for FtsZ, were used to recruit FtsZ from solution to a supported lipid membrane where FtsZ form curved polymers. Due to treadmilling and the anchoring process, these polymers move clockwise on circular paths. Moreover, depending on the anchor concentration, FtsZ polymers assemble into a variety of dynamic patterns including rings or vortices and dense jammed bundles. In our work, we contributed to the theoretical understanding of these collective phenomena.

Motivation and research question

Intrigued by the dynamic ring patterns of FtsZ polymers, observed by Loose and Mitchison, we asked how such collective behavior can emerge in spite of the absence of attractive interactions between the polymers. What are the underlying mechanisms that lead to ring patterns for some conditions and different patterns such as jammed bundles for altered conditions?

Summary of results

Vortex patterns form for intermediate polymer densities and noise levels. In our Brownian dynamics simulations, we fixed the details of polymers such as their length and curvature to values consistent with experiments. Then, the only relevant parameters are polymer density and the level of (stochastic) noise in the polymers' propulsion. By varying these two parameters, we could identify three different regimes with qualitatively different behavior. For low densities or strong noise, the polymers hardly interact and the system resembles an ideal gas of polymers that move along isolated, circular tracks. For intermediate densities and noise values, polymers start to cluster and assemble into rotating ring-like structures seperated by regions where polymers are sparse. For very high densities or weak noise, polymers still cluster; however, the clusters are very short-lived. They rapidly decay and rearrange, and do not show any macroscopic structure when averaged over time. We complemented our Brownian dynamics simulations by a more coarse-grained approach in terms of a kinetic Boltzmann equation suited to our system of propelled particles on circular tracks. Based on linear analyses as well as numerical simulations, we derived a phase diagram in terms of the overall particle density and the noise level. For low densities or large noise values, the disordered state is stable and the system does not show macroscopic order nor patterns. For very high densities or low noise values, the system approaches a state of homogeneous polar order which rotates at the frequency of a single particle. Interestingly, for intermediate densities and noise values, we find dynamic vortex patterns. Here, high-density polar flocks move along circular tracks and are separated by a low-density, disordered background. Thus, though our two approaches involve different levels of description (agent-based vs. field based) on different lengthscales, they both feature a phase of vortex patterns. Furthermore, vortex patterns are restricted to a parameter regime of intermediate densities and noise levels. Too low and too high densities lead to a disordered gas-like state and a state without macroscopic structure, respectively.

Extended polymers assemble into closed rings, reminiscent to experimental observations. While both of our approaches yield vortex patterns for intermediate densities and noise values, the structure of these vortex patterns differ. In the kinetic Boltzmann approach for pointlike particles, we observe circling high-density flocks. In contrast, our Brownian dynamics simulations for extended polymers display rotating ring-structures. Here, we found that the polymer length and curvature in combination with the persistence length is critical for the structure of patterns. For instance, for very short polymers we observe flocks that move on circular tracks; thus the formation of closed rings is lost. For polymer lengths and curvatures similar to those reported by Loose and Mitchison, we find closed ring patterns reminiscent to the FtsZ-polymer rings in their experiments.

A generalized field decription connects active matter theories to the complex Ginzburg-Landau equation. On the basis of the kinetic Boltzmann equation, we derived a hydrodynamic theory for the density and the polar order field close to the onset of macroscopic order. The circular motion of the particles is inherited into the equation for the polar order field in terms of complex coupling coefficients. In detail, the equation for the polar order field contains convective terms resulting from particle propulsion as well as terms also present in the complex Ginzburg-Landau equation [33]. Our hydrodynamic equations thus couple previous active matter theories, where coupling coefficients were real, to the well-studied complex Ginzburg-Landau equation, which is prominent for its rich pattern phenomenology. Numerical solutions of the derived hydrodynamic equations reveal dynamic vortex patterns consistent with the observation of vortex patters in our Brownian dynamics and kinetic Boltmann approaches. Furthermore, these numeric solutions hint towards more complex patterns including irregular, turbulent dynamics.

Relevance and outlook

In combination, our Brownian dynamics and kinetic approaches strongly suggest that a phase of vortex structures at intermediate densities is a generic feature in systems of circling entities. The critical role of polymer density is especially interesting from a biological perspective, since protein densities are typically dynamically regulated in the cell. Indeed, very recent experimental reconstitution experiments on systems of FtsZ polymers confirm our theoretical prediction and found that the formation of vortex structures is restricted to a narrow regime of intermediate densities [34].

Furthermore, our study sheds light on the relation between microscopic particle shape as well as their interaction to the macroscopic structure of emergent patterns. In particular, we found closed ring structures only for a suitable combination of polymer length and bending stiffness; a prediction that should be testable in future experiments.

In a broader context, our hydrodynamic description combines active convection terms with the complex Ginzburg-Landau equation and thereby bridges the gap between active matter theories of straight-moving particles and theories of nonlinear oscillators. Preliminary numerical solutions of our hydrodynamic equations suggest interesting novel phenomena including vortex patterns and turbulent dynamics. A more detailed analysis of these equations poses an interesting challenge for future research.

The results from this project were published in "Active Curved Polymers Form Vortex Patterns on Membranes", Phys. Rev. Lett. 116, 178301 (2016), and are reprinted in section II.2.

IV Coexisting symmetries in active matter systems

with *Lorenz Huber, Timo Krüger, and Erwin Frey.*

Summary

This project of my doctoral thesis deals with systems of self-propelled particles with mixed collision symmetry. Motivated by recent experimental and numerical studies by Lorenz Huber, Timo Krüger, Erwin Frey, and collaborators [3], we theoretically studied systems of propelled particles that align their orientation with a small, tunable bias to polar (i.e. head-to-head) alignment. We implemented such alignment rule in a kinetic Boltzmann approach and studied the respective kinetic Boltzmann equation by means of stability analyses as well as numerical simulations. For small and large polar bias, we recover the well-studied scenarios of purely nematic and polar symmetry, respectively. In particular, above a critical density the systems forms macroscopic nematic or polar order for small or large polar bias, respectively. For intermediate polar bias, our analyses reveal a second transition density, beyond the onset density to macroscopic nematic order. For densities above this second transition, the system forms macroscopic polar order. Interestingly, between the two transition densities, our study reveals dynamic transitions from nematic to polar patterns and even features patterns of alternating polar and nematic symmetry. Based on the notion of local instabilities in the nonlinear dynamics, we propose a hydrodynamic description for the polar, and the nematic order fields. These hydrodynamic equations reproduce the pattern phenomenology of our kinetic Boltzmann approach and also capture the more complex phenomenology observed in [3].

Background

Whenever energy is consumed and transduced into local mechanical forces, a system is called active [35]. Thus, active matter constitutes a major part of biological systems and can be found on various lengthscales ranging from the cytoskeletal network, to bacterial colonies and even to herds of animals [36]. The interactions between individual entities of an active system can lead to intriguing collective effects. When the entities transduce their available energy into directed motion, aligning interactions among the individuals can lead to phenomena such as flocking or collective motion. While theories of propelled agents yielded important insights into these large-scale phenomena [37], they were mostly based on *ad hoc* symmetry assumptions regarding the agents' interactions. Such assumptions are, however, hard to test in a real biological system where the constituents may undergo intricate interactions which (possibly) defy simple interaction rules. Recent experimental studies on an actomyosin motility assay [3] indeed showed that the symmetry of emergent patterns may not be evident from simple symmetry arguments but can

be a dynamic and emergent property of the system. Here, together with their collaborators, Lorenz Huber, Timo Krüger and Erwin Frey observed coexistence as well as dynamic transitions between patterns of different symmetries.

Motivation and research question

How does the system choose between different symmetries, when interactions allow more than one symmetry? Can the symmetry of macroscopic patterns differ from the symmetry of the underlying interactions on the microscale? Intrigued by these questions and the recently observed coexistence of polar and nematic patterns [3], we wanted to understand the mechanisms of pattern formation and selection when the symmetry of a system depends on the systems' dynamics.

Summary of results

A mixed collision rule enables a transition from nematic to polar symmetry. The studies by Huber et al. [3] suggest that even a small bias towards polar alignment can lead to interesting new dynamics as compared to unbiased, nematic alignment. Motivated by this finding, we employed a kinetic Boltzmann ansatz where particles undergo binary nematic alignment with a small (tunable) polar bias. Based on linear stability analyses, we identified different phases of collective behavior as a function of density and polar bias. Consistent with previous studies [36], our phase diagram suggests nematic and polar patterns for respectively small and large polar bias at intermediate densities. For large densities, these patterns are replaced by respectively homogeneous nematic and polar order. For moderate polar bias we find another critical density above which purely nematic order is linearly unstable and polar order is predicted to grow. Indeed, by numerical solutions of the homogeneous Boltzmann equation, we confirm this transition from nematic to polar order for intermediate polar bias.

Pattern formation enables dynamic transitions between states of different symmetries. To gain insights into the nonlinear dynamics especially in the regime where linear stability predicts density patterns, we numerically solved the kinetic Boltzmann equation for different polar bias and average densities. For small and large polar bias, we recover the well-studied nematic band patterns and traveling wave solutions, respectively. Remarkably, in the nematic phase and for intermediate polar bias we observe a dynamic transition from nematic band patterns to polar patterns: First, the system forms high-density nematic bands as for small polar bias. After some time, polar order forms within these bands and leads to polar traveling patterns along the band orientation. Depending on the system size and the initial conditions, this dynamic transition can lead to a total replacement of nematic bands by polar traveling waves, dynamic rearrangements of bands or even alternating local dominance of polar and nematic patterns.

A hydrodynamic approach consolidates the notion of a dynamic pattern transition based on a local destabilization. Our numerical solutions of the kinetic Boltzmann equation suggest that dynamic transitions from nematic to polar patterns are induced by local destabilizations of nematic bands. In detail, although the average density of the system lies in the purely nematic phase, the density distribution into nematic bands can locally push the density beyond the transition to polar order and thereby induce local growth of polar order. Based on this notion and previous hydrodynamic desriptions of purely nematic systems, we propose hydrodynamic equations for the polar and the nematic order fields with variable coupling strength between these fields. Interestingly, these equations yield a phase diagram in terms of this coupling strength and density which closely resembles the phase diagram of the kinetic Boltzmann equation with mixed colllsion symmetry. Numerical integration of the hydrodynamic equations reveals dynamic pattern transitions akin to the ones observed in our kinetic Boltzmann approach. Moreover, for large systems, we find more complex dynamics reminiscent to the experimental and numerical observations by Huber et al. [3]. In detail, we find dynamic bands that buckle, merge, decay and coexist with polar waves, which themselves rearrange, splay and interact with bands and among each other.

Relevance and outlook

In the context of symmetry breaking in active matter, our results show that the symmetry of macroscopic patterns can critically depend on the dynamics of the system. This reveals a novel *mutual* feedback mechanism between pattern formation and symmetry breaking. We argue that this feedback can be understood at the level of stability of local steady states. This notion, which was recently also proposed for reaction-diffusion systems [23], should be testable by a systematic manipulation of local densities in controlled experiments and numerical simulations.

V Ecological suicide in microbes

with *Christoph Ratzke and Jeff Gore.*

Summary

In the last project of my doctoral studies I investigated the collective behavior in bacterial populations. Unlike in the other projects, I mostly performed experiments in the laboratory and employed theory only to test and consolidate our intuition gained from these experiments. This project was initiated during my three-month research stay in the group of Jeff Gore at MIT in Cambridge, USA.

Here, we studied the collective growth dynamics of soil bacteria in well-mixed culture experiments. Consistent with previous studies by Christoph Ratzke and

Jeff Gore, we found that for some soil bacteria, population growth resulted in a severe change in the pH of their medium. This pH change can in turn feed back onto bacterial growth. In particular, we identified a negative feedback where population growth is followed by a fatal acidification of the medium, which in turn can cause extinction of the population. We studied this self-inflicted death, which we also refer to as *ecological suicide*, in controlled growth experiments and dynamic measurements of population size and pH. We find that ecological suicide can lead to interesting, possibly counter-intuitive collective phenomena such as oscillations during daily dilution experiments and a possible rescue of bacterial populations by substances that are usually considered harmful for bacteria.

Background

Organisms influence each other by changing the environment they live in [38, 39]. These environmental modifications can be positive for the organisms, like in the cooperative breakdown of complex nutrients in microbes, the construction of complex architectures of coral reefs, ant colonies or even human cities – where the individual profits from the collective actions of her peers. There is a long tradition of research probing cooperative interactions between organisms and its large number of effects in ecosystems [38, 40]. However, organisms can also change the environment in ways that are bad for them e.g. by resource depletion or the production of toxic byproducts. Recent experiments by Christoph Ratzke and Jeff Gore focused on the collective growth behavior in soil bacteria [41]. Here, bacteria interact by modifying and reacting to the environmental pH which can lead to cooperative as well as growth-inhibiting effects.

Motivation and research question

In this project we wanted to better understand the collective growth behavior of bacterial populations that alter their environment in a way that is detrimental for them. In particular, we were intrigued by the phenomenon of self-inflicted death observed in *Paenibacillus sp.* (most similar to *Paenibacillus tundrae*) and wanted to find its underlying dynamics and ways of manipulation.

Summary of results

Bacteria can change their environmental pH and thereby cause their own extinction. Previous well-mixed growth experiments by Christoph Ratzke and Jeff Gore showed that various soil bacteria can change their environmental pH, which in turn can effect their population growth [41]. In this project of my doctoral studies, I mostly used the soil bacterium *Paenibacillus sp.* and studied its population growth in the presence of glucose as main carbon source and at initially neutral pH. In dynamic

measurements of the population size and the pH, we find an initial population growth followed by a strong acidification in the medium. After this sudden drop in pH, the bacteria started to die, resulting in extinction of the whole population after 24 hours. We were able to manipulate this non-monotonous growth of population size by changing the buffer concentration in the medium: For sufficiently high buffer concentrations, the pH hardly changes and the bacterial population grows until it eventually reaches its carrying capacity and saturates.

Ecological suicide can cause oscillations in the population size over time. Since *Paenibacillus sp.* change their environmental pH collectively, a higher initial population size should lead to a stronger acidification and thereby to a lower final population size. We confirmed this reciprocal relation between initial and final population size in culture growth experiments with different initial bacterial densities. To study long-term effects, we used daily dilution experiments, where in the course of 11 days, every day we diluted the bacteria from the end of the previous day to fresh medium with neutral pH. We did this for media with different buffer concentrations and find that for very low and high buffer concentrations, the bacterial population respectively goes extinct or saturates after the first day already. For intermediate buffer concentrations, we observe oscillations in the population size that can span over five orders of magnitude. Employing fluorescent nanobeads to track the pH dynamics, we find that these oscillations are accompanied by oscillations in the acidification time, i.e. the time when acidification is strongest.

Inhibiting growth of the bacteria can save the population. When bacterial growth leads to self-conflicted death, inhibiting growth might prevent this death. We tested this intuition by adding different amounts of harmful, growth-inhibiting substances like salt, alcohol and antibiotics. Indeed, for moderate amounts, these substances were able to rescue bacteria from ecological suicide. In contrast, too low or too high amounts of the substances lead to ecological suicide or kill the bacteria, respectively.

Ecological suicide is a common phenomenon in bacteria. Although we focused on *Paenibacillus sp.* in our study, many microbes are known to alter their environmental pH by metabolic activities [41, 42]. In 24-hours growth experiments, we studied the pH change and population growth of 119 isolated soil bacteria and identified the 21 species with the largest change in pH (irrespective of in- or decrease). We let grow these 21 species in the presence of low and high buffer concentrations and found that among these species, five show ecological suicide, while another four at least inhibit their own growth by changing their ambient pH. The remaining species either change their pH in a way that promotes their growth or do not show an impact of their environmental pH on population growth.

Relevance and outlook

Our study highlights the important role of the dynamics of the environment in which bacterial communities live. The mutual feedback between population growth and a change in the environment can lead to interesting dynamics such as monotonous growth and oscillations, albeit often neglected in traditional conceptions of bacterial growth. Our work shows that ecological suicide is in many ways a mirror image of prominent, well-studied cooperative interactions. We therefore think that it will be of similar interest especially in the context of microbial ecology and communities.

The results from this project were published in "Ecological suicide in microbes", Nat. Ecol. Evol., 2(2018) 867, and are reprinted in section III.2.

Contents

I Pattern formation in the Min protein system

I.1 The Min protein system in *Escherichia coli*

Correct and robust positioning of proteins is crucial at many stages of bacterial cell division, including chromosome segregation [43, 44], midcell localization [1, 45], and cell wall synthesis [46, 47]. Protein positioning is typically based on the self-organization of protein systems [13], which can lead to intriguing intracellular patterns such as protein accumulation at the cell poles [13, 43], pole-to-pole oscillations [48, 49] (fig. I.1(a)) and dynamic ring patterns [1, 32] (fig. I.1(b)).

In particular, the Min system, which consists of the proteins MinC, MinD and MinE, has been identified as a key component of cell division in *Escherichia coli* [1]. MinC, MinD, and MinE self-organize into pole-to-pole oscillations and thereby establish a time-averaged concentration minimum of MinC at midcell [48, 49]. MinC is an inhibitor of the cell division protein FtsZ, which initiates cell wall synthesis by recruiting the cell division machinery [32, 50, 51]. The pole-to-pole oscillations of the Min proteins thus guide the cell division machinery to midcell and ensure division into equally sized daughter cells. Various *in vivo* experiments have shown that a manipulation of the Min self-organization process by mutations [7, 48, 49, 52, 53], protein overexpression [7, 48, 52], or changes in the cell geometry [48, 54, 55] can alter the pole-to-pole oscillations and lead to a variety of protein patterns including multiple MinC concentration minima [48], traveling wave patterns [52](fig. I.1(c)), short axis oscillations, and circular waves [54, 55]. More recent studies even suggest multistability of these patterns [55].

The first reconstitution of the Min proteins was achieved by Loose et al. [6] in a lipid bilayer assay. Here, in the presence of ATP, the authors observed self-organization of MinD and MinE into robust surface waves on a flat, supported bilayer (fig. I.1(d)). *In vitro* experiments enabled a controlled variation of parameters such as protein densities [15, 57, 58] and the enclosing geometry [16, 59], and gave access to several characteristic properties of Min patterns including wavelengths and velocities of patterns [15, 21, 58], and their concentration profiles on the membrane [15, 21]. Furthermore, these experiments have revealed interesting patterns such as standing, traveling and circular waves in confined geometries [16, 60], as well as more irregular patterns [56, 57](fig. I.1(e)) such as chemical turbulence [57] (fig. I.1(f)).

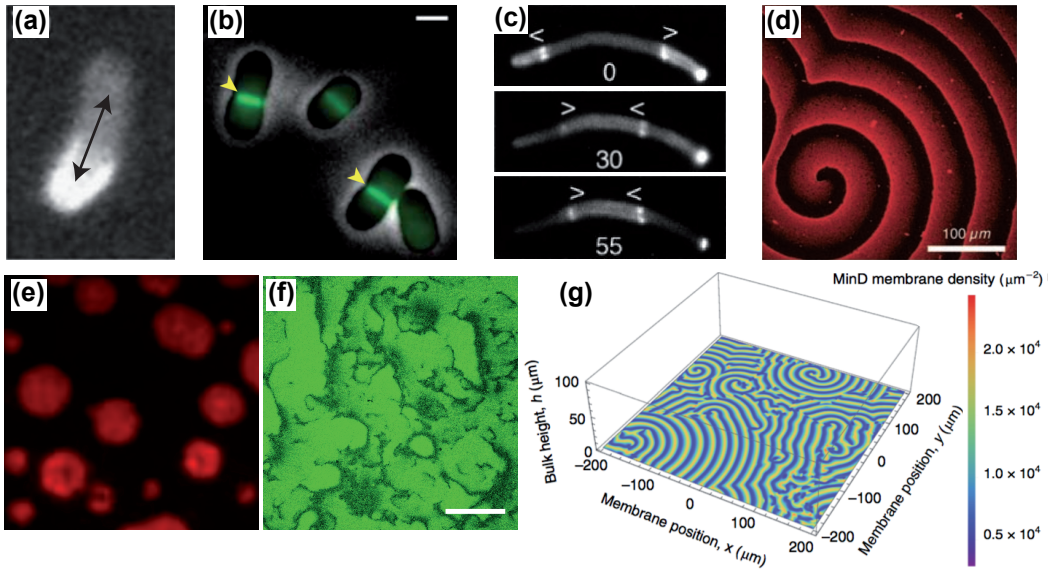

Figure I.1 Examples of protein pattern formation in the cell, in reconstitution experiments, and in simulations, adapted from respective publications. **(a)** in *E. coli*, the Min system organizes into pole-to-pole oscillations (MinD-GFP is shown) [48] (the arrow is added to indicate oscillations). **(b)** Top view of dense ring patterns formed by FtsZ polymers, initiating cell wall synthesis of *E. coli* at midcell [51]. **(c)** In the absence of FtsZ, *E. coli* grows into filamentous cell which lead to traveling waves (MinE-GFP is shown) [52]. **(d)** *In vitro* MinD and MinE self-organize into spiral waves on the supported lipid bilayer (MinE is shown) [6]. **(e)** Irregular "burst"-patterns observed in an *in vitro* flowcell [56] (MinE is shown). **(f)** Chemical turbulence for small MinE concentrations at the onset of pattern formation (MinD is shown, see section I.2, [57]) **(g)** Simulation results of a mathematical reaction-diffusion model for the Min system in an emulated *in vitro* geometry [23].

Both, *in vivo* and *in vitro* experiments have yielded important insights into the reaction-diffusion network underlying the Min self-organization process [13, 61]. MinD is an ATPase, which diffuses in the cytosol and can attach to the plasma membrane, depending on its nucleotide state [8, 13]. More specifically, ATP-bound MinD dimerizes and binds to the membrane [13, 62, 63], where it recruits further MinD as well as its cognate ATPase-activating protein MinE, which together form membrane-bound MinDE complexes [62]. In the complex, MinE stimulates ATP hydrolysis by MinD, which leads to dissociation of the MinDE complex and release of MinE and ADP-bound MinD into the cytosol. After exchange of ADP for ATP, MinD can reattach to the membrane and the cycle starts anew. The apparent simplicity of this ATP-driven reaction cycle together with the rich pattern phenomenology, has motivated numerous theoretical approaches to the Min system [4–6, 14, 23, 55, 64–66]. Based on the above reaction scheme, these theoretical descriptions were able of recapitulating various aspects of the Min systems such as pole-to-pole oscillations [4, 5, 14], geometry sensing [26, 54, 55] and the formation of various patterns in *in vitro*-like geometries including spiral waves (fig. I.1(g)) and turbulent dynamics [23].

Despite the important advances in the field of Min pattern formation over the last 15 years, there are still several open questions regarding the microscopic reaction network of MinD and MinE, as well as the formation of large-scale protein patterns. For instance, recent structural biology experiments [7, 17, 18] pointed towards a neccessary refinement of the MinE dynamics in the above reaction-diffusion protein network. In particular, the results by Park et al. [7] strongly suggest that MinE can switch between two different conformational states, depending on interaction with MinD. While native MinE is present in a six-stranded β sheet structure, interactions with membrane-bound MinD induce a conformational change in MinE to a four-stranded β sheet structure. The remaining two sheets are converted into α helices, which serve as interaction regions with MinD. Structural biology experiments [7, 17, 18] suggest that this conformational switch is critical for MinE's interaction affinity with MinD as well as the membrane; however, the role of MinE's conformational switch in protein pattern formation has been unaddressed.

In the first section of this chapter (section I.2), we discuss the effect of a conformational switch of MinE suggested by [7, 17, 18] on pattern formation. Here, in cooperation with our experimental collaborators Simon Kretschmer and Petra Schwille from the Max Planck Institute of Biochemistry in Martinsried, Germany, we extended a previous mathematical reaction-diffusion model of the Min system [4, 5] by a conformational switch of MinE. We emulated the conformational switch suggested by [7, 17, 18] by a change in MinE's recruitment rate to membrane-bound MinD upon MinE recruitment. On the basis of linear stability analyses and finite element simulations, our results predict that a MinD-dependent switch of MinE between different MinD binding affinities is central for protein pattern formation in a

broad and physiological range of protein concentrations. This prediction is confirmed by *in vitro* experiments with suitable MinE mutuants. Here, Simon Kretschmer and Petra Schwille found that MinE mutants lacking a conformational switch display patterns in a dramatically reduced range of protein concentrations as compared to MinE variants capable of conformational switching. In particular, surface patterns could only be found when MinD exceeds MinE in overall concentration. This confirms previous theoretical studies lacking a conformational switch of MinE [4, 14, 23], which predicted protein patterns only when MinD is more abundant than MinE. Our combined results thus strongly suggest that a mutual switch between MinD and MinE is essential for robust Min pattern formation. The results from this project were published in "MinE conformational switching confers robustness on self-organized Min protein patterns", Proc. Natl. Acad. Sci. (2018), and are reprinted in section I.2.

On the basis of the original reaction-diffusion system presented above (without conformational switching of MinE), a recent theoretical study by Halatek et al. [23] was able to reproduce a variety of surface protein patterns previously observed in reconstitution experiments [6, 56]. In particular, Halatek et al. [23] report the formation of standing wave patterns, spiral waves (fig. I.1(g)) as well as chemical turbulence as a function of the bulk height in an emulated *in vitro* geometry. Remarkably, turbulence is observed right at the onset of pattern formation, in contrast to previous conceptions of pattern formation, where turbulence is typically induced by the nonlinear coupling of multiple unstable modes far beyond the onset of pattern formation [24, 25]. The observation of turbulence at the onset of pattern formation in [23] is consistent with our experimental observations discussed in section I.2 [57], where we find turbulent surface patterns for MinE concentrations close to the threshold to pattern formation (fig. I.1(f)). The critical role of the vertical bulk extension and the observation of turbulence at the onset of pattern formation were leading the way for the second project of this chapter, described in section I.3. Here, we developed a spatial reduction of the mathematical reaction-diffusion model used in [23], where the complete vertical bulk extension is reduced to two layers: a 'reactive layer' close to the membrane, which accounts for the rapid protein flux between the bulk and the membrane, and a 'reservoir layer' further away from the membrane, which accounts for the lateral diffusion in the bulk. Employing linear stability analyses and finite element simulations, we show that this *two-layer model* reproduces the full pattern phenomenology of the original reaction-diffusion model; in particular, we identify a phase of turbulent patterns at the onset of pattern formation. On the basis of the two-layer model, we investigate the mechanisms underlying pattern selection and suggest an unprecedented route to turbulence based on a single-mode instability.

I.2 Publication

MinE conformational switching confers robustness on self-organized Min protein patterns

by

J. Denk[1,*], S. Kretschmer[2,*], J. Halatek[1,*], C. Hartl[1], P. Schwille[2], and E. Frey[1]

[1] Arnold Sommerfeld Center for Theoretical Physics (ASC) and Center for NanoScience (CeNS), Department of Physics, Ludwig-Maximilians-Universität München, Theresienstrasse 37, D-80333 München, Germany

[2] Max-Planck-Institute of Biochemistry, Am Klopferspitz 18, D-82152 Martinsried, Germany

[*] These authors contributed equally

Reprinted on pages 7–33

Published in **Proceedings of the National Academy of Sciences, (2018)**,
DOI: 10.1073/pnas.1719801115,
The supplemental material is reprinted on pages 34–62.

MinE conformational switching confers robustness on self-organized Min protein patterns

Short Title: MinE fold switching makes Min patterns robust

Authors: Jonas Denk[1,†], Simon Kretschmer[2,†], Jacob Halatek[1,†], Caroline Hartl[1], Petra Schwille[2,*], and Erwin Frey[1,*,#]

Affiliations:

[1]Arnold-Sommerfeld-Center for Theoretical Physics and Center for NanoScience, Ludwig-Maximilians-Universität München, Theresienstraße 37, D-80333 München, Germany.

[2]Max-Planck-Institute of Biochemistry, Am Klopferspitz 18, D-82152 Martinsried, Germany.

†These authors contributed equally.

*Correspondence to: schwille@biochem.mpg.de (P.S.), frey@lmu.de (E.F.)

#Lead Contact.

Major Categories: Physical Sciences, Biological Sciences

Minor Categories: Biophysics and Computational Biology

Keywords: Min system, pattern formation, protein reaction-diffusion networks, conformational switching, *in vitro* reconstitution

Abstract:

Protein patterning is vital for many fundamental cellular processes. This raises two intriguing questions: Can such intrinsically complex processes be reduced to certain core principles and, if so, what roles do the molecular details play in individual systems? A prototypical example for protein patterning is the bacterial Min system, in which self-organized pole-to-pole oscillations of MinCDE proteins guide the cell division machinery to midcell. These oscillations are based on cycling of the ATPase MinD and its activating protein MinE between the membrane and the cytoplasm. Recent biochemical evidence suggests that MinE undergoes a reversible, MinD-dependent conformational switch from a latent to a reactive state. However, the functional relevance of this switch for the Min network and pattern formation remains unclear. By combining mathematical modeling and *in vitro* reconstitution of mutant proteins, we dissect the two aspects of MinE's switch, persistent membrane binding and a change in MinE's affinity for MinD. Our study shows that the MinD-dependent change in MinE's binding affinity for MinD is essential for patterns to emerge over a broad and physiological range of protein concentrations. Mechanistically, our results suggest that conformational switching of an ATPase-activating protein can lead to the spatial separation of its distinct functional states and thereby confer robustness on an intracellular protein network with vital roles in bacterial cell division.

Significance Statement:

Many fundamental cellular processes are spatially regulated by self-organized protein patterns, which are often based on nucleotide-binding proteins that switch their nucleotide state upon interaction with a second, activating protein. For reliable function, these protein patterns must be robust against parameter changes, although the basis for such robustness is generally elusive. Here we take a combined theoretical and experimental approach to the *E. coli* Min system, a paradigmatic system for protein self-organization. By mathematical modeling and *in vitro* reconstitution of mutant proteins, we demonstrate that the robustness of pattern formation is dramatically enhanced by an interlinked functional switching of both proteins, rather than one. Such interlinked functional switching could be a generic means of obtaining robustness in biological pattern-forming systems.

Introduction:

Self-organized pattern formation by proteins is vital for many fundamental cellular processes, ranging from cell division (1) and chromosome segregation (2) to chemotaxis (3). To what extent then do these intrinsically complex processes depend on common, core principles and, conversely, what role do specific molecular details play in these biochemical reaction networks? In this context, it is particularly interesting to ask how robust network function is against changes in network structure, and system parameters such as protein concentrations.

Among intracellular pattern-forming networks, the *E. coli* Min system has become a paradigmatic model for both experimental (4-9) and theoretical (4, 6, 10-16) studies of protein pattern formation over the last 15 years.

Here, MinD and MinE self-organize to generate pole-to-pole oscillations that establish a time-averaged concentration minimum of MinC at midcell. Since MinC acts as an inhibitor of the cell division protein FtsZ, the Min system thereby confines the division machinery to mid-cell to ensure division into equally sized daughter cells (17). The Min system is a particularly instructive example, because its components are well characterized and it can be reconstituted in lipid bilayer assays *in vitro* (1, 4, 5). In the presence of ATP, MinD and MinE self-organize into surface waves on a flat, supported membrane (4). Experimental (4, 5, 9, 18) and theoretical (4, 6, 10-16) studies have yielded insights into the reaction network underlying this self-organization process. However, the relationships between pattern formation and the molecular properties of the proteins involved are a matter of ongoing interest, as they bridge the molecular and cellular scales.

The oscillatory dynamics of the Min system are driven by the stimulation of MinD's ATPase activity by MinE. ATP-bound MinD dimerizes and binds to the plasma membrane (9, 19, 20). It then recruits further MinD-ATP, as well as its ATPase-activating protein MinE, which together form membrane-bound MinDE complexes (19). MinE stimulates MinD's ATPase activity, thereby initiating disintegration of MinDE complexes and subsequent release of MinE and ADP-bound MinD into the cytosol (19, 21). After detachment, MinD exchanges ADP for ATP, before the ATP-bound form rebinds to the membrane (19, 20). This biochemical reaction network, which we refer to as the skeleton network (Fig. 1A), is in agreement with various experimental studies (4, 5, 18, 22) and has formed the basis for a number of theoretical models (10, 11, 13) that recapitulate various aspects of Min pattern formation.

Experimental studies have established the crucial role of MinE's stimulation of MinD's ATPase activity in Min protein pattern formation (4, 21). Moreover, mathematical models centered around the conversion of MinD from the ADP- to the ATP-bound state suggest that this step is critical for efficient localization of the FtsZ ring to mid-cell (11), formation of multistable patterns, and adaptation to cell geometry (6, 11, 23). Recently, it has been shown that the skeleton network captures the *in vitro* phenomenology of Min protein patterns on flat lipid bilayers (16). The theory predicts chemical turbulence (spatiotemporal chaos) at the onset of the pattern forming instability, e.g. at low MinE/MinD ratios. Moreover, previous theoretical analyses (10, 11, 13), based solely on the interactions in the skeleton network, found that patterns can form only if MinE is less abundant than MinD (SI Note 3). However, reconstitution experiments clearly show that patterns emerge for MinE/MinD ratios ranging between 0.125 and 5 (4, 7, 24-26). This contradiction prompts a reconsideration of the current perspective on the

Min reaction network, and raises the general question of how pattern-forming networks become robust against variations in protein concentrations. Furthermore, over the course of evolution, the robustness of a network's function, such as protein patterning, against alterations in protein number is essential to enable the system's characteristics to adapt without disrupting its core function.

Indeed, recent biochemical findings (27, 28) suggest a possible extension of the skeleton network. In addition to the MinE-induced switch in MinD's nucleotide state, MinE itself is now believed to undergo a MinD-dependent conformational switch. This conformational switch causes cytosolic MinE to unmask its buried MinD- and membrane-interacting regions, i.e. its anti-MinCD helix and membrane-targeting sequence (MTS), respectively (Fig. 1B) (27). Importantly, in order to expose its anti-MinCD helix, MinE must first "sense" membrane-bound MinD (27), a process that was proposed to involve formation of an "encounter complex" of MinE with MinD, which then triggers the conformational change (28, 29). Once the anti-MinCD domain is released, MinE is assumed to form a tighter complex with membrane-bound MinD and stimulate its ATPase activity (27-29). In addition, after dissociation of the MinDE complex and the release of MinD-ADP into the cytosol, MinE's MTS enables it to remain bound to the membrane, and the protein may reassociate repeatedly with other membrane-bound MinD molecules or (eventually) return to the cytosol (5, 27, 28). This membrane-bound cycling of MinE has been dubbed the "Tarzan of the Jungle" mechanism (27) or persistent MinE membrane binding (24) in the literature. Upon detachment from the membrane, MinE quickly reassumes its latent conformation with its MinD- and membrane-interaction regions buried (Fig. 1B). *In vivo* studies have suggested that the MinD-dependent conformational switch of MinE is important for

correct cell division, as a mutation that locks MinE into the reactive state was not able to restore the WT phenotype when expressed with MinC and MinD in a *Δmin* strain of *E. coli* (30). Despite recent experimental research on the molecular interaction steps involved in this switch (28, 29), the functional role of MinE's conformational switch in the Min reaction-diffusion network and its effect on pattern formation remains unclear. *In vivo*, this question is difficult to address systematically due to the disruptive effects on cell morphology and viability caused by mutations and changes in protein concentration (27, 31). In contrast, *in silico* and *in vitro* approaches both allow highly comparable conditions and the precise variation of parameters. Therefore, we addressed the function of MinE's conformational switch in pattern formation by combining mathematical modeling and cell-free reconstitution experiments.

The two novel properties of MinE's reactive conformation – facilitation of the MinE-MinD interaction and persistent membrane binding of MinE – could independently affect the formation of patterns. To disentangle these two aspects and analyze their respective impacts on pattern robustness to variations in the MinE/MinD ratio, we first numerically studied the dynamics of reaction-diffusion networks that exhibit either aspect of the switch by a linear stability analysis, which predicts the parameter regime within which patterns form (SI Note 1). Then we tested the theoretical predictions by reconstituting the networks using suitable MinE mutants (see Methods and SI Note 2). Our combined theoretical and experimental results demonstrate that the MinE-MinD interaction switch of MinE is critical for the emergence of patterns over a broad and physiological range of protein concentrations. Furthermore, we experimentally show that, unlike the MinE-MinD interaction switch, persistent membrane binding of MinE does not markedly affect the protein concentration range compatible with pattern formation.

Results

The MinE-MinD interaction switch is critical for the robustness of Min patterns against variations in protein concentration. First, we addressed the functional relevance of the MinD-induced exposure of MinE's buried MinD interaction region alone. Upon recruitment of MinE by MinD, a membrane-bound MinDE complex is formed, in which MinE is assumed to be present in its reactive state. After disintegration of a MinDE complex, both partners are released into the cytosol. We assume that switching of reactive MinE to its latent form occurs rapidly, but not simultaneously with the disintegration of a MinDE complex and release of MinE into the cytosol (SI Note 6). The time scale for reversion of reactive MinE to its latent conformation is taken to be of the order of 0.01s, the upper bound for a typical conformational switch (32). To account for the alternative conformations of MinE, we extended the skeleton network (11, 13) to include both a latent MinE conformation and a reactive form with recruitment rates to membrane-bound MinD, k_{dE}^{l} and k_{dE}^{r}, respectively (Fig. 1C). Reactive MinE no longer requires the MinD-dependent release of its anti-MinCD helix, as this structure is already exposed. Thus, it is reasonable to assume the recruitment rate of reactive MinE to be higher than that of latent MinE. Note, that for equal recruitment rates, i.e. $k_{dE}^{l} = k_{dE}^{r}$, the two MinE conformations are identical and the original skeleton network with only one MinE recruitment rate is recovered.

Our mathematical analysis shows that, in a broad regime of low k_{dE}^{l} and high k_{dE}^{r}, patterns are formed over a wide range of MinE/MinD ratios, including those where MinE is present in excess (Figs. 2A, B). To test these theoretical predictions experimentally, we made use of the MinE L3E mutant, which is impaired in membrane interaction (27). It should therefore be capable of

undergoing the MinD-induced interaction switch, but unable to remain attached to the membrane in the absence of MinD (see SI Note 2). Thus, we expect this mutant to mimic MinE in our extended model that includes a MinE-MinD interaction switch without persistent membrane binding (Fig.1C, SI Note 2). When reconstituted together with MinD on flat membranes, MinE L3E promoted pattern formation over a wide range of MinE/MinD ratios, just like wild-type MinE (Fig. 3). In agreement with our theoretical predictions (Fig. 2A, B), experiments showed that patterns formed even when MinE was present in excess over MinD (Fig. 3).

Based on our theoretical observations, which showed a strong increase in pattern robustness upon incorporation of a MinE-MinD interaction switch, we propose that MinE's ability to switch between conformations with high or low affinity for MinD is responsible for the experimental observation that high MinE/MinD concentration ratios are compatible with Min protein patterns. If this hypothesis is true, experiments with MinE mutants that lack the ability to switch between a reactive and a latent state should display a strongly decreased maximal MinE/MinD concentration ratio compatible with patterns. To test this hypothesis, we took advantage of the I24N mutation, which was previously shown to lock MinE into the reactive state ((27), SI Note 2). Strikingly, introducing this mutation into either WT MinE or MinE L3E dramatically reduced the concentration range within which protein patterns formed (Figs. 3, 4). Indeed, in agreement with the above hypothesis based on our theory (11), patterns only prevailed in a very narrow range and only for MinE/MinD concentration ratios far below one (Figs. 3, 4). In particular, MinE I24N formed patterns only outside the physiological concentration range (33). This is consistent with *in vivo* experiments in which the I24N mutant failed to restore mid-cell division when expressed together with MinD and MinC in an *E. coli Δmin* strain (30), most probably due

to the fact that MinC is not recruited to the membrane by MinD. This agrees with our observations that (i) MinD cannot effectively accumulate on the membrane to initiate pattern formation above a certain threshold MinE/MinD ratio, and (ii) that this threshold is strongly decreased for MinE I24N relative to WT MinE (Fig. 3). In summary, our analyses demonstrate that mutually interlinked protein switching is critical for the robustness of an exemplary pattern-forming system against variations in protein concentrations.

The relationship between the MinE/MinD ratio and the ability to generate patterns can be understood by considering the roles of the two proteins in the establishment of Min oscillations. Min oscillations are essentially the result of alternating dominance of MinE and MinD (11, 24). In membrane regions depleted of Min proteins, cooperative binding of MinD first facilitates its own accumulation on the membrane (MinD dominance). Then, recruitment of MinE and MinE-induced detachment of MinD together outpace further MinD accumulation, and progressively deplete the latter from the membrane (MinE dominance). But MinE-induced detachment can only outpace MinD accumulation if the released MinE is recruited more rapidly to membrane-bound MinD than is MinD itself. Thus, the rate of recruitment of MinE must be higher than that of MinD. Since the skeleton network incorporates only a single, rapidly recruited MinE conformation, initial dominance of MinD accumulation is feasible only if MinD exceeds MinE in concentration. In contrast, if MinE can exist in both a latent and a reactive conformation, dominance of MinD over MinE becomes possible even if MinE exceeds MinD in concentration (Fig. 2C). This is because initially most MinE is in the latent form, whose recruitment rate is low. If MinE was always present in its latent form only, MinD would accumulate on the membrane and Min dynamics would cease, because the recruitment of latent MinE will never

dominate MinD recruitment. However, after inducing ATP hydrolysis by MinD, MinE is assumed to be released into the cytosol in its reactive conformation. As this state is short-lived, the reactive species is effectively restricted to a thin boundary layer close to the membrane (Fig.2C, indicated by red shaded region), and will be preferentially recruited (over cytosolic MinD) to membrane-bound MinD. Once the membrane is depleted of MinD, reactive MinE cannot rebind promptly and rapidly switches to its latent cytosolic form. This enables a transient dominance of MinE, which displaces MinD from the membrane. Remarkably, our theoretical analysis predicts an extended range of MinE/MinD ratios that support patterns even for very rapid MinE switching, i.e. when the layer of reactive MinE (~ 0.7 μm) is orders of magnitude thinner than the depth of the cytosol (~ 5,000 μm) (SI Note 5). Note that any effective ad hoc reduction of the cytosol to two dimensions would, by neglecting the protein distribution perpendicular to the membrane (34, 35), fail to uncover such subtle but crucial effects, as the emergence of the thin layer of reactive MinE would be entirely lost. This further emphasizes the importance of accounting for the extended bulk in (3D) quantitative theoretical models (11, 16, 36).

Persistent MinE membrane binding is not a major determinant of the concentration range of Min patterns. As MinE's conformational switch affects its affinity for both MinD and the membrane (27), we independently explored the impact of persistent MinE membrane binding mediated by its MTS (Fig.1D, SI Notes 1, 7, 8). This was previously shown to influence Min patterns (22, 24, 25, 35, 37), and was implied to be required for Min protein pattern formation per se (35), although the validity of the underlying theoretical analysis (35) is controversial (36).

Recent experimental studies have confirmed that Min protein patterns can indeed form without direct MinE membrane interaction, although with altered *in vitro* characteristics (22, 25).

As hypothesized previously (11), persistent membrane binding might also affect the concentration range compatible with pattern formation. Assume that "free" membrane-bound MinE has a weak affinity for membrane-bound MinD, such that membrane-bound MinE is more likely to detach after lingering on the membrane than to reassociate with membrane-bound MinD. Then persistent MinE membrane binding will reduce the overall efficacy of MinE-mediated removal of MinD from the membrane, because free MinE lingering on the membrane does not participate in the depletion process. As a consequence, the maximal MinE/MinD concentration ratio compatible with patterns should increase in this case. On the other hand, if free membrane-bound MinE interacts very strongly with membrane-bound MinD – hypothetically even more strongly than the MinE in the bulk – persistent MinE membrane binding will enhance MinD depletion and patterns should form for even lower MinE/MinD concentration ratios.

We quantitatively studied a reaction network in which MinE can persistently bind to the membrane but is permanently locked into its reactive state (Fig. 1D). We expect this model to be best realized by our experiments with the I24N mutant, which lacks the MinE-MinD interaction switch while retaining the ability to bind persistently to the membrane (SI Note 2). With this mathematical model, we were able to confirm the above intuition regarding the two theoretical scenarios involving weak and strong interaction between free MinE and MinD on the membrane (SI Notes 7, 8, Figs. S4, S5). As reported above, our reconstitution experiments with MinE

mutants that lack the ability to persistently bind to the membrane show no change in the range of MinE/MinD concentrations permissive for patterns when compared to experiments with the respective MinE types without this mutation. In summary, we infer that, unlike the MinE-MinD switch, persistent membrane binding does not markedly affect the range of concentrations compatible with *in vitro* Min patterns (Figs. 3, 4).

The skeleton network suffices to reproduce *in vitro* Min patterns. In the MinE L3E/I24N double mutant, both membrane interactions and the MinE-MinD interaction switch are disabled, mimicking the MinE dynamics in the original skeleton network (11, 13). This mutant still self-organized into dynamic protein patterns, albeit only in a narrow range of MinE/MinD ratios (Fig. 3, 4), and – notably – only if MinD exceeds MinE in concentration, confirming previous theoretical predictions ((11), SI Note 3). This result shows that, given a suitable choice of low MinE/MinD ratios, neither persistent membrane binding nor the MinE-MinD switch is required to generate patterns, and it confirms the skeleton network as a valid and useful basis for the investigation of pattern-forming mechanisms in the Min system. A recent theoretical analysis of *in vitro* Min protein pattern formation based on the skeleton model (16) predicted chemical turbulence (disordered patterns) at the onset of instability (low MinE/MinD ratios). Interestingly, our experiments confirm this prediction (see Fig. 3) and show that this characteristic is preserved for all mutants.

Discussion

Based on recent experimental insights into the molecular structure of MinE and its ability to undergo MinD-dependent conformational changes (27-29), we studied the role of this conformational switch in the context of the Min reaction network. Our combined theoretical and experimental investigation reveals that this switch is essential for the robustness of the key function of the Min reaction network - the formation of spatio-temporal protein patterns.

Previous experiments (27, 28) strongly suggested that the different conformations of MinE are not in chemical equilibrium with each other, i.e. MinE does not switch between the two states independently of external triggers. Instead, MinE's conformational switch from latent to reactive critically depends on the "sensing" of membrane-bound MinD (27). In the context of a reaction-diffusion network, the spatial confinement of MinE's switched state to the immediate vicinity of membrane-bound MinD leads to a *spatial* separation of reactive MinE close to the membrane and latent MinE in the bulk. With regard to the change in MinE's binding affinity for MinD, this spatial separation provides for dynamic control of MinE's two distinct modes of action: in its latent form, MinE allows MinD to accumulate on the membrane even if the total MinE concentration exceeds that of MinD. Accumulation of MinD on the membrane in turn facilitates the formation of a thin reactive layer of MinE above the membrane, which eventually depletes MinD from the membrane (Fig. 2C). In contrast to networks with only one MinE conformation (10, 11, 13), the dynamic switching of MinE enables patterns to form even when MinE is much more abundant than MinD.

Furthermore, it was proposed that the exposure of MinE's MTS not only leads to persistent membrane binding of MinE but might even enable direct attachment of MinE to the membrane (25, 28), the stabilization of MinD by membrane-bound MinE (25), and might also be involved in the release of the anti-MinCD helix (28, 29). While MinE membrane interaction is evidently relevant for regulating the detailed characteristics of Min patterns, such as the wavelength (Fig. 3, (22, 25)) and proper function of the Min system *in vivo* (27, 38), our analyses show that the concentration range of Min patterns is not markedly affected by this factor, either in terms of persistent membrane binding or direct MinE attachment to the membrane (Fig. 3, SI Note 8). Instead, this concentration range is primarily determined by the MinD-dependent switch in MinE's affinity for MinD. This emphasizes that interlinked switching of the mutual binding affinities of MinD and MinE plays an important role in regulating the ability to form patterns.

The bacterial Min system is a prominent example for a class of intracellular pattern-forming networks that are based on the self-organization of nucleoside triphosphatases (NTPases). NTPases function as molecular switches, which upon interaction with a cognate NTPase activating protein transition from an NTP-bound to a nucleoside diphosphate (NDP)-bound form. In the context of network motifs, we identify a reciprocal switch – triggered in the ATPase-activating protein MinE by the cognate ATPase MinD – as a critical factor in the robustness of patterns over a broad range of protein concentrations. In view of the ubiquity of structurally switchable proteins, including NTPases and possibly further NTPase-activating proteins (39, 40), our study highlights the role of alternative conformations and mutual switches for robust pattern formation.

From a structural perspective, MinE can be seen as a “metamorphic” protein, a type of protein that can reversibly switch between alternative conformations with distinct functions (41). Among various examples for such proteins (41, 42), it has recently been discovered that fold switching of the metamorphic protein KaiB plays an important role in the KaiABC system, a prototypical protein oscillator that serves as a circadian clock in cyanobacteria (43-45). The observation of fold switching for both KaiB and MinE suggests that metamorphic proteins may be widespread in dynamical systems with important roles in cell physiology.

Intracellular pattern-forming systems are often based on reaction-diffusion networks (46, 47). Their underlying nonlinearities render these networks sensitive to even small variations in system parameters, such as reaction rates and the (approximately constant) concentrations. However, such sensitivity can also provide evolutionary benefits, as changes in protein concentrations can be harnessed to adjust features of the patterns, such as the oscillation period or characteristic wavelength (22). In this context, it is essential that the ability to generate patterns in the first place (regardless of their quantitative characteristics) is robust against variations in the concentrations of the relevant components. This provides a large parameter regime within which pattern formation is possible, thus facilitating the emergence of patterns with different spatiotemporal characteristics that may lead to evolutionary adaptations in cell morphology or other favorable phenotypic features. Furthermore, retention of the ability to form patterns in the face of alterations in protein numbers is essential for evolution, since this allows for protein mutations while the key functions of the organism, such as protein patterning, remain intact (48).

We propose that mutually interlinked switching is likely to be a general design principle that enhances the robustness of important regulatory patterns to variations in protein concentrations in many biological reaction-diffusion systems. In particular, interlinked switches have been reported for the widely conserved F1hF-F1hG circuit (39, 49), which is essential for flagellar patterning (39). Pattern robustness due to functional switching may also be relevant in other pattern-forming systems, such as for chemotaxis patterns (3), or chromosome segregation (2), and may even play a major role in eukaryotic systems, for instance in the process of cell polarization in budding yeast (50).

Materials and Methods:

Theoretical prediction of MinE/MinD ratios that permit the formation of patterns

Our theoretical analyses are based on different biochemical reaction networks that incorporate either a MinE-MinD interaction switch or persistent MinE membrane binding. These networks extend a previous theoretical model (11, 13) for the Min system, which accounts for the molecular interactions that are believed to be essential for Min protein dynamics, to include a MinE-MinD interaction switch and persistent MinE membrane binding, respectively, as additional features (SI Note 1). The data presented in Figs. 2A, and B and S2-S5 has been obtained numerically by performing stability analyses over an extensive range of reaction rates and protein contentrations (SI Note 1).

Protein purification

Expression and purification of His-MinD, His-eGFP-MinD as well as WT and mutant His-MinE were performed as described previously (4, 22).

Self-organization assays

Self-organization assays on flat supported lipid bilayers were performed essentially as described previously (4, 22). Briefly, SLBs composed of *E. coli* polar lipids (Avanti Polar Lipids, Alabaster, AL, USA) were prepared on glass as described in (22). Then, 1 μM MinD incl. 20% eGFP-MinD, 2.5 mM ATP (F. Hoffmann-La Roche AG, Basel, Switzerland) and MinE of varying concentration were added to Min buffer (25 mM Tris-HCl pH 7.5, 150 mM KCl, 5 mM $MgCl_2$) in a total volume of 200 μL. The samples were then incubated for several hours to provide ample time for protein patterns to form. The concentration ranges compatible with

pattern formation reported here were consistently observed in at least three independent experiments. For 0.3 μM MinE L3E/I24N, patterns were observed in only 50% of experiments. We therefore categorized this concentration as being incapable of reliable pattern formation.

Microscopy and image processing

Fluorescence imaging was performed with a ZEISS LSM780 confocal laser scanning microscope equipped with a Zeiss C-Apochromat 40x/1.20 water-immersion objective (Carl Zeiss AG, Oberkochen, Germany). Image processing was performed with Fiji (51). As fluorescence intensities were low around the upper bounds in MinE concentration compatible with pattern formation, we adjusted the brightness and contrast levels to better visualize the transition. As, for consistency, the same adjustments were equally made for all images, the intensities in the micrographs can be displayed outside the dynamic range.

Data availability

All relevant data are within the paper and its Supporting Information files.

Acknowledgments: We thank Laeschkir Hassan, Fridtjof Brauns, and Philipp Glock for discussions, and the MPI-B Core Facility for help with protein purification. E.F acknowledges support from the DFG via project B02 and P.S. via the project A09 within SFB 1032 and the German Excellence Initiatives via the 'NanoSystems Initiative Munich (NIM)'. J.D. and S.K. are supported by a DFG fellowship through the Graduate School of Quantitative Biosciences Munich (QBM).

Author contributions: J.H., J.D., S.K., P.S., and E.F. designed the research. J.D., J.H, C.H., and E.F. designed the theoretical models and performed the mathematical analyses. S.K. and P.S. designed and carried out the experiments. J.D., S.K., J.H., P.S., and E.F. discussed and interpreted the results, and wrote the manuscript.

Competing financial interest: The authors declare no competing financial interest.

References:

1. Kretschmer S & Schwille P (2016) Pattern formation on membranes and its role in bacterial cell division. *Curr Opin Cell Biol* 38:52-59.
2. Schofield WB, Lim HC, & Jacobs-Wagner C (2010) Cell cycle coordination and regulation of bacterial chromosome segregation dynamics by polarly localized proteins. *EMBO J* 29(18):3068-3081.
3. Sourjik V & Wingreen NS (2012) Responding to chemical gradients: bacterial chemotaxis. *Curr Opin Cell Biol* 24(2):262-268.
4. Loose M, Fischer-Friedrich E, Ries J, Kruse K, & Schwille P (2008) Spatial regulators for bacterial cell division self-organize into surface waves in vitro. *Science* 320(5877):789-792.
5. Vecchiarelli AG, Li M, Mizuuchi M, & Mizuuchi K (2014) Differential affinities of MinD and MinE to anionic phospholipid influence Min patterning dynamics in vitro. *Mol Microbiol* 93(3):453-463.
6. Wu F*, et al.* (2016) Multistability and dynamic transitions of intracellular Min protein patterns. *Mol Syst Biol* 12(6):873.
7. Caspi Y & Dekker C (2016) Mapping out Min protein patterns in fully confined fluidic chambers. *Elife* 5.
8. Raskin DM & de Boer PA (1999) Rapid pole-to-pole oscillation of a protein required for directing division to the middle of Escherichia coli. *Proc Natl Acad Sci U S A* 96(9):4971-4976.
9. Lutkenhaus J (2012) The ParA/MinD family puts things in their place. *Trends Microbiol* 20(9):411-418.
10. Fange D & Elf J (2006) Noise-induced Min phenotypes in E. coli. *PLoS Comput Biol* 2(6):e80.
11. Halatek J & Frey E (2012) Highly canalized MinD transfer and MinE sequestration explain the origin of robust MinCDE-protein dynamics. *Cell Rep* 1(6):741-752.
12. Howard M, Rutenberg AD, & de Vet S (2001) Dynamic compartmentalization of bacteria: accurate division in E. coli. *Phys Rev Lett* 87(27 Pt 1):278102.
13. Huang KC, Meir Y, & Wingreen NS (2003) Dynamic structures in Escherichia coli: spontaneous formation of MinE rings and MinD polar zones. *Proc Natl Acad Sci U S A* 100(22):12724-12728.
14. Kruse K (2002) A dynamic model for determining the middle of Escherichia coli. *Biophys J* 82(2):618-627.
15. Meinhardt H & de Boer PA (2001) Pattern formation in Escherichia coli: a model for the pole-to-pole oscillations of Min proteins and the localization of the division site. *Proc Natl Acad Sci U S A* 98(25):14202-14207.
16. Halatek J & Frey E (2018) Rethinking pattern formation in reaction-diffusion systems. *Nature Physics*.
17. Lutkenhaus J (2007) Assembly dynamics of the bacterial MinCDE system and spatial regulation of the Z ring. *Annu Rev Biochem* 76:539-562.
18. Wu F, van Schie BG, Keymer JE, & Dekker C (2015) Symmetry and scale orient Min protein patterns in shaped bacterial sculptures. *Nat Nanotechnol* 10(8):719-726.
19. Hu Z, Gogol EP, & Lutkenhaus J (2002) Dynamic assembly of MinD on phospholipid vesicles regulated by ATP and MinE. *Proc Natl Acad Sci U S A* 99(10):6761-6766.

20. Lackner LL, Raskin DM, & de Boer PA (2003) ATP-dependent interactions between Escherichia coli Min proteins and the phospholipid membrane in vitro. *J Bacteriol* 185(3):735-749.
21. Hu Z & Lutkenhaus J (2001) Topological regulation of cell division in E. coli. spatiotemporal oscillation of MinD requires stimulation of its ATPase by MinE and phospholipid. *Mol Cell* 7(6):1337-1343.
22. Kretschmer S, Zieske K, & Schwille P (2017) Large-scale modulation of reconstituted Min protein patterns and gradients by defined mutations in MinE's membrane targeting sequence. *PLoS One* 12(6):e0179582.
23. Thalmeier D, Halatek J, & Frey E (2016) Geometry-induced protein pattern formation. *Proc Natl Acad Sci U S A* 113(3):548-553.
24. Loose M, Fischer-Friedrich E, Herold C, Kruse K, & Schwille P (2011) Min protein patterns emerge from rapid rebinding and membrane interaction of MinE. *Nat Struct Mol Biol* 18(5):577-583.
25. Vecchiarelli AG*, et al.* (2016) Membrane-bound MinDE complex acts as a toggle switch that drives Min oscillation coupled to cytoplasmic depletion of MinD. *Proc Natl Acad Sci U S A* 113(11):E1479-1488.
26. Zieske K & Schwille P (2014) Reconstitution of self-organizing protein gradients as spatial cues in cell-free systems. *Elife* 3.
27. Park KT*, et al.* (2011) The Min oscillator uses MinD-dependent conformational changes in MinE to spatially regulate cytokinesis. *Cell* 146(3):396-407.
28. Park KT, Villar MT, Artigues A, & Lutkenhaus J (2017) MinE conformational dynamics regulate membrane binding, MinD interaction, and Min oscillation. *Proc Natl Acad Sci U S A* 114(29):7497-7504.
29. Ayed SH*, et al.* (2017) Dissecting the role of conformational change and membrane binding by the bacterial cell division regulator MinE in the stimulation of MinD ATPase activity. *J Biol Chem* 292(50):20732-20743.
30. Zheng M*, et al.* (2014) Self-assembly of MinE on the membrane underlies formation of the MinE ring to sustain function of the Escherichia coli Min system. *J Biol Chem* 289(31):21252-21266.
31. Hale CA, Meinhardt H, & de Boer PA (2001) Dynamic localization cycle of the cell division regulator MinE in Escherichia coli. *EMBO J* 20(7):1563-1572.
32. Shamir M, Bar-On Y, Phillips R, & Milo R (2016) SnapShot: Timescales in Cell Biology. *Cell* 164(6):1302-1302 e1301.
33. Shih YL, Fu X, King GF, Le T, & Rothfield L (2002) Division site placement in E.coli: mutations that prevent formation of the MinE ring lead to loss of the normal midcell arrest of growth of polar MinD membrane domains. *EMBO J* 21(13):3347-3357.
34. Bonny M, Fischer-Friedrich E, Loose M, Schwille P, & Kruse K (2013) Membrane binding of MinE allows for a comprehensive description of Min-protein pattern formation. *PLoS Comput Biol* 9(12):e1003347.
35. Schweizer J*, et al.* (2012) Geometry sensing by self-organized protein patterns. *Proc Natl Acad Sci U S A* 109(38):15283-15288.
36. Halatek J & Frey E (2014) Effective 2D model does not account for geometry sensing by self-organized proteins patterns. *Proc Natl Acad Sci U S A* 111(18):E1817.

37. Arjunan SN & Tomita M (2010) A new multicompartmental reaction-diffusion modeling method links transient membrane attachment of E. coli MinE to E-ring formation. *Syst Synth Biol* 4(1):35-53.
38. Hsieh CW*, et al.* (2010) Direct MinE-membrane interaction contributes to the proper localization of MinDE in E. coli. *Mol Microbiol* 75(2):499-512.
39. Bange G & Sinning I (2013) SIMIBI twins in protein targeting and localization. *Nat Struct Mol Biol* 20(7):776-780.
40. Leipe DD, Wolf YI, Koonin EV, & Aravind L (2002) Classification and evolution of P-loop GTPases and related ATPases. *J Mol Biol* 317(1):41-72.
41. Murzin AG (2008) Biochemistry. Metamorphic proteins. *Science* 320(5884):1725-1726.
42. Goodchild SC, Curmi PMG, & Brown LJ (2011) Structural gymnastics of multifunctional metamorphic proteins. *Biophys Rev* 3(3):143.
43. Chang YG*, et al.* (2015) Circadian rhythms. A protein fold switch joins the circadian oscillator to clock output in cyanobacteria. *Science* 349(6245):324-328.
44. Snijder J*, et al.* (2017) Structures of the cyanobacterial circadian oscillator frozen in a fully assembled state. *Science* 355(6330):1181-1184.
45. Tseng R*, et al.* (2017) Structural basis of the day-night transition in a bacterial circadian clock. *Science* 355(6330):1174-1180.
46. Frey E, Halatek J, Kretschmer S, & Schwille P (2017) Protein Pattern Formation. *Physics of Biological Membranes*, eds Bassereau P & Sens PCA (Springer-Verlag GmbH, Heidelberg).
47. Halatek J, Brauns F, & Frey E (2018) Self-organization principles of intracellular pattern formation. *Philosophical Transactions B*
48. Laan L, Koschwanez JH, & Murray AW (2015) Evolutionary adaptation after crippling cell polarization follows reproducible trajectories. *Elife* 4.
49. Schuhmacher JS, Thormann KM, & Bange G (2015) How bacteria maintain location and number of flagella? *FEMS Microbiol Rev* 39(6):812-822.
50. Klunder B, Freisinger T, Wedlich-Soldner R, & Frey E (2013) GDI-mediated cell polarization in yeast provides precise spatial and temporal control of Cdc42 signaling. *PLoS Comput Biol* 9(12):e1003396.
51. Schindelin J*, et al.* (2012) Fiji: an open-source platform for biological-image analysis. *Nat Methods* 9(7):676-682.
52. Ghasriani H*, et al.* (2010) Appropriation of the MinD protein-interaction motif by the dimeric interface of the bacterial cell division regulator MinE. *Proc Natl Acad Sci U S A* 107(43):18416-18421.
53. Wu W, Park KT, Holyoak T, & Lutkenhaus J (2011) Determination of the structure of the MinD-ATP complex reveals the orientation of MinD on the membrane and the relative location of the binding sites for MinE and MinC. *Mol Microbiol* 79(6):1515-1528.

Figure Legends:

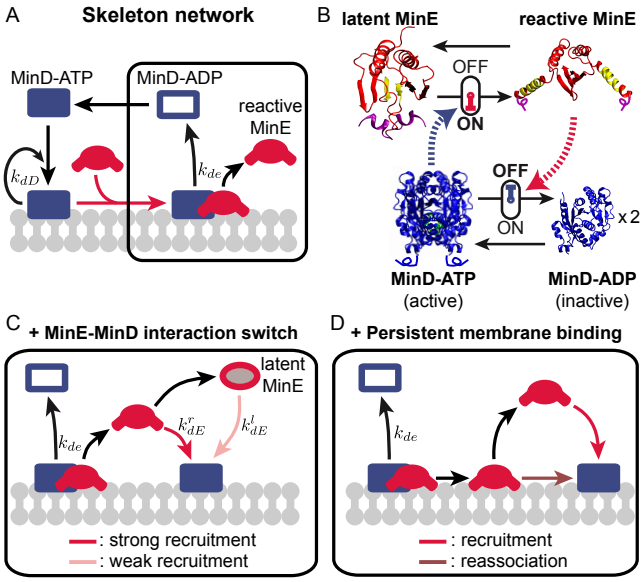

Figure 1. **MinE's conformational switch suggests distinct ways to form MinDE complexes.**

(*A*) The skeleton model only accounts for one MinE conformation. (*B*) Scheme of interlinked MinDE protein switches: While reactive MinE is known to trigger MinD's ATPase activity, membrane-bound (active) MinD induces the switching of MinE from a latent to a reactive state in which the previously inaccessible MinD interaction region (yellow) and membrane-targeting sequence (purple) are exposed (PDB files 3R9J (27), 2KXO (52) and 3Q9L (53) are used to illustrate reactive and latent MinE and MinD, respectively). (*C*) The extension to the skeleton network includes a MinE-MinD interaction switch for interconversion between latent and reactive states of MinE, which are weakly or strongly recruited to MinD with rates k^l_{dE} or k^r_{dE}, respectively. (*D*) Persistent MinE membrane binding allows MinDE complexes to form either by recruitment of cytosolic MinE or reassociation of already membrane-bound MinE with membrane-bound MinD. For both extensions the MinD reaction dynamics remains unchanged.

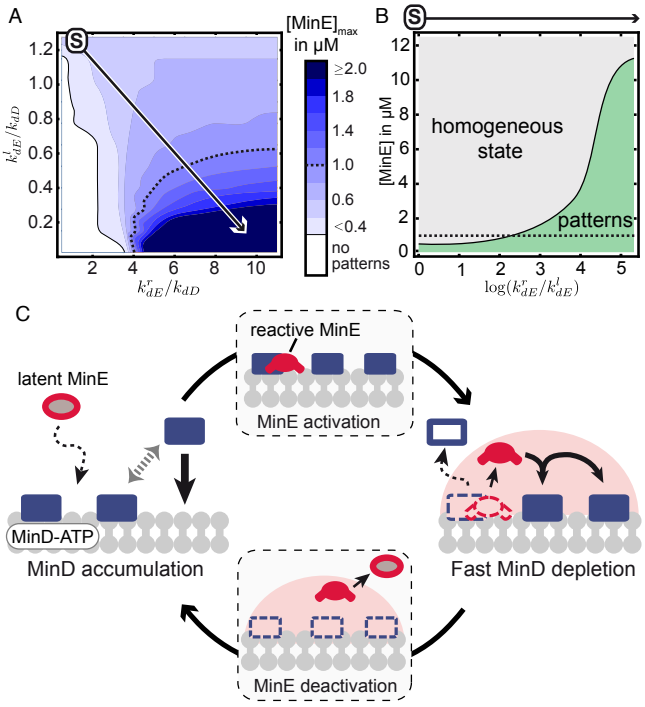

Figure 2. **The MinE-MinD interaction switch is essential for the robustness of Min patterns *in silico*.** (*A*) For high k_{dE}^{r} and low k_{dE}^{l} (compared to the MinD recruitment rate k_{dD}), linear stability analysis predicts an increase in the maximal MinE concentration compatible with patterns ($[\mathrm{MinE}]_{\mathrm{max}}$) relative to the skeleton network where $k_{dE}^{r} = k_{dE}^{l}$ (the case $k_{dE}^{r} = k_{dE}^{l} = 1.25\ k_{dD}$, indicated by S, is given as an example). [MinD] is fixed at 1 µM. (*B*) Along the arrow in (*A*) the range of [MinE] compatible with patterns dramatically increases with k_{dE}^{r} / k_{dE}^{l}. For k_{dE}^{l} close to zero, MinE eventually ceases to cycle between the bulk and the membrane, and pattern formation is suppressed (SI Note 4). (*C*) MinD-induced switching of MinE facilitates alternation of MinD accumulation and MinD depletion on the membrane. For kinetic rates see Table S1.

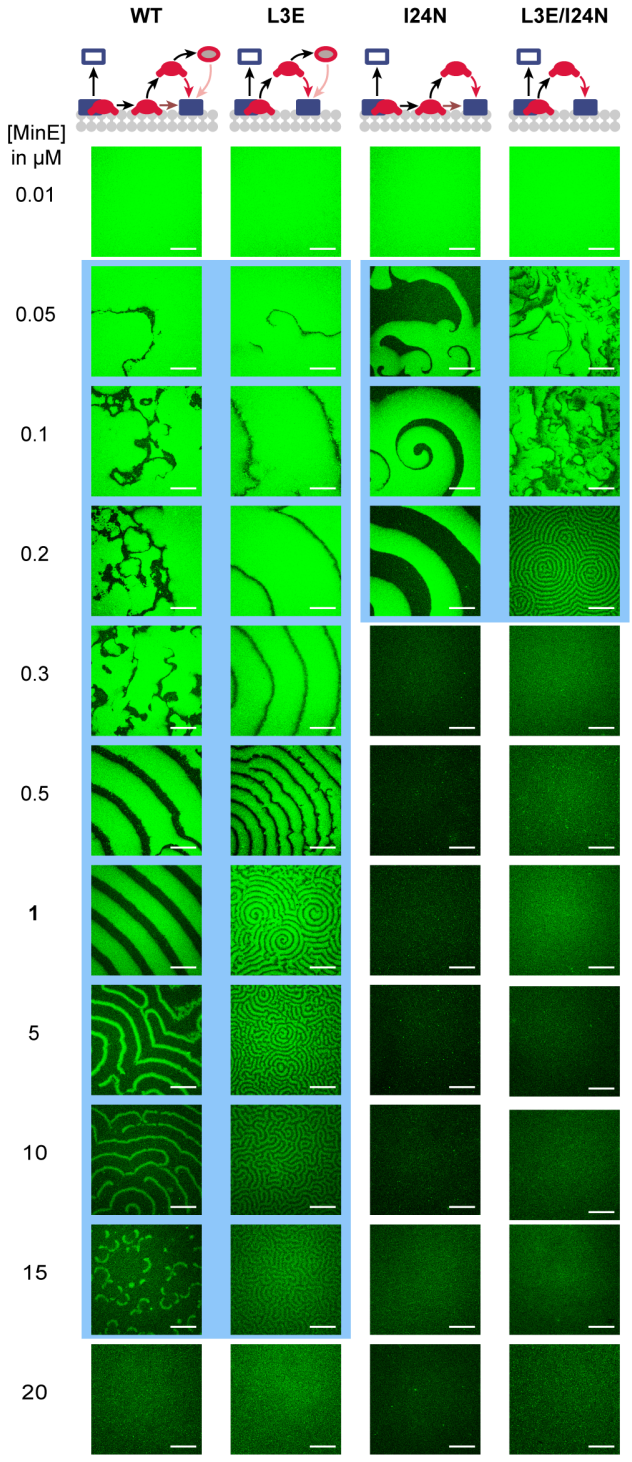

Figure 3. **Impairment of MinE's MinE-MinD interaction switch dramatically decreases the robustness of Min protein patterns *in vitro*.** Reconstitution assays were performed on flat supported lipid bilayers in the presence of 1 µM MinD with 20 % eGFP-MinD. The L3E

mutation, which impairs MinE membrane binding, permits pattern formation (blue background) over a similar range of MinE concentrations as WT MinE. In contrast, the I24N mutation, which locks MinE into its reactive conformation, dramatically decreases the maximal MinE concentration at which patterns can form. Scale bar: 50 µm.

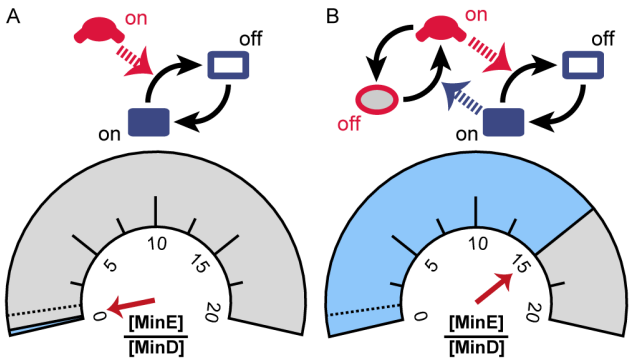

Figure 4. Mutually interlinked switching dramatically increases the robustness of protein pattern formation. (*A*) The MinE variants in which the MinE-MinD interaction switch is disabled (I24N and L3E/I24N) display patterns only within a narrow range (blue region) of MinE/MinD ratios below one (dotted line). (*B*) In contrast, variants that retain the interaction switch (WT and L3E) also form patterns even when MinE is present in great excess. The schematic networks highlight the roles of MinE and MinD in dynamically switching the activity of their respective interaction partner.

MinE conformational switching confers robustness on self-organized Min protein patterns

Supplemental Information

J. Denk[1,*], S. Kretschmer[2,*], J. Halatek[1,*], C. Hartl[1], P. Schwille[2], and E. Frey[1]

[1]*Arnold-Sommerfeld-Center for Theoretical Physics and Center for NanoScience, Department of Physics, Ludwig-Maximilians-Universität München, Theresienstraße 37, D-80333 München, Germany*

[2]*Max-Planck-Institute of Biochemistry, Am Klopferspitz 18, D-82152 Martinsried, Germany*

[*]*These authors contributed equally*

Note 1: Reaction-diffusion equations accounting for a MinD-dependent switch of MinE

Reaction-diffusion equations including a MinE-MinD interaction switch

We base our mathematical models on previous models [1, 2, 3] for the Min system that account for the molecular interactions that are taken to be essential for the Min protein dynamics. This model, which we referred to as *skeleton network* in the manuscript, includes the following set of biochemical reactions (Fig. S1A):

1. The attachment of MinD-ATP from the bulk, u_{DT}, to the membrane with rate constant k_D.

2. The recruitment of bulk MinD-ATP, u_{DT}, to the membrane by membrane-bound MinD, u_d, with rate constant k_{dD}.

3. The formation of membrane bound MinDE complexes, u_{de}, through the recruitment of bulk MinE.

4. The disintegration and detachment of membrane bound MinDE complexes, u_{de}, into bulk MinD-ADP, u_{DD}, and bulk MinE with rate k_{de}.

5. The reactivation of bulk MinD-ADP, u_{DD}, by nucleotide exchange to MinD-ATP, u_{DT}, with rate λ.

To incorporate a MinE-MinD interaction switch of MinE we extend this skeleton network by the following reactions (Fig. S1B):

1. MinE exists in a latent and a reactive conformation, $u_{E,l}$ and $u_{E,r}$, respectively. The recruitment rates of latent and reactive MinE, k^l_{dE} and k^r_{dE}, respectively, can be different while the skeleton network is recovered for $k^r_{dE} = k^l_{dE}$, i.e. if there is only one MinE conformation.

2. Recruitment of latent or reactive MinE leads to the formation of MinDE complexes, in which MinE exists in its reactive form. After disintegration and detachment of membrane-bound MinDE complexes bulk MinE persists in its reactive form for a very short time before it undergoes a conformational switch to latent MinE with a rate μ.

For a detailed discussion of our assumption that after dissociation from MinD reactive MinE shortly persists in its reactive form please refer to supplemental Note 6.

All components are able to diffuse in their respective domains (bulk or membrane). Since only the distinction between bulk and membrane diffusion is important for the dynamics, and since the diffusion coefficients with a domain (bulk or membrane) are very similar for different proteins, we only distinguish between bulk and membrane diffusion with diffusion constants D_c for the bulk and D_m for the membrane, respectively.

In coordinate-free form (with index c or m denoting that an operator acts in the bulk or at the membrane, respectively) the ensuing system of partial differential equations for a model with MinE-MinD interaction switch reads:

$$\partial_t u_{DD} = D_c \nabla_c^2 u_{DD} - \lambda u_{DD}\,, \tag{1a}$$
$$\partial_t u_{DT} = D_c \nabla_c^2 u_{DT} + \lambda u_{DD}\,, \tag{1b}$$
$$\partial_t u_{E,r} = D_c \nabla_c^2 u_{E,r} - \mu u_{E,r}\,, \tag{1c}$$
$$\partial_t u_{E,l} = D_c \nabla_c^2 u_{E,l} + \mu u_{E,r}\,, \tag{1d}$$
$$\partial_t u_d = D_m \nabla_m^2 u_d + f_d(u_d, \tilde{u}_{DT}, \tilde{u}_{E,r}, \tilde{u}_{E,l}), \tag{1e}$$
$$\partial_t u_{de} = D_m \nabla_m^2 u_{de} + f_{de}(u_{de}, u_d, \tilde{u}_{E,r}, \tilde{u}_{E,l})\,, \tag{1f}$$

where the biochemical reactions on the membrane are given by the nonlinear functions

$$f_d(u_d, \tilde{u}_{DT}, \tilde{u}_{E,r}, \tilde{u}_{E,l}) := (k_D + k_{dD} u_d)\,\tilde{u}_{DT} - u_d\,(k_{dE}^l \tilde{u}_{E,l} + k_{dE}^r \tilde{u}_{E,r})\,, \tag{2a}$$
$$f_{de}(u_{de}, u_d, \tilde{u}_{E,r}, \tilde{u}_{E,l}) := u_d\,(k_{dE}^l \tilde{u}_{E,l} + k_{dE}^r \tilde{u}_{E,r}) - k_{de}\,u_{de}\,, \tag{2b}$$

with $\tilde{u}_i$ denoting the respective bulk densities right at the membrane. These equations are complemented by nonlinear reactive boundary conditions at the membrane surface stating that the biochemical reactions involving both membrane-bound and bulk proteins equal the diffusive flux onto and off the membrane (the index n denoting the outward normal vector at the boundary)

$$D_c \nabla_n u_{DD}|_m = k_{de}\,u_{de} =: f_{DD}\,, \tag{3a}$$
$$D_c \nabla_n u_{DT}|_m = -(k_D + k_{dD} u_d)\,\tilde{u}_{DT} =: f_{DT}\,, \tag{3b}$$
$$D_c \nabla_n u_{E,r}|_m = k_{de}\,u_{de} - k_{dE}^r\,u_d\,\tilde{u}_{E,r} =: f_{E,r}\,, \tag{3c}$$
$$D_c \nabla_n u_{E,l}\big|_m = -k_{dE}^l\,u_d\,\tilde{u}_{E,l} =: f_{E,l}\,. \tag{3d}$$

For all other boundaries, we employed periodic boundary conditions or no-flux boundary conditions (Fig. S1B) (the surface is denoted by s)

$$D_c \nabla_n u_{DD}\big|_s = 0\,, \tag{4a}$$
$$D_c \nabla_n u_{DT}\big|_s = 0\,, \tag{4b}$$
$$D_c \nabla_n u_{E,r}\big|_s = 0\,. \tag{4c}$$
$$D_c \nabla_n u_{E,l}\big|_s = 0\,. \tag{4d}$$

The above set of reaction-diffusion equations locally conserves the total mass of MinD as well as MinE. This implies that the spatial averages, $\overline{[\mathrm{MinD}]}$ and $\overline{[\mathrm{MinE}]}$, of the total densities of MinD and MinE obey the relation

$$\overline{[\mathrm{MinD}]}\,\Omega = \int_\Omega \mathrm{d}c\ (u_{DD} + u_{DT}) + \int_{\delta\Omega} \mathrm{d}m\ (u_d + u_{de})\,, \tag{5a}$$
$$\overline{[\mathrm{MinE}]}\,\Omega = \int_\Omega \mathrm{d}c\ (u_{E,r} + u_{E,l}) + \int_{\delta\Omega} \mathrm{d}m\ u_{de}\,, \tag{5b}$$

where $\int_\Omega \mathrm{d}c$ and $\int_{\delta\Omega} \mathrm{d}m$ signify integration over the whole bulk volume Ω and membrane surface $\delta\Omega$, respectively. In order to study the robustness of patterns against variations in protein concentrations we performed extensive parameter scans in $\overline{[\mathrm{MinE}]}$ and $\overline{[\mathrm{MinD}]}$. We found that changing the total protein concentration $\overline{[\mathrm{MinE}]} + \overline{[\mathrm{MinD}]}$ only yields small changes in the robustness. We therefore focused on varying $\overline{[\mathrm{MinE}]}$ while fixing $\overline{[\mathrm{MinD}]}$ to the experimental concentration of $1\,\mu$M.

The advantage of such a general (coordinate-free) model definition is that it can be adjusted to any system geometry, allowing one to consistently use the same model for different experimental setups. For the *in vitro* experiments a simple box geometry is typically used, where the lipid bilayer (membrane) is located at the bottom of the box and the bulk extends into the vertical direction. Since the lateral extension of *in vitro* box geometries is typically very large $\mathscr{O}(10^3\,\mu m)$ compared to the wavelength of the patterns $\mathscr{O}(10\,\mu m)$, we perform our analyses in a two-dimensional box of length $L = 250\,\mu m$ and employ periodic boundary conditions on the two sides. The bottom of the box represents the membrane with reactive boundary conditions and we assume no-flux boundary conditions on the top of the box (Fig. S1C). The height h of the experimental box geometry is similarly very large $\mathscr{O}(10^3\,\mu m)$ such that the dynamics perpendicular to the membrane can, in principle, not be neglected [4].

Reaction-diffusion equations including persistent membrane binding of MinE

In addition to the biochemical reactions of the skeleton network, we included the following biochemical reactions to allow for persistent membrane binding of MinE (Fig. S1D):

1. MinE exists in only one conformation, u_E, and is recruited by membrane-bound MinD, u_d to the membrane with a rate k_{dE}, which leads to the formation of MinDE complexes, u_{de}. Membrane-bound MinDE complexes disintegrate with a rate k_{de} whereupon MinD-ADP detaches into the bulk and MinE remains membrane-bound.

2. Free, membrane-bound MinE, u_e, reassociates with membrane-bound MinD, u_d, with a rate k_{ed} or detaches from the membrane with a rate k_e.

In coordinate-free form (with index c or m denoting that an operator acts in the bulk or at the membrane, respectively) the ensuing system of partial differential equations for a model accounting for persistent membrane binding of MinE reads:

$$\partial_t u_{DD} = D_c \nabla_c^2 u_{DD} - \lambda u_{DD}\,, \tag{6a}$$
$$\partial_t u_{DT} = D_c \nabla_c^2 u_{DT} + \lambda u_{DD}\,, \tag{6b}$$
$$\partial_t u_E = D_c \nabla_c^2 u_E\,, \tag{6c}$$
$$\partial_t u_d = D_m \nabla_m^2 u_d + f_d(u_d, u_e, \tilde{u}_{DT}, \tilde{u}_E), \tag{6d}$$
$$\partial_t u_{de} = D_m \nabla_m^2 u_{de} + f_{de}(u_{de}, u_d, u_e, \tilde{u}_E)\,, \tag{6e}$$
$$\partial_t u_e = D_m \nabla_m^2 u_e + f_e(u_{de}, u_d, u_e)\,, \tag{6f}$$

where the biochemical reactions on the membrane are given by the nonlinear functions

$$f_d(u_d, u_e, \tilde{u}_{DT}, \tilde{u}_E) := (k_D + k_{dD} u_d)\,\tilde{u}_{DT} - u_d\,(k_{dE}\tilde{u}_E + k_{ed} u_e)\,, \tag{7a}$$
$$f_{de}(u_{de}, u_d, u_e, \tilde{u}_E) := u_d\,(k_{dE}\tilde{u}_E + k_{ed} u_e) - k_{de}\,u_{de}\,, \tag{7b}$$
$$f_e(u_{de}, u_d, u_e) := k_{de}\,u_{de} - u_d\,k_{ed} u_e - k_e u_e\,, \tag{7c}$$

with $\tilde{u}_i$ denoting the respective bulk densities right at the membrane. The reactive

boundary conditions at the membrane surface read:

$$D_c \nabla_n u_{DD}|_m = k_{de}\, u_{de} =: f_{DD}\,, \tag{8a}$$
$$D_c \nabla_n u_{DT}|_m = -(k_D + k_{dD} u_d)\, \tilde{u}_{DT} =: f_{DT}\,, \tag{8b}$$
$$D_c \nabla_n u_E|_m = k_e\, u_e - k_{dE}\, u_d\, \tilde{u}_E =: f_E\,, \tag{8c}$$

and no-flux boundary condition at the top of the box geometry (denoted by the index s)

$$D_c \nabla_n u_{DD}|_s = 0\,, \tag{9a}$$
$$D_c \nabla_n u_{DT}|_s = 0\,, \tag{9b}$$
$$D_c \nabla_n u_E|_s = 0\,. \tag{9c}$$

In analogy to our model including the MinE-MinD interaction switch we perform our analyses in a two-dimensional box of length $L = 250\,\mu m$ and employ periodic boundary conditions on the two sides (Fig. 1C).

The spatial averages, $\overline{[\mathrm{MinD}]}$ and $\overline{[\mathrm{MinE}]}$, of the total densities of MinD and MinE obey the relation

$$\overline{[\mathrm{MinD}]}\,\Omega = \int_\Omega \mathrm{d}c\ (u_{DD} + u_{DT}) + \int_{\delta\Omega} \mathrm{d}m\ (u_d + u_{de} + u_e)\,, \tag{10a}$$
$$\overline{[\mathrm{MinE}]}\,\Omega = \int_\Omega \mathrm{d}c\ u_E + \int_{\delta\Omega} \mathrm{d}m\ (u_{de} + u_e)\,, \tag{10b}$$

Again, to study the robustness of patterns against variations in protein concentrations we performed extensive parameter scans in $\overline{[\mathrm{MinE}]}$ and $\overline{[\mathrm{MinD}]}$ and then fixed $\overline{[\mathrm{MinD}]}$ to $1\,\mu$M while varying $\overline{[\mathrm{MinE}]}$.

Linear stability analysis in a box geometry

In order to make predictions about the stability of steady solutions, we performed linear stability analyses of the sets of equations (1)–(9). The starting point of a linear stability analysis is the computation of a steady state around which the system can be linearised. In the box geometry under consideration the steady state is spatially uniform along the membrane (in the lateral direction). Along the vertical direction, however, the nucleotide exchange and the MinE-MinD interaction switch in the bulk induce density gradients even for the steady state. Here, one considers the time evolution of small perturbations with respect to the respective steady states. When the (exponential) growth rate of these perturbations is positive, these perturbations grow and will eventually lead to spatial or temporal patterns. In contrast, for negative growth rates perturbations decay and the system will eventually relax to a stable steady state, which is uniform on the membrane. Calculating the growth rates of small perturbations for different rate constants and protein concentrations thus yields the regimes in terms of these parameters where patterns are predicted or where uniform protein concentrations on the membrane prevail.

In the following we will focus on the linear stability analysis of the network including a MinE-MinD interaction switch. The stability analysis for the network with persistent MinE membrane binding is carried out analogously. In the following we consider a 2D slice geometry as described above, with the lateral dimension x and the extended bulk dimension z. A spatially uniform state at the membrane means that $\nabla_x u_i = 0$ for all protein densities. Using the network with a MinE-MinD interaction switch, eqs.(1),(3)–(4), the stationary density profiles in the bulk are then given by

$$u_{DD}(z) = \tilde{u}^*_{DD} \frac{\cosh\left((h-z)/\ell_D\right)}{\cosh\left(h/\ell_D\right)}, \tag{11a}$$

$$u_{DT}(z) = \tilde{u}^*_{DT} + \tilde{u}^*_{DD}\left(1 - \frac{\cosh\left((h-z)/\ell_D\right)}{\cosh\left(h/\ell_D\right)}\right), \tag{11b}$$

$$u_{E,r}(z) = \tilde{u}^*_{E,r} \frac{\cosh\left((h-z)/\ell_E\right)}{\cosh\left(h/\ell_E\right)}, \tag{11c}$$

$$u_{E,l}(z) = \tilde{u}^*_{E,l} + \tilde{u}^*_{E,r}\left(1 - \frac{\cosh\left((h-z)/\ell_E\right)}{\cosh\left(h/\ell_E\right)}\right), \tag{11d}$$

$$\tag{11e}$$

where $\tilde{u}^*_i$ denote the spatially uniform stationary bulk densities at the mem-

brane, and $\ell_D = \sqrt{D_c/\lambda}$ and $\ell_E = \sqrt{D_c/\mu}$ give the penetration depth of respectively MinD-ADP and reactive MinE into the bulk; note that the corresponding stationary profiles of the total mass densities, $u_E(z) = u_{E,r}(z) + u_{E,l}(z)$ and $u_D(z) = u_{DD}(z) + u_{DT}(z)$, are spatially uniform in the bulk. Upon inserting all these stationary bulk density profiles into the reactive boundary conditions at the membrane, (3), one finds

$$\ell_D\, \tilde{u}^*_{DD} \tanh(h/\ell_D) = f_{DD}(u^*_{de})/\lambda\,, \tag{12a}$$
$$-\ell_D\, \tilde{u}^*_{DD} \tanh(h/\ell_D) = f_{DT}(\tilde{u}^*_{DT}, u^*_d)/\lambda\,, \tag{12b}$$
$$\ell_E\, \tilde{u}^*_{E,r} \tanh(h/\ell_E) = f_{E,r}(u^*_{de}, u^*_d, \tilde{u}^*_{E,r})/\mu\,, \tag{12c}$$
$$-\ell_E\, \tilde{u}^*_{E,l} \tanh(h/\ell_E) = f_{E,r}(\tilde{u}^*_{E,l}, u^*_d)/\mu\,, \tag{12d}$$
$$\tag{12e}$$

which are complemented by the stationarity conditions for the membrane dynamics, Eq. (1d)-(1e),

$$0 = f_d(u_d, \tilde{u}_{DT}, \tilde{u}_{E,r}, \tilde{u}_{E,l})\,, \tag{13a}$$
$$0 = f_{de}(u_{de}, u_d, \tilde{u}_{E,r}, \tilde{u}_{E,l})\,. \tag{13b}$$

Moreover, the stationary states have to satisfy global mass conservation

$$\overline{[\mathrm{MinD}]} = \tilde{u}^*_{DD} + \tilde{u}^*_{DT} + (u^*_d + u^*_{de})/h\,, \tag{14a}$$
$$\overline{[\mathrm{MinE}]} = \tilde{u}^*_{E,r} + \tilde{u}^*_{E,l} + u^*_{de}/h\,. \tag{14b}$$

In a linear stability analysis one considers the time evolution of small perturbations with respect to these stationary states, i.e. $u_i(x,z,t) = u^*_i(z) + \delta u_i(x,z,t)$ (where membrane densities lack the dependence on the z-coordinate). Expanding

the dynamics of the small perturbations in terms of Fourier modes

$$\delta u_{DD}(x,z,t) = \sum_q e^{\sigma_q t} \cos(qx)\, \zeta_{DD}(z;q)\,, \tag{15a}$$

$$\delta u_{DT}(x,z,t) = \sum_q e^{\sigma_q t} \cos(qx)\, \zeta_{DT}(z;q)\,, \tag{15b}$$

$$\delta u_{E,r}(x,z,t) = \sum_q e^{\sigma_q t} \cos(qx)\, \zeta_{E,r}(z;q)\,, \tag{15c}$$

$$\delta u_{E,l}(x,z,t) = \sum_q e^{\sigma_q t} \cos(qx)\, \zeta_{E,l}(z;q)\,, \tag{15d}$$

$$\delta u_{d}(x,t) = \sum_q e^{\sigma_q t} \cos(qx)\, \delta\tilde{u}^q_{d}\,, \tag{15e}$$

$$\delta u_{de}(x,t) = \sum_q e^{\sigma_q t} \cos(qx)\, \delta\tilde{u}^q_{de}\,, \tag{15f}$$

and inserting $u_i(x,z,t) = u_i^*(z) + \delta u_i(x,z,t)$ into the (linear) bulk diffusion equations (Eq. 1a-1c) and taking the boundary conditions (Eq. 3a-4b) into account, the corresponding bulk functions $\zeta_i(z;q)$ are obtained analytically as

$$\zeta_{DD}(z;q) = \delta\tilde{u}^q_{DD}\, \frac{\cosh\left(\frac{h-z}{\ell_q(\lambda+\sigma_q)}\right)}{\cosh\left(\frac{h}{\ell_q(\lambda+\sigma_q)}\right)}\,, \tag{16a}$$

$$\zeta_{DT}(z;q) = (\delta\tilde{u}^q_{DT} + \delta\tilde{u}^q_{DD})\, \frac{\cosh\left(\frac{h-z}{\ell_q(\sigma_q)}\right)}{\cosh\left(\frac{h}{\ell_q(\sigma_q)}\right)} - \delta\tilde{u}^q_{DD}\, \frac{\cosh\left(\frac{h-z}{\ell_q(\lambda+\sigma_q)}\right)}{\cosh\left(\frac{h}{\ell_q(\lambda+\sigma_q)}\right)}\,, \tag{16b}$$

$$\zeta_{E,r}(z;q) = \delta\tilde{u}^q_{E,r}\, \frac{\cosh\left(\frac{h-z}{\ell_q(\mu+\sigma_q)}\right)}{\cosh\left(\frac{h}{\ell_q(\mu+\sigma_q)}\right)}\,, \tag{16c}$$

$$\zeta_{E,l}(z;q) = (\delta\tilde{u}^q_{E,r} + \delta\tilde{u}^q_{E,l})\, \frac{\cosh\left(\frac{h-z}{\ell_q(\sigma_q)}\right)}{\cosh\left(\frac{h}{\ell_q(\sigma_q)}\right)} - \delta\tilde{u}^q_{E,r}\, \frac{\cosh\left(\frac{h-z}{\ell_q(\mu+\sigma_q)}\right)}{\cosh\left(\frac{h}{\ell_q(\mu+\sigma_q)}\right)}\,, \tag{16d}$$

$$\tag{16e}$$

where we have defined

$$\ell_q(\chi_q) := \sqrt{\frac{D_c}{\chi_q + D_c q^2}}\,, \tag{17}$$

generalizing the penetration depths ℓ_D and ℓ_E to wave vector dependent quantities. $\delta\tilde{u}^q_i$ are Fourier coefficients that depend on the wavenumber q.

Using the shorthand notation for a term describing the coupling between the membrane concentrations and the density profiles in the bulk

$$\Gamma_q(\chi_q) = \frac{D_c}{\ell_q(\chi_q)} \tanh\left(\frac{h}{\ell_q(\chi_q)}\right), \tag{18}$$

and the first Taylor coefficient for the reaction terms

$$f_j^i = \left.\frac{\partial f_j(\mathbf{u})}{\partial u_i}\right|_{\mathbf{u}=\mathbf{u}^*}, \tag{19}$$

the linear system reads $\mathscr{L}_q\,\delta\tilde{\mathbf{u}}_q = 0$, for each $\delta\tilde{\mathbf{u}}_q = \left[\delta\tilde{u}^q_{DD}, \delta\tilde{u}^q_{DT}, \delta\tilde{u}^q_{E,r}, \delta\tilde{u}^q_{E,l}, \delta\tilde{u}^q_{d}, \delta\tilde{u}^q_{de}\right]^T$, where $\mathscr{L}_q$ is given by

$$\mathscr{L}_q = \begin{bmatrix}
f^{DD}_{DD}-\Gamma_q(\sigma_q+\lambda) & f^{DT}_{DD} & f^{E,r}_{DD} & f^{E,l}_{DD} & f^{d}_{DD} & f^{de}_{DD} \\
f^{DD}_{DT}+\Gamma_q(\sigma_q+\lambda)-\Gamma_q(\sigma_q) & f^{DT}_{DT}-\Gamma_q(\sigma_q) & f^{Eo}_{DT} & f^{E,l}_{DT} & f^{d}_{DT} & f^{de}_{DT} \\
f^{DD}_{E,r} & f^{DT}_{E,r} & f^{E,r}_{E,r}-\Gamma_q(\sigma_q+\mu) & f^{E,l}_{E,r} & f^{d}_{E,r} & f^{de}_{E,r} \\
f^{DD}_{E,l} & f^{DT}_{E,l} & f^{E,r}_{E,l}+\Gamma_q(\sigma_q+\mu)-\Gamma_q(\sigma_q) & f^{E,l}_{E,l}-\Gamma_q(\sigma_q) & f^{d}_{E,l} & f^{de}_{E,l} \\
f^{DD}_{d} & f^{DT}_{d} & f^{E,r}_{d} & f^{d}_{d}-\sigma_q-D_m q^2 & f^{de}_{d} & \\
f^{DD}_{de} & f^{DT}_{de} & f^{E,r}_{de} & f^{E,l}_{de} & f^{d}_{de} & f^{de}_{de}-\sigma_q-D_m q^2
\end{bmatrix} \tag{20}$$

The first four rows of $\mathscr{L}_q$ are the linearisation of the reactive boundaries Eq. (3), and the last two rows are the linearisation of the membrane dynamics Eq. (1d)-(1e).

The dispersion relation as a function of q ist then given by the maximum of $\mathrm{Re}[\sigma_q]$ (i.e. the fastest growth rates of each wavenumber q) are then obtained as solutions of

$$\det \mathscr{L}_q = 0\,. \tag{21}$$

Since $\mathscr{L}_q$ is non-algebraic in σ_q, solutions can only be obtained numerically. For this purpose we use the iterative solver `FindRoot[]` provided by Wolfram Mathematica 11 to compute the linear stability of stationary solutions for the extended models including a MinE-MinD interaction switch or persistent membrane binding of MinE.

For Figs. 2A, B and S2-S5, we numerically determined the linear stability of the stationary solutions for MinE protein concentration between $0.0001\,\mu$M and $20\,\mu$M for a fixed MinD protein concentration of 1μM. The reaction rates for the extended models with either MinE-MinD interaction switch or persistent membrane binding of MinE were fixed as detailed in Tables S1 and S2, repectively. To cover the lengthscale of experimentally observed patterns we determined the linear stability against perturbations of wavelengths in a range of approx. $5-250\,\mu m$. In Figs. 2A, B, and S2-S5 we identified the regimes of MinE protein concentrations in which perturbations with respect to the steady state grow and patterns are predicted. In Figs. 2A, S3 and S4A, the maximal MinE concentrations are plotted for different recruitment rates of latent and reactive MinE (Figs. 2A and S3) or different reassociation rates and MinE detachment rates (Fig. S4A), respectively. The parameter regime where linear stability analysis predicts the steady state to be linearly stable over the whole range of tested MinE concentrations (i.e. between $0.0001\,\mu$M and $20\,\mu$M) is denoted as regime of 'no patterns' in Figs. 2A, S3, and S4A. In addition to the reaction rates shown in Table S1 and S2, we carried out an extensive survey of different reaction rates for both presented models, and obtained qualitatively similar results for the respective models.

Note 2: Relation of MinE mutant proteins to model extensions

Here, we discuss how the biochemical characteristics of the tested MinE variants (Fig. 3) relate to our reaction networks (Figs. 1A, C, and D).

WT MinE

As stated in the main text, MinE is recruited to membrane-bound MinD, whereupon it forms a MinDE complex in its reactive conformation. Upon stimulation of MinD's ATPase activity, disintegration of the complex and MinD detachment, MinE can stay attached to the membrane, a behavior termed persistent binding. In the persistently membrane-bound state, MinE can either reassociate with another MinD on the membrane or detach from the membrane and quickly revert to its latent state in the bulk phase. It is assumed to then again be recruited to membrane-bound MinD either in the short-lived reactive or, after conformational switching, in the latent state. Experiments [5, 6, 7] suggest that attachment of MinE to the membrane depends on prior interaction with membrane-bound MinD [5, 6, 7]. Very recent studies [8, 9] also suggest the possibility of direct, MinD-independent MinE membrane interactions. In any case, we argue that direct membrane binding is not responsible for the observed robustness of Min patterns, as detailed below (see Note 8).

MinE L3E

The L3 residue lies on the hydrophobic face of MinE's amphipathic membrane targeting sequence and is inserted into the lipid bilayer during membrane interaction [7, 10]. Thus, substitution with a polar residue is expected to impair membrane binding. In agreement with this, *in vivo* experiments confirmed that this mutation perturbs membrane interaction [7]. In these experiments, the L3E mutation was introduced on top of the I25R or I24N mutation, both of which release the MTS [7]. As the I24N mutation locks MinE in its reactive conformation with exposed MTS [7], this state also represents the conformation of MinE that would persist on the membrane after MinD detachment. As the L3E mutation disrupts membrane interaction of MinE I24N [7], we reason that it also abolishes persistent membrane interaction of WT MinE. In conclusion, these observations indicate that MinE L3E can neither bind to, nor persist on the membrane in the absence of MinD.

We note that Park et al. [7] suggested that the L3E mutation also interferes with MinE's sensing of MinD, i.e. the MinD-dependent conversion of MinE from the latent to the reactive state. However, there is no experimental evidence for this notion, which was based on the observation that the L3E mutation resulted in a defect in cell division and colony growth *in vivo* [7]. In principle, it would be possible that the L3E mutation slows down recruitment of MinE to MinD. However, it is impossible that the mutant is completely deficient in binding to MinD, as this would impair its ability to form patterns and stimulate MinD's ATPase activity. In contrast, we observe pattern formation with the L3E mutant and even in a similar range as for WT MinE (Fig. 3).

In summary, the L3E mutation is a suitable means to impair persistent MinE membrane binding without disabling MinE's conformational switch. Therefore, it emulates our model extension with MinE-MinD interaction switch but without MinE membrane interaction.

MinE I24N

As noted above, the I24N mutation locks MinE in its membrane- and MinD-interactive conformation [7]. In this state, the $\beta 1$ strand of each MinE subunit in the dimer is converted to a contact helix that interacts with MinD in the membrane-bound MinDE complex [7]. The reactive state of MinE is expected to have a higher affinity to MinD than the latent form, which is incorporated as fast and slow recruitment in our model, respectively. Thus, locking MinE in the reactive conformation through the I24N mutation prevents switching to the latent form, resulting in an overall higher affinity and faster recruitment to membrane-bound MinD.

Like the WT, MinE I24N would be expected to persist on the membrane even in the absence of MinD. In conclusion, the I24N mutation disrupts reversion of MinE from the reactive to the latent state, without disabling persistent MinE membrane binding.

We note that, due to its constitutively exposed MTS, MinE I24N is expected to have a higher effective membrane affinity than the WT and was shown to bind the membrane independently of MinD *in vivo* [7]. Again, we argue that direct membrane binding is not responsible for the observed change in robustness for MinE I24N, as detailed below (see Note 8).

MinE L3E/I24N

This double mutant combines the effects of the I24N and L3E mutations. Consequently, the mutant cannot undergo switching from the reactive to the latent form. Furthermore, even though the MTS is exposed, the L3E mutation prevents the mutant from binding the membrane directly or persistently [7]. Due to these deficiencies in switching and membrane interaction, MinE L3E/I24N closely mimics MinE in the skeleton network [1, 2] (Fig. 1A).

Notably, while the skeleton model is a good approximation of the L3E/I24N mutant, it also represents a suitable network configuration for a peptide comprising just the anti-MinCD domain of MinE. Analogously to MinE L3E/I24N, such a peptide can bind and stimulate the ATPase activity of MinD, but neither switch from the reactive to the latent state, nor bind the membrane. However, in contrast to the dimeric full-length protein, an anti-MinCD peptide is monomeric as it lacks MinE's C-terminal topological specificity domain, which serves to dimerize MinE [11] and sequester the anti-MinCD domain in the latent state [7].

Interestingly, reconstitution experiments with an anti-MinCD peptide (MinE_{13-31}) did not show pattern formation [12], whereas we observe pattern formation with MinE L3E/I24N (Fig. 3). Although both variants are captured by the configuration of interactions in the skeleton network, they are not identical from a biochemical point-of-view, which also impacts the choice of modeling parameters. In particular, the simultaneous presence of two anti-MinCD domains in a MinE dimer would be expected to result in different interaction rates with MinD compared to a single peptide. Accordingly, we observe that for a certain choice of recruitment rates of MinE to membrane-bound MinD (Fig. S2) the model does not support pattern formation, as observed for MinE_{13-31} [12]. Furthermore, it has been proposed that MinE's topological specificity domain is involved in potential intermolecular interactions of MinE [13], which could also impact pattern formation.

In summary, it is not inconsistent to observe differences in pattern formation for a full-length MinE variant and an anti-MinCD peptide. Rather, our results motivate future experimental and theoretical studies that focus in-depth on the underlying differences between full-length WT and mutant Min proteins as well as short peptides.

Note 3: The skeleton model cannot explain pattern formation when MinE excedes MinD in concentration

As stated in the main text, previous models based on the skeleton network [2, 1, 14] suggest that patterns can form only if MinE is less abundant than MinD. Recall from Note 1, that the skeleton model is recovered from the model including a MinE-MinD interaction switch by setting $k^l_{dE} = k^r_{dE}$. We performed extensive parameter sweeps in the skeleton model (i.e. $k^l_{dE} = k^r_{dE}$) over all remaining reaction rates and found that the homogeneous state can only get unstable when the MinD concentration exceeds the MinE concentration. Fig. S2 shows a parameter sweep for different recruitment rates of MinE to membrane-bound MinD. Since for the skeleton model $k^l_{dE} = k^r_{dE}$, we denote the recruitment rate of MinE as k_{dE}. Also note that, in agreement with previous studies [1] patterns can only be found when the recruitment rate of MinE to membrane-bound MinD is higher than the recruitment rate of MinD to membrane-bound MinD (Fig. S2).

Note 4: In the limit case of vanishing recruitment of latent MinE by membrane-bound MinD, the ability to form patterns is lost

Fig. 2A shows that there is a regime of low k^l_{dE} and high k^r_{dE} for which patterns are predicted for MinE/MinD concentration ratios much larger than one. Yet, in the limiting case of vanishing recruitment of latent MinE to membrane-bound MinD (i.e. $k^l_{dE} \to 0$) one would expect, that the cycling of MinE between bulk and membrane ceases, MinE remains in its latent conformation in the bulk for all times and patterns are suppressed. In analogy to Fig. 2, Fig. S2 depicts the range of MinE/MinD concentration ratios in a window of very low recruitment of latent MinE k^l_{dE}. In the limiting case $k^l_{dE} = 0$, patterns are suppressed for all values of $k^r_d E$. Note that in the stationary state of $k^l_{dE} = 0$, all MinE is present in its latent form and uniformly distributed in the bulk, while all MinD is membrane-bound and also uniformly distributed over the membrane. In agreement with our intuition, for a finite, fixed k^r_{dE}, the range of MinE concentrations compatible with patterns eventually decreases for k^l_{dE} approaching zero until patterns are suppressed for all MinE concentrations.

Note 5: Thickness of reactive MinE layer

In the network with MinE-MinD interaction switch, after detachment of MinE from the membrane MinE remains in its reactive state until it quickly reassumes its latent form of low MinD binding affinity at a rate μ. Thus, the region in which reactive MinE exists is limited by the region it can diffuse through before it changes its conformation. The extension of this region into the bulk is given by the penetration depth of reactive MinE, $\ell_E = \sqrt{D_c/\mu}$. For our analyses we assumed $D_c = 60\,\mu m^2 s^{-1}$ and $\mu = 100 s^{-1}$ such that $\ell_E = \sqrt{0.6}\,\mu m \approx 0.77\,\mu m$. The vertical extension of the box geometry used in our analyses is assumed to be $5000\,\mu m$ which is a good approximate of the bulk height in our *in vitro* experiments. This means that a bulk layer of reactive MinE that is three orders of magnitude thinner than the total bulk is sufficient to dramatically increase the robustness of patterns as shown in Figs. 2A and B in the main text.

Note 6: On the assumption of dissociation of reactive MinE from MinD and its switch to latent MinE as a two-step process

The precise sequence of events during MinE's dissociation from MinD and switching to the latent form is still unclear. In our study, we assume that after dissociation of MinD, reactive MinE quickly switches to its latent form at a certain (large) rate μ. In principle, this switch could also precede and initiate dissociation of MinE from MinD. Although this cannot be ruled out, we think that it is unlikely for the following reason.

MinE L3E/I24N is a mutant that can neither bind the membrane nor switch to the latent form. This mutant still supported pattern formation, which is indicative of MinE cycling between membrane-bound MinD and the bulk. Hence, the conformational switch is not required to initiate dissociation of MinE from MinD and it appears likely that MinE mutants that retain the ability of switching will change conformation (shortly) after dissociation from MinD.

Based on this assumption, our results (Fig. 2) strongly suggest that treating reactive MinE's dissociation from MinD and its transition to a latent state as a two-step process is essential in order to understand the origin of pattern robustness. When the lifetime of reactive MinE is changed, the thickness of the reactive MinE layer above the membrane (illustrated by the red shaded region in Fig. 2C) is altered (revised SI Note 5). When changing the lifetime of reactive MinE $(1/\mu)$ we found that increasing/decreasing reactive MinE's lifetime has an effect similar

to that of increasing/decreasing its recruitment rate to membrane-bound MinD. Thus, when the lifetime of reactive MinE is reduced, the broad concentration range of MinE compatible with patterns as shown in Fig. 2A and B is restored when the recruitment rate of reactive MinE to membrane-bound MinD is simultaneously increased. This is reasonable, since one may expect both processes (changing reactive MinE's lifetime or its recruitment rate) to have similar effects on the total affinity of reactive MinE for a region of membrane-bound MinD. We note here that, in our model, the wide range of MinE concentrations permissive for pattern formation exists even for an arbitrarily short lifetime (as long as it is larger than zero). Hence, treating dissociation of reactive MinE from MinD and switching to its latent form as two non-simultaneous steps is crucial to explain the wide protein concentration range compatible with pattern formation. More generally, our results highlight the importance of two-step processes in pattern-forming systems even when these steps occur in very rapid succession.

Note 7: Effect of persistent MinE membrane binding on the concentration range of pattern formation

To determine the impact of persistent membrane binding on the concentration range of pattern formation we studied a reaction network in which MinE remains on the membrane after detachment of MinD (Fig. 1D, Fig. S1D). Membrane-bound MinE can either detach at a rate k_e or reassociate at a rate k_{ed} with membrane-bound MinD to form a new MinDE complex. We find that this model exhibits two qualitatively different regimes (Fig S2), depending on whether reassociation with MinD or detachment of MinE is the faster process. If MinE detachment is dominant, the range of MinE/MinD ratios that allows pattern formation increases as the minimal residence time of free MinE on the membrane is increased, as previously suggested [1] (Fig. S4B, the x-axes of Fig. S4B and C show the minimal residence time of MinE on the membrane with persistent membrane binding $(1/k_{ed} + 1/k_e)$ as compared to the residence time without persistent membrane binding $(1/k_{ed})$). Conversely, if reassociation is favored, the maximal MinE/MinD ratio compatible with pattern formation decreases as the residence time of free MinE on the membrane is increased (Fig. S4C).

In analogy to the case with MinE-MinD interaction switch the change in robustness can be understood by considering the opposing roles of MinE and MinD in the establishment of Min oscillations.

For 'slow' reassociation, i.e. when reassociation of membrane-bound MinE

with membrane-bound MinD is slower than detachment of free MinE from the membrane, the maximal MinE/MinD ratio compatible with pattern formation increases as the residence time of free MinE on the membrane is increased (Fig. S4B). As previously suggested [1], in this case, persistent membrane binding would partially sequester MinE on the membrane where it hardly contributes to the formation of MinDE complexes. This sequestration partially disables MinE in its action to deplete MinD on the membrane and thereby enables MinD accumulation for an increased MinE/MinD ratio.

For 'fast' reassociation, i.e. when reassociation of free membrane-bound MinE with membrane-bound MinD is faster than detachment of free MinE from the membrane, the maximal MinE/MinD ratio compatible with pattern formation decreases as the residence time of free MinE on the membrane is increased (Fig. S4C). We argue, that for fast reassociation, the overall binding of free MinE to MinD on the membrane is amplified with respect to the skeleton network, which in turn favors depletion over accumulation of MinD on the membrane. As a consequence, initial MinD accumulation and subsequent patterns require lower MinE/MinD concentration ratios than without persistent membrane binding.

These predictions can be tested with the MinE I24N mutant, which is capable of persistent membrane binding but defective in the MinE-MinD interaction switch as discussed in the main text (see also SI Note 2). For MinE I24N patterns only form in a very narrow range of MinE/MinD concentration ratios far below one (Figs. 3 and 4). This demonstrates that, unlike the MinE-MinD switch, persistent MinE membrane binding cannot explain the robustness of *in vitro* Min patterns.

Note 8: Direct attachment of MinE to the membrane does not affect the MinE concentration range compatible with pattern formation

In SI Note 7, we addressed membrane interactions of MinE by theoretically studying a reaction network that includes persistent MinE membrane binding in the absence of a MinE-MinD interaction switch. To test our theory regarding this reaction network, we employed the MinE I24N mutant. The MinE I24N mutant is deficient in conformational switching while retaining the ability to independently bind to the membrane [7]. In addition to the persistent MinE membrane binding included in our mathematical approach (SI Note 7), MinE I24N is able to directly bind to the membrane even in the absence of MinD due to its permanently exposed

MinD binding region and membrane targeting sequence [7]. Furthermore, recent studies [9, 12] suggest weak MinD-independent membrane interactions of MinE, even in WT MinE, that may allow MinE attachment to the membrane independent of MinD [9] or stabilization of MinD by membrane-bound MinE [12]. To rule out that the observed change in robustness for MinE I24N (Fig. 3) is due to stronger direct, MinD-independent attachment of MinE to the membrane, we included an extra term in the equations (6)–(9) which enables direct attachment of MinE to the membrane with a rate k_E. The terms f_e and f_E introduced in eq. 6 and eq. 8 then read:

$$f_E := k_e u_e - k_{dE} u_d \tilde{u}_E - k_E \tilde{u}_E \tag{22}$$

$$f_e := k_E \tilde{u}_E + k_{de} u_{de} - u_d k_{ed} u_e - k_e u_e \,. \tag{23}$$

We performed a parameter scan in the attachment rate k_E of MinE to the membrane. For low values of k_E the effect of persistent MinE membrane binding on the range of MinE/MinD concentration ratios compatible with pattern formation is unchanged and independent of whether or not direct attachment of MinE to the membrane is included (Fig. S5). In particular, in Fig. S5A, the maximal MinE concentration compatible with patterns increases when increasing the minimal persistence time of free MinE on the membrane (going from left to right on the x-axis of Fig. S5A). In Fig. S5B the maximal MinE concentration compatible with patterns decreases when increasing the minimal persistence time of free MinE on the membrane. Only for very high k_E, when attachment of MinE is more than two orders of magnitude faster than attachment of MinD ($k_E \gtrsim 316 k_D$), the maximal MinE concentration where patterns are predicted decreases for slow (Fig. S5A) as well as for fast (Fig. S5B) reassociation. This is likely because for very high k_E MinE is so abundant on the membrane that reassociation of free MinE and MinD on the membrane becomes more likely than MinE sequestration.

However, we note that the physiological rate of the direct membrane attachment of MinE I24N is very likely of the same order as the MinD attachment rate or even smaller considering the approximately equal lengths of MinD's and MinE's amphipathic membrane targeting sequences [7]. Thus, our theory suggests, that direct, MinD-independent attachment of MinE does not change the effect of persistent membrane binding on the range of MinE/MinD concentration ratios compatible with patterns (Fig. S5, small k_E).

Furthermore, as discussed in the main text (Fig. 3), introducing a L3E mutation–and thereby disabling possible MinD-independent membrane interactions of MinE–does not affect the MinE concentration range compatible with patterns. This

strongly suggests that, while possibly important for the characteristic details of patterns (such as the wavelength, etc.) MinD-independent interactions of MinE with the membrane (also including possible MinD stabilization by membrane-bound MinE [12]) do not affect the range of MinE/MinD concentration ratio in which patterns form.

Note 9: Detailed Experimental Materials and Methods

Protein purification

Expression and purification of His-MinD, His-eGFP-MinD as well as WT and mutant His-MinE were performed as described previously [15, 16].

Self-organization assays

Self-organization assays on flat supported lipid bilayers were performed essentially as described previously [15, 16]. Briefly, SLBs composed of *E. coli* polar lipids (Avanti Polar Lipids, Alabaster, AL, USA) were prepared on glass as described in [16]. Then, 1μM MinD incl. 20% eGFP-MinD, 2.5mM ATP (F. Hoffmann-La Roche AG, Basel, Switzerland) and MinE of varying concentration were added to Min buffer (25mM Tris-HCl pH 7.5, 150mM KCl, 5mM MgCl2) in a total volume of 200μL. The samples were then incubated for several hours to provide ample time for protein patterns to form. The concentration ranges compatible with pattern formation reported here were consistently observed in at least three independent experiments. For 0.3μM MinE L3E/I24N, patterns were observed in only 50% of experiments. We therefore categorized this concentration as being incapable of reliable pattern formation.

Microscopy and image processing

Fluorescence imaging was performed with a ZEISS LSM780 confocal laser scanning microscope equipped with a Zeiss C-Apochromat 40x/1.20 water-immersion objective (Carl Zeiss AG,Oberkochen, Germany). Image processing was performed with Fiji [17]. As fluorescence intensities were low around the upper bounds in MinE concentration compatible with pattern formation, we adjusted the brightness and contrast levels to better visualize the transition. As, for consistency, the same adjustments were equally made for all images, the intensities in the micrographs can be displayed outside the dynamic range.

References

[1] Halatek J & Frey E (2012) Highly canalized MinD transfer and MinE sequestration explain the origin of robust MinCDE-protein dynamics. *Cell reports* 1(6):741-752.

[2] Huang KC, Meir Y, & Wingreen NS (2003) Dynamic structures in Escherichia coli: spontaneous formation of MinE rings and MinD polar zones. *Proc Natl Acad Sci U S A* 100(22):12724-12728.

[3] Wu F, *et al.* (2016) Multistability and dynamic transitions of intracellular Min protein patterns. *Mol Sys Biol* 12(6):873.

[4] Halatek J & Frey E (2014) Effective 2D model does not account for geometry sensing by self-organized proteins patterns. *Proc Natl Acad Sci U S A* 111(18):E1817.

[5] Hu Z, Gogol EP, & Lutkenhaus J(2002) Dynamic assembly of MinD on phospholipid vesicles regulated by ATP and MinE. *Proc Natl Acad Sci U S A* 99(10):6761-6766.

[6] Loose M, Fischer-Friedrich E, Herold C, Kruse K, & Schwille P (2011) Min protein patterns emerge from rapid rebinding and membrane interaction of MinE. *Nat Struct Mol Biol* 18(5):577-583.

[7] Park KT, *et al.* (2011) The Min oscillator uses MinD-dependent conformational changes in MinE to spatially regulate cytokinesis. *Cell* 146(3):396 – 407.

[8] Ayed SH, *et al.* (2017) Dissecting the role of conformational change and membrane binding by the bacterial cell division regulator MinE in the stimulation of MinD ATPase activity. *J Biol Chem* 292(50):20732-20743.

[9] Park KT, Villar MT, Artigues A, & Lutkenhaus J (2017) MinE conformational dynamics regulate membrane binding, MinD interaction, and Min oscillation. *Proc Natl Acad Sci U S A* 114(29):7497-7504.

[10] Shih YL *et al.* (2002) The N-terminal Amphipathic Helix of the topological specificity factor MinE is associated with shaping membrane curvature. *PLoS ONE*, 6(6).

[11] Pichoff S, Vollrath B, Touriol C, & Bouché JP (1995) Deletion analysis of gene MinE which encodes the topological specificity factor of cell division in Escherichia coli *Mol Microbiol* 18(2):1365-2958.

[12] Vecchiarelli AG, *et al.* (2016) Membrane-bound MinDE complex acts as a toggle switch that drives Min oscillation coupled to cytoplasmic depletion of MinD. *Proc Natl Acad Sci U S A* 113(11):E1479-E1488.

[13] Zheng M, *et al.* (2014) Self-Assembly of MinE on the Membrane Underlies Formation of the MinE Ring to Sustain Function of the Escherichia coli Min System *J Biol Chem* 289(31):21252-21266.

[14] Fange D & Elf J (2006) Noise-Induced Min Phenotypes in E. coli. *PLoS Comput Biol* 2(6):e80.

[15] Loose M, Fischer-Friedrich E, Ries J, Kruse K, & Schwille P (2008) Spatial regulators for bacterial cell division self-organize into surface waves in vitro. *Science* 320(5877):789-792.

[16] Kretschmer S, Zieske K, & Schwille P (2017) Large-scale modulation of reconstituted Min protein patterns and gradients by defined mutations in MinE's membrane targeting sequence. *PLoS One* 12(6):e0179582.

[17] Schindelin J, et al. (2012) Fiji: an open-source platform for biological-image analysis. *Nat Methods* 9(7):676-682.

Supplemental Tables

Parameter	Symbol	Value
MinD and MinE bulk diffusion	D_c	$60\,\mu m^2 s^{-1}$
MinD and MinDE membrane diffusion	D_m	$0.013\,\mu m^2 s^{-1}$
MinD mean total density	$\overline{[\mathrm{MinD}]}$	$638\,\mu m^{-3}$
MinD attachment rate constant	k_D	$0.065\,\mu m s^{-1}$
MinD recruitment rate constant	k_{dD}	$0.02\,\mu m^3 s^{-1}$
MinDE detachment rate	k_{de}	$0.34\,s^{-1}$
Nucleotide exchange rate	λ	$6\,s^{-1}$
Conformational switch of MinE	μ	$100\,s^{-1}$

Table S1. Kinetic rate constants for the MinE-MinD interaction switch network. The values of the diffusion coefficients and protein densities are chosen in accordance with experimental data [6]. The kinetic rate constants are chosen within the order of magnitude of the values fitted to reproduce the *in vitro* phenomenology qualitatively and the wavelengths and velocities quantitatively within the order of magnitude of the experimental data. In our analyses we performed extensive parameter scans in the recruitment rates k_{dE}^r and k_{dE}^l and the mean total MinE density $\overline{[\mathrm{MinE}]}$.

Parameter	Symbol	Value
MinD and MinE bulk diffusion	D_c	$60\,\mu m^2 s^{-1}$
MinD and MinDE membrane diffusion	D_m	$0.013\,\mu m^2 s^{-1}$
MinD mean total density	$\overline{[\mathrm{MinD}]}$	$638\,\mu m^{-3}$
MinD attachment rate constant	k_D	$0.065\,\mu m s^{-1}$
MinD recruitment rate constant	k_{dD}	$0.02\,\mu m^3 s^{-1}$
MinE recruitment rate constant	k_{dE}	$0.126\,\mu m^3 s^{-1}$
MinDE disintegration rate	k_{de}	$0.34\,s^{-1}$
Nucleotide exchange rate	λ	$6\,s^{-1}$

Table S2. Kinetic rate constants for the network including persistent MinE membrane binding. All rates that appear in both studied networks, the one with a MinE-MinD interaction switch and the one with persistent MinE membrane binding, are chosen equal. To study the impact of persistent membrane binding on the robustness of patterns, we performed extensive scans in MinE's reassociation rate k_{ed} with MinD and its detachment rate k_e from the membrane and the mean total MinE density $\overline{[\mathrm{MinE}]}$.

Supplemental Figures and Figure Legends

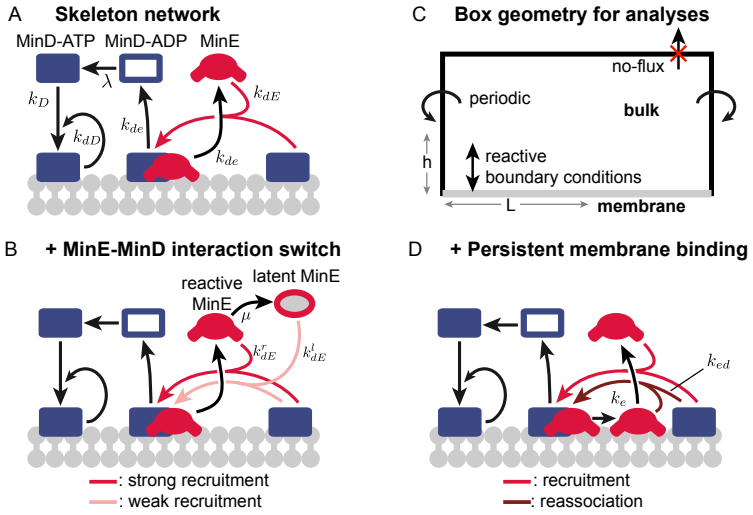

Fig. S1. Studied reaction networks. (*A*), In the previously studied skeleton network [1], MinD-ATP attaches to the membrane, where it recruits further MinD-ATP and MinE. Upon recruitment of MinE, MinE and membrane-bound MinD form a membrane-bound MinDE complex. MinE induces a switch of MinD to its ADP-bound form and thereby leads to MinDE disintegration and detachment of MinD-ADP and MinE into the cytosol. There, MinD has to exchange ATP for ADP before it can attach to the membrane anew. The kinetic rates are indicated next to arrows of their respective reactions. (*B*), To emulate a MinE-MinD interaction switch, the respective reaction network includes a switch with rate μ from reactive MinE with a high recruitment rate k^r_{dE} to latent MinE with a low recruitment rate k^l_{dE}. (*C*), Since the lateral extension of patterns *in vitro* are typically very large compared to their wavelength, we assume a reduced box geometry. Here, the membrane is modeled as the bottom line. The perturbations in our linear stability analysis are given by planar waves extending along the membrane. (*D*), When MinE is able to persist on the membrane after MinD detachment, it can either reassociate with membrane-bound MinD at a rate k_{ed} or detach at a rate k_e.

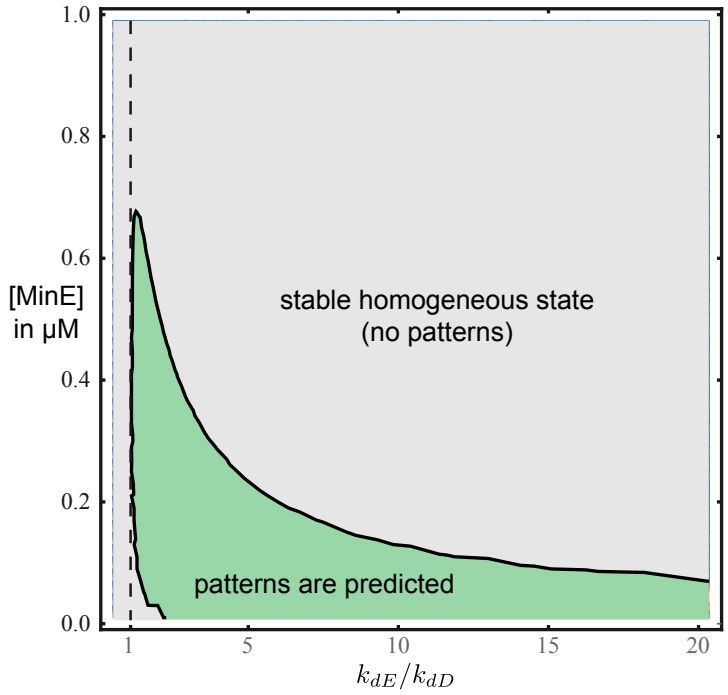

Fig. S2. In the skeleton model, the homogeneous state can only get unstable when MinD exceeds MinE in concentration. When changing the recruitment rate of MinE to membrane-bound MinD k_{dE} (relative to the recruitment rate of MinD to membrane-bound MinD), patterns are only predicted for MinE/MinD concentration ratios lower than one (the MinD concentration is chosen as 1μM). Furthermore, patterns can only form for $k_{dE} > k_{dD}$ (dashed line), which was discussed as another necessary condition previously [1]. We performed extensive sweeps over different rate constants and found a qualitatively similar behavior. For this diagram, the reaction rates were chosen as in Table S1.

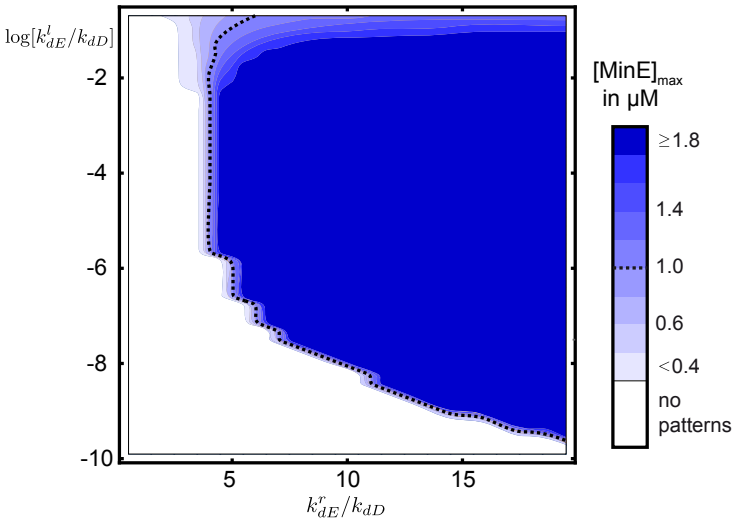

Fig. S3. When recruitment of latent MinE approaches zero patterns are absent. For fixed k^r_{dE} and decreasing k^l_{dE} to very small values (much smaller than show in Fig. 2), the homogeneous state is eventually stable and patterns are absent. The color code denotes the maximal MinE concentration for which the stationary homogeneous state is linearly unstable and patterns are predicted. The MinD concentration is fixed to 1μM and all reaction rates are chosen as in Fig. 2 (Table S1).

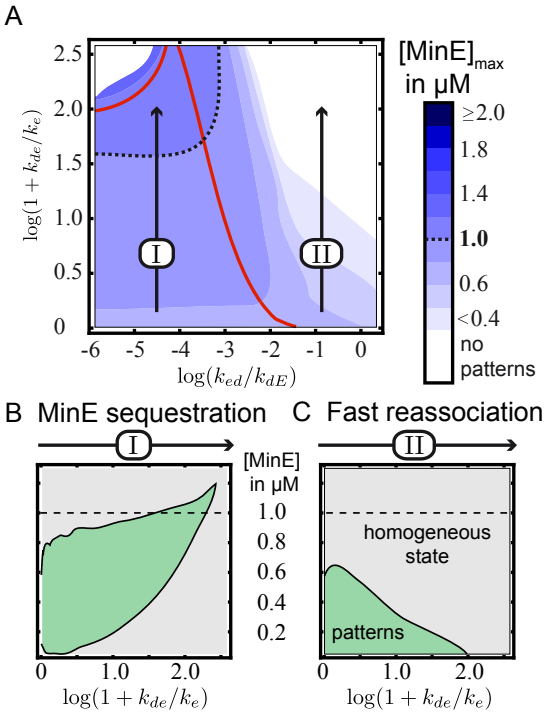

Fig. S4. Persistent membrane binding can modulate the range of pattern formation *in silico*. (*A*) Persistent MinE membrane binding can either increase or decrease $[\mathrm{MinE}]_{\max}$, depending on whether detachment or reassociation is favored (inside or outside the red lines), respectively (red lines denote equal detachment and reassociation). The y-axis depicts the minimal persistence time of MinE $(1/k_{ed} + 1/k_e)$ as compared to the disintegration time $1/k_{de}$). (*B*), (*C*) Along the trajectories (I) and (II) in (*A*) the region of MinE concentrations compatible with patterns increases (*B*) and shifts to higher MinE concentrations or decreases (*C*), when detachment or reassociation is favored, respectively. For kinetic rates see Table S2.

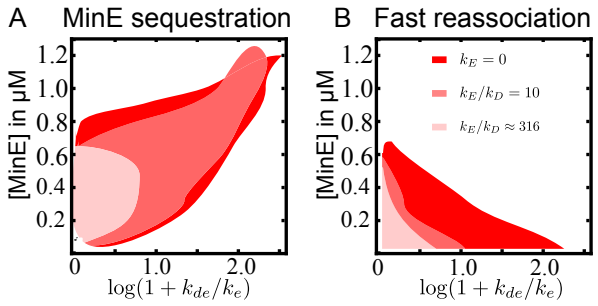

Fig. S5. Theory suggests that direct, MinD-independent attachment of MinE to the membrane does not change the effect of persistent MinE membrane binding qualitatively. (*A*), For slow reassociation ($\log(k_{ed}/k_{dE}) \approx -4.5$) the maximal MinE concentrations compatible with patterns (upper bound of red shaded regions) mostly increase when increasing the minimal persistence time of free MinE on the membrane (going from left to right in the x-axis). Only for unphysiologically high MinE attachment rates to the membrane ($k_E \gtrsim 316$) the maximal MinE concentration compatible with patterns decreases when increasing the minimal persistence time of free MinE on the membrane. (*B*), For fast reassociation ($\log(k_{ed}/k_{dE}) \approx -1$), including direct, MinD-independent MinE attachment to the membrane ($k_E > 0$) leads to a stronger decrease of the maximal MinE concentration compatible with patterns when increasing the minimal persistence time of free MinE on the membrane.

I.3 Single-mode turbulence and a spatially-reduced model for protein pattern formation

Over the last 15 years, the Min protein system has become a prototypical example for intracellular pattern formation [13, 67]. Numerous experimental studies [6, 13, 21, 48, 55, 68] have helped to derive useful theoretical descriptions of this self-organization process. Such theoretical descriptions [4, 5, 14] have been useful in predicting critical parameters for pattern formation such as reaction rates [5, 55], the enclosing geometry [5, 23, 26, 55], and protein densities [5, 57]. Indeed, many of these predictions are consistent with *in vitro* experiments, which studied the role of spatial extensions [16, 59] as well as protein concentrations [57, 58] in protein pattern formation.

In particular, recent theoretical studies [23] identified the bulk height as a critical parameter for the self-organization process in the Min system. For very low heights, a state of uniform membrane concentrations is stable and surface patterns are absent. When increasing the height above a certain value, the system starts to form surface patterns and approaches a turbulent state which is replaced by regular standing and traveling wave patterns for larger heights. This is consistent with recent experiments [57], which show a transition from turbulent dynamics (see fig. I.1(f)) at the onset of pattern formation to regular patterns further away from this threshold.

From a theoretical point of view, pattern formation is often studied in terms of dispersion relations, which indicate the initial growth (linear instability) of wave-like perturbations to a steady state solution of the system [24, 25]. Close to the onset of pattern formation, only a narrow range of wavelengths is linearly unstable. For supercritical reaction-diffusion systems, the growth of these wavelengths will eventually be saturated by nonlinear terms and the system assumes a state of regular patterns [24, 25]. Further away from the onset of pattern formation, the range of unstable wavelengths broadens and nonlinear coupling between multiple unstable wavelengths can lead to turbulent dynamics [24, 25].

The observation of turbulence in the Min system right at the onset of pattern formation [23, 57] thus points towards a neccessary rethinking of pattern formation in reaction-diffusion systems [23]. Especially for subcritical systems, such as the Min system [23], the mechanisms for pattern selection are largely elusive. More specifically, the observation of turbulence at the onset of pattern formation suggests that already the very few unstable wavelengths at this onset suffice to generate the rich phenomenology of the Min system.

To investigate this hypothesis, we studied a spatially-reduced model for intracellular pattern formation based on the Min skeleton network [4, 5]. In this model,

the complete vertical bulk extension is reduced to a bulk layer further away from the membrane coupled to a bulk-membrane layer close to the membrane. By finite element simulations, we show that for a suitable choice of thicknesses of these two layers, the reduced model reproduces the rich pattern phenomenology of the original skeleton model [23] including standing waves, traveling wave and turbulent patterns.

Combining our numerical results with linear stability analyses, we find a classification of the observed patterns in terms of representative dispersion relations. In particular, the formation of either standing wave patterns or turbulence can already be predicted based on a single-mode instability of the dispersion relation. Here, the only unstable wavelength is the largest wavelength compatible with the (periodic) boundary conditions. This wavelength is given by the lateral extension of the system. Increasing the lateral extension, we find a transition from standing wave patterns to turbulent patterns: as long as the lateral extension is smaller than the wavelength with the largest (positive) growth rate, we find standing wave patterns. For larger lateral extensions, we observe turbulence.

We also investigated the impact of a lateral discretization on the two-layer model. Our results suggest that while a coarse discretization may not be able to resolve the resulting regular or turbulent patterns, the transition between different lengthscales of patterns based on a single-mode instability is preserved even for a very coarse discretization.

Our study provides a simple and meaningful description of pattern formation in an intracellular reaction-diffusion network that involves protein-protein reactions on the membrane coupled to a diffusive bulk. In particular, we show that while the extension of the bulk (cytosol) cannot be neglected, the bulk can be reduced to two layers. This reduction not only yields a great advantage in terms of numerical cost but may also allow an analytically feasible description of reaction-diffusion systems where a reactive surface is coupled to a diffusive bulk. Such systems are not only wide-spread in the cell [13] but can also be found in more general model systems such as the catalytic carbon monoxide oxidation on platinum (CO-Pt system) [27, 28, 69].

I.3.1 Spatial reduction of the Min skeleton model

Numerous experimental [6, 13, 21, 48, 55, 68] and theoretical [4–6, 14, 23, 55, 64–66] studies have helped to gain insights into the reaction network underlying pattern formation in the Min protein system. Among mathematical approaches, the Min *skeleton model* [4, 5] (fig. I.2(a)) has proven especially useful, since it agrees with various experimental studies [6, 21, 54, 58] and has identified important mechanisms which could be confirmed experimentally [5, 54, 55, 57]. In particular, a very recent study based on the Min skeleton model [23] reports the formation of

regular standing wave patterns, traveling waves, and turbulent patterns reminiscent to the protein patterns observed in previous *in vitro* experiments [6, 56, 70].

The mathematical Min skeleton model [4, 5, 23] is based on a set of reaction-diffusion equations, where MinD-ATP, MinD-ADP, and MinE diffuse in the cytosol while reactions happen at the membrane. To be precise, ATP-bound MinD attaches to the membrane where it recruits further bulk MinD-ATP as well as MinE. On the membrane, MinD together with MinE then form membrane-bound MinDE complexes. In these complexes, MinE stimulates MinD's ATPase activity, thereby initiating disintegration of MinDE complexes and subsequent release of MinE and ADP-bound MinD into the cytosol. Reattachment of MinD to the membrane is delayed by exchange of ADP for ATP (fig. I.2(a)). Attachment to and detachment from the membrane can be modeled through reactive boundary conditions at the membrane [5, 23, 57]. To investigate the Min system in the geometry of *in vitro* experiments [6], a simple box geometry is typically assumed, where the lipid bilayer (membrane) is located at the bottom of the box and the bulk extends into the vertical direction. Furthermore, we focus on one slice of the $3D$ box geometry and assume a $2D$ box with periodic boundary conditions on the two sides and no-flux boundary condition at the top (fig. I.2(b), [23, 57])

Even in this simple box geometry especially the flux between bulk and membrane concentrations complicates numerical implementations. Theoretical studies suggest, that the flux between bulk and membrane is crucial to understand the mechanisms underlying Min pattern formation [23, 26, 57] and that neglecting the vertical extension of the bulk [59, 71] does not provide a meaningful description of the Min system [26]. On the other hand, concentration gradients coming from membrane-bulk fluxes will have a penetration depth above which vertical fluxes in the bulk should be negligible.

Motivated by these considerations, we propose a spatially-reduced Min skeleton model consisting of two layers, where the bottom layer (bulk-membrane layer) represents the membrane and a bulk region close to the membrane, and the top layer (bulk layer) represents the remaining bulk further away from the membrane (fig. I.1(c)). For the assumed $2D$ box geometry, these layers are one-dimensional and are thus given by horizontal lines as depicted in figure I.1(c). This choice implicitely assumes that there are two regions in the bulk: a bulk region close to the membrane, where the dynamics is dominated by protein fluxes due to attachment and detachment, and a region further away from the membrane, which can be understood as a reservoir, in which proteins are redistributed quickly in horizontal direction .[1] In our discretization scheme, we take into account that the thickness of the bulk-membrane layer is typically much smaller than the thickness of the bulk layer, consistent with experiments [73] and simulations [23, 57]. In the following,

1 This notion of a surface layer coupled to a reservoir is similar to previous considerations for the CO-Pt system [72]

we will refer to the thicknesses of the bulk-membrane layer and the bulk layer as h_0 and h_1, respectively, where $h_0 + h_1$ equals the total bulk height h. The distribution of the total bulk height onto the two layers (i.e. the ratio h_0/h_1) turns out to be an important system parameter of our reduced model and will be discussed in section I.3.2.

In addition to the vertical discretization present in this *two-layer model* (fig. I.2(c)) we investigate a spatial reduction of the lateral extension in section I.3.4. Since the lateral redistribution of concentrations in the original mathematical skeleton model [23] is purely diffusive, we will assume a regular discretization in the lateral direction with periodic boundary conditions (fig. I.2(d)). Here, a system of length L is represented by N lateral nodes where the distance between each node is L/N.

Whereas the original skeleton model [23] is based on partial differential equations for the protein concentrations together with reactive boundary conditions, the fully discretized Min model (fig. I.2(d)) is given by a set of ordinary differential equations. Without the lateral extension, the dynamics is given by the following equations for the protein concentrations on the bulk-membrane layer and the bulk layer.

In the bulk-membrane layer (close to the membrane):

$$\partial_t c_d(t) = c_{DT,0}(k_D + k_{dD}\, c_d) - k_{dE}\, c_d\, c_{E,0} \tag{I.1a}$$
$$\partial_t c_{de}(t) = k_{dE}\, c_d c_{E,0} - k_{de}\, c_{de} \tag{I.1b}$$
$$\partial_t c_{DT,0}(t) = -\, c_{DT,0}\,(k_D/h_0 + (k_{dD}/h_0)\, c_d) + \lambda\, c_{DD,0} + D_b \mathcal{D}_V[c_{DT,0}] \tag{I.1c}$$
$$\partial_t c_{DD,0}(t) = (k_{de}/h_0) c_{de} - \lambda\, c_{DD,0} + D_b \mathcal{D}_V[c_{DD,0}] \tag{I.1d}$$
$$\partial_t c_{E,0}(t) = (k_{de}/h_0) c_{de} - (k_{dE}/h_0)\, c_d\, c_{E,0} + D_b \mathcal{D}_V[c_{E,0}] \tag{I.1e}$$

In the bulk layer (further away from the membrane):

$$\partial_t c_{DT,1}(t) = \lambda\, c_{DD,1} + D_b \mathcal{D}_V[c_{DT,1}] \tag{I.1f}$$
$$\partial_t c_{DD,1}(t) = -\,\lambda\, c_{DD,1} + D_b \mathcal{D}_V[c_{DD,1}] \tag{I.1g}$$
$$\partial_t c_{E,1}(t) = D_b \mathcal{D}_V[c_{E,1}]\,. \tag{I.1h}$$

Here, c_d and c_{de} denote the concentrations of MinD and MinDE complexes on the membrane, respectively, c_{DT}, c_{DD}, and c_E are the bulk concentrations of respectively MinD-ATP, MinD-ADP, and MinE, and the index (0/1) specifies the layer (0 : bulk-membrane layer, 1 : bulk layer). The reaction rates k_D, k_{dD}, k_{dE}, k_{de}, and λ denote the rates for MinD attachment, MinD recruitment, MinE recruitment, MinDE dissociation, and nucleotide exchange, respectively (compare fig. I.2(a)). D_b is the diffusion constant in the bulk and $\mathcal{D}_V[\cdot]$ denotes the vertical hopping between the bulk-membrane layer and the bulk layer and is given by

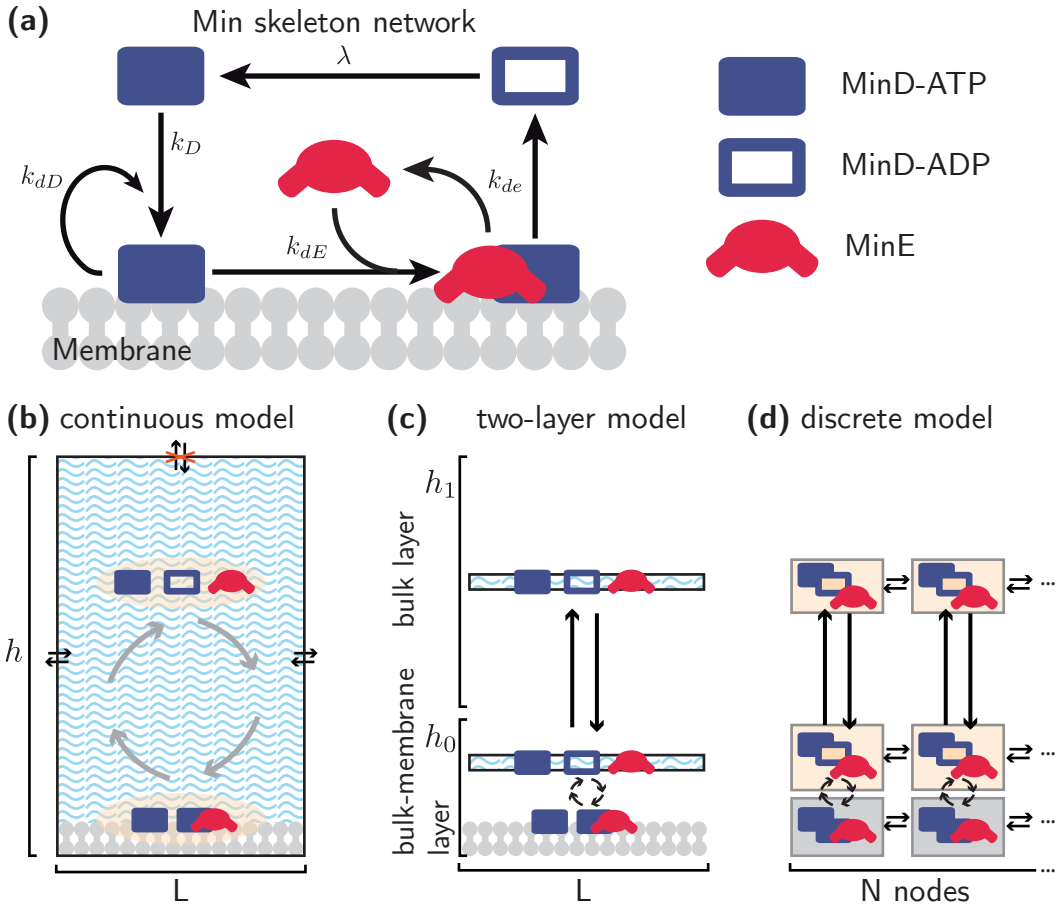

Figure I.2 The Min skeleton model and the presented reduction schemes. **(a)** Protein reaction network of the Min skeleton network [4, 5]. The reaction rates k_D, k_{dD}, k_{dE}, k_{de}, and λ denote the kinetic reaction rates for MinD attachment, MinD recruitment, MinE recruitment, MinDE dissociation, and nucleotide exchange, respectively. **(b)** In the original Min skeleton model [23], a $2D$ box geometry is assumed where MinD and MinE diffuse in the bulk and bind/unbind with the membrane according to (a). While the bulk-membrane flux is modeled through reactive boundary conditions at the membrane (bottom boundary), periodic and no-flux boundary conditions are assumed for the lateral boundaries and the top boundary, respectively. **(c)** In the *two-layer model*, the vertical bulk extension is reduced to a layer close to the membrane (bulk-membrane layer) and a layer further away from the membrane (bulk layer) which are both homogeneous in the vertical direction. In the lateral extension, (continuous) diffusion is retained. **(d)** In the fully discretized model, we further reduced the two-layer model by employing a regular lateral discretization.

$$\mathcal{D}_V[c_{j,\{0,1\}}] := \frac{c_{j,\{1,0\}} - c_{j,\{0,1\}}}{0.5h_{\{0,1\}}(h_0 + h_1)} \qquad \text{with} \qquad j \in \{DT, DD, E\}\,. \tag{I.2}$$

In particular, the definition I.2 takes into account, that the bulk-membrane layer and the bulk layer can have different thicknesses. The choice I.2 ensures that the hopping probability is inversely proportional to the distance between the layers ($0.5(h_0 + h_1)$) and the layer of origin ($h_{\{0,1\}}$), and reduces to the usual discrete diffusion operator $(c_{j,\{1,0\}} - c_{j,\{0,1\}})/(0.5h)^2$ for a regular discretization (i.e. for $h_0 = h_1$). Note, that equations (I.1) together with (I.2) conserve the overall concentrations of MinD and MinE (respectively [MinD] and [MinE]) given by

$$h[\text{MinD}] = c_d + c_{de} + h_0(c_{DT,0} + c_{DD,0}) + h_1(c_{DT,1} + c_{DD,1})\,, \tag{I.3a}$$
$$h[\text{MinE}] = c_{de} + h_0 c_{E,0} + h_1 c_{E,1}\,. \tag{I.3b}$$

In the following, we will mostly study the two-layer model, which assumes a continuous lateral extension (fig. I.2(c)). Here, lateral diffusion is readily included by complementing equations I.1 with a lateral diffusion term

$$\mathcal{D}_L[c_i] := D_c \nabla^2 c_i\,, \tag{I.4}$$

where the index $i \in \{d, e, (DT, 0), (DD, 0), (E, 0), (DT, 1), (DD, 1), (E, 1)\}$ denotes the respective protein concentration. For the geometry in figure I.2(c), $\nabla^2 = \partial_x^2$ and D_c is the lateral diffusion constant of the respective concentration and will be denoted as D_m for the membrane concentrations c_d and c_{de} and D_b for all other concentrations.

In section I.3.4 we will turn to a fully discretized model (fig. I.2(d)) of L/N nodes where for every lateral node $m \in \{1, 2, \ldots, N\}$ a lateral diffusion operator $\mathcal{D}_L[c^m]$ is added to each of the equations in I.1. For a regular grid with lattice spacing L/N this operator is given by

$$\mathcal{D}_L[c^m] := D_c \frac{c^{m+1} + c^{m-1} - 2c^m}{(L/N)^2}\,, \tag{I.5}$$

where the concentration c stands for the respective protein concentration. Furthermore, we will employ periodic boundary conditions in the lateral direction such that $c^{-1} = c^N$ and $c^{N+1} = c^1$.

I.3.2 Phase diagram and pattern phenomenology of the *two-layer model*

For any reduction of a model to be meaningful, the reduction has to (at least qualitatively) preserve the crucial properties of the original model. Halatek et al. [23] suggest that the dispersion relation is central for the dynamics in the Min skeleton model, especially at the onset of pattern formation.

In the following, we will compare the continuous Min skeleton model (fig. I.2(b)) and the two-layer model (fig. I.2(c)) in terms of their dispersion relations for varying overall MinD and MinE concentrations. The dispersion relation is given by the growth rates of wave-like perturbations with wavelengths λ to a steady state solution that is uniform on the membrane (see Supplemental Material of [57] reprinted in section I.2). We will often characterize these wave-like perturbations in terms of their wavenumber q where $q = 2\pi/\lambda$. For the two-layer model, the dispersion relation can be calculated by linearizing equations (I.1), (I.2) and (I.4) with respect to their steady state solution and substituting wave-like perturbations $\delta c(x, t)$ of the form

$$\delta c(x, t) \sim \mathrm{e}^{\Omega t + \mathrm{i} q x} \delta \hat{c}_q \,, \tag{I.6}$$

where $\delta \hat{c}_q$ denotes the amplitude of perturbations with wavelength $\lambda = 2\pi/q$. The linearized equations then compose a simple eigenvalue problem which can be solved to obtain Ω. This yields the dispersion relation $\sigma(q) := \Re[\Omega](q)$ as a function of the wavenumber q [24, 25]. For simplicity, we fix the reaction rates and diffusion constants to values studied previously in the original Min skeleton model [5, 23, 57] and which are consistent with experimental observations. In detail, $k_D = 0.065\,\mu\mathrm{m\,s^{-1}}$, $k_{dD} = 0.098\,\mu\mathrm{m^3\,s^{-1}}$, $k_{dE} = 1.126\,\mu\mathrm{m^3\,s^{-1}}$, $k_{de} = 0.34\,\mathrm{s^{-1}}$, $\lambda = 0.34\,\mathrm{s^{-1}}$, $D_b = 60\,\mu\mathrm{m^2\,s^{-1}}$ and $D_m = 0.013\,\mu\mathrm{m^2\,s^{-1}}$. The height of the system (i.e. the vertical bulk extension) is set to $h = 20\,\mu\mathrm{m}$, which allows a rich phenomenology in the original Min model [23].

Calculating the dispersion relation for the original Min skeleton model is more involved than for the two-layer model due to the reactive boundary conditions at the membrane. In particular, finding the growth rate $\sigma(q)$ is no longer an eigenvalue problem as for the two-layer model. For a detailed discussion we refer to section I.2 (Supplemental Material of [57]). The linear stability of steady state solutions in the original Min skeleton model is depicted in the phase diagram of figure I.3(a) as a function of the overall protein concentrations [MinD] and [MinE]. Here, we focused on overall concentrations of MinD around $1\,\mu\mathrm{M}$ (i.e. $1\,\mu\mathrm{mol\,l^{-1}}$), which is a typical concentration used in Min reconstitution experiments [6, 57]. In particular, we find concentration regimes where the steady state solution is unstable against a homogeneous perturbation, i.e. $q = 0$, (Hopf instability) and regimes in

which the steady state is unstable against perturbations with finite wavelengths only (Turing instability). These instabilities suggest the formation of concentration patterns on the membrane. A numerical solution of the original skeleton network as in [23] would give access to the long-term dynamics and the resulting patterns; however, such numerical solution can be costly mostly due to the reactive boundary conditions at the membrane causing fluxes between the membrane and the bulk.

Instead, we take a different approach: varying the height distribution in our two-layer model (i.e. h_0/h_1), we first seek the best match of this model with the original model in terms of their phase space structure. Halatek et al. suggest that the shape of the dispersion relation is critical for pattern formation and selection. We therefore match their dispersion relations in terms of the band of unstable wavenumbers (bounded by q_{min} and q_{max}) as well as the fastest growing wavenumber q_c (see fig. I.3(b)). To calculate dispersion relations in the two-layer model, we solved the above-discussed eigenvalue problem numerically using `Wolfram Mathematica 11` [74].

Phase diagrams for the two-layer model with different h_0/h_1 are shown in figure I.3(c). When the two layers are equally thick (i.e. $h_0 = h_1 = h/2$), as it would be the case for a regular vertical discretization, and when $h_0 > h_1$, we do not find a regime of unstable steady states. This is in agreement with our above perception of a thin reactive layer close to the membrane and a large reservoir further away from the membrane.

For the chosen set of reaction rates and parameters, we find a very good agreement with the original skeleton model in terms of their phase diagrams when $h_0/h_1 = 0.1235$. For our choice of $h = 20\,\mu\text{m}$ this yields $h_0 = 2.1985\,\mu\text{m}$ and $h_1 = 17.8015\,\mu\text{m}$ (fig. I.3(b)).

I.3.2a Numerical solutions of the two-layer model

In contrast to the original Min skeleton model, the two-layer Min model can be implemented numerically at very low cost. Here, we employed the above presented two-layer discretization scheme with $h_0 = 2.1985\,\mu\text{m}$ and $h_1 = 17.8015\,\mu\text{m}$ and numerically solved equations (I.1), (I.2) and (I.4) for a system of length $L = 24\,\mu\text{m}$. All simulations were performed using `PYTHON 3.6.3` software [75][2] and the numerical results were evaluated using `Wolfram Mathematica 11`. Figure I.4(a) shows typical kymographs of the membrane concentration ($c_d + c_{de}$) for different overall MinE concentrations at an overall MinD concentration of $1.06\,\mu\text{M}$. In particular,

2 Our numerical implementation is based on a spatially finite difference method and temporal Euler forward scheme. The lateral discretization is chosen sufficiently fine to exclude discretization effects in the lateral extension and to best account for the continuous lateral extension in the two-layer model.

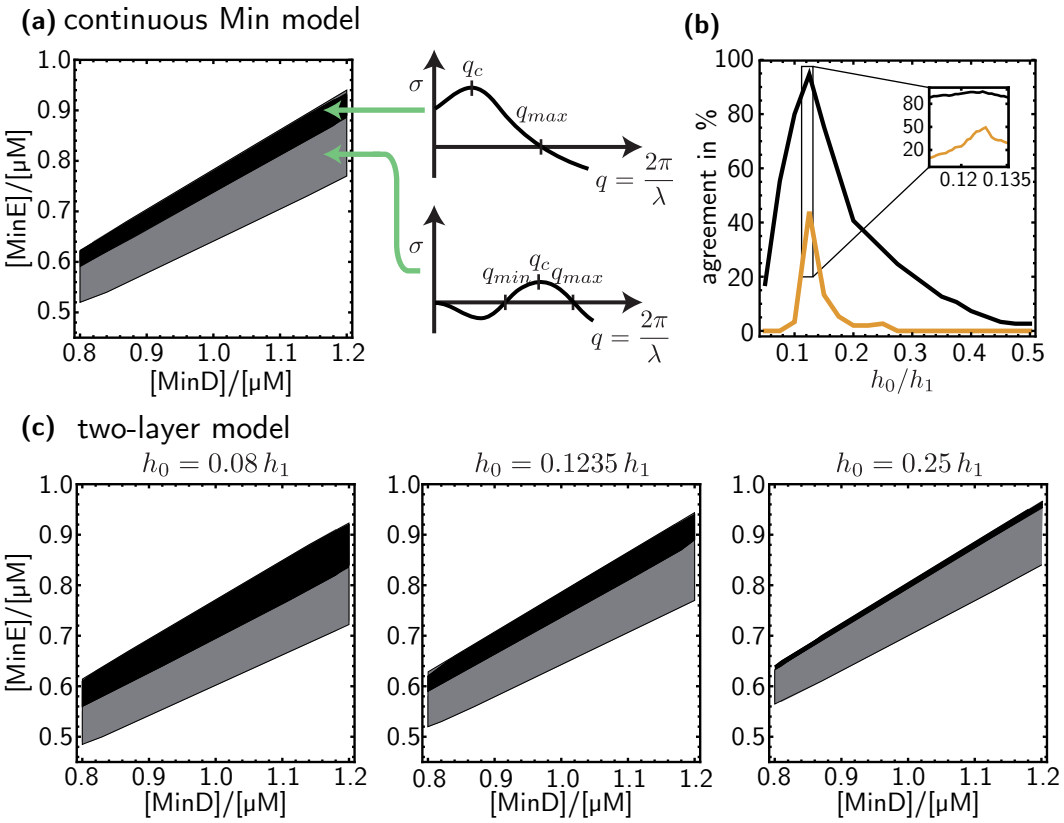

Figure I.3 Comparison of phase diagrams of the original Min skeleton model and the two-layer Min model for different ratios h_0/h_1. **(a)** Depending on the overall MinD and MinE concentrations, [MinD] and [MinE], respectively, the dispersion relation shows instabilities against homogeneous perturbations (black regime) and wave-like perturbations with finite wavenumber q (gray regime), which grow at a rate $\sigma(q)$. **(b)** The agreement between the dispersion relations of the continuous model and the two-layer model depends on the choice of h_0 and h_1, where $h_0 + h_1 = h$. The agreement was calculated in terms of a match of overall MinD and MinE concentrations that lie in the unstable regime (black line) and a match of q_{min}, q_{max}, and q_c in the unstable regime (orange line). **(c)** Example phase diagrams of the two-layer Min model for different h_0/h_1.

we observe the formation of traveling waves ([MinE] $= 0.73\,\mu\mathrm{M}$), standing waves ([MinE] $= 0.7\,\mu\mathrm{M}$), and more irregular, turbulent dynamics ([MinE] $= 0.68\,\mu\mathrm{M}$).

In order to characterize coherent patterns with well-defined wavelengths and periodicities and distinguish them from more irregular patterns such as turbulence, it often proves useful to study the power spectral density of the pattern-forming observable [24, 25]; in our case, we focus on the protein concentration on the membrane. The power spectral density of a concentration c at the position x is given by

$$S^{cc}(x,\omega) = \lim_{\tau\to\infty} \frac{1}{\tau}\langle |c(x,\omega)|^2\rangle \tag{I.7}$$

where $c(x,\omega) = \int_{-\tau/2}^{\tau/2} \mathrm{d}t\, \mathrm{e}^{\mathrm{i}\omega t} c(x,t)$ denotes the temporal Fourier transform of $c(x,t)$, which is a function of the frequency ω, and $\langle\cdot\rangle$ should be understood as ensemble average. When $c(x,t)$ shows patterns with well-defined frequencies, these frequencies will be pronounced in its Fourier transform $c(x,\omega)$. The direct relation between $c(x,\omega)$ and the power spectral density thus indicates that the power spectral density is a useful measure to distinguish between coherent patterns with a characteristic timescale and patterns with more irregular dynamics that involve dynamics on different timescales. Our numerical simulations yield datasets for concentration values $c_{m,t}$, where $m \in \{1,2,\ldots,N\}$ denotes the node of the lateral discretization of our finite element method and $t \in \{0,1,\ldots,T-1\}$ is the recorded timepoint. $c_{m,0}$ and $c_{m,T-1}$ are the first and last samples of the concentration c at the node m, respectively. In this case of a discrete dataset, it is more convenient to estimate the power spectral density using a periodogram [76]. Here, the spectral density of a concentration at the node m is estimated by the absolute square of its discrete Fourier transform:

$$S^{cc}_{m,r} = |c_{m,r}|^2 \tag{I.8}$$

with the discrete Fourier transform defined by

$$c_{m,r} = \sum_{t=0}^{T-1} c_{m,t} \mathrm{e}^{2\pi\mathrm{i}\,(tr/T)}\,, \qquad c_{m,t} = \frac{1}{T}\sum_{r=0}^{T-1} c_{m,r}\mathrm{e}^{-2\pi\mathrm{i}\,(tr/T)}\,. \tag{I.9}$$

In analogy to the power spectral density, pronounced frequencies in the dataset of concentrations result in pronounced peaks in the periodogram.

All observed patterns in our numeric solutions show periodicity in time whose frequency is indicated by the maximum of the respective periodogram. However, whereas for standing and traveling wave solutions this maximally pronounced frequency is also the smallest pronounced frequency in the periodogram, for irregular patterns we also find pronounced frequencies that are much smaller than the

maximally pronounced frequency (compare periodograms in fig. I.4(b) for regular and irregular patterns). Furthermore, we make use of the fact that for standing wave solutions, concentration maxima and minima are fixed whereas for traveling wave solutions concentration maxima experience the whole lateral extension. Also for irregular patterns, we find solutions where concentration maxima are bounded to certain regions and solutions where concentration maxima experience the whole lateral extension. For very high MinE concentrations, we observe homogeneous oscillations with zero spatial variance. The numerical characterization of our simulation results based on all these criteria is displayed in fig. I.4(b).

Our numerical analysis shows that for small overall MinE concentrations at the onset of pattern formation, the dynamics shows multiple pronounced frequencies. This is confirmed by the respective kymographs (e.g. fig. I.4(a), [MinE] $= 0.68\,\mu\mathrm{M}$), which reveal irregular patterns on multiple time- and lengthscales. Furthermore, we observe a jump (discontinuous increase) in the membrane concentration amplitude when crossing the onset of pattern formation. This strongly suggests, that the bifurcation to pattern formation is subcritical, consistent with previous studies of the original skeleton model [23].[3]

When increasing the overall MinE concentration, the respective periodograms mark one characteristic, maximally pronounced frequency. Indeed, the respective kymographs show coherent (regular) patterns. Here, we find standing waves for lower overall MinE concentrations (fig. I.4(a), [MinE] $= 0.7\,\mu\mathrm{M}$) and traveling waves (fig. I.4(a), [MinE] $= 0.73\,\mu\mathrm{M}$) for higher overall MinE concentrations.

Increasing the overall MinE concentration even further, we find that the number of pronounced frequencies present in the periodogram again increases and more complex patterns can emerge including superpositions of traveling and standing waves (e.g. I.4(a), [MinE] $= 0.76\,\mu\mathrm{M}$).

At the limiting case of high overall MinE concentrations, we also observe homogeneous oscillations ([MinE] $= 0.83\,\mu\mathrm{M}$, kymograph not shown).

All of the observed patterns and their assignment to the respective overall MinD and MinE concentrations in the phase diagram (fig. I.4(b)) are consistent with previous studies of the original Min skeleton model [23]. In particular, the two-layer Min model reproduces a phase of irregular patterns close to the onset of pattern formation.

I.3.2b Regimes of dispersion relations

We have shown that for a convenient ratio h_0/h_1, the spatially-reduced two-layer model yields similar dispersion relations as the original skeleton model (fig. I.3).

3 Preliminary simulations of the two-layer model suggest there is also a regime for low MinD concentrations where the bifurcation to pattern formation is supercritical and the amplitude of patterns increases gradually when crossing the onset of pattern formation.

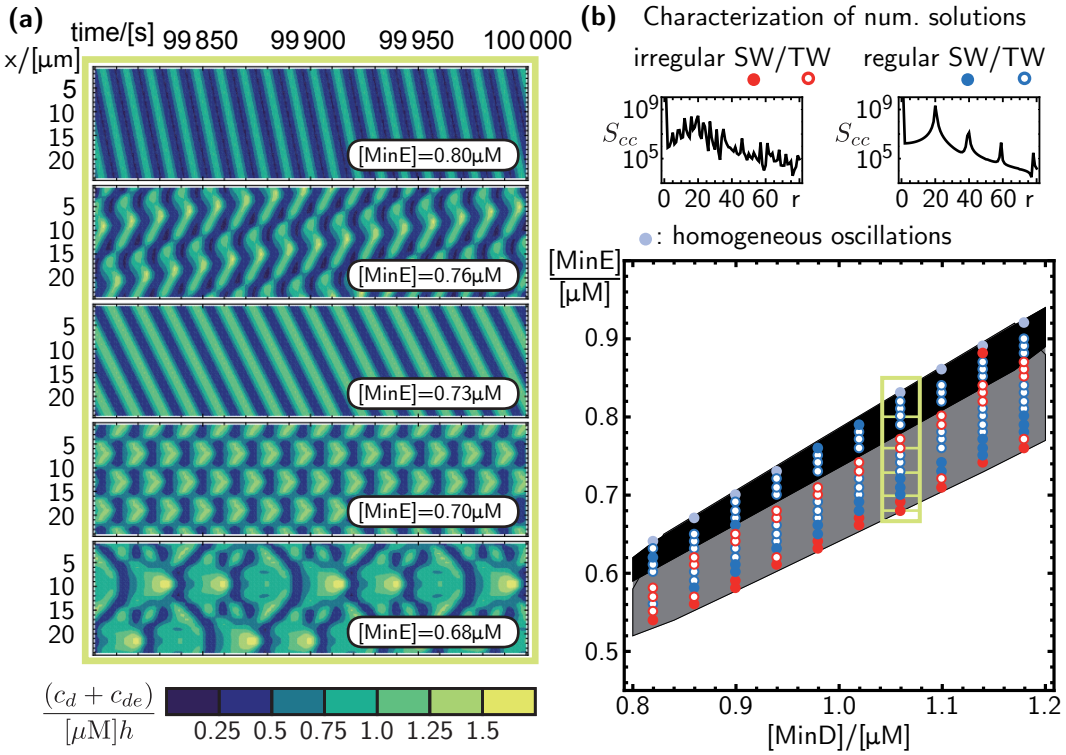

Figure I.4 The two-layer model displays traveling and standing wave patterns as well as turbulent dynamics depending on the overall protein concentrations. **(a)** Simulation results of the two-layer model for [MinD] $= 1.06\,\mu\mathrm{M}$ and different MinE concentrations for a system size of $L = 24\,\mu$m. For our finite element method, we used a lateral discretization $L/N = 1\,\mu$m and periodic boundary conditions. As initial conditions, we employed homogeneous MinD and MinE distributions in the bulk and an empty membrane. The kymographs show the membrane density $c_d + c_{de}$ for the last $200\,$s of our simulations. **(b)** The periodograms of the membrane densities help to distinguish irregular pattern (left periodogram, [MinD] $= 1.06\,\mu\mathrm{M}$, [MinE] $= 0.68\,\mu\mathrm{M}$) from regular patterns (right periodogram, [MinD] $= 1.06\,\mu\mathrm{M}$, [MinE] $= 0.73\,\mu\mathrm{M}$). Furthermore, the position of concentration maxima indicates standing wave patterns (SW) or moving/traveling wave patterns (TW). The green box in the phase diagram highlights the numerical sweep shown in (a) (the exact MinE concentrations for which simulations are shown are indicated by horizontal lines in the box).

Furthermore, the two-layer Min model shows a remarkably similar pattern phenomenology including standing and traveling wave patterns as well as turbulent dynamics close to the onset of pattern formation (fig. I.4). These results consolidate the two-layer model as a useful basis to investigate pattern formation and selection in the Min system. At the beginning of this chapter, we hypothesized that the rich phenomenology of Min patterns can be understood in terms of dispersion relations and is based on the instability of only a few wavelengths. In this section we use the two-layer model in order to test this hypothesis and to study a possible relation between Min protein patterns and the underlying dispersion relations.

In section I.3.2, we calculated dispersion relations for a system of infinite lateral extension; however, any numerical simulation as well as experiment can only treat systems of a finite size. Importantly, not all wave-like perturbations that would grow in an infinite system are supported in a finite system. In particular, only wave-like perturbations that obey the boundary conditions of the system are physically relevant. In our simulations (fig. I.4), where we employed periodic boundary conditions, this means that only perturbations with wavelengths $\lambda_n = L/n$ with $n \in \mathbb{N}$ are eligible and can destabilize the pattern-free state. This restricts the wavenumber q to the discrete modes $q_n = n(2\pi/L)$. The sketch in figure I.5(a) shows the dispersion relation for a Turing instability, where the band of unstable modes is bounded by q_{min} and q_{max}, and q_c denotes the mode where the growth rate σ is maximal. A finite system with periodic boundary conditions only supports discrete modes, denoted as q_1, q_2, q_3, and q_4 in figure I.5(a). A closer look at the relative positions of q_{min}, q_{max}, q_c, and the discrete modes q_n suggests an interesting link to the approached final patterns in our numerical solutions. In figures I.5(b) and (c), we provide a heuristic characterization of patterns based on different types of dispersion relations:

Single-mode instability: For low overall MinE concentrations at the onset of pattern formation, only the first mode q_1 with a wavelength L lies in (q_{min}, q_{max}) and is thus the only unstable mode. Furthermore, $q_1 < q_c$, which means that perturbations with a shorter wavelength $2\pi/q_c < L$ would in fact grow faster than any other perturbation; however, they are not eligible due to the periodic boundary conditions of the finite system. Our numerical simulations (fig. I.4(a), $[\mathrm{MinE}] = 0.68\,\mu\mathrm{M}$) reveal interesting irregular patterns, which involve multiple length- and timescales. We hypothesize, that these irregular patterns arise due to a competition between the first mode q_1 and the maximally growing mode q_c, which cannot establish a solution that obeys the boundary conditions but still drives the system away from a coherent pattern where q_1 would set the only lengthscale. We will investigate this hypothesis in the next section I.3.3.

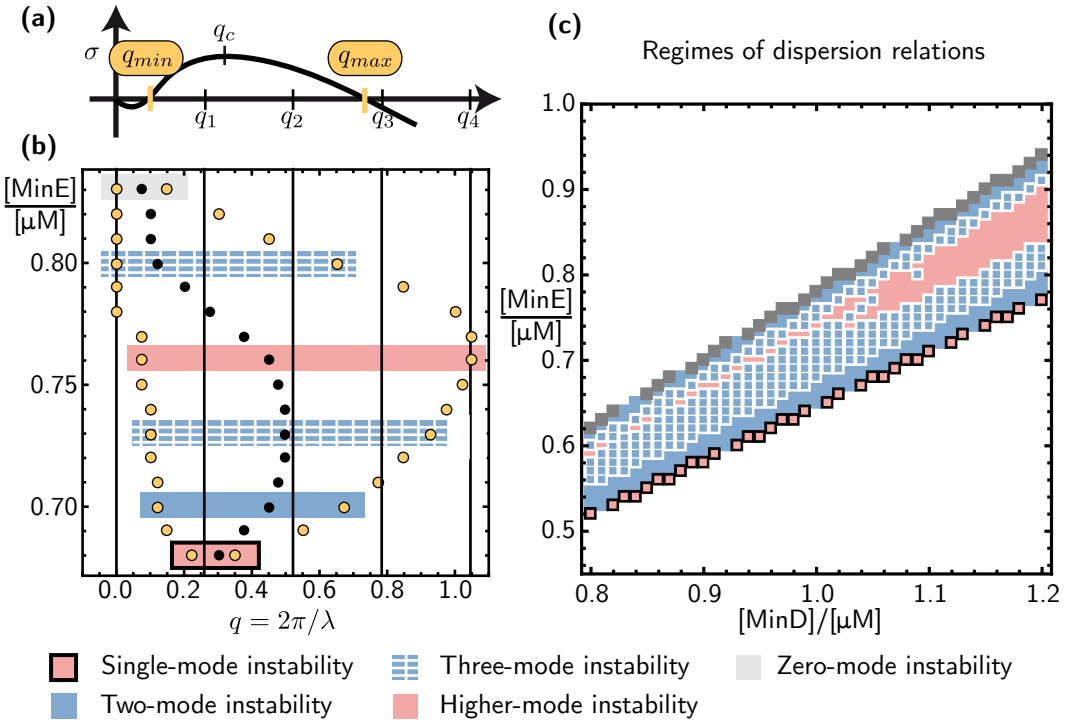

Figure I.5 Characterization of typical dispersion relations for the two-layer model. **(a)** Sketch of the dispersion relation of a Turing instability. The band of unstable modes is bounded by (q_{min}, q_{max}), and q_c denotes the mode with the maximal growth rate. A finite system with periodic boundary conditions only supports discrete modes denoted here as q_1, q_2, q_3, and q_4. In this example, only the modes q_1 and q_2 are unstable. **(b)** Diagram of (q_{min}, q_{max}) and q_c as a function of the overall MinE concentration [MinE] ([MinD] $= 1.06\,\mu\mathrm{M}$). The shaded MinE concentrations correspond to the simulation results shown in fig. I.4(a) and represent typical scenarios for single-, two-, three-, four- and zero-mode instabilities. **(c)** Using the color code of the shaded cases in (b) for respectively single-, two-, three-, four- and zero-mode instabilities, we indicated the regimes of respective dispersion relations in the phase portrait.

Two-mode instability: Increasing the overall MinE concentration, the dispersion relation gradually changes until also the second mode q_2 is unstable. q_c approaches q_2, suggesting that perturbations with a wavelength $2\pi/q_2 = L/2$ grow most rapidly. Indeed, the system approaches a state of standing wave patterns with a characteristic lengthscale of $L/2$ (fig. I.4(a), [MinE] $= 0.7\,\mu\mathrm{M}$). We also find 'two-mode instabilities' for larger overall MinE concentrations (e.g. [MinE] $= 0.82\,\mu\mathrm{M}$), where q_0 and q_1 are unstable. Accordingly, our numerical simulations show a superposition of standing wave patterns and homogeneous oscillations (not shown).

Three-mode instability: For even higher overall MinE concentrations, also the third mode q_3 lies in the band of unstable modes. The maximal growing mode that obeys periodic boundary conditions is still given by q_2. Accordingly, our numerical solution shows traveling waves with a characteristic wavelength $L/2$ (fig. I.4(a), [MinE] $= 0.73\,\mu\mathrm{M}$). In addition, we also find traveling waves when not the modes q_1, q_2 and q_3 but q_0, q_1 and q_2 are unstable. Here, q_c is closer to q_1 than to q_2 which matches with the observation that the wavelength in this case is no longer $L/2$ but L (fig. I.4(a), [MinE] $= 0.8\,\mu\mathrm{M}$).

Higher-mode instability: Increasing the overall MinE concentration further, the dispersion relations broadens and the unstable band can also include q_4. Our numerical solution shows that the coupling of unstable modes can lead to more complex patterns such as superpositions of standing and traveling waves including more irregular dynamics (fig. I.4(a), [MinE] $= 0.76\,\mu\mathrm{M}$).

Zero-mode instability: At the limit of high overall MinE concentrations, we find dispersion relations where only q_0 has a positive growth rate. Our simulations suggest that here the system approaches a state of homogeneous oscillations (e.g. [MinE] $= 0.83\,\mu\mathrm{M}$, kymograph not shown).

A classification of dispersion relations according to these criteria yields the 'regimes of dispersion relations' shown in figure I.5(c). First, we find that the discussed types of dispersion relations are not particular for [MinD] $= 1.06\,\mu\mathrm{M}$, but that the sequence of these types when increasing [MinE] is a robust feature of the phase diagram (i.e. first single-mode, then two-mode, three-mode, higher-mode, again three-mode, and finally zero-mode instability). In particular, we find a transition from a single-mode to a two-modes instability close above the threshold overall MinE concentration. Furthermore, a comparison of figure I.5(c) and figure I.4(b) reveals a remarkable correspondence between the regimes of typical dispersion relations and the classification of our simulation results in terms of periodograms. Especially at the onset of pattern formation, the regimes of

single-mode and two-modes instability match. This correllation suggests that the above heuristic characterization of the dispersion relation indeed hints towards an underlying relationship between dispersion relations and the long-term dynamics of the system. This is especially interesting since albeit the dispersion relation has proven useful to characterize patterns close to supercritical bifurcations [24, 25], its predictive power for subcritical patterns remains largely elusive. In particular, we observe turbulent protein patterns close the onset of protein pattern formation where only one single mode is unstable. While this agrees with previous studies on the original Min skeleton model [23] and *in vitro* experiments [57], this sheds new light on to traditional conceptions of turbulence, where turbulence is often explained on the basis of nonlinear coupling of multiple unstable modes [24, 25]. In the following, we will focus on the single-mode instability close to the onset of protein pattern formation and investigate pattern selection as well as the emergence of turbulent dynamics.

I.3.3 The onset of pattern formation: single-mode instabilities and turbulence

Consistent with previous studies [23, 57], our combined phase diagrams (fig. I.5(c)) and numerical simulation (fig. I.4) strongly suggest, that close to the onset of protein pattern formation, turbulent dynamics can be induced by a single unstable mode. So far, we have manipulated the dispersion relation by changing the overall protein concentrations [MinD] and [MinE]. This resulted in different types of dispersion relations with one and more unstable modes. In the following, we want to focus on the scenario where only the first mode is unstable and ask how such single-mode instability can lead to turbulent patterns. Instead of manipulating the dispersion relation for a fixed system size L, we now fix the dispersion relation by fixing [MinD] and [MinE], and systematically vary the position of the first mode $q_1 = 2\pi/L$ by varying L. This allows us to precisely control the position of the unstable mode(s) and investigate their role for the formation of patterns. In the following, we will focus on fixed overall protein concentrations [MinD] $= 1.06\,\mu\mathrm{M}$ and [MinE] $= 0.68\,\mu\mathrm{M}$, which led to turbulent patterns for a system size of $L = 24\,\mu$m (fig. I.4).

Based on a linear stability analysis of the two-layer model, figure I.6(a) shows the growth rates of perturbations with wavelength λ_1 (solid), λ_2 (dashed), and λ_3 (dotted) with $\lambda_n = L/n$. Increasing the system size L gradually, there is a critical length $\tilde{L}$ beyond which the wavelengh $\lambda_1 = L$ (i.e. the first mode) is unstable marked by a positive growth rate σ. Furthermore, figure I.6(a) displays a maximum growth rate for perturbations with wavelength λ_c. Similar to I.3.2a, we numerically solved equations (I.1), (I.2) and (I.4) for the two-layer model based on a finite element method with a fine lateral resolution using `PYTHON` software.

We then numerically calculated the periodograms of the obtained datasets using `Mathematica 11` to analyze our simulation results. In order to investigate the role of unstable wavelengths for the lengthscales in the emerging patterns, we now focused on the *spatial* periodogram given by

$$S_{k,t}^{cc} = |c_{k,t}|^2 \tag{I.10}$$

with the discrete spatial Fourier transform defined by

$$c_{k,t} = \sum_{m=0}^{N-1} c_{m,t} e^{2\pi i\,(km/N)}\,, \qquad c_{m,t} = \frac{1}{N}\sum_{k=0}^{N-1} c_{k,t} e^{-2\pi i\,(km/N)}\,. \tag{I.11}$$

Whereas the position of the periodogram's maximum indicates the dominant mode in the system, additional pronounced modes in the periodogram reflect the presence of multiple lengthscales as we expect them in turbulent patterns. We calculated the temporal mean of the dominant mode (green circles in fig. I.6(b)) as well as the average number of contributing wavelengths (gray circles in fig. I.6(b)) for the last 300 timesteps of our simulations.

Close above the onset of pattern formation at $\tilde{L}$, our numerical solutions reveal a regime of coherent standing wave patterns (fig. I.6(c), $L = 18.5\,\mu\text{m}$). Accordingly, the periodograms show that the mean characteristic wavelength of patterns is approximately given by L (first mode) but also involves dynamics on smaller lengthscales (the average dominant mode lies between the first and the second mode) (fig. I.6(b)). This behavior appears unchanged also for larger system sizes as long as $L < \lambda_c$.

Increasing the lateral extension L, the growth rate of perturbations with wavelength L increases until it reaches its maximum at $L = \lambda_c$. Interestingly, here our numerical simulations reveal a second transition: For $L > \lambda_c$ regular standing wave patterns are replaced by more irregular patterns which show dynamics on multiple lengthscales (fig. I.6(c), $L > \lambda_c \simeq 21\,\mu\text{m}$). Accordingly, the periodograms clearly mark an onset of a rapid increase in the number of contributing modes at λ_c. In particular, while the dominant mode of the patterns appears to still rely on the unstable mode, the number of contributing modes shows a gradual increase for increasing L (fig. I.6(b)).

As mentioned in section I.3.2b, we argue that the irregular patterns observed for $L > \lambda_c$ emerge from an interplay between the only unstable wavelength $\lambda = L$, which is compatible with periodic boundary conditions, and the wavelength λ_c, which has the maximal growth rate. Although perturbations with wavelength λ_c would in fact grow faster than any other perturbation, they are not able to establish since they do not obey the periodic boundary conditions (fig. I.6(d)). Based on this argument, the emergence of turbulence relies on the fact that in a finite system,

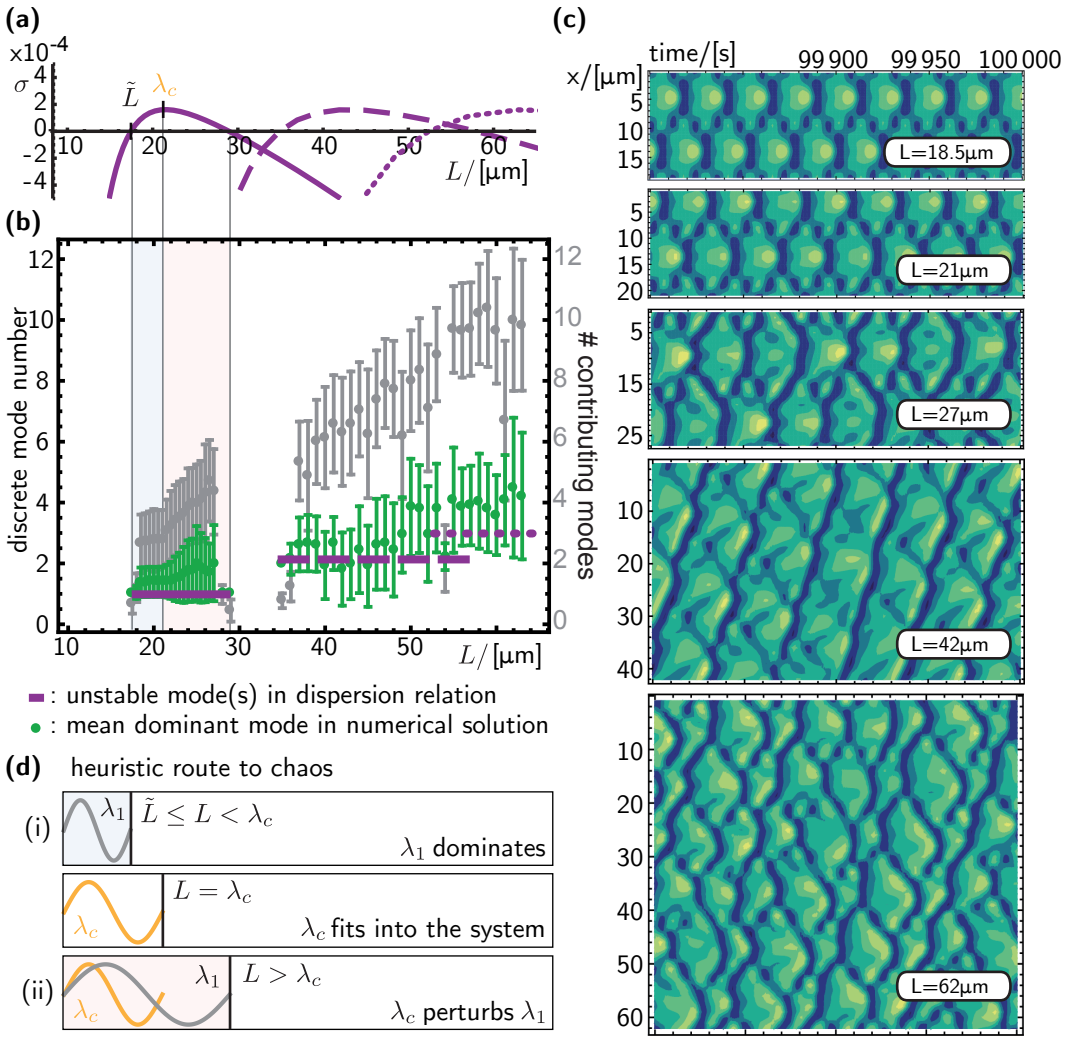

Figure I.6 Turbulent patterns emerge from single-mode instabilities. **(a)** The dispersion relation gives the growth rate of a wave-like perturbation with wavelength $\lambda_1 = L$ (solid), $\lambda_2 = L/2$ (dashed) and $\lambda_3 = L/3$ (dotted) and shows a maximum growth rate for a perturbation with wavelength λ_c. **(b)** Unstable modes in the dispersion relation and numerical simulations. Purple lines indicate unstable modes q_1 (solid), q_2 (dashed), and q_3 (dotted) as given in (a). Green circles indicate the mean maximally pronounced mode in the periodograms of the simulation results averaged over the last $300\,\mathrm{s}$ (the total simulation time was $10^5 s$ to assure that the simulations have relaxed to the steady state solution); error bars show the standard deviation. Gray circles denote the number of modes that contribute in the periodogram averaged over the last $300\,\mathrm{s}$; errorbars denote standard deviations. A mode was considered to contribute, when its weight is larger than $p\times$ the maximal contribution, where p was set to 0.05 (whereas varying p slightly changes the number of contributing modes, the trend of an increasing number of modes for increasing length is preserved).**(c)** Simulation results (kymographs) for $[\mathrm{MinD}] = 1.06\,\mu\mathrm{M}$, $[\mathrm{MinE}] = 0.68\,\mu\mathrm{M}$ and different lengths L. A very fine lateral resolution of $L/N = 0.5\,\mu\mathrm{m}$ is used. All simulations started at the homogeneous steady state; initial conditions as in fig. I.4(a) did not yield a qualitative difference. The colorbar is as in figure I.4(a). **(d)** We argue that regular standing patterns arise as long as λ_1 is the maximally growing lengthscale, as shown in (i). (ii): For $L > \lambda_c$, perturbations with wavelength λ_c would dominate but cannot establish since they do not obey the periodic boundary conditions.

the continuous range of unstable wavelengths is restricted to discrete wavelengths λ_n that obey the (periodic) boundary conditions. Nevertheless, we emphasize that the emergence of turbulent patterns is not a small-size effect: at the very onset of pattern formation, the dispersion relation of a finite system would in fact always show an instability of one mode only. Our simulation results (fig. I.6(b) and (c)) clearly show, that for larger systems the dynamics gets even 'more turbulent', i.e. involves more and more modes although only one single mode is unstable (e.g. $L = 62\,\mu\text{m}$, fig. I.6(b)).

I.3.4 Towards a minimal model of protein pattern formation and a fully discretized Min model

In section I.3.2a we have shown that the two-layer model reproduces the complete phenomenology of the original continuous Min model [23] including standing and traveling wave patterns as well as turbulent dynamics. Intrigued by the emergence of irregular patterns at the onset of pattern formation, we then focused on this onset behavior and could systematically show, that irregular patterns can indeed be induced by a single mode instability. Moreover, we found that patterns get turbulent when the maximally growing wave-like perturbation is smaller than the system size but does not obey the (periodic) boundary conditions.

All of the observed patterns (standing and traveling wave patterns and turbulence) can arise from an initial Turing instability (see figs. I.4, I.5). Since a Turing instability is based on lateral (diffusive) coupling, lateral coupling is also central for pattern formation and selection in the two-layer model. In this section we will shortly discuss the role of lateral coupling by studying the fully discretized model (fig. I.2(d)), where also the lateral extension is explicitely discretized. A discretization of the lateral extension into N nodes will affect the dispersion relation of the pattern-free steady state. In contrast to our hitherto calculation of dispersion relations for the two-layer model with continuous lateral extension (fig I.3(c), fig. I.5, fig. I.6(a)), we now explicitely calculate the dispersion relation for a model of N lateral nodes where each node has eight equations for the respective concentrations on the membrane and in the bulk (eqs. I.1), and nodes are coupled by the discretized diffusion operator (I.5). Thus, we calculate the dispersion relation for a system of $8N$ variables which amounts to finding the eigensystem of a $8N \times 8N$ matrix. From the structure of eigenvectors with positive growth rates (i.e. positive real part of the eigenvalue), we can then deduce the unstable modes of the system. In order to systematically reduce the number of lateral nodes N while preserving the characteristic form of the dispersion relation in the original Min skeleton model [23], we used the ratio h_0/h_1 as a fitting parameter. To be precise, we varied h_0/h_1 to obtain the best fit in terms of the onset length of pattern formation, $\tilde{L}$, and the wavelength with the maximal growth rate, λ_c.

Figure I.7(a) displays qualitative fits between the dispersion relations of the fully discretized Min model for different N and the original Min skeleton model. In particular, we are interested in regimes of system lengths where only the first mode is unstable and which contain the wavelength λ_c. As in section I.3.3, we fixed the overall protein concentrations to $[\text{MinD}] = 1.06\,\mu\text{M}$, $[\text{MinE}] = 0.68\,\mu\text{M}$. We remark that for this choice of overall protein concentrations and for $N \geq 6$, the choice $h_0/h_1 = 0.1235$ yields the best qualitative fit between the fully discretized Min model and the original Min skeleton model within a precision of $\sim 1\%$. We numerically solved the discrete system (I.1), (I.2) and (I.5) for various N with the respective h_0/h_1 that yielded the best qualitative fit and varying the system length.[4] Figure I.7(b) shows simulaton results for $N = 8$, 10 and 12. While a characterization of involved lengthscales in terms of a spectral analysis might not be very insightful due to the intentionally poor discretization, the kymographs already show clear signatures of regular and turbulent patterns. For a resolution of $N = 12$, our simulations recover the transition from standing wave patterns for $\tilde{L} \leq L < \lambda_c$ to turbulent patterns for $L > \lambda_c$ as observed and discussed in the previous section (see fig. I.6).

In contrast, for $N \leq 8$ we find irregular patterns right at the onset length of pattern formation, i.e. for $L \gtrsim \tilde{L}$. To better understand this discrepancy, we note that the standing wave patterns in the two-layer model already involved more than one mode (the green circles in figure I.6(b) for $L < \lambda_c$ in fact indicate an interplay of the first and the second mode). Thus, regular standing wave patterns might not be resolvable with $N \leq 8$ and thus appear irregular. Furthermore, for $L > \lambda_c$ the kymographs for $N \leq 8$ display regular linear zigzag patterns with wavelength $L/2$ instead of the turbulent dynamics observed for fine resolutions in the two-layer model. We argue that these zig-zag patterns point towards the inability of a coarse discretization to resolve the gradients in the emerging patterns. In fact, the transition from patterns with a typical wavelength of L to linear zig-zag patterns with wavelength $L/2$ indicates that shorter lengthscales become important and higher modes start to contribute. This is consistent with the transition to turbulent dynamics as observed for fine resolutions (fig. I.7(a), $N = 12$) and in the two-layer model (fig. I.6(b)). We argue that unlike for a fine lateral resolution, a too coarse discretization (here $N \leq 8$) cannot resolve the turbulent dynamics on short lengthscales and runs into regular zig-zag patterns.

In summary, our numerical analyses show that the fully discretized Min model (fig. I.2(d)) is able to reproduce the phenomenology of the original Min skeleton model even for a relatively coarse resolution (for our choice of parameters, twelve lateral nodes are sufficient). Moreover, we find that for a too coarse discretization, patterns cannot be resolved sufficiently and the systems shows irregular patterns

4 As in the previous sections we employed `PYTHON` software with an Euler forward scheme in time.

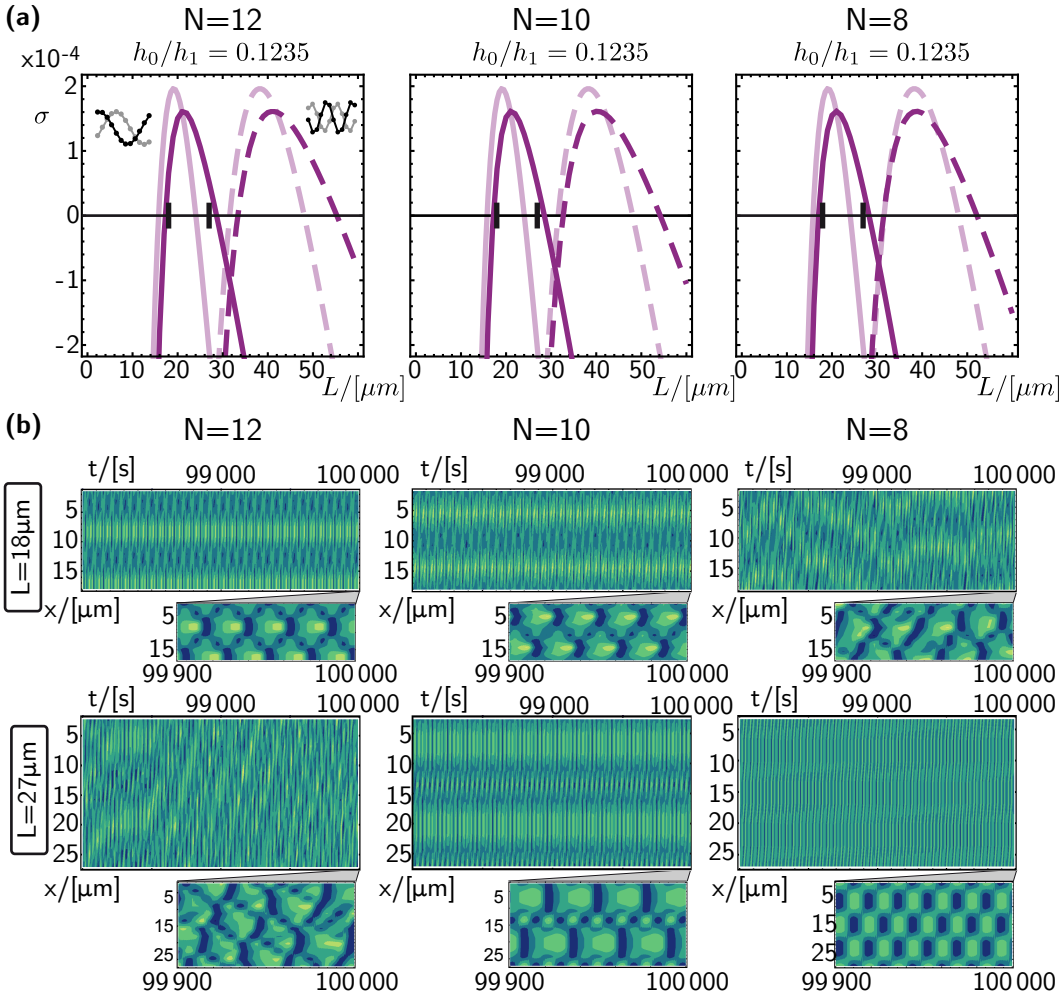

Figure I.7 Effect of a lateral discretization on single-mode turbulence. Protein concentrations are [MinD] $= 1.06\,\mu\mathrm{M}$, [MinE] $= 0.68\,\mu\mathrm{M}$. **(a)** Comparison between the dispersion relations of a discrete model (dark purple) with 12, 10 and 8 lateral nodes and the original, fully continuous Min skeleton model (light purple). The growth rates of the first and second mode, i.e. the wavelengths λ_1 and λ_2, are given by the solid and dashed lines, respectively. The inset for $N = 12$ illustrates the structure of the respective eigenvectors and show the normalized real eigenvector component for the membrane density of the different nodes. **(b)** Kymographs for the numerical solutions. The two shown lateral extensions $L = 18\,\mu\mathrm{M}$, and $L = 27\,\mu\mathrm{M}$ are indicated in the x-axes of (a) as black ticks. Whereas for $N = 12$, the transition from standing wave to turbulent patterns is preserved, for $N \leq 8$ this transition appears to be reversed, most likely because the poor discretization is no longer able to resolve patterns on sufficient lengthscales.

and short-wavelength zig-zag oscillations, where the two-layer model approaches regular standing wave patterns and turbulent dynamics, respectively. Nevertheless, the transition between different patterns still occurs at $L = \lambda_c$. The transition from long-wavelength dynamics to short-wavelength dynamics at $L = \lambda_c$ is in fact preserved even for a discretization into four lateral nodes only. For $N = 4$, we first find standing waves with wavelength L for $\tilde{L} \leq L < \lambda_c$, which are replaced first by traveling wave patterns for $L \approx \lambda_c$ and finally by standing waves with wavelength $L/2$ for $L > \lambda_c$.

I.3.5 Conclusion

Based on the self-organization of MinD and MinE, reconstitution experiments of the Min system have revealed a rich phenomenology in terms of pattern formation including spiral waves [6, 58] but also more irregular patterns [56, 57]. Consistent with numerous experimental observations [6, 54–57, 59], the Min skeleton network [4, 5, 23] forms a useful basis to theoretically study protein pattern formation in the Min system. Nevertheless, the underlying mechanisms that select between different patterns are largely elusive.

For pattern formation and selection in the *in vitro* geometry, recent theoretical studies [23] suggest that the vertical protein distributions in the bulk above the membrane are critical. In our study, we find that the vertical extension of the bulk can be dramatically reduced by coupling a bulk layer close to the membrane to a bulk layer further away from the membrane (fig. I.2(c)). Here, the layer close to the membrane can be understood as *reactive layer* which accounts for the bulk-membrane flux close to the membrane. The layer further away from the membrane acts like a *reservoir*, which accounts for diffusion in the bulk and enables fast lateral redistribution of proteins. For a reasonable choice of a thin reactive layer and a very large reservoir, this two-layer model is able to reproduce the complete pattern phenomenology including pattern selection of the original, continuous skeleton Min model (fig. I.4).

In particular, the two-layer model reproduces a transition from turbulent patterns to regular standing and traveling wave patterns at the onset of pattern formation as reported in the original Min skeleton model [23] as well as in recent *in vitro* experiments [57]. Combining linear stability analyses and finite element simulations of the presented two-layer model, we showed that the emergence of standing wave patterns as well as turbulent patterns is based on a single-mode instability, i.e. only a single mode is unstable and compatible with the (periodic) boundary conditions (section I.3.3). Moreover, the transition between standing wave patterns and turbulence based on a single-mode instability is still recognisable even for a very coarse lateral discretization (section I.3.4). The emergence of turbulence from such single-mode instability points towards a novel mechanism for turbulence,

which is conventionally understood in terms of the nonlinear coupling of multiple unstable modes [24, 25]. Our combined analyses suggest the following 'route to turbulence' (fig. I.6(d)): As long as the single unstable wavelength compatible with the (periodic) boundary conditions has the maximal growth rate among all wavelength that fit into the system, this wavelength dominates and will eventually lead to the formation of regular standing wave patterns (fig. I.6(d),(i)). In contrast, when the wavelength with the maximal growth rate is smaller than the lateral extension of the system, but does not obey periodic boudary conditions, the competition between the wavelength with the largest growth rate and the single unstable mode compatible with the boundary conditions can lead to turbulence (fig. I.6(d),(ii)).

This result strongly suggest that the wavelength with the maximal growth rate is critical for pattern formation and selection albeit it might not be compatible with the system's boundary conditions. This, in turn, reveals a predictive role of the shape of dispersion relations for protein pattern formation and selection. Especially for subcritical transitions to pattern formation, such as present in the Min skeleton model [23], the role of dispersion relations had remained largely unexplored.

The Min system represents a fairly simple protein network based on only two kinds of proteins (MinD and MinE) that diffuse in the bulk and undergo molecular reactions at the membrane. In fact, the coupling of a diffusive bulk to a reactive membrane (surface) is not particular for the Min system, but is widespread in many intracellular reaction-diffusion networks [8, 13] as well as more general model systems such as in the CO-Pt system [27, 28, 69]. In contrast to previous, numerically expensive approaches [4, 5, 14, 23], our spatially-reduced models provide numerically (and possibly analytically) feasible approaches to address various interesting questions in systems with such bulk-membrane coupling. In particular, we plan to investigate local instabilities arising from the vertical membrane-reservoir coupling [72] as well as their interplay with lateral (Turing) instabilities. We think that here, the spatially-reduced models can help to elucidate pattern forming mechanisms based on the notion of diffusively coupled, local steady states [23].

I.4 Conclusion and outlook

In this chapter, we studied collective effects in a wide-spread class of reaction-diffusion systems. Here, the constituents of the systems diffuse in the bulk and also bind to a surface, to which they recruit other constituents and undergo reactions. An extensively studied example for such systems is the intracellular Min system, where the proteins MinD and MinE cycle between a diffusive cytosol and a reactive membrane driven by ATP [8, 13]. This cycling leads to interesting collective effects including pole-to-pole oscillations in the cell [48, 52] and spiral waves on a flat supported bilayer [6], depending on the parameters in the system such as protein densities or the enclosing geometry. The Min system is a particularly instructive example for protein reaction-diffusion patterns, since it can be studied in the cell [48, 49, 52, 54], in reconstitution experiments [6, 21, 58] and also on the basis of mathematical reaction-diffusion models in emulated *in vivo* [4, 5, 14] or *in vitro* [22, 23] geometries. The accessibility of Min pattern formation on three different levels of description (*in vivo*, *in vitro*, and *in silico*) facilitates a mutual exchange of insights and helps to form a meaningful and general conception of the self-organization process in the Min system. For instance, while *in vivo* studies have advanced our understanding of the underlying reaction-diffusion network [1, 49, 62, 63], *in vitro* studies enabled controlled quantitative measurements of relevant properties such as wavelengths, velocities, and ATPase activity [15, 21, 58]. Mathematical models [4–6, 14, 23, 64–66] were able to test experimentally suggested protein reaction networks and have helped to identify underlying mechanisms for pattern selection and formation. In particular, theoretical studies have pointed out the important role of the nucleotide exchange rate for efficient pole-to-pole oscillations [4, 5] and have yielded insights into the adaptation process of patterns to their enclosing geometry [14, 26, 55].

In the same spirit, in section I.2 we investigated recent findings from *in vivo* studies on the basis of a mathematical analysis, which was eventually tested and confirmed by suited *in vitro* experiments. More specifically, we were motivated by recent results from structural biology experiments [7, 17, 18], which suggested a neccessary extension of previously considered models of Min pattern formation [4, 5, 14, 64, 65] by a MinD-dependent conformational switch of MinE. We included such switch in a previously studied model of Min pattern formation [4, 5], the *skeleton model*, and showed, that this switch of MinE dramatically broadens the predicted range of protein concentrations compatible with protein pattern formation. By means of *in vitro* experiments, in which protein concentrations were varied systematically, we confirmed this theoretical prediction and thus came to the conclusion that a mutual switch between MinD and MinE forms a central mechanism for robust protein pattern formation. Our study has resolved a long-standing conflict in theoretical studies of Min pattern formation [4, 5, 14], which

were able to reproduce protein patterns only when MinD is more abundant than MinE, in contrast to the experimental observation of surface patterns in much broader concentration ranges [6, 15, 16, 21, 68]. Our study sheds new light on the role of molecular details, such as molecular switches, in the context of protein pattern formation and suggests a mutual switch between proteins as an important motif to enable pattern formation over a broad range of protein concentrations. Molecular switches are ubiquitous in intracellular protein systems and can be found in various forms, such as in NTPases [8, 13] and metamorphic proteins [9, 77]. We hypothesize that mutual switches between proteins can be viewed as a more general design principle to achieve robustness of protein patterns with vital roles in the cell. Such robustness might be especially beneficial in the context of evolvability, since the ability to form patterns in a large range of protein concentrations allows for protein mutations while the key functions of the organism, such as protein patterning, remain intact. Our study has shown that while the original Min skeleton model is able to capture protein pattern formation at least for low MinE concentrations, molecular details can add interesting features such as pattern robustness. Similarly as for the MinD-dependent switch of MinE, we think that a quantitative experimental analysis of further components in the Min reaction network, such as recruitment rates or the MinD dynamics, could yield insights into further mechanisms that shape and facilitate Min pattern formation.

As discussed in section I.2, our study consolidates the mathematical skeleton model [4, 5, 23] as a valid and useful basis to study Min pattern formation. In section I.3, we took advantage of this model in order to investigate protein pattern formation and especially pattern selection in an emulated *in vitro* geometry. We developed a spatial reduction of the Min skeleton model which dramatically reduces the cost of numerical solutions and thereby facilitates the analysis of pattern formation and selection in broad parameter regimes. In this spatially-reduced model, the entire vertical bulk extension is represented by a 'reactive' layer close to the membrane, which accounts for the fast bulk-membrane flux of proteins, coupled to a 'reservoir' layer further away from the membrane, accounting for lateral bulk diffusion. By employing finite element simulations, we showed that for a suitable choice of thicknesses of these layers, this two-layer model reproduces the full pattern phenomenology observed recently in the original Min skeleton model [23], including standing waves, traveling waves and turbulence. This confirms the two-layer model as a valid and meaningful description of Min pattern formation. The fact, that only two layers can capture the pattern phenomenology, supports the notion of the two roles of the bulk: first the bulk close to the membrane is dominated by fast protein fluxes to and from the membrane due to the molecular reactions on the membrane. Second, further away from the membrane, the bulk can be viewed as a 'reservoir', where proteins are 'stored' and diffusively distributed along the lateral extensions of the system. We think that the notion of a reactive layer coupled to a

reservoir can help to better understand the important roles of local instabilities and lateral protein redistribution, which were recently emphasized by Halatek et al. [23]. The notion of reactive and reservoir layers has already been useful in other pattern forming systems such as the catalytic carbon monoxide oxidation on platinum [27, 28, 69], where its has helped to investigate the oscillatory instability in terms of nullclines of the underlying nonlinear dynamics [72].

On the basis of the two-layer model, we focused on a very recent observation in a theoretical study of the mathematical skeleton model [23]. Here, Halatek et al. [23] observed the formation of turbulent protein patterns at the onset of pattern formation which are replaced by more regular patterns further away from the onset. The observation of turbulence close to the threshold of pattern formation is in contrast to traditional conceptions of turbulence [24, 25], where turbulence is typically based on the nonlinear coupling of multiple unstable modes far beyond this threshold, and thus points towards a neccessary rethinking of protein pattern formation in reaction-diffusion systems [23]. The numerical accessibility of the two-layer model enables a straightforward sweep through different control parameters such as the overall protein concentrations and the system size. By varying the the overall protein concentration, we identified a phase of turbulence for overall protein concentrations at the onset of pattern formation. Further away from this onset, we recovered standing wave patters and traveling waves, consistent with [23]. Using linear stability analyses and finite element simulations, we found that turbulence is induced by a single-mode instability, in contrast to traditional studies of turbulence based on multiple unstable modes [24, 25]. We focused on this single-mode instability by varying the lateral extension of our emulated *in vitro* geometry. Here, our results revealed a transition between regular patterns and turbulence which critically depends on the shape of the dispersion relation: We observed regular standing wave patterns as long as the lateral extension of the system is smaller than the wavelength with the maximal growth rate in the dispersion relation. For larger lateral system extensions, our numerical simulations approached turbulent patterns. Our study thus sheds new light on the predictive role of the dispersion relation in pattern formation. Especially for subcritical bifurcations to pattern formation, as present in the Min system [23], the role of the dispersion relation has remained largely elusive. In summary, the two-layer model provides a numerically (and possibly analytically) feasible description of pattern formation in systems where a diffusive bulk is coupled to a reactive surface, such as in the Min protein system. We think, that it will contribute to a better understanding of protein pattern formation in the *in vitro* Min system and that it can also be adapted to more complex geometries such as an emulated *in vivo* (rod-like) geometry. Due to the ubiquity of pattern forming reaction-diffusion systems with bulk-membrane coupling in the cell [8, 13] but also in more general model systems [27, 28, 69, 72], we think that the spatial reduction of the presented two-layer model will be of

general relevance for identifying and investigating pattern formation and selection in reaction-diffusion systems.

II Pattern formation in active systems

II.1 Introduction: symmetries and order in active matter

Over the last 20 years, active matter has become one of the most prominent fields in non-equilibrium statistical physics. The term active matter denotes systems of entities which can transduce internal or ambient energy into directed motion [35]. The increasing interest in active matter systems certainly arises from its ubiquity in nature but also from the fact that it adds a novel class to the theory of nonequilibrium statistical physics [37].

In particular, active systems are omnipresent in biology, where living organisms can move in a directed fashion. Examples include cells that crawl on a substrate [78], insects, or even larger mammals, including us. Moreover, biological active systems can also be found on much smaller lengthscales such as in in the cell [79–81]. In fact, many vital functions of the cell depend on the exertion of directed forces mediated by molecules upon the consumption of nucleoside triphosphate (NTP). In the actomyosin cortex, molecular motors (myosin molecules) apply local forces on the actin network and are thereby critical for the control of cell shape [82]. Another intracellular example of directed motion is given by the treadmilling dynamics of FtsZ polymers, which plays a major role during bacterial cell division [32, 83].

Importantly, the entities of active systems do not only move, but also interact with each other and thereby form a collective. Depending on these interactions, this collective can have a qualitatively different behavior than expected from the sum of its entities [36]. A particularly prominent example for such collective behavior is the formation of macroscopic order and structure such as in flocks of birds, swarms of insects [84–86](fig. II.1(a)), but also–less obviously–in bacterial colonies [87–89](fig. II.1(b)). On the intracellular level, *in vitro* experiments have helped to gain insights into the collective behavior of active protein systems. For instance, reconstituted actin filaments can move on a carpet of myosin molecules and show interesting collective phenomena such as flocking and the formation of traveling large-scale density waves [90, 91]. Furthermore, *in vitro* experiments with the bacterial cell-division protein FtsZ revealed the formation of dense ring patterns by treadmilling FtsZ polymers [2, 34](fig. II.1(c)). Nonbiological examples for collective effects in active systems are found in numerous artificial systems including self-propelled colloids [92, 93], rods [94–96](fig. II.1(d)), and shaken discs [97, 98].

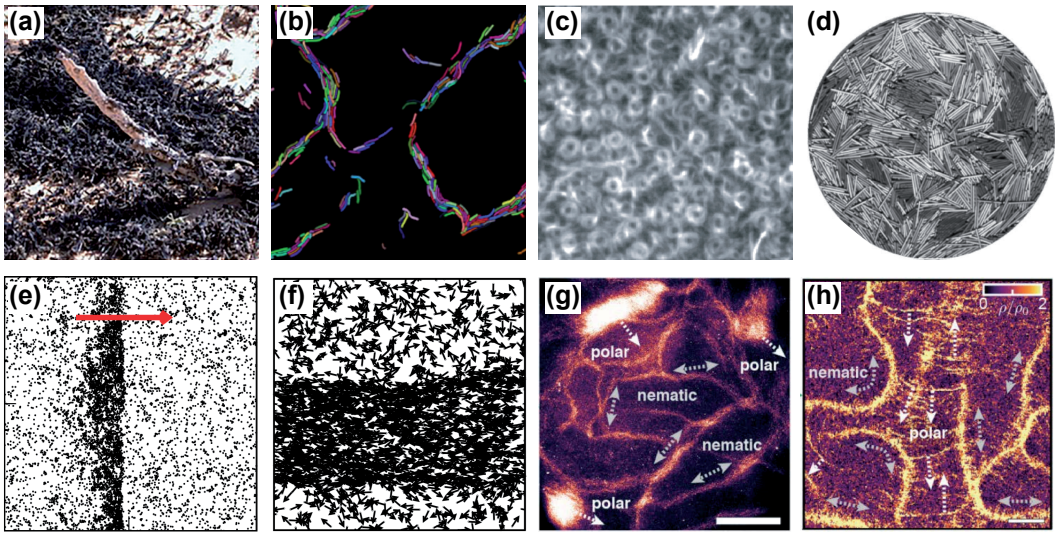

Figure II.1 Examples of macroscopic order and patterns in active systems adapted from respective publications. **(a)** Aggregations of locusts in their gregarious phase [84]. **(b)** Stream-like aggregates of *Myxococoxcus Xanthus* on a nutrient-less surface [87]. **(c)** Ring patterns of FtsZ polymers on a lipid blayer assay [2]. **(d)** Nematic order and structure in vertically-vibrated granular rods [94]. **(e)** Traveling polar waves in agent-based simulations of propelled particles with polar velocity alignment [99]. **(f)** Nematic bands in agent-based simulations of propelled particles with nematic velocity alignment. **(g)** and **(h)**, Recently observed coexistence of polar and nematic patterns revealed by actomyosin assays (g) as well as large-scale simulations of propelled flexible filaments with mixed interaction symmetry (h).

The experimental observation of macroscopic patterns based on microscopic interactions of active entities has also attracted many theorists from biophysics as well as soft matter physics. Theoretical descriptions of active matter are manifold and act on different lengthscales [37]. The first theoretical approach to flocking in active systems dates back to the seminal work by Vicsek et al. [100]. The authors studied a system of self-propelled agents with move at constant speed. At each timestep, particles align their velocities with the average velocity of their neighbors within a certain interaction radius. Collisions that lead to velocity alignment are more generally also refered to as *polar alignment*. For high densities or low noise values, Vicsek et al. observed the formation of dense moving flocks. Within these flocks, the system exhibits macroscopic *polar order* (fig. II.2), which is proportional to the macroscopic velocity of the flock. Based on the numeric approach by Vicsek et al. for particles with polar alignment, subsequent studies [101, 102] also investigated systems of particles with *nematic alignment*. For nematic alignment, agents align their orientations in a rod-like fashion, i.e. they glide past each other when they collide under an obtuse angle and align their velocities when they collide under an acute angle. For high enough densities or low noise values, nematic alignment between the agents results in the formation of macroscopic *nematic order* (fig. II.2). Numerous agent-based studies based on different implementations such as Vicsek-like [99, 103, 104] or Langevin-type [105–108] models have helped to better understand the mechanisms underlying the formation of macroscopic order. All these models feature a transition to macroscopic order when increasing the global density or decreasing the noise strength. This theoretical prediction of a transition to macroscopic order as a function of density and noise strength is consistent with various *in vitro* experiments [3, 34, 90, 91] as well as experiments with artificial entities, such as propelled discs [97] and motile colloids [92, 93].

In the case of polar alignment, i.e. velocity alignment, flocking can lead to the formation of traveling density waves [99, 100](fig. II.1(e)). On the other hand, for nematic alignment, agent-based simulations [3, 102] suggest the formation of nematic density bands above the onset of macroscopic (nematic) order (fig. II.1(f)). Within these bands, the particles' orientations–but not neccessarily their velocities–are approximately aligned, reminiscent to ant trails.

Observations like these indicate, that systems of propelled entities can be described in terms of the relevant order fields such as the macroscopic polar and nematic order as well as the density. In this spirit, Toner and Tu [109, 110] were the first to propose a hydrodynamic description of flocking in systems of self-propelled particles with polar alignment. Based on symmetry arguments, Toner and Tu presented a continuum equation for the polar order field accompanied by a continuity equation for the density. The equation for the polar order field inherits terms from the Navier-Stokes equation and includes Ginzburg-Landau terms to account for spontaneous symmetry breaking at the flocking transition. A dynamical

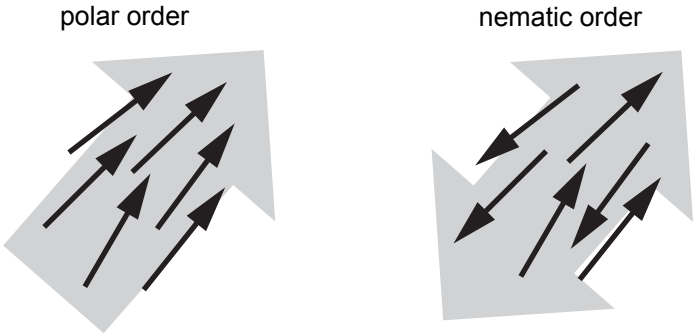

Figure II.2 Polar and nematic symmetries in systems of self-propelled (polar) agents. Polar or nematic alignment between directed active agents can lead to macroscopic polar or nematic order. Black arrows denote the directions of the agents' motion, shaded arrows indicate the macroscopic polar and nematic order often described in continuum theories.

renormalization group analysis of this continuum description revealed exponents characterizing the velocity-velocity and density-density correlation functions and showed that flocks exhibit a true long-range ordered state in $2D$. Following the seminal work by Toner and Tu, subsequent continuum models for active matter [111–114] have helped to gain insights into the large-scale behavior of active systems such as instabilities [112] and giant number fluctuations [111, 113] in the ordered state as well as more recent phenomena such as active turbulence [115, 116], which was previously observed in experiments [117].

Hydrodynamic theories have also been derived explicitely from the microscopic interactions between active agents [118–125]. In particular, Bertin et al. [123, 124] took a kinetic Boltzmann approach for particles with noisy propulsion that undergo binary collisions with polar alignment. The kinetic Boltzmann approach describes the dynamics of active particles in terms of the orientational particle distribution function and includes terms accounting for convection of particles, diffusion, as well as (binary) particle collisions, which follow simplified collision rules. From the underlying kinetic Boltzmann equation for propelled particles with polar alignment, Bertin et al. expanded the dynamics of the system in terms of the polar order field, the density, and spatial gradients. In contrast to earlier continuum descriptions based on symmetry arguments [109, 110], the resulting hydrodynamic equations include coupling coefficients that are fixed by the microscopic details of the imposed polar collision rule. The hydrodynamic equations derived by Bertin et al. [123, 124] thus enable a quantitative investigation of the phase diagram, and especially the flocking transition. In particular, the authors find that above a certain density, the disordered state is linearly unstable and macroscopic polar order starts to grow. Close to this threshold density, their hydrodynamic equations show a linear instability of the polar state, which leads the formation of traveling

high-density waves. A direct numerical implementation of the kinetic Boltzmann equation [126] confirmed these traveling waves and could show that further away from the threshold density, waves are replaced by homogeneous polar order. All of these observations are consistent with the above-mentioned agent-based models [99, 100], hydrodynamic approaches [109, 110], as well as experiments [90, 93].

In recent years, the kinetic Boltzmann approach has been applied to various classes of systems of active particles that undergo aligning interactions [127]. In addition to propelled particles with polar alignment [123, 124], it has been adapted to account for nematic alignment [128] and metric-free, topological interaction rules with polar symmetry [129]. Furthermore, it was employed to study systems with altered particle motion such as for fluctuating apolar particles [130], particles with velocity reversal [131], and particles with angular motion [22]. As a common feature, all of these 'kinetic Boltzmann models' display a transition from a disordered state for low densities or strong noise to a state with macroscopic order for high densities or weak noise. Close to this order transition, the system can form high-density patterns depending on the imposed interaction rule and particle motion. Whereas polar alignment can lead to traveling waves [123, 124, 126], nematic alignment can lead to nematic lane structures [128]. These lane structures resemble the band patterns in agent-based simulations discussed above ([102], fig. II.1(f)). Similar nematic band structures have also been observed more recently in simulations with flexible filaments as well as in an actomyosin motility assay [3]. In summary, the kinetic Boltzmann approach has been successfully applied to various systems of active matter. It is consistent with the previously observed pattern phenomenology in experiments and simulations and thereby provides a useful basis to study various aspects of collective phenomena in active systems.

In section II.2, we discuss an intracellular example of active matter, the bacterial Z-ring, which has recently been made more accessible by controlled *in vitro* experiments by Loose and Mitchison [2]. Here, Loose and Mitchison were able to reconsitute the bacterial FtsZ protein system on a flat lipid bilayer and observed self-organization of curved FtsZ polymers into dense ring patterns. Motivated by these experiments, we employ a kinetic Boltzmann approach as well as agent-based Brownian dynamics simulations to study the collective behavior in systems of curved, propelled polymers. Our results predict a confined phase of vortex patterns for intermediate densities and noise strength, which is consistent with the flocking behavior in previously studied active systems discussed above. The results from this project were published in "Active Curved Polymers Form Vortex Patterns on Membranes", Phys. Rev. Lett. 116, 178301 (2016), and are reprinted in section II.2. Indeed, our theoretical prediction of a confined vortex phase has recently been confirmed in FtsZ reconstitution experiments by Ramirez et al. [34], where ring patterns formed only in a narrow range of polymer concentration.

The classical conception of active matter as presented above suggests that active systems can be typically assigned to different classes of active matter [127]. For instance, interactions between propelled particles are often assumed to lead to either polar or nematic alignment classifying the system as polar or nematic active matter, respectively [37]. Relatively little attention was given to systems where theses classes are mixed [3, 132–134]. In particular, Huber et al. [3] were able to manipulate interactions between actin filaments in an actomyosin assay and found a novel 'coexistence state', where polar wave patterns and nematic lanes coexist (fig. II.1(g)). In addition, they were able to reproduce this coexistence state in agent-based simulations of propelled filaments with mixed interaction symmetries (fig. II.1(h)). Motivated by these observations, in section II.3 we study pattern formation in an active system with mixed interaction symmetries. More specifically, we employ a kinetic Boltzmann approach for a system of self-propelled particles, where particle collisions lead to nematic alignment with a small polar bias. The presented model reproduces the coexistence state observed in [3] and gives access to the nonlinear dynamics underlying this pattern forming mechanism. Our study reveals dynamic transitions between polar wave patterns and nematic bands and thereby sheds new light on the conception of symmetry breaking in active matter discussed above.

II.2 The bacterial Z-ring and FtsZ polymer self-organization

As discussed in section I.1, bacterial cell division is coordinated by the interplay of a variety protein systems including the Min system. The protein FtsZ plays a particularly important role since it constitutes the prominent Z-ring, which initiates septum formation and constriction of the cell into two daughter cells [10, 11, 47] (fig. I.1(b)). Within the Z-ring, FtsZ is present in protofilaments [32] which are highly dynamic [50, 51, 83]. Experiments have shown that FtsZ polymerizes into filaments with structural polarity that exhibit treadmilling dynamics upon GTP consumption [2, 50, 51]. This means, FtsZ polymers constantly grow at their front end while they shrink preferentially at their back end leading to an effective motion of FtsZ polymers along their backbone. In addition, FtsZ polymers are not straight but have an intrinsic curvature [32, 135], which may depend on the nucleotide state of the monomers [31, 136]. To study the dynamics and collective behavior of FtsZ, Loose and Mitchison [2] reconstituted FtsZ in a lipid bilayer assay. In the presence of the anchor proteins FtsA and ZipA as well as ATP and GTP, FtsZ attached to the membrane and formed curved polymers that performed treadmilling on circular paths. After some time, FtsZ polymers assembled into macroscopic patterns such as fast-moving filament bundles and rotating rings (fig. II.1(b)), reminiscent to the intracellular Z-ring.

From a theoretical perspective, the instrinsic curvature of FtsZ polymers together with their effective propulsion due to treadmilling, suggests that these polymers can be viewed more generally as propelled objects on circular tracks. Motivated by this analogy, we studied the collective behavior of self-propelled curved polymers on a membrane (i.e. in $2D$) that only interact via steric repulsion. Our study (see publication [22] and the reprint below) predicts a phase of vortex patterns including closed rings, which is confined to intermediate polymer densities and noise levels. By now, this prediction has been confirmed by very recent *in vitro* experiments with FtsZ in a lipid bilayer assay, which showed that ring patterns of FtsZ polymers are only present in a narrow range of FtsZ concentrations [34].

Publication

Active curved polymers form vortex patterns on membranes

by

J. Denk*, L. Huber*, E. Reithmann, and E. Frey

Arnold Sommerfeld Center for Theoretical Physics (ASC) and Center for NanoScience (CeNS), Department of Physics, Ludwig-Maximilians-Universität München, Theresienstrasse 37, D-80333 München, Germany

* These authors contributed equally

Reprinted on pages 99–112

Published in **Physical Review Letters, 116, 178301 (2016)**,
DOI: 10.1103/PhysRevLett.116.178301,
also available on arXiv:1602.08976.

The supplemental material is reprinted on pages 113–126.

Active Curved Polymers form Vortex Patterns on Membranes

Jonas Denk,[1] Lorenz Huber,[1] Emanuel Reithmann,[1] and Erwin Frey[1,*]

[1] *Arnold Sommerfeld Center for Theoretical Physics (ASC) and Center for NanoScience (CeNS), Department of Physics, Ludwig-Maximilians-Universität München, Theresienstrasse 37, D-80333 München, Germany*

Abstract

Recent *in vitro* experiments with FtsZ polymers show self-organization into different dynamic patterns, including structures reminiscent of the bacterial Z-ring. We model FtsZ polymers as active particles moving along chiral, circular paths by Brownian dynamics simulations and a Boltzmann approach. Our two conceptually different methods point to a generic phase behavior. At intermediate particle densities, we find self-organization into vortex structures including closed rings. Moreover, we show that the dynamics at the onset of pattern formation is described by a generalized complex Ginzburg-Landau equation.

Intracellular structuring is often facilitated by the active dynamics of cytoskeletal constituents. The origin of these driven dynamics and their impact on pattern formation has been extensively studied using artificial motility assays of cytoskeletal filaments [1–4]. Another intriguing example of self-organization due to driven filaments was reported recently by Loose and Mitchison [5]. *In vitro*, the bacterial protein FtsZ forms membrane-bound, intrinsically curved polymers. These seem to exhibit treadmilling dynamics (consuming GTP) and, as a result, move clockwise on the membrane. Depending on the protein density, polymers cluster into dynamic structures such as rotating rings or jammed bundles, despite the absence of attractive interactions [6]. These ring structures are of particular interest, since *in vivo*, FtsZ builds the contractile Z-ring which drives cell division in a yet unknown way [7–9]. But also in the *in vitro* experiments, the pattern forming mechanism remain unclear even on a qualitative level.

Motivated by these experimental findings, we have studied pattern formation in a class of active systems, where particles move on circular tracks and interact only via steric repulsion. To assess the dynamics of this class, we consider two conceptually different models: First, we emulate active particles as elastic polymers with fixed intrinsic curvature that move with a constant tangential velocity [Fig. 1(a)] and perform Brownian dynamics simulations. Second, we employ a kinetic Boltzmann approach, where point-like particles move on circular paths and undergo diffusion and binary collisions (with polar symmetry) according to a simplified collision rule [Fig. 1(b)]. As a result, we identify different phases of collective behavior as a function of density and noise level. With both approaches, we find flocking into vortex patterns in the regime of intermediate density and noise strength. Our simulations for extended particles predict the formation of closed ring structures reminiscent of those found in Ref. [5], even in the absence of any attractive interactions. In the mesoscopic limit, our analysis yields that, close to the onset of vortex formation, the dynamics at onset of ordering is characterized by a novel generalization of the complex Ginzburg-Landau equation.

In our Brownian dynamics simulations we consider a system of M curved polymers of the same chirality embedded in a two-dimensional membrane of area A with periodic boundary conditions. Each polymer is described as an inextensible worm-like chain [10, 11] of length L, persistence length ℓ_p, and intrinsic curvature κ_0. For a given polymer conformation $\mathbf{r}(s)$, parameterized in terms of arc length s, the overall bending energy is given by $E_{\text{bend}}=\frac{1}{2}\ell_p k_B T \int_0^L \mathrm{d}s\,[\kappa(s)-\kappa_0]^2$, where $\kappa(s)=|\partial_s^2\mathbf{r}(s)|$ denotes the local curvature. Ex-

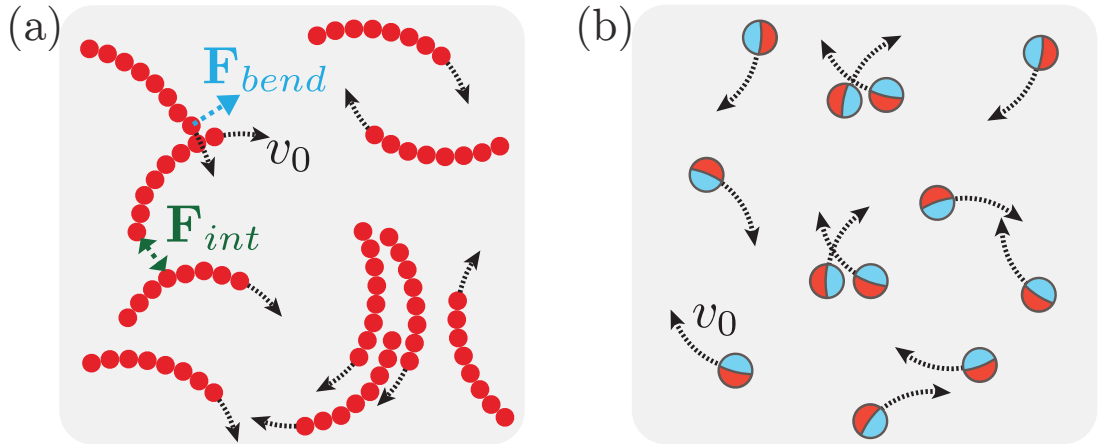

FIG. 1. Systems of active particles, which are driven on chiral, circular tracks with speed v_0: **(a)** *Microscopic view*: extended, elastic polymers with intrinsic curvature, where noise and steric interaction trigger bending of filaments. **(b)** *Mesoscopic view*: point-like particles that undergo diffusion as well as binary collisions.

cluded volume interaction is implemented by a repulsive truncated Lennard-Jones potential (for details see the Supplemental Material [12]). To assure motion of the filament contour on a circular track (apart from noise), polymers are propelled with a tangential velocity $\mathbf{v}_0(s)=v_0\partial_s\mathbf{r}(s)$. This accounts for the effective motion of treadmilling in a simplified way [12]. Note that for this choice, the area explored by a circling polymer is minimal. In the free draining limit, the dynamics of the polymer system is then determined by a set of coupled Langevin equations for the contours $\mathbf{r}^{(m)}(t,s)$ of each polymer $m=1,2...,M$: $\zeta\left(\partial_t\mathbf{r}^{(m)}-\mathbf{v}_0^{(m)}\right)=-\delta E[\{\mathbf{r}^{(n)}\}]/\delta\mathbf{r}^{(m)}+\boldsymbol{\eta}^{(m)}$, balancing viscous friction with elastic and repulsive forces generated by the total energy E and Langevin noise $\boldsymbol{\eta}$ with zero mean and $\langle\boldsymbol{\eta}(t,s)\cdot\boldsymbol{\eta}(t',s')\rangle=4k_BT\zeta\delta(t-t')\delta(s-s')$. To numerically solve the polymer dynamics we employ a bead-spring representation of the polymers [13, 14]. For most simulations, we adapted length scales close to those observed in Refs. [5, 8]: $\kappa_0^{-1}=0.5\,\mu$m, $L=0.9\,\mu m$, $\ell_p=10\,\mu m$. The relevant dimensionless parameters that characterize the system are the reduced noise σ and density ρ. Here, $\sigma:=k_BT\ell_p/(\zeta v_0L^2)$ relates thermal forces at length scale ℓ_p with friction forces, and $\rho:=(R_0/b)^2$ denotes the squared ratio of the radius of curvature $R_0=\kappa_0^{-1}$ to the mean polymer distance $b=\sqrt{A/M}$.

For dilute systems, $\rho\ll1$, our simulations show that each polymer is propelled on a circular path and collisions between polymers are infrequent; see Fig. 2(a) and Movie 1

in the Supplemental Material [12]. The positions of the polymers' centers of curvature $\mathbf{r}_{cc}^{(m)}$ are uncorrelated as in a gas, and we refer to this state as a *disordered state*. On increasing ρ, we observe that a significant fraction of filaments begin to collide and collect into localized vortex structures (*vortex state*). These ring-like structures are highly dynamic. They assemble and persist for several rotations, during which their centers of mass remain relatively static; see Fig. 2(b) and Movie 2 [12]. Despite our simplified kinetic assumption, the overall phenomenology resembles the FtsZ patterns observed by Loose and Mitchison [5], including vortex assembly, disassembly and localization. In the dense regime, $\rho \gtrsim 1$, where each polymer is likely to collide, these vortices are unstable. Instead, the polymers cluster and form jammed 'trains' that travel through the system in an irregular fashion; see Fig. 2(c) and Movie 3 [12].

In order to quantitatively distinguish between the various observed patterns and organize them into a 'phase diagram' we consider the pair correlation function $g(d_{cc})$ [15, 16] of distances $d_{cc}=|\mathbf{r}_{cc}^{(m)}-\mathbf{r}_{cc}^{(n)}|$ between the centers of curvature [Fig. 2(d)]. We regard a system as *disordered* if $g(d_{cc})$ exhibits a minimum at a distance $d_{cc}^{\min}$ equal to the diameter of a free circular path, $d_{cc}^{\min} \approx 2R_0$. This is distinct from *vortex states*, where $d_{cc}^{\min}$, defining an effective vortex diameter, is larger than $2R_0$. Finally, for *train states*, $g(d_{cc})$ does not exhibit a local minimum, indicating the absence of an isolated vortex structure; for more details see the Supplemental Material [12]. The ensuing 'phase diagram' is shown in Fig. 2(d). As in other active systems [17–24], pattern formation is favored by increasing density and decreasing noise strength. Jammed states prevail only when density is high and noise level low. Note also that the structure of the phase diagram depends on the ratio of filament length L to radius of curvature R_0. Polymers with an arc angle close to $\kappa_0 L = 2\pi$ (closed circles) retain a single-circle structure and do not form any collective structures upon increasing ρ [Movie 4 [12]]. Conversely, reducing $\kappa_0 L$ suppresses the formation of closed ring structures, due to inefficient alignment of short polymers. Instead, these polymers cluster into flocks which move on approximately circular paths [Movie 5 [12]]. Hence, we conclude that the range of arc angles of FtsZ polymers, $\kappa_0 L \approx 0.6\pi$, observed *in vitro* [5], facilitates the formation of closed polymer rings particularly well [Fig. 2(b)]. In summary, closed polymer rings require explicit curvature and filament lengths larger than a certain threshold value. For other interactions than local, steric repulsion ring structures may also emerge [1, 25, 26]; straight, rotating rods may form vortex arrays but not closed rings [27].

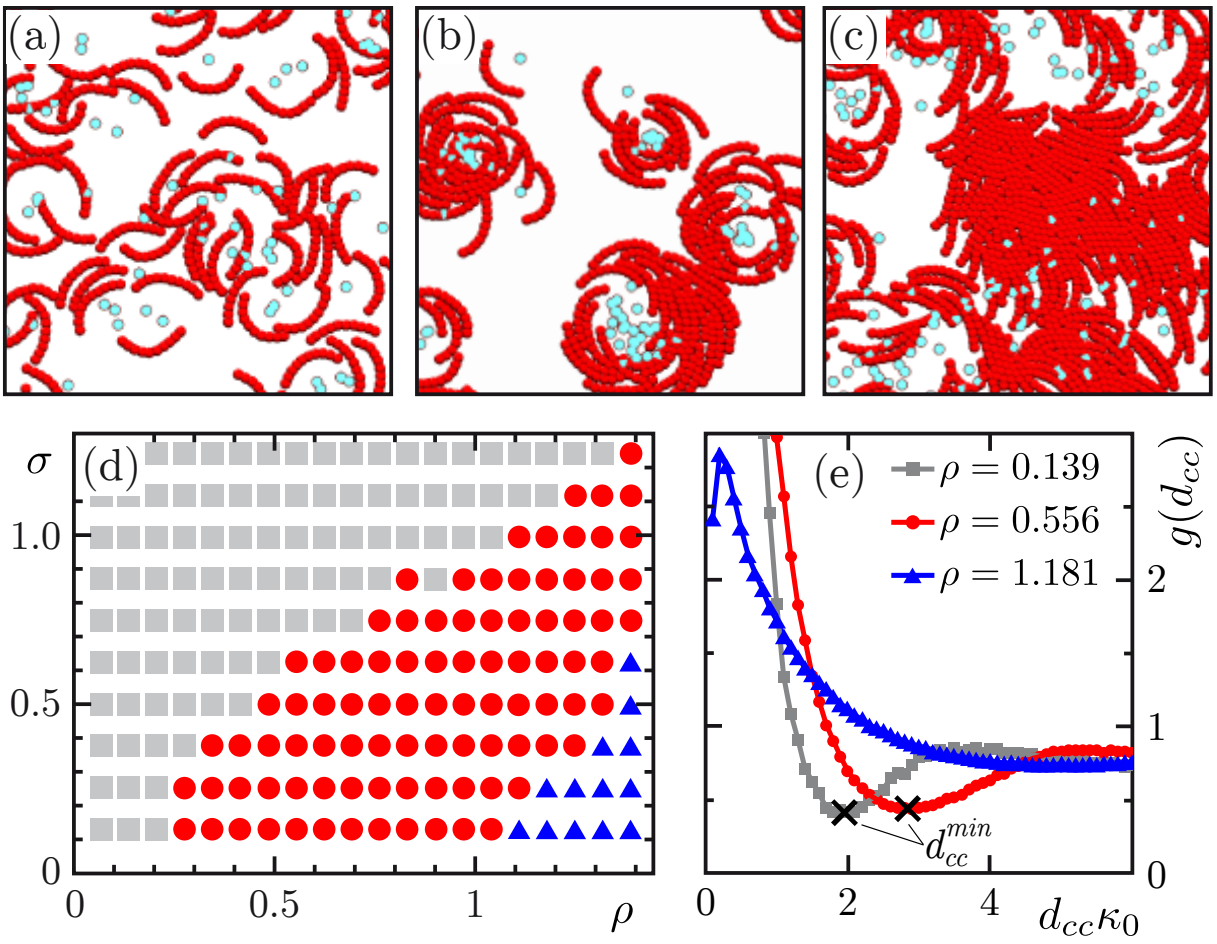

FIG. 2. System snapshots are provided to depict **(a)** disorder (ρ=0.556, σ=0.987), **(b)** vortices (ρ=0.556, σ=0.247) and **(c)** trains (ρ=1.389, σ=0.247). Curvature centers $\mathbf{r}_{cc}^{(m)}$ are depicted by light blue dots. **(d)** Phase portrait for varying density ρ and noise σ: *disorder* states (gray rectangles), *vortex* states (red circles), *train* states (blue triangles). **(e)** Pair correlation function $g(d_{cc})$ for the three different states with σ=0.247 and ρ indicated in the graph.

We complement the Brownian dynamics simulations of active particles that are propelled on circular tracks by considering the mesoscopic limit of vanishing particle extension. To this end, we have employed a kinetic Boltzmann approach [20, 28–33] to determine the collective behavior and the corresponding phase transitions in this limit, irrespective of the microscopic details of the constituent particles. In detail, we simplified the active system to one consisting of spherical particles (of diameter d) moving clockwise with constant speed v_0 on circular orbits of radius R_0. This accounts for both self-propulsion and spontaneous curvature but neglects the finite extension of the polymers as compared to our Brownian

dynamics simulations.

We further assume that a particle's orientation is altered by 'self-diffusion' as well as by local binary collisions. In self-diffusion, a particle's instantaneous orientation θ changes at rate λ into $\theta+\eta$, where we assume η to be Gaussian-distributed with standard deviation σ. As in other particle-based active systems [29, 31, 34], binary collisions are modeled by a polar alignment rule where the orientations of the collision partners align along their average angle plus a Gaussian-distributed fluctuation; for simplicity, we take the same width σ as for self-diffusion.

The kinetic Boltzmann equation [20, 28–33] for the one-particle distribution function $f(\mathbf{r},\theta,t)$ then reads

$$\partial_t f+v_0\left[\mathbf{e}_\theta\cdot\partial_{\mathbf{r}}+\kappa_0\partial_\theta\right]f=\mathcal{I}_d[f]+\mathcal{I}_c[f,f]\,. \tag{1}$$

It describes the dynamics of the density of particles in phase-space element $\mathrm{d}\mathbf{r}\mathrm{d}\theta$ which is being convected due to particle self-propulsion and which undergoes rotational diffusion and binary particle collisions, as given by the collision integrals $\mathcal{I}_d[f]$ and $\mathcal{I}_c[f,f]$, respectively; for explicit expressions please see the Supplemental Material [12]. Note here the critical difference to field theories for straight-moving particles [29, 35–37]; there is an additional angular derivative in the convection term, which reflects the fact that the particles are moving on circular orbits. In the following we rescale time, space and density such that $v_0{=}\lambda{=}d{=}1$. Then, the only remaining free parameters are the noise amplitude σ, κ_0, and the mean particle density $\bar{\rho}{=}A^{-1}\int_A\mathrm{d}\mathbf{r}\int_{-\pi}^{\pi}\mathrm{d}\theta\,f(\mathbf{r},\theta,t)$ measured in units of $\lambda/(dv_0)$, i. e. the number of particles found within the area traversed by a particle between successive self-diffusion events.

To identify possible solutions of the Boltzmann equation and analyze their stability, we performed a spectral analysis. Upon expanding the one-particle distribution function in terms of Fourier modes of the angular variable, $f_k(\mathbf{r},t){=}\int_{-\pi}^{\pi}\mathrm{d}\theta\,\mathrm{e}^{\mathrm{i}\theta k}f(\mathbf{r},\theta,t)$, one obtains

$$\begin{aligned}\partial_t f_k+\frac{v_0}{2}\Big[\partial_x(f_{k+1}+f_{k-1})-\mathrm{i}\partial_y(f_{k+1}-f_{k-1})\Big]-\mathrm{i}kv_0\kappa_0 f_k\\ =-\lambda(1-\mathrm{e}^{-(k\sigma)^2/2})f_k+\sum_{n=-\infty}^{\infty}\mathcal{I}_{n,k}f_n f_{k-n}\,,\end{aligned} \tag{2}$$

where explicit expressions for the collision kernels $\mathcal{I}_{n,k}(\sigma)$ are given in the Supplemental Material [12]. For $k{=}0$, Eq. (2), yields the continuity equation $\partial_t\rho{=}-\nabla\cdot\mathbf{j}$ for the local density

$\rho(\mathbf{r},t):=f_0(\mathbf{r},t)$ with the particle current given by $\mathbf{j}(\mathbf{r},t)=v_0(\mathrm{Re}f_1,\mathrm{Im}f_1)^T$. In general, Eq. (2) constitutes an infinite hierarchy of equations coupling lower with higher order Fourier modes.

A linear stability analysis of Eq. (2) enables further progress. Since $\mathcal{I}_{n,0}=0$ for all n, a state with spatially homogeneous density $\bar{\rho}=f_0$ and all higher Fourier modes vanishing is a stationary solution to Eq. (2) (*disordered state*). To linear order, the dynamics of small perturbations δf_k with respect to this uniform state is given by $\partial_t\,\delta f_k=\mu_k(\bar{\rho},\sigma)\,\delta f_k$, where $\mu_k(\bar{\rho},\sigma)=(\mathcal{I}_{0,k}+\mathcal{I}_{k,k})\bar{\rho}-\lambda(1-\mathrm{e}^{-(k\sigma)^2/2})$. For a polar collision rule, as considered here, only μ_1 can become positive, defining a critical density $\rho_c(\sigma)$ at $\mu_1(\rho_c,\sigma):=0$ [Fig 3(a)]. Above threshold ($\bar{\rho}>\rho_c$), the spatially homogeneous state is unstable, the particle current grows exponentially, and collective motion may emerge.

In close proximity to the critical density $\rho_c(\sigma)$ a weakly non-linear analysis yields further insights into the dynamics of the system and the ensuing steady states. Here we follow Ref. [28] and assume small currents $f_1\ll 1$ at onset. Then, balancing of the terms in the continuity equation, the equation for f_1, and terms involving f_1 in the equation for f_2 implies the scaling $\rho-\bar{\rho}\sim f_1$, $f_2\sim f_1^2$ as well as weak spatial and temporal variations $\partial_{x/y}\sim f_1$, $\partial_t\sim f_1$. To include the lowest-order damping term in f_1, we retain terms up to cubic order in f_1. This yields the following hydrodynamic equation for the complex particle current $v_0 f_1(\mathbf{r},t)=j_x(\mathbf{r},t)+\mathrm{i}j_y(\mathbf{r},t)$

$$\begin{aligned}\partial_t f_1(\mathbf{r},t) = &\left[\alpha(\rho-\rho_c)+\mathrm{i}v_0\kappa_0\right] f_1-\xi|f_1|^2 f_1-\frac{v_0}{2}\nabla\rho\\ &-\beta f_1^*\nabla f_1-\gamma f_1\nabla^* f_1+\nu\nabla^*\nabla f_1\,,\end{aligned}\tag{3}$$

where $\nabla:=\partial_x+\mathrm{i}\partial_y$. While this equation shows the same functional dependencies on local density and current as found in systems with straight propulsion [29], the coefficients α, ξ, ν, γ and β are now *complex-valued* (for explicit expressions please see the Supplemental Material [12]). This can be traced back to the angular convection term in Eq. (1), or equivalently to the corresponding phase-shift term in Eq. (2). As a consequence, the field theory of active systems with particles moving on circular orbits with defined chirality is generically given by a *complex Ginzburg-Landau (GL) equation with convective spatial coupling* as well as *density-current coupling*. This constitutes a highly interesting generalization of the standard (diffusive) complex GL equations [38, 39], and is qualitatively different to real GL-type equations that were previously applied in the context of self-propelled particles [28]. Above threshold, $\bar{\rho}>\rho_c(\sigma)$, the active chiral hydrodynamics described by the

generalized GL equation Eq. (3) exhibits a uniform oscillatory solution with $f_1{=}F_1 e^{i\Omega_0 t}$, i. e. a state in which particles move on a circular (chiral) path with an angular velocity $\Omega_0{=}v_0\kappa_0{-}\alpha(\bar{\rho}{-}\rho_c)\mathrm{Im}[\xi]/\mathrm{Re}[\xi]$; the amplitude $F_1{=}\left(\alpha(\bar{\rho}{-}\rho_c)/\mathrm{Re}[\xi]\right)^{1/2}$ gives the particle density. However, a linear stability analysis of Eq. (3) shows that for densities slightly larger than ρ_c this oscillatory solution is linearly unstable against finite wavelength perturbations in the current and density fields. Preliminary numerical solutions of the generalized GL equation, Eq. (3), take the form of rotating spots of high density that appear to show turbulent dynamics [12, 40]. This is qualitatively distinct from the high-density bands found for straight-moving particles [19, 41] and the vortex field of a fluid coupled to torque dipoles [42, 43].

Far above threshold, closure relations such as those discussed above [28] may become invalid and with them the ensuing hydrodynamic equations. Therefore, we proceed with the full spectral analysis of the Boltzmann equation, Eq. (2), as detailed in the Supplemental Material [12]. First, we numerically calculate the spatially homogeneous solutions for all angular Fourier modes f_k below some cutoff wave vector $k_{\max}$. For given values of $\bar{\rho}$ and σ and a desired accuracy ε of this mode truncation scheme, the cutoff is chosen such that $|f_{k_{\max}+1}|{<}\varepsilon$. We find that for $\bar{\rho}{<}\rho_c(\sigma)$ a spatially homogeneous state where all modes but f_0 vanish is the only stable state. In contrast, above threshold ($\bar{\rho}{>}\rho_c(\sigma)$) there is a second solution for which $|f_1|{>}0$. It corresponds to a polar ordered state whose orientation is changing periodically in time with frequency $v_0\kappa_0$. For moderate $\bar{\rho}{-}\rho_c$, the amplitude quantitatively agrees with the result from the generalized GL equation; see Supplemental Material [12]. In a second step, we consider wave-like perturbations, $\delta f_k(\mathbf{q})$ with wave-vector $\mathbf{q}$, of the spatially homogeneous oscillatory solution in a co-rotating frame. The largest real part of all eigenvalues of the corresponding linearized system for δf_k then yields the linear growth rate $S(q)$ [Fig. 3(b)]. In accordance with the linear stability analysis of Eq.(3), we find that for densities slightly larger than ρ_c a spatially homogeneous solution is unstable against finite wavelength perturbations. The dispersion relation $S(q)$ exhibits a band of unstable modes, with the maximal growth rate $S_{\max}$ decreasing as one moves away from the threshold ρ_c [Fig. 3(a,b)]. Actually, there is lobe-like regime in parameter space where $S(q){<}0$ [Fig. 3(a)], and hence a homogeneously polar ordered state with rotating direction is stable. We emphasize here that our stability portrait [Fig. 3(a)] is independent of κ_0 and hence equally valid for systems of straight-moving particles. For our two approaches

(Fig. 3(a) and Fig. 2(d)), the onset to order is governed by a similar trend [12], common for active systems [24, 44]: disorder prevails for low density or high noise, order is promoted for high density or low noise.

To determine the spatiotemporal dynamics in the regime where neither a spatially homogeneous state nor a homogeneously polar ordered state are stable, we resort to a modified version of the SNAKE algorithm [31] to numerically solve Eq. (1). It accurately reproduces the threshold value $\rho_c(\sigma)$ at which the spatially homogeneous state becomes unstable [Fig. 3(c)]. Above threshold ($\bar{\rho}>\rho_c$) we find that local density fluctuations quickly grow and evolve into stable swirls, i. e. disc-like flocks of high density and polar order moving on circular paths; see Fig. 3(d), and Movie 6 in Supplemental Material [12]. The radius of such a path is approximately given by R_0. These swirl patterns closely resemble the swirling flocks observed in the Brownian dynamics simulations for short polymer arc angles [Movie 5 [12]], as well as our preliminary numerical solutions of the generalized GL equation, Eq. (3) [12, 40]. Moreover, in accordance with the spectral analysis, we find a second threshold density, above which the system settles into a homogeneously polar ordered state with a periodically changing orientation [Movie 7 [12]]. The amplitude and frequency of the polar order agree with the numerical results of the spectral analysis to high accuracy [12], while the numerically determined phase boundaries differ. The SNAKE algorithm produces stable swirl patterns only in a parameter regime where our linear stability analysis yields significant growth rates. This is mainly due to spurious noise caused by the discretization of the angular variable, which tends to suppress inhomogeneities in the regime of small growth rates. Furthermore, the finite system size constricts the band of possible modes and allows only for patterns of sufficiently short length scales.

For active systems of circling particles that interact via steric repulsion, our microscopic and mesoscopic treatments strongly suggests that a phase of collective vortex structures is a generic feature. Within this class, our work shows that extended polymers which as a whole follow circular tracks can form closed rings. Concerning our motivation of circling FtsZ, further research is needed to elucidate the dynamics of treadmilling; yet our minimal kinetic assumption suggests that varying particle density alone suffices to regulate the patterns as observed by Loose and Mitchison [5]. Compared to systems of straight moving particles we find qualitatively new phenomena [12, 40]. For those systems, it was already reported that (globally achiral) vortices can occur due to collisions of particles of asymmetric shape [45] or

due to memory in orientation [25, 46]. Some of our findings, like the polymer length dependence of patterns and the possible emergence of active turbulence [47, 48], pose interesting questions for future work. Our analysis yields a mapping of the emergent dynamics onto a generalized Ginzburg-Landau equation, providing a connection between active matter and nonlinear oscillators [40].

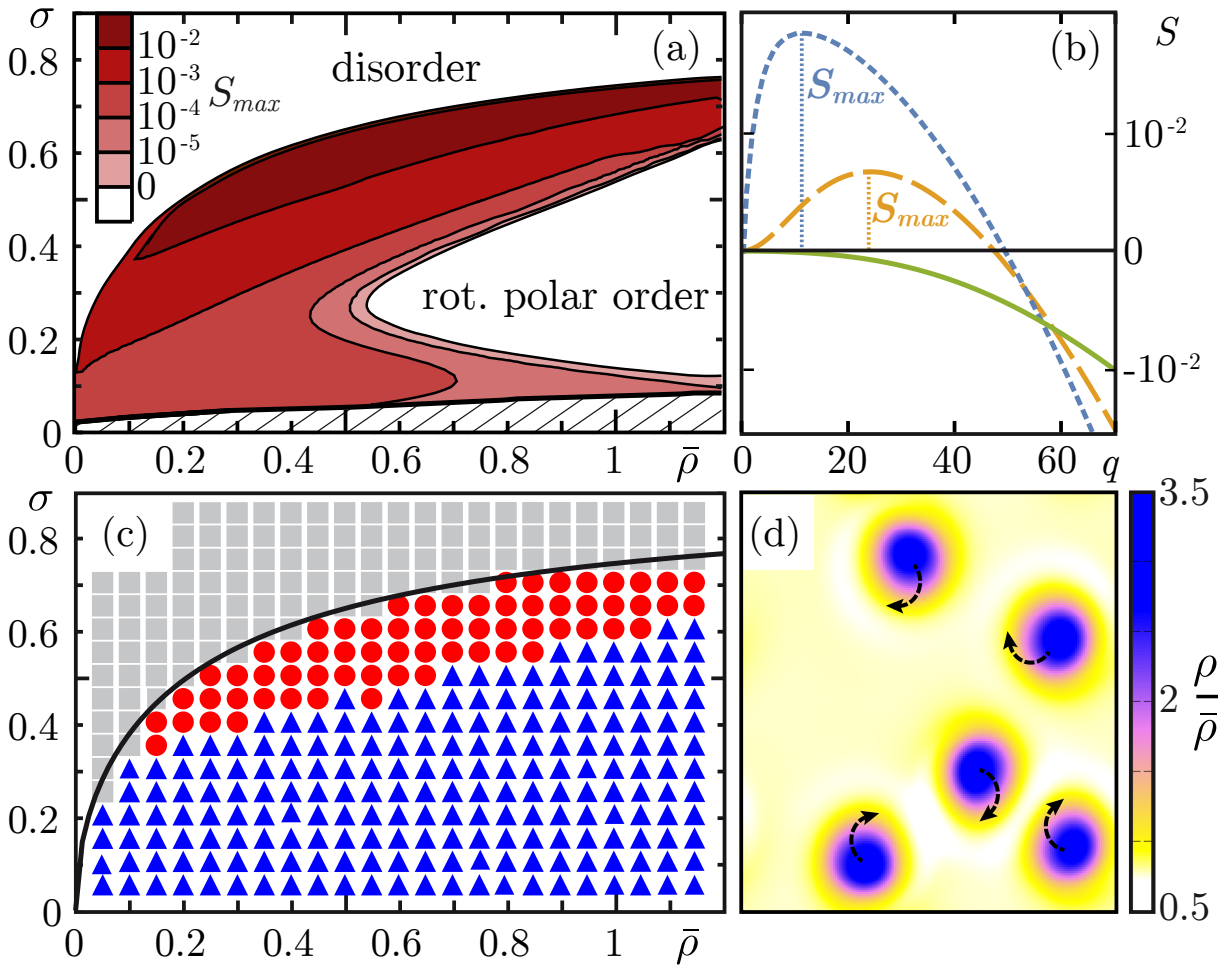

FIG. 3. **(a)** Stability of homogeneous solutions of Eq. (2) as a function of σ and $\bar{\rho}$ in units of $\lambda/(dv_0)$. White and red areas denote regions where finite wavelength perturbations of the homogeneous solutions are stable and unstable, respectively. The color code denotes the value of the maximal growth rate S_{max}. **(b)** Dispersion relation of $S(q)$ (q in units of $2\pi/\sqrt{A}$) for $\bar{\rho}$=0.8 and σ=0.7 (short dashed line), σ=0.6 (long dashed line) and σ=0.4 (solid line). Vertical lines indicate $S_{\max}$. **(c)** Phase diagram for density $\bar{\rho}$ and σ displaying phases of homogeneous disorder (gray rectangles), swirls (red circles) and homogeneous order (blue triangles). The solid line marks the analytic solution of $\rho_c(\sigma)$. An overlay of **(a)**, **(c)** can be found in the Supplemental Material [12]. **(d)** Snapshot of swirl patterns ($\bar{\rho}$=0.8, σ=0.7). All swirls are moving clockwise on circular paths.

We thank F. Thüroff, L. Reese, and J. Knebel for helpful discussions. This research was supported by the German Excellence Initiative via the program 'NanoSystems Initiative Munich' (NIM), and the Deutsche Forschungsgemeinschaft (DFG) via project B02 within the Collaborative Research Center (SFB 863) "Forces in Biomolecular Systems".

J.D. and L.H. contributed equally to this work.

---

* frey@lmu.de

[1] V. Schaller, C. A. Weber, B. Hammerich, E. Frey, and A. R. Bausch, Proc. Natl. Acad. Sci. U.S.A. **108**, 19183 (2011).

[2] V. Schaller, C. A. Weber, C. Semmrich, E. Frey, and A. R. Bausch, Nature **467**, 73 (2010).

[3] Y. Sumino, K. H. Nagai, Y. Shitaka, D. Tanaka, K. Yoshikawa, H. Chaté, and K. Oiwa, Nature **483**, 448 (2012).

[4] R. Suzuki, C. A. Weber, E. Frey, and A. R. Bausch, Nat Phys **11**, 839 (2015).

[5] M. Loose and T. J. Mitchison, Nat. Cell Biol. **16**, 38 (2013).

[6] E. L. Meier and E. D. Goley, Curr. Opin. Cell Biol. **26**, 19 (2014).

[7] M. Ingerson-Mahar and Z. Gitai, FEMS Microbiol. Rev. **36**, 256 (2012).

[8] H. P. Erickson, D. E. Anderson, and M. Osawa, Microbiol. Mol. Biol. R. **74**, 504 (2010).

[9] P. Szwedziak, Q. Wang, T. A. M. Bharat, M. Tsim, and J. Löwe, eLife Sciences **3**, e04601 (2015).

[10] O. Kratky and G. Porod, Recl. Trav. Chim. Pays-B. **68**, 1106 (1949).

[11] N. Saitô, K. Takahashi, and Y. Yunoki, J. Phys. Soc. Jpn. **22**, 219 (1967).

[12] See Supplemental Material, which includes [5].

[13] G. Chirico and J. Langowski, Biopolymers **34**, 415 (1994).

[14] H. Wada and R. R. Netz, Europhys. Lett. **77**, 68001 (2007).

[15] J. K. G. Dhont, *An Introduction to Dynamics of Colloids* (Elsevier, Amsterdam, 1996).

[16] X. Lu and Y. Hu, *Molecular Thermodynamics of Complex Systems* (Springer, Heidelberg, 2008).

[17] T. Vicsek, A. Czirók, E. Ben-Jacob, I. Cohen, and O. Shochet, Phys. Rev. Lett. **75**, 1226 (1995).

[18] I. H. Riedel, K. Kruse, and J. Howard, Science **309**, 300 (2005).

[19] H. Chaté, F. Ginelli, G. Grégoire, and F. Raynaud, Phys. Rev. E **77**, 046113 (2008).

[20] E. Bertin, M. Droz, and G. Grégoire, Phys. Rev. E **74**, 022101 (2006).

[21] T. Ihle, Phys. Rev. E **83**, 030901 (2011).

[22] F. Ginelli, F. Peruani, M. Bär, and H. Chaté, Phys. Rev. Lett. **104**, 184502 (2010).

[23] F. Peruani, J. Starruß, V. Jakovljevic, L. Søgaard-Andersen, A. Deutsch, and M. Bär, Phys. Rev. Lett. **108**, 098102 (2012).

[24] M. C. Marchetti, J. F. Joanny, S. Ramaswamy, T. B. Liverpool, J. Prost, M. Rao, and R. A. Simha, Rev. Mod. Phys. **85**, 1143 (2013).

[25] Y. Sumino, K. H. Nagai, Y. Shitaka, D. Tanaka, K. Yoshikawa, H. Chaté, and K. Oiwa, Nature **483**, 448 (2012).

[26] Y. Yang, F. Qiu, and G. Gompper, Phys. Rev. E **89**, 012720 (2014).

[27] A. Kaiser and H. Löwen, Phys. Rev. E **87**, 032712 (2013).

[28] A. Peshkov, E. Bertin, F. Ginelli, and H. Chaté, Eur. Phys. J.-Spec. Top. **223**, 1315 (2014).

[29] E. Bertin, M. Droz, and G. Grégoire, J. Phys. A-Math. Theor. **42**, 445001 (2009).

[30] A. Peshkov, I. S. Aranson, E. Bertin, H. Chaté, and F. Ginelli, Phys. Rev. Lett. **109**, 268701 (2012).

[31] F. Thüroff, C. A. Weber, and E. Frey, Phys. Rev. X **4**, 041030 (2014).

[32] C. A. Weber, F. Thüroff, and E. Frey, New J. Phys. **15**, 045014 (2013).

[33] F. Thüroff, C. A. Weber, and E. Frey, Phys. Rev. Lett. **111**, 190601 (2013).

[34] A. Peshkov, S. Ngo, E. Bertin, H. Chaté, and F. Ginelli, Phys. Rev. Lett. **109**, 098101 (2012).

[35] J. Toner and Y. Tu, Phys. Rev. Lett. **75**, 4326 (1995).

[36] A. Baskaran and M. C. Marchetti, Phys. Rev. E **77**, 011920 (2008).

[37] S. Mishra, A. Baskaran, and M. C. Marchetti, Phys. Rev. E **81**, 061916 (2010).

[38] I. S. Aranson and L. Kramer, Rev. Mod. Phys. **74**, 99 (2002).

[39] V. García-Morales and K. Krischer, Contemp. Phys. **53**, 79 (2012).

[40] In preparation.

[41] H. Chaté, F. Ginelli, G. Grégoire, F. Peruani, and F. Raynaud, Eur. Phys. J. B **64**, 451 (2008).

[42] S. Fürthauer, M. Strempel, S. W. Grill, and F. Jülicher, Eur. Phys. J. E **35**, 89 (2012).

[43] S. Fürthauer, M. Strempel, S. W. Grill, and F. Jülicher, Phys. Rev. Lett. **110**, 048103 (2013).

[44] S. Ramaswamy, Annual Review of Condensed Matter Physics **1**, 323 (2010), arXiv:1004.1933

[cond-mat.soft].

[45] H. H. Wensink, V. Kantsler, R. E. Goldstein, and J. Dunkel, Phys. Rev. E **89**, 010302 (2014).

[46] K. H. Nagai, Y. Sumino, R. Montagne, I. S. Aranson, and H. Chaté, Phys. Rev. Lett. **114**, 168001 (2015).

[47] J. Dunkel, S. Heidenreich, K. Drescher, H. H. Wensink, M. Bär, and R. E. Goldstein, Phys. Rev. Lett. **110**, 228102 (2013).

[48] V. Bratanov, F. Jenko, and E. Frey, PNAS , 201509304 (2015).

Supplemental Material: Active Curved Polymers form Vortex Patterns on Membranes

Jonas Denk,[1] Lorenz Huber,[1] Emanuel Reithmann,[1] and Erwin Frey[1,*]

[1] *Arnold Sommerfeld Center for Theoretical Physics (ASC) and Center for NanoScience (CeNS), Department of Physics, Ludwig-Maximilians-Universität München, Theresienstrasse 37, 80333 München, Germany*

COMMENT ON TREADMILLING

In their experiments [1], Loose and Mitchison observe that FtsZ polymers undergo depolymerization and polymerization processes leading to an effective translation in the direction of the polymers' backbones. However, the underlying molecular details are unclear, as they involve many qualitatively and quantitatively unknown reactions and a yet unstudied interplay of different auxiliary proteins (*e.g.* FtsA, ZipA). Here, we neglect these details and focus on the collective effects of many FtsZ polymers retaining only their effective movement along circular tracks. To realize this kind of motion we assume an intrinsic particle velocity.

NUMERICAL IMPLEMENTATION OF BROWNIAN DYNAMICS

In the following, we discuss the details of the implementation of the Brownian dynamics simulations. We use a bead-spring model [2, 3] that comprises the following discretization scheme: a polymer of length L is subdivided into N beads at positions $\mathbf{r}_i = (x_i, y_i)^T$ ($i = 1, 2, ..., N$), with $N-1$ bonds of length a; the (normalized) bond vectors are given by $\partial_s \mathbf{r} \approx \frac{\mathbf{r}_{i+1}-\mathbf{r}_i}{a} =: \hat{\mathbf{t}}_i$; the bending angle between two adjacent bonds is given by $\theta_i = \arccos(\hat{\mathbf{t}}_{i+1} \cdot \hat{\mathbf{t}}_i)$. The corresponding bending energy reads

$$E_{bend} = \frac{\ell_p}{2a} k_B T \sum_{i=1}^{N-2} (\theta_i - \theta_0)^2. \tag{S1}$$

where $\theta_0 \approx a\kappa_0$ is the spontaneous bending angle. In the bead-spring model, neighboring beads are connected by stiff harmonic springs. The corresponding stretching energy is given by

$$E_{stretch} = \frac{k}{2} \sum_{i=1}^{N-1} (|\mathbf{r}_{i+1} - \mathbf{r}_i| - a)^2. \tag{S2}$$

In the simulations, the spring constant k is chosen larger than all other force constants to account for the fact that biopolymers are nearly inextensible; as a consequence, stretching modes relax fast compared to other dynamic processes. At the same time, k cannot be chosen arbitrarily large as this would strongly limit the maximal simulation time T_{max} (see below for values).

In the two-dimensional system of M polymers, we assume steric repulsion between adjacent polymer segments $\mathbf{r}_i^{(m)}$ ($m = 1, 2, ..., M$). As an interaction potential we use a truncated

Lennard-Jones potential [4–6]

$$(E_{int})_{ij}^{(mn)} = \epsilon \left[\left(\frac{a}{r_{ij}^{(mn)}} \right)^{12} - \left(\frac{a}{r_{ij}^{(mn)}} \right)^{6} \right] \Theta(a - r_{ij}^{(mn)}), \tag{S3}$$

with $r_{ij}^{(mn)} = |\mathbf{r}_i^{(m)} - \mathbf{r}_j^{(n)}|$, ϵ the potential strength, and $\Theta(r)$ the Heaviside step function. At distances smaller than the bond length a, the potential is strongly repulsive.

In the Langevin description, the equation of motion is given by a force balance between elastic, active, thermal and dissipative terms. For the i-th bead of a polymer, the equation of motion reads

$$\begin{aligned} \zeta \partial_t \mathbf{r}_i &= -\frac{\delta E}{\delta \mathbf{r}_i} + \mathbf{F}_i^{prop} + \boldsymbol{\eta}_i \\ &= \mathbf{F}_i^{bend} + \mathbf{F}_i^{stretch} + \mathbf{F}_i^{int} + \mathbf{F}_i^{prop} + \boldsymbol{\eta}_i \end{aligned} \tag{S4}$$

where $E = E_{bend} + E_{stretch} + E_{int}$, $\mathbf{F}_{prop}$ is the propulsive force and the amplitude of the thermal forces is given by $\langle \boldsymbol{\eta}_i(t) \cdot \boldsymbol{\eta}_j(t') \rangle = 4k_B T \zeta \delta_{ij} \delta(t - t')$. The bending, stretching and interaction forces $\mathbf{F}_i^{bend}, \mathbf{F}_i^{stretch}, \mathbf{F}_i^{int}$ are obtained by variation of the corresponding energetic terms with respect to the position vector $\mathbf{r}_i$ [2, 3]. We employ the following implementation of the tangential propulsive force $\mathbf{F}^{prop} = \zeta v_0 \partial_s \mathbf{r}$:

$$\mathbf{F}_i^{prop} = \zeta v_0 \begin{cases} \hat{\mathbf{t}}_1 & i = 1 \\ (\hat{\mathbf{t}}_{i-1} + \hat{\mathbf{t}}_i)/2 & 1 < i < N \\ \hat{\mathbf{t}}_{N-1} & i = N \end{cases} \tag{S5}$$

For the integration of Eq. (S4) we use an Euler-Maruyama iteration scheme [7] with sufficiently small time steps $\Delta = 0.0001\tau$ with the unit time $\tau = \zeta a^2/(k_B T)$. In our simulations, we used the following set of parameters: $L = 9a, \ell_p = 100a, k = 500 k_B T/a^2, \epsilon = 1 k_B T, \theta_0 = 0.2, \zeta = 1$ and a periodic system of area $A = 60a \times 60a$ (such that it can contain many consecutive polymer lengths). In the main text, the unit of length is set to $a = 100\,nm$, such that $L = 0.9\,\mu m, \ell_p = 10\,\mu m$ are roughly similar to FtsZ filaments. The noise strength $\sigma = k_B T \ell_p/(\zeta v_0 L^2)$ was varied as follows: we changed the temperature scale in the interval $k_B T \in [0, 1]$ for $v_0 = 5$, and for $k_B T = 1$ varied v_0 in the range $v_0 \in [1, 5]$. The maximal simulation times T_{max} for all simulations in the main text were chosen such that the single polymer rotation time $\tau_R = 2\pi/(\kappa_0 v_0)$ is much smaller. We took $T_{max} > 400\tau_R$ and $T_{max} > 700\tau$ for our data to provide a sufficiently large sampling interval

for both convective and diffusive motion. To consolidate the results, data were recorded for 10 independent simulation for each given set of parameters.

ANALYSIS OF THE PAIR CORRELATION FUNCTION

To analyze the patterns observed in the Brownian dynamics simulations, we consider the pair correlation function $g(d_{cc})$ [8, 9] of center distances $d_{cc} = |\mathbf{r}_{cc}^{(m)} - \mathbf{r}_{cc}^{(n)}|$. The positions $\mathbf{r}_{cc}^{(m)}$ are the curvature centers of each polymer, generated by averaging over the local curvature and all local reference positions on a contour (see Fig. S1(a)). In contrast to the positions $\mathbf{r}^{(m)}$, the curvature centers do not oscillate due to self-propulsion and hence represent a more stable measure of particle position.

Figure S1(b) displays the contour of $g(d_{cc})$ for parameters $k_BT = 0.5$ and $v_0 = 5$ (i. e. $\sigma = 0.247$). For sufficiently small ρ, the density exhibits a local minimum at d_{cc}^{min}, the diameter of a vortex. This implies that there is a preferred vortex size and structure connected to the distance d_{cc}^{min}. These minima were determined after applying a Gaussian filter to suppress random fluctuation artifacts and then used to distinguish the observed patterns according to the 'phase' criteria introduced in the main text: *disordered states* for $d_{cc}^{min} \approx 2R_0$, *vortex states* for $d_{cc}^{min} > 2R_0$ and *train states* without d_{cc}^{min}.

DERIVATION OF THE HYDRODYNAMIC EQUATIONS

To assess the dynamics at larger scales, we employed a kinetic Boltzmann approach. The corresponding generalized Boltzmann equation for $f(\theta, \mathbf{r}, t)$ is given by Eq. (1). The self-diffusion and collision integrals $\mathcal{I}_d$ and $\mathcal{I}_c$, respectively, are given by

$$\mathcal{I}_d[f] = \lambda \langle \int_{-\pi}^{\pi} \mathrm{d}\phi f(\phi) \left[\delta(\theta - \phi - \eta) - \delta(\theta - \phi)\right] \rangle_\eta \,, \tag{S6}$$

$$\begin{aligned} \mathcal{I}_c[f; f] = \langle \int_{-\pi}^{\pi} \mathrm{d}\phi_1 \int_{-\pi}^{\pi} \mathrm{d}\phi_2 \mathcal{S}(|\phi_1 - \phi_2|) f(\phi_1) f(\phi_2) \\ \times \left[\delta(\theta - \frac{1}{2}(\phi_1 + \phi_2) - \eta) - \delta(\theta - \phi_1)\right] \rangle_\eta \,, \end{aligned} \tag{S7}$$

where $\mathcal{S}(\psi) = 4dv_0 |\sin(\frac{\psi}{2})|$ is the scattering cross section for spherical particles of diameter d and velocity v_0 in two dimensions as detailed in Ref. [10]. The collision integral represents

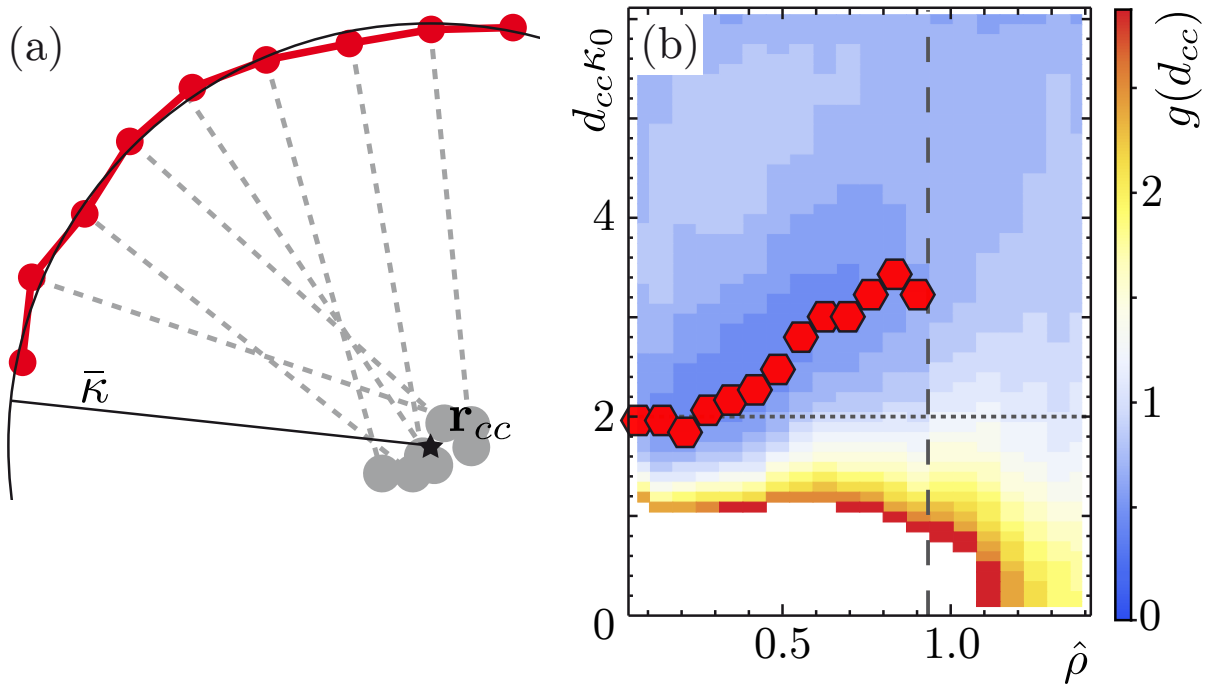

FIG. S1. **(a)** Illustration of the curvature center $\mathbf{r}_{cc}$ as determined by averaging over local centers with a mean contour curvature $\bar{\kappa}$ (polymer in red). **(b)** Heat map of the pair correlation function for $\sigma = 0.247$ in terms of distances d_{cc} and densities ρ. Red polygons denote the positions of d_{cc}^{min}. The short dashed line depicts the free polymer radius and the long dashed line marks the regime where d_{cc}^{min} vanishes.

ferromagnetic alignment of two particles with orientation ϕ_1 and ϕ_2 along their average angle $\theta = \frac{1}{2}(\phi_1 + \phi_2)$. The brackets denote an average over a Gaussian-distributed noise variable η. To obtain a dimensionless form we used the rescaling

$$
\begin{aligned}
t &\to t \cdot \lambda^{-1}\,, \\
\mathbf{x} &\to \mathbf{x} \cdot v_0 \lambda^{-1}\,, \\
f &\to f \cdot \rho_0\,, \\
\kappa_0 &\to \kappa_0 \cdot v_0 \lambda^{-1}\,,
\end{aligned}
$$

with $\rho_0 = \lambda/(d v_0)$. Measuring time, space and density in units of λ^{-1}, $v_0\lambda^{-1}$, and ρ_0, respectively, allows to set $d = \lambda = v_0 = 1$. Then, the only remaining free parameters are the noise amplitude σ, κ_0, and the mean particle density $\bar{\rho} = A^{-1}\int_A \mathrm{d}\mathbf{r}\int_{-\pi}^{\pi}\mathrm{d}\theta\, f(\mathbf{r},\theta,t)$. To proceed, we performed a Fourier transformation of the angular variable: $f_k(\mathbf{r},t) = \int_{-\pi}^{\pi}\mathrm{d}\theta\, \mathrm{e}^{\mathrm{i}\theta k} f(\mathbf{r},\theta,t)$.

This leads to the Boltzmann equation in Fourier space, Eq. (2), where the Fourier transforms $\mathcal{I}_{n,k}$ are given by

$$\mathcal{I}_{n,k} = \int_{-\pi}^{\pi} \frac{\mathrm{d}\Phi}{2\pi} \mathcal{S}(|\Phi|) \left[\hat{P}_k \cos(\Phi(n - k/2)) - \cos(\Phi n) \right] . \tag{S8}$$

$\hat{P}_k = \mathrm{e}^{-(k\sigma)^2/2}$ is the Fourier transform (characteristic function) of the Gaussian noise with standard deviation σ. Note that $\mathcal{I}_{n,0} = 0$ for all n. For $k = 0$, Eq. (2) hence yields the continuity equation $\partial_t \rho = -\frac{1}{2}(\nabla f_1^* + \nabla^* f_1) = -\nabla \cdot \mathbf{j}$ for the local density $\rho(\mathbf{r}, t) := f_0(\mathbf{r}, t)$ with the particle current given by $\mathbf{j}(\mathbf{r}, t) = v_0(\mathrm{Re} f_1, \mathrm{Im} f_1)^T$. In order to get a closed equation for the particle current at onset, we assume small currents $f_1 \ll 1$ and use the truncation scheme: $\rho - \bar{\rho} \sim f_1$, $\partial_{x/y} \sim f_1$, $\partial_t \sim f_1$, $f_2 \sim f_1^2$ with vanishing higher modes as presented for polar particles with ferromagnetic interaction in Ref. [11]. In analogy to Ref. [10], we retained only terms up to cubic order in f_1 in the Boltzmann equation, Eq. (2), for $k = 1$. The equation for f_1 then couples to the nematic order field f_2 via a term $\sim f_1^* f_2$ of order f_1^3, where the star denotes complex conjugate. Writing down contributions from Eq. (2) for $k = 2$ of quadratic order in f_1 yields an expression for f_2 as a function of f_1. The expression for f_2 can then be substituted into Eq. (2) for $k = 1$ to obtain a closed equation for f_1. Together with the continuity equation, the hydrodynamic equations for the density and the particle current read

$$\partial_t \rho = -\frac{1}{2}(\nabla f_1^* + \nabla^* f_1) , \tag{S9a}$$

$$\begin{aligned} \partial_t f_1 = {} & [\alpha(\rho - \rho_c) + \mathrm{i} v_0 \kappa_0] f_1 - \xi |f_1|^2 f_1 + \nu \nabla^* \nabla f_1 \\ & - \gamma f_1 \nabla^* f_1 - \beta f_1^* \nabla f_1 - \frac{v_0}{2} \nabla \rho , \end{aligned} \tag{S9b}$$

where $\nabla := \partial_x + \mathrm{i}\partial_y$. The coefficients are given by

$$\begin{aligned} \alpha &:= (\mathcal{I}_{0,1} + \mathcal{I}_{1,1}), \\ \rho_c &= \frac{\lambda(1 - \hat{P}_1)}{\mathcal{I}_{0,1} + \mathcal{I}_{1,1}} , \\ \nu &:= -\frac{1}{4} \frac{1}{\lambda(\hat{P}_2 - 1) + 2\mathrm{i} v_0 \kappa_0 + (\mathcal{I}_{0,2} + \mathcal{I}_{2,2})\rho} , \\ \xi &:= -4(\mathcal{I}_{-1,1} + \mathcal{I}_{2,1}) \nu \mathcal{I}_{1,2} , \\ \beta &:= 2(\mathcal{I}_{-1,1} + \mathcal{I}_{2,1}) \nu , \\ \gamma &:= 4\nu \mathcal{I}_{1,2} . \end{aligned} \tag{S10}$$

We note that the employed truncation scheme implies fast relaxation of the nematic order field f_2 such that $\partial_t f_2$ is assumed to be negligible on time scales of the dynamics of f_1. f_2 is then slaved to f_1 via $f_2 = -2\nu\nabla f_1 + \gamma f_1^2$.

Linear stability analysis

For $\rho < \rho_c$ Eqs. (S9) are solved by the homogeneous isotropic state: $\rho = \bar{\rho} = const.$, $f_1 = 0$. For $\rho > \rho_c$ there is a second solution given by the homogeneous oscillatory state: $\rho = \bar{\rho}$, $f_1 = F_1 e^{i\Omega_0 t}$ with $F_1 = (\alpha(\bar{\rho} - \rho_c)/\mathrm{Re}[\xi])^{1/2}$ and $\Omega_0 = v_0\kappa_0 - \alpha(\bar{\rho} - \rho_c)\mathrm{Im}[\xi]/\mathrm{Re}[\xi]$.

Homogeneous isotropic state

To study the stability of the homogeneous isotropic state we substitute $\rho = \bar{\rho} + \delta\rho$ and $f_1 = \delta f_1$ with the wave-like perturbations of the form

$$\begin{aligned} \delta\rho(\mathbf{r}, t) &\sim \delta\rho_{\mathbf{q}}\, e^{i\mathbf{q}\cdot\mathbf{r}}\,, \\ \delta f_1(\mathbf{r}, t) &\sim \delta f_{1,\mathbf{q}}\, e^{i\mathbf{q}\cdot\mathbf{r}}\,, \end{aligned} \tag{S11}$$

where $\delta\rho_{\mathbf{q}}$ and $\delta f_{1,\mathbf{q}}$ are in general complex amplitudes that are assumed to be small. Periodic boundary conditions in our numeric solution impose $|\mathbf{q}| = n\frac{2\pi}{L}$, $n\epsilon\mathbb{Z}$, where $L = \sqrt{A}$ and A is the area of the (quadratic) system. The linearized set of equations of motion for the perturbations $\delta\rho_{\mathbf{q}}(t)$, $\delta f_{1,\mathbf{q}}(t)$ and $\delta f^*_{1,\mathbf{q}}(t)$ has the characteristic polynomial

$$\begin{aligned} &- q^2\alpha(\bar{\rho} - \rho_c) + q^4\Re[\nu] \\ &+ \left(2(\alpha(\bar{\rho} - \rho_c) - \Re[\nu]q^2)^2 + 2(v_0\kappa_0 - \Im[\nu]q^2)^2 + q^2\right) S \\ &+ 4\left(-\alpha(\bar{\rho} - \rho_c) + \Re[\nu]q^2\right) S^2 + 2S^3\,. \end{aligned} \tag{S12}$$

where S is the eigenvalue of the linearized set of equations for $\delta\rho_{\mathbf{q}}(t)$, $\delta f_{1,\mathbf{q}}(t)$ and $\delta f^*_{1,\mathbf{q}}(t)$. We note that $\Re[\nu]$ is positive for all densities. For $\bar{\rho} < \rho_c$, all coefficients in (S12), including the S-independent terms are positive, such that (S12) only yields S with negative real part. Thus, for $\bar{\rho} < \rho_c$ the homogeneous isotropic state is linearly stable against inhomogeneous wave-like perturbations. For $\bar{\rho} - \rho_c > 0$, the real part of S becomes positive where the fastest growing mode is always at $q = 0$.

Homogeneous oscillatory state

To study the stability of the homogeneous oscillatory solution we substitute small perturbations in the basis of the homogeneous oscillating solution:

$$\begin{aligned}\rho =&\bar{\rho} + \delta\rho_{(0)} \\ &+ \sqrt{\frac{\alpha(\bar{\rho}-\rho_c)}{\Re[\xi]}}\,\delta\rho_{(1)}\mathrm{e}^{\mathrm{i}\Omega_0 t} + \sqrt{\frac{\alpha(\bar{\rho}-\rho_c)}{\Re[\xi]}}\,\delta\rho^*_{(1)}\mathrm{e}^{-\mathrm{i}\Omega_0 t}, \\ f_1 =&F_1\mathrm{e}^{\mathrm{i}\Omega_0 t} + \delta f_{(0)} \\ &+ \sqrt{\frac{\alpha(\bar{\rho}-\rho_c)}{\Re[\xi]}}\,\delta f_{(1)}\mathrm{e}^{\mathrm{i}\Omega_0 t} + \sqrt{\frac{\alpha(\bar{\rho}-\rho_c)}{\Re[\xi]}}\,\delta f_{(2)}\mathrm{e}^{-\mathrm{i}\Omega_0 t},\end{aligned} \tag{S13}$$

where the amplitudes $\delta\rho_{(0)}$, $\delta\rho_{(1)}$, $\delta f_{(0)}$, $\delta f_{(1)}$ and $\delta f_{(2)}$ are again of the form (S11). Truncating at the lowest order of $(\bar{\rho}-\rho_c)$, which is $\sqrt{\alpha(\bar{\rho}-\rho_c)}$, yields a closed set of linear equations for the amplitudes. The eigenvalue with the largest real part of this linear system determines the growth rate $S(q)$ of wave-like perturbations. We find that the dispersion relation yields positive $S(q)$ for finite q (see Fig S2).

NUMERICAL LINEAR STABILITY ANALYSIS IN THE FULL PHASE SPACE

In the derivation and the stability analysis of Eqs. (S9) we rely on the assumption of small particle currents which might be justified at onset. However, this assumptions is in general questionable and not well justified for densities much larger than ρ_c. To obtain a stability map for the full phase space (Fig. 3), we first calculated the homogeneous solution of Eq. (2) retaining only modes up to $k_{\max}$. Given some values of $\bar{\rho}$ and σ and a desired accuracy ϵ of this mode truncation scheme the cutoff is chosen such that $|f_{k_{max+1}}| < \epsilon$. As a next step, we linearized Eq. (2) with respect to this solution and calculated the maximal growth rate $S(\mathbf{q})$ of wave-like perturbations with wave vector $\mathbf{q}$. If $S(\mathbf{q}) > 0$ for some $|\mathbf{q}|$, the homogeneous solution is unstable whereas if $S(\mathbf{q}) < 0$ for all $|\mathbf{q}|$, the corresponding homogeneous solution is stable.

Note that the homogeneous version of Eq. (2) (neglecting all gradient terms) is invariant under a phase shift $f_k \to f_k \mathrm{e}^{\mathrm{i}kv_0\kappa_0 t}$. Choosing the orientation of the polar order at $t = 0$ to be aligned along the x-axis, Eq. (2) is solved by $f_k = |f_k|\mathrm{e}^{\mathrm{i}kv_0\kappa_0 t}$ with the time and space independent amplitude $|f_k|$. $|f_k|$ is then determined by the stationary homogeneous version

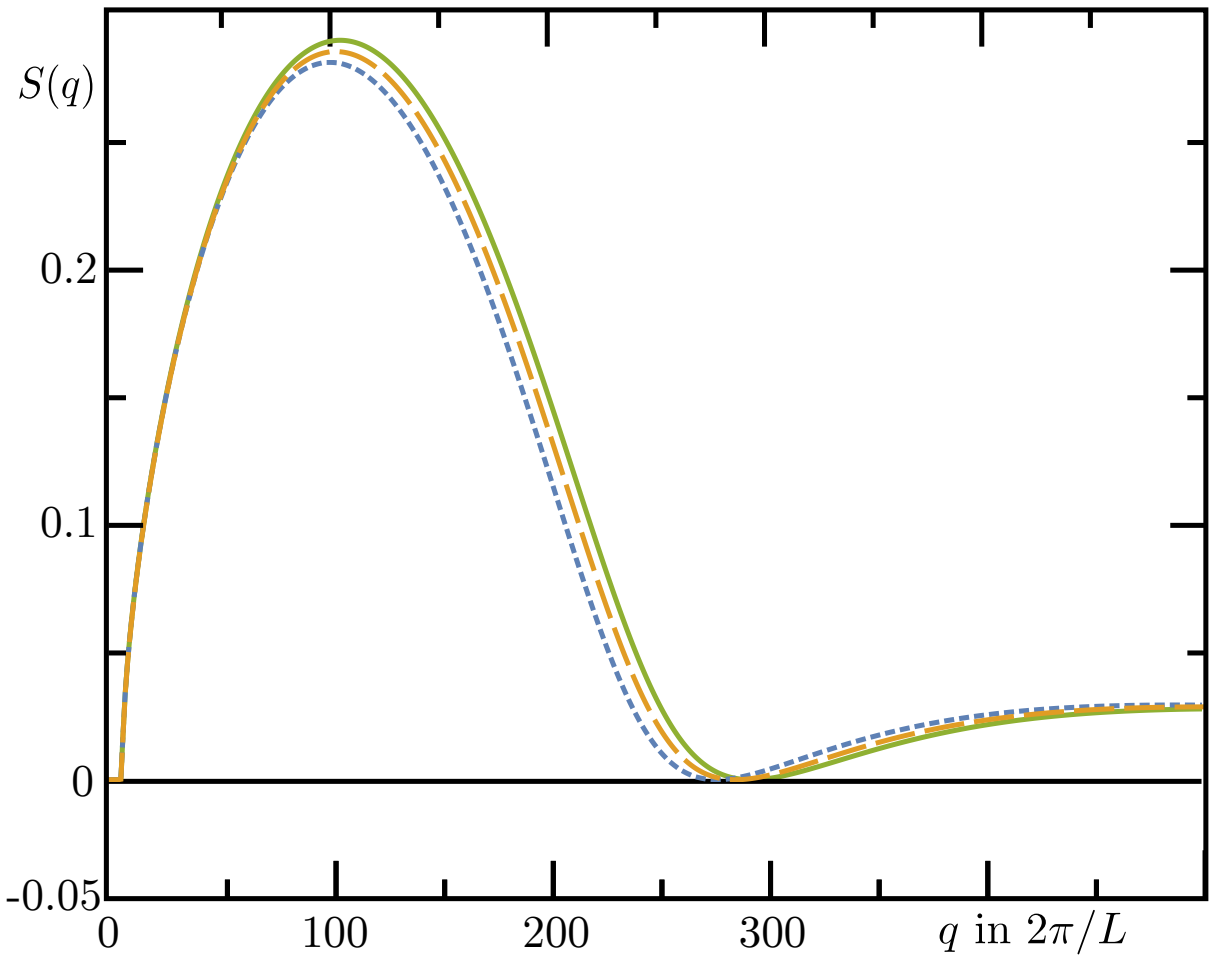

FIG. S2. Dispersion relations for $\sigma = 0.6$, 0.4 and 0.1 (short-dashed, long-dashed and solid lines, respectively) at $\bar{\rho} = 0.8$.

of Eq. (2):

$$0 = \lambda(\hat{P}_k - 1)|f_k| + \sum_{n=-\infty}^{\infty} \mathcal{I}_{n,k}\,|f_n||f_{k-n}|\,. \tag{S14}$$

This equation is identical to the stationary homogeneous Boltzmann equation for straight moving particles; i.e. where $\kappa_0 = 0$. Hence, the solutions for the amplitudes $|f_k|$ are identical to the solutions for the Fourier modes in systems of straight moving particles [10]. To proceed, we truncate the infinite sum in Eq. (S14) at $k_{\max}$ and calculate the solution of all $|f_k|$ with $|k| \leq k_{\max}$. Fig. S3 depicts the solution for the amplitude $|f_1|$ as compared to the solution of the generalized Ginzburg-Landau equation as well as the SNAKE algorithm. The explicit solution for $|f_1|$ and higher modes justifies the scaling scheme used to derive

Eqs. (S9) in the vicinity of ρ_c [Fig. S3, inset]. For decreasing noise σ or increasing density $\bar{\rho}$ an increasing number of Fourier modes starts to grow [Fig. S3, inset]. In our numerical calculations we typically included $30 - 50$ Fourier modes. The dashed region in Fig. 3(a) indicates the regime where we cannot find a nontrivial solution to Eq. (S14) by neglecting Fourier modes above the chosen $k_{\max} = 50$ and where we would have to choose a larger $k_{\max}$.

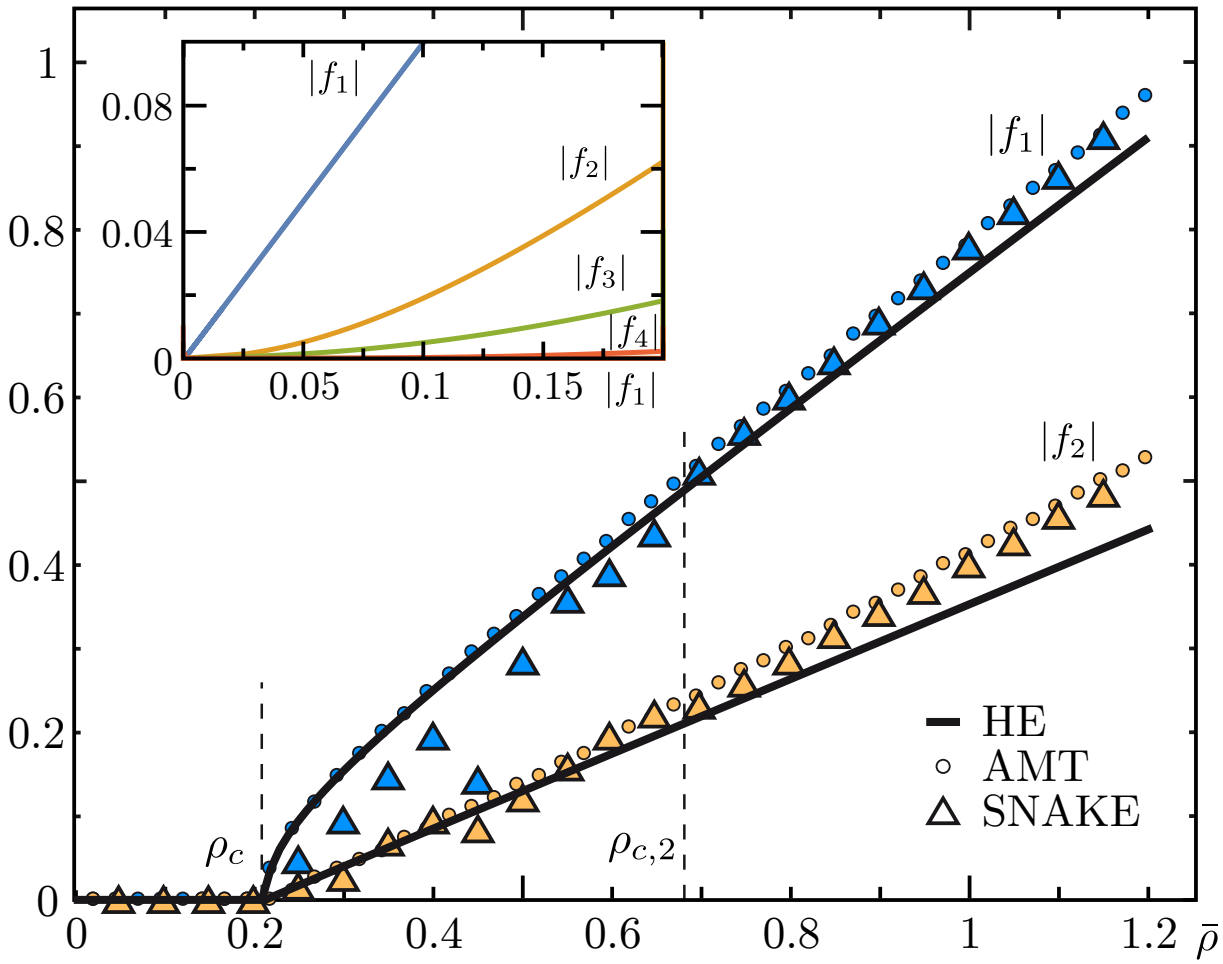

FIG. S3. Homogeneous solution for f_1 and f_2 for $\sigma = 0.5$ obtained from the hydrodynamic equations Eqs. (S9) (HE), the adapted mode truncation scheme (AMT), and the SNAKE algorithm. Note that within ρ_c and $\rho_{c,2}$ (dashed vertical lines), the SNAKE algorithm yields swirl states and hence the corresponding mode values do not represent homogeneous states. The inset depicts the solutions for the first modes obtained from the AMT and shows nonlinear scaling of higher modes with respect to $|f_1|$.

With the substitution $f_k = (|f_k| + \delta f_k)\mathrm{e}^{\mathrm{i}kv_0\kappa_0 t}$ the linear system for δf_k then reads

$$\begin{aligned}\partial_t \delta f_k = &-\tfrac{v_0}{2}(\nabla \delta f_{k-1} + \nabla^* \delta f_{k+1}) + \lambda(\hat{P}_k - 1)\delta f_k \\ &+ \sum_{n=-\infty}^{\infty} (\mathcal{I}_{n,k} + \mathcal{I}_{k-n,k})|f_{k-n}|\delta f_n \,. \end{aligned} \tag{S15}$$

Here, we performed a coordinate transformation to a frame rotating with angular frequency κ_0 such that $\nabla \to \mathrm{e}^{\mathrm{i}kv_0\kappa_0}\nabla$. Assuming wave-like perturbations as in Eq. (S11), we solved Eq. (S15) for the maximal eigenvalue and get the growth rate as a function of the wavenumber in the rotating frame (see Fig. 3(b)). The maximum taken over all wavenumbers $|\mathbf{q}| > 0$ then defines the maximal growth rate S_{max} of wave-like perturbations. In agreement to previous results [10], we found that the growth rate is maximal for $\mathbf{q}$ parallel to the particle current. The contour plot of S_{max} as a function of $\bar{\rho}$ and σ yields the phase diagram Fig. 3(a). Note again, that our stability analysis and the resulting phase diagram Fig. 3(a) is independent of curvature and also valid for the well-studied system of propelled particles without curvature [10, 12, 13]. Hence, Fig. 3(a) shows that the Boltzmann approach is capable of reproducing phases of all states observed in [12, 14] including a transition from travelling wave patterns to global homogeneous order.

NUMERICAL SOLUTION OF THE BOLTZMANN EQUATION WITH SNAKE

In order to study the resulting steady states in the regime where our linear stability analysis predicts inhomogeneities, we numerically solved the generalized Boltzmann equation, Eq. (1). To this end we employed the SNAKE algorithm as introduced in Ref. [15]. As tesselations we used a quadratic periodic regular lattice with equally sized angular slices. Circling propulsion was included by rotating the angular distribution of each lattice site with a frequency $v_0\kappa_0$ in addition to the straight convection steps. The system was initialized with a disordered state with small random density fluctuations around the mean density $\bar{\rho} = A^{-1}\int_A \rho(\mathbf{r}, t)$. Changing κ_0 did not change the observed patterns qualitatively. In the limiting case of very small κ, we observed traveling wave patterns as reported in Refs. [12, 14, 15]. For Fig. 3(c), Movie 6, and Movie 7 we used a lattice of of 200×200 grid points with lattice field size 2 and angular disretization of 24 angular slices; hence, $A = 400 \times 400 = 160000$. In the swirl phase the swirl size grows for growing $\bar{\rho} - \rho_c$ whereas the radius of a swirl's motion stays at approximately κ_0^{-1}. Fig. S4 shows the parameter

values of $\bar{\rho}$ and σ where the SNAKE algorithm exhibits steady swirl patterns together with the phase diagram obtained from the adapted mode truncation scheme.

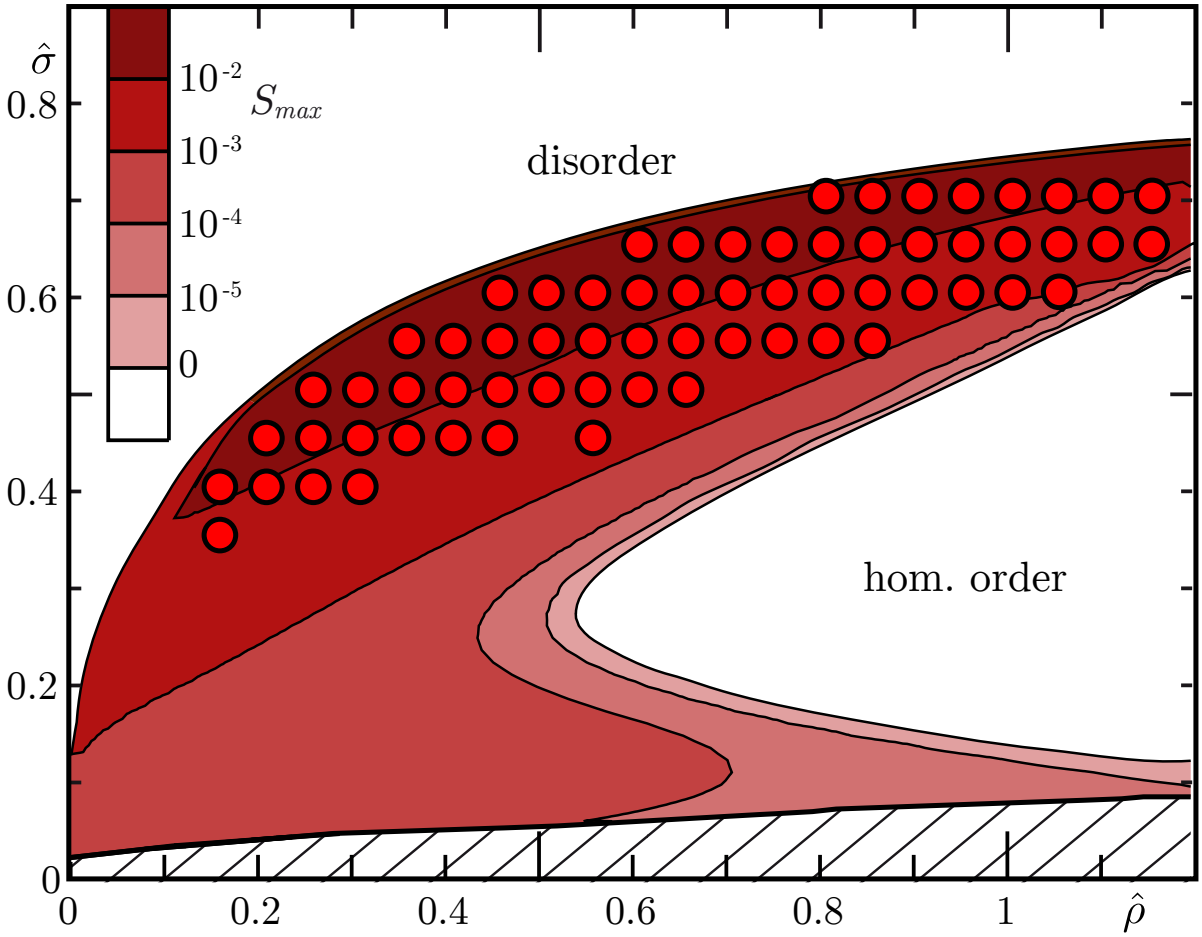

FIG. S4. Overlay of the parameter values where the SNAKE algorithm exhibits steady swirl patterns (red dots) together with the phase diagram obtained from the adapted mode truncation scheme (with $k_{\max} = 50$). In the shaded region, neglected Fourier modes become important.

REMARK ON THE SHAPE OF THE PHASE CURVES

When comparing the transition to order in the phase diagrams 2 and S4 it should be noted that our particle-based and continuum approaches are distinct in the following features: polymer fluctuations vs. effective diffusion, multi-particle collisions vs. binary alignment, extended polymers vs. point particles. The functional form of $\rho_c(\sigma)$ (S10) depends on the

choice of diffusion and collision noise (e.g. equally Gaussian distributed). In contrast, the form of the transition line in our Brownian dynamics simulations depends on the choice of the phenomenological criteria (*disordered states* for $d_{cc}^{min} \approx 2R_0$, *vortex states* for $d_{cc}^{min} > 2R_0$ and *train states* without d_{cc}^{min}). These differences result in different shapes of the phase boundaries. In addition, the observed patterns in the vortex phase are distinct. While for our particle-based model we find closed, rotating rings, dense, rotating swirls are observed in the continuum model (Fig. 2(b) and Fig. 3(d)). These differences are interesting and should be considered as part of the results we obtained. For example, these differences will guide future model building for specific models, e.g. the dynamics of FtsZ, as they emphasise what molecular details need to be accounted for. For the discussion of this work, however, our emphasis was on the topology of the phase diagram (similar trend of the onset to order) and the fact that in both models one finds a vortex phase.

MOVIE DESCRIPTIONS

Movie1.mp4: Brownian dynamics simulation of a system with $M = 10$ polymers with $v_0 = 5, k_BT = 1$ and hence $\rho = 0.069$, $\sigma = 0.247$.

Movie2.mp4: Brownian dynamics simulation of a system with $M = 80$ polymers with $v_0 = 5, k_BT = 1$ and hence $\rho = 0.556$, $\sigma = 0.247$.

Movie3.mp4: Brownian dynamics simulation of a system with $M = 200$ polymers with $v_0 = 5, k_BT = 1$ and hence $\rho = 1.389$, $\sigma = 0.247$.

Movie4.mp4: Brownian dynamics simulation with parameters as in Movie 3, except for a changed curvature angle $\theta_0 = 0.333$, resulting in an polymer arc angle $L\kappa_0 = 3$.

Movie5.mp4: Brownian dynamics simulation with parameters as in Movie 3, except for a changed contour length $L = 6$, resulting in an polymer arc angle $L\kappa_0 = 1.2$.

Movie6.mp4: SNAKE solution for $\bar{\rho} = 0.2$ and $\sigma = 0.45$ with $\kappa_0 = 0.1$. The colour code denotes the local density $\rho/\bar{\rho}$. The orientation and length of the arrows indicates the orientation and amplitude of the local particle current.

Movie7.mp4: SNAKE solution for $\bar{\rho} = 0.75$ and $\sigma = 0.2$ with $\kappa_0 = 0.1$. The colour code denotes the local density $\rho/\bar{\rho}$. The orientation and length of the arrows indicates the orientation and amplitude of the local particle current.

Hydroswirl.mp4: Preliminary results of the explicit integration [16] of the hydrody-

namic Eqs. (S9). The video shows the time evolution of the density field $\rho(\mathbf{r}, t)$, for parameters close above threshold $\bar{\rho} > \rho_c$. The system size is $A = 80 \times 80 = 640$, $\bar{\rho} = 0.5$, $\sigma = 0.6$, and $R_0 = 5$.

---

* frey@lmu.de

[1] M. Loose and T. J. Mitchison, Nat. Cell Biol. **16**, 38 (2013).

[2] G. Chirico and J. Langowski, Biopolymers **34**, 415 (1994).

[3] H. Wada and R. R. Netz, Europhys. Lett. **77**, 68001 (2007).

[4] R. E. Goldstein and S. A. Langer, Phys. Rev. Lett. **75**, 1094 (1995).

[5] M. Hinczewski, X. Schlagberger, M. Rubinstein, O. Krichevsky, and R. R. Netz, Macromol. **42**, 860 (2009).

[6] C. Bennemann, J. Baschnagel, W. Paul, and K. Binder, Comput. Theor. Polym. Sci. **9**, 217 (1999).

[7] P. Kloeden and E. Platen, *Numerical Solution of Stochastic Differential Equations* (Springer, Berlin, 1992).

[8] J. K. G. Dhont, *An Introduction to Dynamics of Colloids* (Elsevier, Amsterdam, 1996).

[9] X. Lu and Y. Hu, *Molecular Thermodynamics of Complex Systems* (Springer, Heidelberg, 2008).

[10] E. Bertin, M. Droz, and G. Grégoire, J. Phys. A-Math. Theor. **42**, 445001 (2009).

[11] A. Peshkov, E. Bertin, F. Ginelli, and H. Chaté, Eur. Phys. J.-Spec. Top. **223**, 1315 (2014).

[12] H. Chaté, F. Ginelli, G. Grégoire, F. Peruani, and F. Raynaud, Eur. Phys. J. B **64**, 451 (2008).

[13] T. Ihle, Phys. Rev. E **83**, 030901 (2011).

[14] H. Chaté, F. Ginelli, G. Grégoire, and F. Raynaud, Phys. Rev. E **77**, 046113 (2008).

[15] F. Thüroff, C. A. Weber, and E. Frey, Phys. Rev. X **4**, 041030 (2014).

[16] In preparation.

II.3 Coexisting symmetries in active matter systems

In section II.1 we discussed theoretical approaches to systems of self-propelled agents and more general active matter systems that have been successful in reproducing various phenomena observed in nature such as flocking. Any theory for systems of propelled agents has to be based on assumptions on the agents' propulsion as well as their interactions. For instance, flocking can occur when agents align their propulsion direction upon interaction [36]. As an essential common result in active matter theories, aligning interactions between agents, even when short-ranged, can lead to the formation of macroscopic order in the agents' orientations [35–37]. Furthermore, close to the onset to macroscopic order the system can undergo phase separation. Here, agents form high-density clusters separated by a disordered background rather than being uniformly distributed. The symmetry of the macroscopic order and the emergent patterns is typically dictated *a priori* by the assumed symmetry of the used model: interactions with polar symmetry can lead to propagating high-density waves [99, 100, 124](fig. II.3(a)) while interactions with nematic symmetry can lead to bands (lanes) within which the agents' orientations are (preferentially) parallel [101, 102, 130] (fig. II.3(a)). In the above example of systems of curved, propelled polymers (section II.2) we saw that interactions with polar symmetry can lead to circling flocks with polar order. Thus, the (polar) interaction symmetry as well as the rotational symmetry of the polymer propulsion was retained.

The direct manifestation of *ad hoc* symmetry assumptions in the emergent order and patterns highlights their critical role in constructing active matter theories that should be predictive and insightful for observations in nature and experiments. However, for most active systems in nature or even in the laboratory, the microscopic details of propulsion and interactions are hardly accessible. Even more, these details might not even be fixed by external parameters but could in principle depend critically on the emergent dynamics of the agents. This raises the question: what if a symmetry on the microscopic scale not only results in macroscopic patterns, but if these patterns can in turn feed back into the system's symmetries?

Indeed, there are examples in nature which show such mutual feedback between collective effects and the characteristics of individuals. For instance, upon crowding, the desert locust switches from a solitorious to a gregarious state which in turn affects its collective swarming behaviour [84, 86, 137](fig. II.1(a)). A feeback between different collective properties has also been observed recently by Huber et al. [3]. Here, the authors were able to reconstitute an actomyosin motility assay that promotes patterns of polar as well as nematic symmetry. Interestingly, these patterns can coexist and single agents (actin filaments) switch between clusters of different symmetry (compare fig. II.1(g)). The authors concluded that the symmetry of the resulting patterns is not determined *a priori* but is itself an emergent dynamic

property of the system. Previous studies with mixed alignment interactions assumed different interaction symmetries depending on particle distance [133], chance [134] or particle species [132]. Although these models display patterns of polar or nematic symmetry wherever polar or nematic interactions dominate, respectively, a transition between patterns of different symmetries as in [3] has not yet been studied nor reported.

Motivated by the experimental as well as numerical observations in [3], we propose a model based on a kinetic Boltzmann approach where particles undergo binary interactions that lead to nematic alignment with a small (tunable) polar bias. Whereas for a very small or large polar bias this model recovers the well-studied scenarios of a respectively nematic or polar interaction symmetry, for a moderate polar bias this model predicts a transition from nematic order at intermediate densities to polar order at high densities. Close to this transition, we find that in the density regime of nematic order the system organizes into high-density nematic bands that can induce polar patterns. This polar instability can eventually lead to an alternating dominance between nematic bands and polar wave patterns.

Our study suggests that the transition between nematic and polar patterns can be understood in terms of the stability of local steady states in phase space. We further argue that transitions between patterns are generic for systems where the particle density acts as bifurcation parameter. We consolidate this hypothesis by simple hydrodynamic equations that yield a qualitatively similar phase diagram as our original kinetic Boltzmann approach and that are able to reproduce the complete phenomenology of experiments and simulations presented in [3] including coexistence and cycling between nematic lanes and polar waves.

Our study reveals an interesting mutual feedback between pattern formation and symmetry. This feedback occurs because the particle density, which is prone to form patterns in active systems, is itself a critical parameter for the interaction symmetry. In particular, the resulting feedback classifies the symmetry of interactions itself as an emergent and dynamic property of the system.

II.3.1 The kinetic Boltzmann equation for a collision rule with mixed symmetries

The kinetic Boltmann equation describes the orientational particle distribution function of self-propelled particles that undergo binary collision [127]. For an imposed polar or nematic (binary) interaction rule, it predicts a transition from disorder to respectively global polar or nematic order for high densities or low noise. As detailed in section II.1, close to the onset of order it qualitatively reproduces the formation of patterns as observed in various experiments as well as numerical simulations. Although the binary interaction rules that promotes order in the kinetic Boltzmann approach might quantitatively deviate from the collision

statistics observed in experiments and simulations (most likely since it neglects multi-particle collisions [138, 139]), the kinetic Boltzmann equation thus serves as a useful basis to qualitatively study systems of self-propelled paricles.

Previous studies that used the kinetic Boltzmann approach for propelled particles exclusively assumed an either fully polar [123, 124] or nematic [128] alignment rule, resulting in the formation of respectively polar or nematic order.[1] On the basis of binary collision statistics, Huber et al. [3] suggest that while nematic collisions can yield nematic lane patterns, already a small polar bias in the collision statistics can lead to polar clusters. In the framework of the kinetic Boltzmann approach, a fully nematic interaction rule means that particles colliding at an acute angle assume their average orientation (polar alignment) while particles colliding at an obtuse angle also align, but with opposite orientations (antipolar alignment) (fig. II.3(a)). To qualitatively incorporate nematic interactions with a polar bias into the kinetic Boltzmann approach, we propose an interaction rule, where alignment is polar even when the colliding particles form an angle slightly larger than $\pi/2$ (fig. II.3(b)). In the following, we will discuss the consequences of this adapted interaction rule on the formation of order and in particular patterns in a two dimensional system.

II.3.1a Phase diagram

Following a kinetic Boltzmann approach [22, 124, 127] we decribe the dynamics of particles in terms of the orientational one-particle distribution function $f(\mathbf{r}, \theta, t)$ with $\mathbf{r} \in \mathbb{R}^2$, $\theta \in [0, 2\pi)$, where $f(\mathbf{r}, \theta, t)\mathrm{d}\mathbf{r}\mathrm{d}\theta$ gives the number of particles in the phase-space element $\mathrm{d}\mathbf{r}\mathrm{d}\theta$. We assume spherical particles with diameter d that move along their orientations θ at constant speed v_0 and can change their orientation by diffusion as well as by local binary interactions. Diffusion is modeled by a shift in a particle's orientation at a rate λ from θ to $\theta + \eta$, where we assume η to be Gaussian distributed with standard deviation σ. Binary collisions change the colliding particles' propulsion direction according to the proposed mixed collision rule (fig. II.3(b)), where we also allow a Gaussian distributed fluctuation. For simplicity, for collisional noise we take the same standard deviation σ as for diffusion. The kinetic Boltzmann equation for $f(\mathbf{r}, \theta, t)$ then reads

$$\partial_t f(\mathbf{r}, \theta, t) + v_0 \mathbf{e}(\theta) \cdot \partial_{\mathbf{r}} f(\mathbf{r}, \theta, t) = \mathcal{I}_d[f] + \mathcal{I}_c[f, f]\,, \tag{II.1}$$

1 In following, we focus on systems of propelled polar particles and exclude systems of apolar particles [140, 141] and polar particles with instantaneous orientational reversal[131].

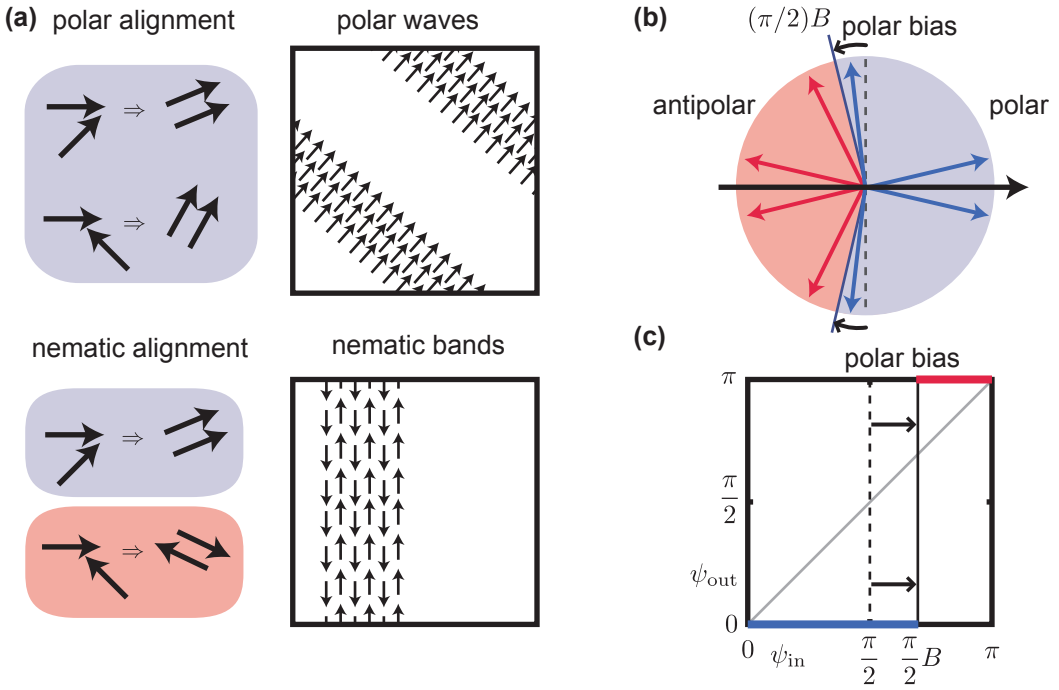

Figure II.3 Extension of previous polar and nematic alignment rules to a mixed alignment rule. **(a)** Particles with fully polar collisions align their velocities irrespective of their intermediate angle. In the case of nematic collisions, particles align or antialign their velocities depending on whether their intermediate alignment is acute or obtuse, respectively. Close to the onset of order, the kinetic Boltzmann equations predicts either polar waves [123, 126] or nematic bands (lanes) [128] depending on the collision symmetry (snapshots of polar waves and nematic bands are only meant for illustration of typical structures of patterns). **(b)** We propose a nematic collision rule with variable polar bias B, where polar alignment occurs also for obtuse intermediate angles. More specifically, colliding particles align polar when their velocities form an intermediate angle $\psi_{in} < (\pi/2)B$ with $B \in [1, 2]$ and align antipolar otherwise. The black arrow indicates the pre-collision orientation of the particle of reference. Alignment with a second particle is polar if the orientation of the second particle lies in the blue shaded angular range, whereas alignment is antipolar in the red shaded angular range. Blue and red arrows show example orientations of incoming particles that lead to respectively polar and antipolar alignment with the reference particle. **(c)** Illustration of the 'collision statistics' for the imposed binary collision rule. Polar alignment occurs for intermediate angles $\psi_{in} < (\pi/2)B$ and antipolar alignment otherwise. ψ_{out} denotes the intermediate angle between the particles' propulsion direction after the collision. The gray line indicates the neutral case without aligning collisions, i.e. when $\psi_{out} = \psi_{in}$.

where $\mathcal{I}_d$ and $\mathcal{I}_c$ denote the diffusion and collision integrals, respectively:

$$\mathcal{I}_d[f] = -\lambda f(\theta) + \lambda \int_{-\pi}^{\pi} \mathrm{d}\theta' \int_{-\infty}^{\infty} \mathrm{d}\eta\ f(\theta')\, P_\sigma(\eta) \delta_{2\pi}(\theta' - \theta + \eta)\,,$$

$$\mathcal{I}_c[f] = -f(\theta) \int_{-\pi}^{\pi} \mathrm{d}\theta'\ \mathcal{R}(\theta, \theta')\, f(\theta') + \int_{-\pi}^{\pi} \mathrm{d}\theta_1\ f(\theta_1) \int_{-\pi}^{\pi} \mathrm{d}\theta_2$$
$$\times\, \mathcal{R}(\theta_1, \theta_2) f(\theta_2) \int_{-\infty}^{\infty} \mathrm{d}\eta\ P_\sigma(\eta)\ \Psi_\eta(\theta_1, \theta_2, \theta)\,. \tag{II.2}$$

$P_\sigma(\eta)$ is a Gaussian distribution with standard variation σ and $\delta_{2\pi}$ is a generalized Kronecker delta, imposing that the argument is zero modulo 2π. $\mathcal{R}(\theta_1, \theta_2)$ denotes the differential cross section of two particles with orientations θ_1 and θ_2 and is given by $\mathcal{R}(\theta_1, \theta_2) = 4 v_0 d \sin(\frac{\theta_1 - \theta_2}{2})$ [124]. The binary interaction rule enters in the function $\Psi(\theta_1, \theta_2, \theta)$:

For polar alignment:

$$\Psi_\eta(\theta_1, \theta_2, \theta) = \delta_{2\pi}(\frac{\theta_1 - \theta_2}{2} - \theta + \eta)$$

For antipolar alignment:

$$\Psi_\eta(\theta_1, \theta_2, \theta) = \frac{1}{2}\delta_{2\pi}\left(\frac{\theta_1 - \theta_2}{2} - \theta + \frac{\pi}{2} + \eta\right) + \frac{1}{2}\delta_{2\pi}\left(\frac{\theta_1 - \theta_2}{2} - \theta - \frac{\pi}{2} + \eta\right)$$

For an interaction rule with variable polar bias, we assume polar alignment for an intermediate angle with $|(\theta_1 - \theta_2)| < (\pi/2)\, B$ and antipolar alignment otherwise (fig. II.3(b)). The parameter $B \in [1, 2]$ thus characterizes the strength of the polar bias, where for $B = 1$ and $B = 2$ the collision rule reduces to fully nematic or polar collisions, respectively.

In the following, we rescale time, space, and density such that $v_0 = \lambda = d = 1$. Then, the only remaining free parameters are the noise amplitude σ, the polar bias B, and the mean particle density $\bar{\rho} = A^{-1} \int_A \mathrm{d}\mathbf{r} \int_{-\pi}^{\pi} \mathrm{d}\theta\, f(\mathbf{r}, \theta, t)$ measured in units of $\lambda/(d v_0)$, i.e., the number of particles found within the area traversed by a particle between successive diffusion events. In order to study solutions of the the kinetic Boltzmann equation (II.1), we expand this equation for f in terms of

Fourier modes of the angular variable given by

$$f_k(\mathbf{r},t) = \int_{-\pi}^{\pi} \mathrm{d}\theta \; \mathrm{e}^{\mathrm{i}\theta k} f(\mathbf{r},\theta,t)\,. \tag{II.3}$$

The dynamics of $f_k(\mathbf{r},t)$ is then given by (also see [124] and II.2)

$$\begin{aligned} \partial_t f_k + \frac{v_0}{2}\left[\partial_x(f_{k+1}+f_{k-1}) - \mathrm{i}\partial_y(f_{k+1}-f_{k-1})\right] = \\ = -\lambda(1-\mathrm{e}^{-(k\sigma)^2/2})f_k + \sum_{n=-\infty}^{\infty} \mathcal{I}^B_{n,k} f_n f_{k-n}\,, \end{aligned} \tag{II.4}$$

where the collision integral has contributions coming from polar and antipolar alignment depending on the polar bias B:

$$\begin{aligned} \mathcal{I}^B_{n,k} = & \underbrace{\int_{-\frac{\pi}{2}B}^{\frac{\pi}{2}B} \frac{\mathrm{d}\Delta}{2\pi}\,\mathcal{R}(|\Delta|)\left[\mathrm{e}^{-(k\sigma)^2/2}\cos(\Delta(n-\frac{k}{2}) - \cos(\Delta n)\right]}_{\rightsquigarrow\text{polar alignment}} \\ & + \underbrace{\int_{\frac{\pi}{2}B}^{2\pi-\frac{\pi}{2}B} \frac{\mathrm{d}\Delta}{2\pi}\,\mathcal{R}(|\Delta|)\left[\mathrm{e}^{-(k\sigma)^2/2}\cos(\frac{k\pi}{2})\cos(\Delta(n-k\omega) - \cos(\Delta n)\right]}_{\rightsquigarrow\text{antipolar alignment}} \end{aligned} \tag{II.5}$$

By inspection of (II.3), the mode f_0 is the local density $\rho(\mathbf{r},t) := f_0(\mathbf{r},t)$ while f_1 and f_2 yield the polar order $\mathbf{P}(\mathbf{r},t)$ and the nematic tensor $Q(\mathbf{r},t)$ according to

$$\rho\mathbf{P} = \begin{pmatrix} \mathrm{Re}[f_1] \\ \mathrm{Im}[f_1] \end{pmatrix}, \qquad \rho\mathbf{Q} = \frac{1}{2}\begin{pmatrix} \mathrm{Re}[f_2] & \mathrm{Im}[f_2] \\ \mathrm{Im}[f_2] & -\mathrm{Re}[f_2] \end{pmatrix}. \tag{II.6}$$

To simplify notation, we will often also refer to f_1 and f_2 as polar and nematic order fields, respectively. Setting $k=0$ yields the continuity equation $\partial_t\rho(\mathbf{r},t) = -v_0\nabla\cdot(\rho\mathbf{P})$.

Homogeneous solutions and linear stability analysis

Since $\mathcal{I}_{n,0} = 0 \,\forall n$, equation II.1 posseses a homogeneous disordered solution with density $\bar{\rho} = f_0$ and $f_k = 0$ for $k \neq 0$. Up to linear order, a small perturbation δf_k of this disordered state evolves according to $\partial_t \delta f_k(t) = \mu_k(\bar{\rho}, \sigma, B)\delta f_k$ where $\mu_k(\bar{\rho}, \sigma, B) = (\mathcal{I}^B_{0,k} + \mathcal{I}^B_{k,k})\bar{\rho} - \lambda(1 - \mathrm{e}^{-(k\sigma)^2/2})$. This defines a critical density $\rho^c_k(\sigma, B)$ at $\mu_k(\rho^c_k, \sigma, B) = 0$ above which f_k grows exponentially. All following calculations based on linear stability analyses were performed numerically using `Wolfram Mathematica 11` [74].

We find that for vanishing and small polar bias (i.e. $B \gtrsim 1$) there is a critical density $\rho^c_2(\sigma, B)$ above which f_2 and thus nematic order grows. For large polar bias, there is a critical density $\rho^c_1(\sigma, B)$ above which f_1 and thus polar order starts to grow. In principle, these transition densities also depend on the noise value σ; however, we fix σ in the following and focus on a variable polar bias B and global density $\bar{\rho}$. To be precise, we set $\sigma = 0.2$ in the following. For this choice of σ, we find that for intermediate polar bias the critical densities for nematic and polar order cross, meaning that beyond that crossing point the disordered state is unstable against both polar and nematic perturbations (fig. II.4(a), red and blue lines denote $\rho^c_2(B)$ and $\rho^c_1(B)$, respectively).[2]

Beyond a transition to polar or nematic order, solutions of equation (II.4) are no longer analytically accessible due to the infinite sum, which couples the modes f_k for inifinitely large k. Nevertheless, close above the transition to order it is reasonable to assume that modes with very large $|k|$ are still negligible [22, 124]. To progress, we follow [22] and include only modes up to a certain cutoff k_c and neglect all modes f_k with $k > k_c$ in equation (II.4). We then numerically calculate the homogeneous solutions of this truncated equation for varying global densities $\bar{\rho}$ and polar bias B.

Above the critical transition densities $\rho^c_2(B)$ and $\rho^c_1(B)$, we find solutions with nonzero nematic and polar order, respectively. Figure II.4(a) indicates linearly stable solutions of the truncated equation (II.4) for $k_c = 10$. Interestingly, polar order is not limited to a regime beyond $\rho^c_1(B)$ but is even present beyond $\rho^c_2(B)$ when the polar bias and the global density are high enough (e.g. $B = 1.2$, $\bar{\rho} = 0.4$). Hence, in this parameter regime of moderate polar bias and high global density, we find a direct transition between nematic and polar order (blue dashed line in fig. II.4(a)). Furthermore, our analysis also reveals stable solutions with nonzero polar order below the transition densities where also the disordered state is linearly stable. Notably, we find that the bifurcation from a disorder state to a state with homogeneous polar order is subcritical, as opposed to the usually assumed supercritical bifurcation in standard hydrodynamic active models [110, 124]. While

2 We remark, that the intersection point between the transition densities moves to larger $\bar{\rho}$ when increasing σ. For too large σ the transition densities no longer cross.

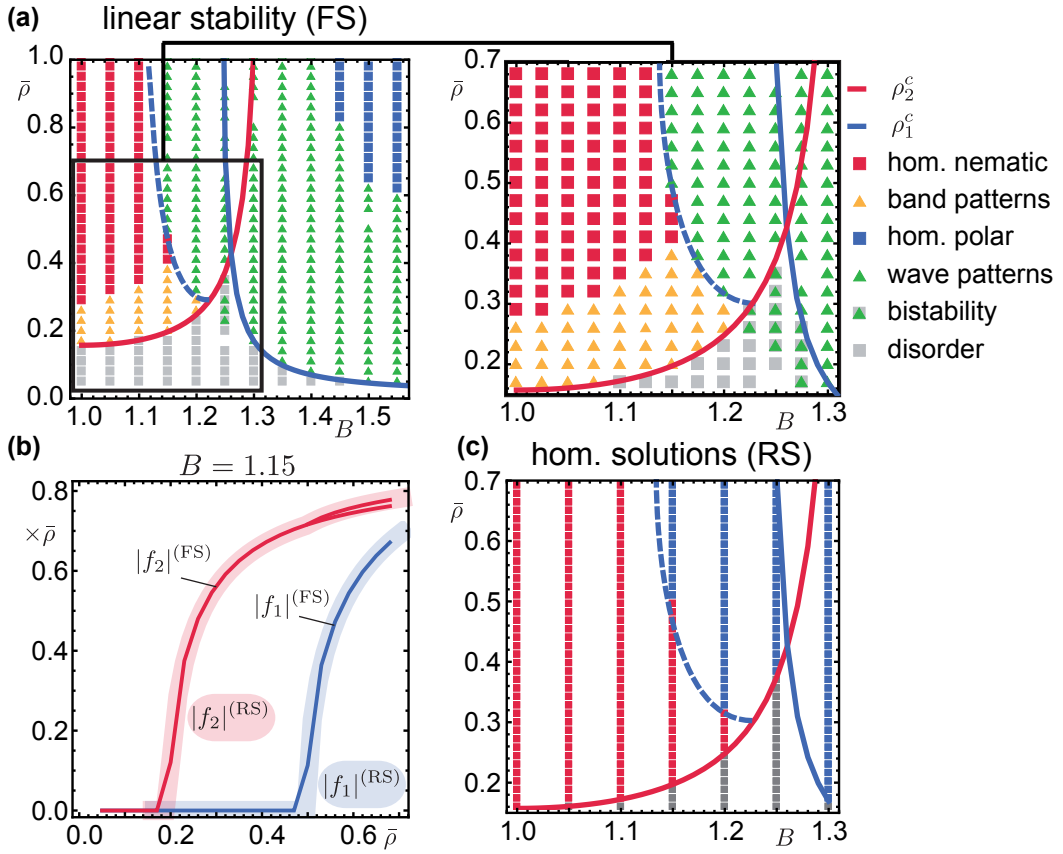

Figure II.4 Macroscopic order and linear stability as a function of the global density $\bar{\rho}$ and polar bias B. **(a)** Regimes of macroscopic order for equation II.4 in angular Fourier space (FS) with a truncation at $k_c = 10$. Squares denote stable solutions, triangles indicate solutions that are unstable against spatial perturbations. **(b)** Homogeneous solutions for f_1 and f_2 at $B = 1.15$ calculated from the truncated Boltzmann equation in angular Fourier space (FS, solid lines) as compared to homogeneous solutions of the Boltzmann equation in real space (eq. (II.1)) calculated with the generalized `SNAKE` algorithm (RS, shaded lines). Above the onset of polar order, our analysis in Fourier space reveals two homogeneous solutions for f_2 where only the one with larger $|f_2|$ is linearly stable. This is consistent with the solution in real space, where the `SNAKE` algorithm approaches the solution with higher $|f_2|$. **(c)** Phase diagram of homogeneous solutions using the generalized `SNAKE` algorithm. Simulations where done with a single lattice point starting at a disordered state with small fluctuations in the angular distribution. Both (a) and (c) reproduce the critical transition densities ρ_2^c and ρ_1^c to nematic and polar order indicated by red and blue solid lines, respectively. Furthermore, both phase portraits display a transition from nematic order to polar order at intermediate polar bias in very good quantitative agreement (blue dashed line serves as guide to the eye). The noise value has been fixed to $\sigma = 0.2$.

this bistability is certainly interesting for hysteresis effects close to the transition density, we will not investigate it further here and instead focus on the cases where the disordered state is linearly unstable and the system self-organizes into ordered states.

To investigate pattern formation, we calculated the linear stability of the homogeneous solutions against wave-like perturbations $\delta f_k(\mathbf{r}, t)$ by employing the spatial Fourier transforms

$$f_k(\mathbf{q}, t) = \int_{-\infty}^{\infty} \mathrm{d}\mathbf{r}\ \mathrm{e}^{-\mathrm{i}\mathbf{q}\cdot\mathbf{r}}\, f_k(\mathbf{r}, t)\,. \tag{II.7}$$

Previous studies suggest that polar traveling wave solutions are indicated by an instability of polar order against predominantly longitudinal perturbations [123, 124]. Similarly, nematic band solutions base on an instability against predominantly transversal perturbations [128]. We therefore focused on spatial perturbations $f_k(\mathbf{q}, t)$ with $\mathbf{q}$ parallel or perpendicular to the homogeneous order. Within the regimes of nonzero nematic or polar order, we find subregimes in which the growth rate of spatial perturbations is positive, indicating the formation of spatial patterns (triangles in fig. II.4(a)). In particular, we find a Turing instability, i.e. we find positive growth rates only for spatial perturbations with finite $|\mathbf{q}|$. Close above the transition density to nematic order, $\rho_2^c(B)$, homogeneous nematic order is unstable against spatial perturbations perpendicular to the nematic order, which suggests formation of nematic band patterns. On the other hand, in a regime above the transition to polar order (both above $\rho_2^c(B)$ as well as above the direct nematic-polar order transition), homogeneous polar order is unstable against spatial perturbations parallel to the orientation of polar order, which suggests the emergence of polar waves. The prediction of nematic bands and polar waves for small and large polar bias is in line with previous studies on systems with either dominantly nematic or polar interaction symmetries, respectively [36, 37]. Interestingly, our linear stability analysis suggests an additional transition from nematic band patterns to polar wave patterns when increasing the particle density at intermediate polar bias (e.g. $B = 1.2$ in fig. II.4(a)). In the following, we will focus on the parameter regime centered around the nematic-polar order transition (fig. II.4(a), right).

Alternatively to our linear stability analysis based on equation II.4, we studied the existence of steady states with nonzero order by solving equation (II.1) numerically in real space. To this end, we employed a modified version of the `SNAKE` algorithm [126], where we included a nematic collision rule with variable polar bias. The solutions of a system without spatial extension are depicted in figure II.4(b,c). The homogeneous solutions agree very well with the solutions of the truncated Boltzmann equation in

angular Fourier space. We will discuss the solutions for a spatially extended system in the next section.

All of the transitions shown in figure II.4(a) are in agreement with a previous study, where Ngo et al. [134] studied a mixed interaction rule using Vicsek-style agent-based simulations. Here, with probability s, particles align their propulsion directions with the average propulsion direction of nearby particles within an interaction distance. With probability $1 - s$, the alignment is antipolar. Our phase diagram (fig. II.4(a)) predicts all regimes of nematic as well as polar order including polar and nematic patterns present in the numeric phase portrait of [134].

II.3.1b Pattern formation and dynamic transitions

To find nonlinear solutions of the kinetic Boltzmann equation (II.1) especially in regimes where homogeneous solutions are unstable, we employ a modified version of the SNAKE algorithm [126] for a spatially extended system and performed extensive parameter sweeps in the global density and polar bias. The numerical solutions are summarized in figure II.5(a).

Our numerical simulations confirm an instability of the disorded state beyond the transition densities $\rho_2^c(B)$ and $\rho_1^c(B)$, which mark the onset of nematic and polar order, repectively. For vanishing and small polar bias, our numerical simulations approach nematic band solutions close above the transition density $\rho_2^c(B)$ (fig. II.5(b)). For larger densities, nematic bands are replaced by homogeneous nematic states consistent with previous theoretical studies on systems with purely nematic collision symmetry [99, 102, 128]. For larger polar bias and above the transition density to polar order $\rho_1^c(B)$, we find traveling wave solutions (fig. II.5(c)) as predicted by our linear stability analysis. Increasing the polar bias even further, the traveling waves close at onset (i.e. at $\bar{\rho} \gtrsim \rho_2^1$) are replaced by homogeneous polar ordered states, consistent with previous numerical solution of the kinetic Boltzmann equation with purely polar alignment [126].

We also find homogeneous solutions where linear stability predicts patterns (compare shaded regions in fig. II.5 with simulation results). In fact, in section II.2 [22] we already observed that for purely polar alignment, the predicted regime of patterns in the kinetic Boltzmann equation spreads far into the polar ordered regime, although the SNAKE algorithm only shows patterns close to the onset density. As in section II.2, we argue that this discrepancy arises from spurious noise in the Euler forward scheme of our implementation resulting in numeric diffusion.

Remarkably, for moderate polar bias we find a regime of polar patterns (gray hatched region in fig. II.5(a)) even below the nematic-polar order transition predicted by linear stability (blue dashed line in fig. II.5(a)). Here, a closer look at the formation of patterns reveals a dynamic transition between patterns of nematic and polar symmetry (fig. II.6). A typical temporal evolution of this pattern transition

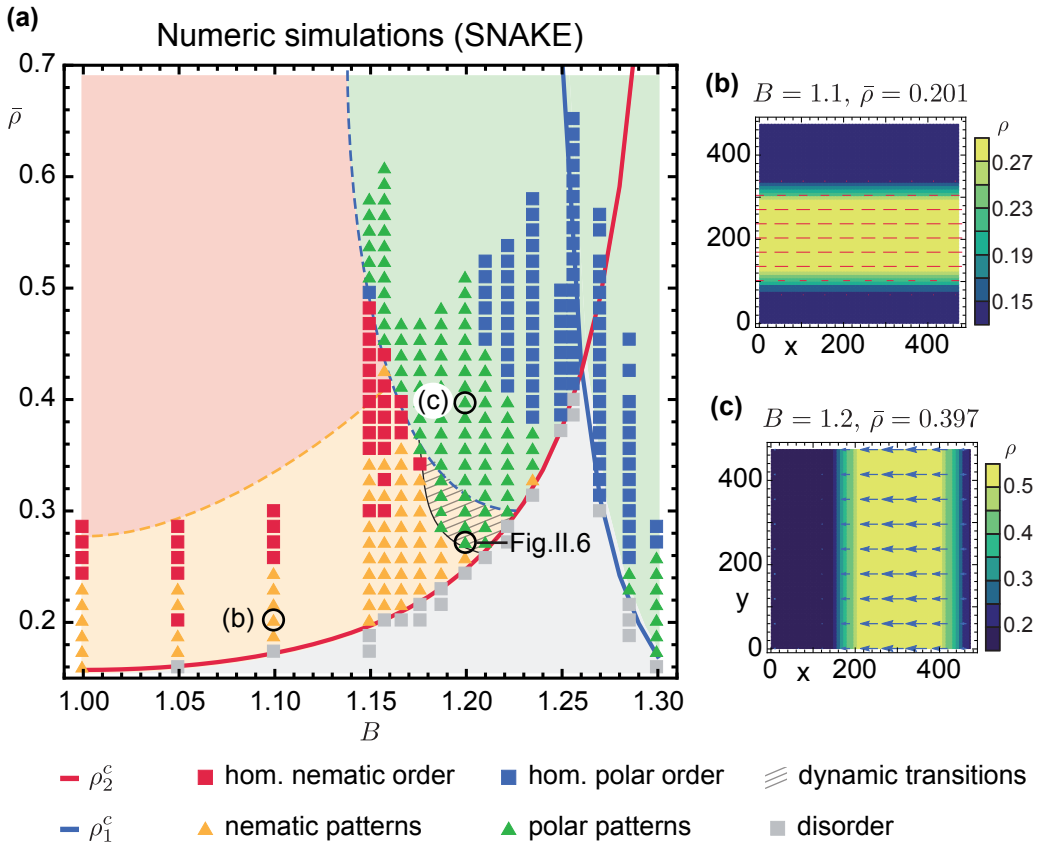

Figure II.5 Numerical solutions of the kinetic Boltzmann equation (eq. (II.1)). (a) Our simulations display regimes of homogeneous nematic and polar order as well as nematic band patterns and traveling wave solutions. Shaded regions indicate regimes in which our linear stability analysis (fig. II.4(a), see section II.3.1a) predicts nematic homogeneous order (red), band patterns (orange), wave patterns (green) and disorder (gray). The gray hatched region highlights a regime of dynamic transitions from nematic to polar patterns. **(b)** Snaphot of a nematic band pattern. Red bars indicate the orientation and strength of local nematic order. **(c)** Snaphot of a polar traveling wave. Blue arrows indicate the strength and direction of local polar order. All simulations started at a homogeneous disordered state with small random fluctuations. Regarding the discretization scheme presented in [126], we employed $\epsilon_x = 8$, $\tau = 0.4$ and an angular discretization between 60 and 80 angular slices to acount for different values of polar bias.

is shown in figure II.6. Starting at a disordered state, the nematic order grows quickly and the system approaches a high-density nematic band pattern (fig. II.6(a), $t = 9000$) in line with our linear stability analysis. While the average nematic order in the system is roughly given by the solution for the homogeneous system, the local nematic order is very high within the high-density bands and approaches zero in the disordered low-density regions between the bands. In particular, the local densities within a band exceed by far the density of the nematic-polar order transition. This suggests that within a band, purely nematic order is unstable and polar order starts to grow. Indeed, we observe that after some time, polar order locally builds up in the bands and can lead to polar waves that propagate along the nematic band (fig. II.6(a), $t = 13000$).

Depending on the initial conditions as well as the system size, we find that this instability can lead to different final patterns. In some cases, when initially two nematic bands form, typically the broader band undergoes a polar instabilty leading to a density wave traveling along this band (fig. II.6(a)). Subsequently, polar waves are also induced in the thinner band. However, the traveling waves do not replace the band pattern completely but can also decay again, leaving bands with dominant nematic order. This can result in the coexistence of one band with predominantly nematic order and another band with polar waves traveling along the band's orientation (compare fig. II.6(a) for $t = 13000$ and $t = 17000$). Over time, this leads to bands which show alternating predominantly nematic and polar order. The average nematic and polar order as well as the average spatial density variation of the system oscillate (fig. II.6(a),(b)). Here, the phase shift between oscillations in the average nematic and polar order is consistent with our notion of patterns with alternating symmetry (compare fig. II.6(a) for $t = 13000$ and $t = 17000$, where predominantly nematic and polar order alternates in the band patterns).

For different (random) initial conditions, the polar instability can also lead to a complete replacement of nematic bands by traveling polar waves (fig. II.6(c)). After an initial formation of nematic bands, which is accompanied by an increase of the average nematic order and the spatial density variation, a polar instability leads to a sudden increase of the average polar order to a value higher than the average nematic order. Together with the growth of polar order, the spatial density variation grows and saturates at a nonzero value. This indicates the presence of a steady traveling wave solution.

In some rare cases we also find a dynamic merging and splitting of nematic bands (fig. II.6(d)). Here, a nematic band with polar instability first decays into polar waves which themselves decay into two nematic bands that are much thinner than the original band. However, these bands are not stable but after some time merge to one broad nematic band again. In some simulations, this cycle is repeated

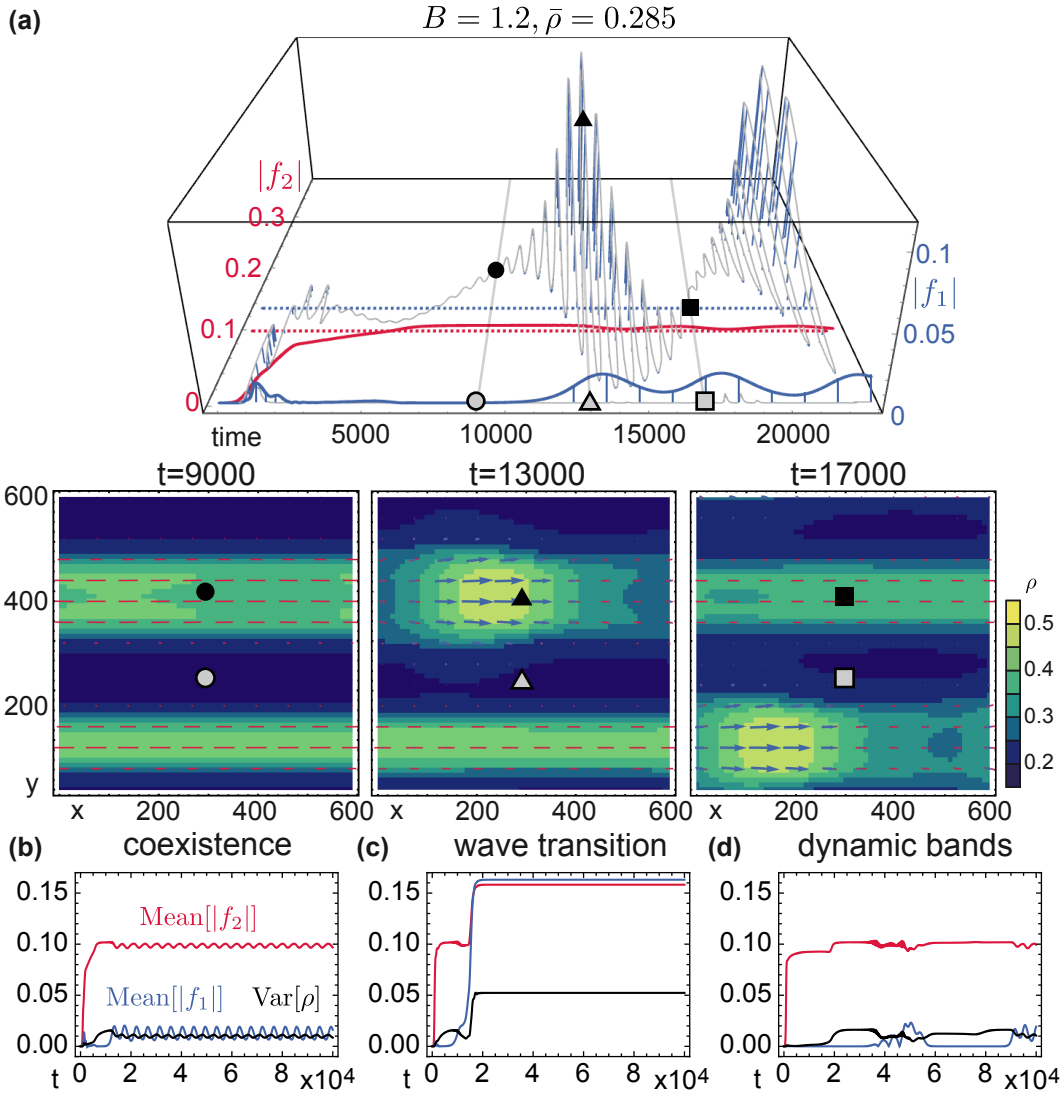

Figure II.6 Nematic patterns can induce polar instabilities.**(a)** Gray lines show the dynamics of two spatial points in the regime of nematic patterns. The position of these points is shown in the below snaphots. Different symbols in the top graph and the simulation snapshots (circles, triangles and squares) indicate different representative time points. Whereas the average nematic order (solid red line in top graph) approaches the homogeneous steady state value (red dashed line), the local order between the two points differ strongly. During nematic band formation (e.g. $t = 9000$) one point (gray circle) lies in the disordered region of zero nematic and polar order. The other point (black circle) lies in the high-density band. Here, nematic order rapidly grows and eventually exceeds the nematic-polar order transition (blue dashed line in top graph) predicted by linear stability analysis. Indeed, the polar order in the band rapidly increases (black triangle, $t = 13000$). Accordingly, the average polar order (solid blue line in top graph) grows. After some time, the local polar order in the band decays (black square, $t = 17000$) and the other nematic band experiences a polar instability. **(b)-(d)** Depending on initial conditions and system size, we find different final patterns. (b): coexisting polar waves and nematic patterns show an oscillating mean nematic order and polar order. (c): Nematic bands can also decay completely into traveling polar waves, (wave transition). (d): Dynamic splittings and rearrangments of bands (dynamic bands).

for several times. In a few simulations and for very small system sizes, we also find stable bands in which polar order does not grow during our simulation time.

In summary, our kinetic Boltzmann approach is consistent with the classical conception of systems of self-propelled particles with predominantly nematic or polar symmetry [36, 37]. In particular, we observe nematic band patterns and traveling polar waves at the onset of nematic and polar order, that are replaced by homogeneous nematic and polar order deeper in the ordered phase, respectively. In addition, we find novel interesting dynamics in a regime of moderate polar bias between the transition densities to nematic order and the transition density of polar order. Here, our numerical simulations reveal a dynamic transition from nematic bands to polar order. Supported by our analyses, this transition occurs, since in the density nematic bands can locally cross the transition density to polar order. This induces growth of polar order in the bands and can eventually lead to traveling wave solutions as well as more complex dynamics such as coexisting polar waves and nematic bands and dynamic rearrangements of bands. Our findings thus show that already for purely binary collisions, a mixed collision rule can lead to patterns whose symmetry is not evident from the assumed symmetries nor linear stabilities of homogeneous solutions. Instead, the symmetry of the emerging patterns can critically depend on the dynamics of the system. We argue that the symmetry of the system is thus itself an emergent property, whose dynamics is based on a mutual feedback between pattern formation and (local) symmetry breaking.

We note that the phenomenology of our phase diagram II.5 resembles the phenomenology observed in [3] (compare fig. II.1(g),(h)), including regimes of purely nematic and polar order as well as coexistence regimes. In contrast to our simulations in the coexistence regime, the dynamics in [3] include more irregular patterns such as highly bended nematic lanes and propagating waves that also cross, splay and rotate. These differences in the dynamics of our simulations vs. the simulations in [3] could in principle stem from a variety of differences in the underlying model assumptions such as binary vs. multiparticle interactions, disc-like particles vs. extended polymers and also different system sizes.

In the next part, we will investigate the emergent character of symmetries in pattern formation in a more general model based on coarse-grained hydrodynamic equations. First, we will discuss polar instabilities in previously derived hydrodyamic equations. As a next step, we explore the pattern phenomenology of these equations for more general coupling coefficients. By varying the coupling strength between the polar and nematic order fields, we show that these equations can reproduce the full phenomenology observed in [3].

II.3.2 Coexisting symmetries in active matter field equations

As discussed in section II.1, theoretical descriptions of active matter have been based on various lengthscales. Whereas flocking was first studied on a microscopic level using agent-based simulations [100, 142], hydrodynamic field theories [109, 110] have been proposed on the basis of symmetry arguments to study macroscopic features such as long-range order. The kinetic Boltzmann approach provides an interesting link between a microscopic conception of particle collisions and a more macroscopic description in terms of order fields. In particular, the kinetic Boltzmann equation has been useful as a starting point to derive hydrodynamic field equations for the dynamics close to the onset of order [127, 143]. Such field equations, which are much more feasible than the full kinetic Boltzmann equation, have been successful in reproducing a variety of observations in active systems close to the order transition [22, 124, 128–130].

II.3.2a Hydrodynamic equations based on the kinetic Boltzmann equation

In order to derive closed hydrodynamic equations from the kinetic Boltzmann equation (II.1), one typically assumes that close to the onset of order the relevant order fields (e.g. f_1 and f_2) as well as temporal and spatial variations are small. This assumption suggests scaling relations which allow to truncate the infinite sum in (II.4) and get closed equations for the dominant hydrodynamic fields. Balancing terms in the Boltzmann equation Peshkov et al. [127, 128] have proposed scaling relations for a system of polar particles with fully nematic collisions (i.e. $B = 1$) according to

$$\rho - \bar{\rho} \sim \varepsilon,\ \{f_{2k-1}, f_{2k}\}_{k\geq 1} \sim \varepsilon^k,\ \partial_t \sim \varepsilon,\ \partial_{x/y} \sim \varepsilon\,. \tag{II.8}$$

With these scaling relations, one can expand the sum in (II.4) retaining only terms of order ε^3 to get closed equations for the order fields $f_{1,2,3,4}$ [128]. The equations for f_3 and f_4 yield expressions for f_3 and f_4 in terms of f_1 and f_2 and one arrives at the following hydrodynamic equations for f_1 and f_2 (including orders of ε^3):

$$\begin{aligned}
\partial_t f_1 \;=\; & -(\alpha_0 + \rho\alpha_1) f_1 + \alpha_2 f_1^* f_2 - \alpha_3 |f_2|^2 f_1 \\
& - \frac{1}{2}(\nabla\rho + \nabla^* f_2) + \gamma_1 f_2^* \nabla f_2 && \text{(II.9a)} \\
\partial_t f_2 \;=\; & (-\beta_0 + \rho\beta_1) f_2 + \beta_2 f_1^2 - \beta_3 |f_2|^2 f_2 - \beta_3' |f_1|^2 f_2 \\
& - \frac{1}{2}\nabla f_1 + \gamma_2 \nabla\nabla^* f_2 - \gamma_3 f_1^* \nabla f_2 - \gamma_4 \nabla^*(f_1 f_2)\,, && \text{(II.9b)}
\end{aligned}$$

where $\nabla := \partial_x + \mathrm{i}\partial_y$ and the star denotes complex conjugation. The coefficients are given by

$$\alpha_0 = 1 - P_1(\sigma)\,, \tag{II.10a}$$
$$\alpha_1 = -\left(\mathcal{I}^B_{0,1}(\sigma) + \mathcal{I}^B_{1,1}(\sigma)\right)\,, \tag{II.10b}$$
$$\alpha_2 = \left(\mathcal{I}^B_{-1,1}(\sigma) + \mathcal{I}^B_{2,1}(\sigma)\right)\,, \tag{II.10c}$$
$$\alpha_3 = -4\gamma_2\left(\mathcal{I}^B_{-2,1}(\sigma) + \mathcal{I}^B_{3,1}(\sigma)\right)\left(\mathcal{I}^B_{1,3}(\sigma) + \mathcal{I}^B_{2,3}(\sigma)\right) \tag{II.10d}$$
$$\beta_0 = 1 - P_2(\sigma)\,, \tag{II.10e}$$
$$\beta_1 = \left(\mathcal{I}^B_{0,2}(\sigma) + \mathcal{I}^B_{2,2}(\sigma)\right) \tag{II.10f}$$
$$\beta_2 = \mathcal{I}^B_{1,2}(\sigma)\,, \tag{II.10g}$$
$$\beta_3 = -4\gamma_2\mathcal{I}^B_{2,4}(\sigma)\left(\mathcal{I}^B_{-2,2}(\sigma) + \mathcal{I}^B_{4,2}(\sigma)\right) \tag{II.10h}$$
$$\beta_3' = -4\gamma_2\left(\mathcal{I}^B_{1,3}(\sigma) + \mathcal{I}^B_{2,3}(\sigma)\right)\left(\mathcal{I}^B_{-1,2}(\sigma) + \mathcal{I}^B_{3,2}(\sigma)\right)\,, \tag{II.10i}$$
$$\gamma_1 = -2\gamma_2\left(\mathcal{I}^B_{3,1}(\sigma) + \mathcal{I}^B_{-2,1}(\sigma)\right)\,, \tag{II.10j}$$
$$\gamma_2 = 1/\left(4\left(1 - P_3(\sigma) - \left(\mathcal{I}^B_{3,3}(\sigma) + \mathcal{I}^B_{0,3}(\sigma)\right)\right)\right)\,, \tag{II.10k}$$
$$\gamma_3 = 2\gamma_2\left(\mathcal{I}^B_{-1,2}(\sigma) + \mathcal{I}^B_{3,2}(\sigma)\right)\,, \tag{II.10l}$$
$$\gamma_4 = 2\gamma_2\left(\mathcal{I}^B_{1,3}(\sigma) + \mathcal{I}^B_{2,3}(\sigma)\right)\,, \tag{II.10m}$$

where $P_k(\sigma) = \mathrm{e}^{-(k\sigma)^2/2}$ and $\mathcal{I}^B_{n,k}(\sigma)$ are collision integrals defined in (II.5). The dynamics of the density is given by the continuity equation $\partial_t\rho = -\Re[\nabla^* f_1]$. For a fully nematic collision rule, the coefficients α_0, α_1, α_2, α_3, β_0, β_1, β_2, β_3' are positive. This defines a critical density at $\rho_2^c = \beta_0/\beta_1$ above which the coefficient of equation (II.9b), that is linear in f_2, is positive. For $\bar{\rho} > \rho_2^c$, the disordered state is unstable and f_2, and thus nematic order, will grow. In contrast, since for nematic collisions α_0 and α_1 are positive, f_1 will always decay to linear order.

In principle, one could argue that these equations for a fully nematic collision rule might still be useful to study a system including a small polar bias. Indeed, as discussed in II.3.1a, the coefficient α_1 becomes negative for larger polar bias, defining a critical density at $\rho_1^c = -\alpha_0/\alpha_1$ above which the disordered state is linearly unstable against growth of polar order.[3] Note that even for $(\alpha_0 + \alpha_1\rho) < 0$, the nonlinear terms in equation (II.9a) might allow a polar instability when the second term, which is quadratic in the order fields, dominates the first, linear term. To explore the phenomenology of equations (II.9) in the presence of a (small) polar bias, we studied the linear stability of equations (II.9) with the definitions (II.10), where the collision integrals depend on the polar bias B according to (II.5). As in

3 The transition densities for nematic order $\rho_2^c = \beta_0/\beta_1$ and polar order $\rho_1^c = -a_0/a_1$ are in fact equivalent representations of the conditions $\mu_2(\rho_2^c, \sigma, B) = 0$ and $\mu_1(\rho_1^c, \sigma, B) = 0$, respectively, derived in section II.3.1a.

section II.3.1a, we fixed the noise value to $\sigma = 0.2$. Already for zero and small polar bias we find a transition from nematic to polar order for densities far beyond the transition to nematic order. However, this is likely an artefact from the truncation procedure, which is suited for densities close to the order transition. In this high density regime, numerical solutions of equations (II.9) for a nematic collision rule without polar bias show unbounded growth [128], indicating that higher orders that were neglected in the derivation of equations (II.9) become important [128]. Apart from this unphysical transition to polar order for high densities and small polar bias, the phase diagram of equations (II.9) also features a second regime of polar order for larger polar bias. Here, similar as in fig. II.4, polar order is not restricted to densities above ρ_1^c but is also present above the transition to nematic order marked by ρ_2^c. Hovever, unlike the phase diagram for the kinetic Boltzmann equation (fig. II.4(a)), the phase diagram of equations (II.9) lacks a transition from a purely nematic phase to a phase of polar order. Hence, equations (II.9) with the coefficients (II.10) are not suitable to study a dynamic transition of patterns as reported and discussed in section II.3.1b.

From our linear stability analysis II.3.1a we already know that truncating the Boltzmann equation in Fourier space at a high enough cutoff k_c accurately reproduces the phase diagram of the full kinetic Boltzmann equation including the transition between nematic and polar order in the nematic phase. We therefore studied the nonlinear solutions of the Boltzmann equation in Fourier space (II.4) for a certain cutoff k_c and neglecting order fields f_k with $k > k_c$. To this end, we solved the respective partial differential equations for the order fields f_k with $k \leq k_c$ using `XMDS2` software [144]. `XMDS2` is a free software package which can solve partial differential equations employing fast Fourier transform (FFT)-based spectral methods. Numerical integration by `XMDS2` of the truncated Boltzmann equation in angular Fourier space thus significantly complements our numerical study of the full Boltzmann equation in real space using the `SNAKE` algorithm. In agreement with our numerical simulations based on the generalized `SNAKE` algorithm, we find that for small polar bias and close to the onset of nematic order the system evolves towards high-density nematic bands separated by disordered low-density regions. For moderate polar bias, our numerical integration reproduces a dynamic transition from nematic band patterns to polar patterns (fig. II.7) as reported and discussed in section II.3.1b. To be precise, we find that for densities between the onset of nematic and polar order, the system first forms nematic band patterns in which the density locally exceeds the transition to polar order. Accordingly, these nematic bands are destabilized by polar instabilities that lead to the formation of polar patterns along the bands. Shortly after a replacement of the nematic bands by polar wave patterns, the numeric solutions for the order fields $f_{\{k \leq k_c\}}$ grow without bound even for a relatively high cutoff at $k_c = 12$. This indicates that here even higher modes become relevant and a crude truncation does not provide a sufficient

saturation of the order fields. Simulations for different k_c suggest that already for $k_c \leq 8$ the dynamic transition from nematic bands to polar waves is lost and the order fields locally diverge before wave patterns are formed.

In summary, our linear stability analysis of (II.9) with the fixed coefficients (II.10) together with our numeric solutions of the truncated Boltzmann equation strongly suggest that a rigoros derivation of hydrodynamic equations from the kinetic Boltzmann equation requires a suitable description of additional higher order fields and possibly saturation terms. In the following, we take an alternative approach and use the functional forms derived for equations (II.9) with general coefficients and study a dynamic pattern instability based on the polar and nematic order fields (i.e. f_1 and f_2).

II.3.2b Towards minimal field equations for coexisting nematic and polar patterns

While the functional dependencies on the polar and nematic order fields in equations (II.9) result from the structure of the Boltzmann equation (II.4), the coupling coefficients (II.10) are expressed in terms of the collision integrals (II.5) and contributions from angular diffusion. In particular, the collision integrals are based on assumptions on the particles' shape, their interaction range as well as their alignment rule upon collisions. We already discussed alternative approaches that proposed hydrodynamic equations mainly on the basis of symmetry arguments [109, 110, 113, 145, 146]. In those approaches, the coupling coefficients, which reflect microscopic details, are typically left general. In this section, we take a hybrid approach where we retain the functional dependencies of equations (II.9) while exploring their phenomenology for general coupling coefficients.

Hence, in the following we consider equations for the polar and the nematic order fields of the form (II.9), i.e.

$$\begin{aligned}\partial_t f_1 &= -(\alpha_0 + \rho\alpha_1) f_1 + \alpha_2 f_1^* f_2 - \alpha_3 |f_2|^2 f_1 \\ &\quad - \frac{1}{2}(\nabla\rho + \nabla^* f_2) + \gamma_1 f_2^* \nabla f_2 \qquad \text{(II.11a)} \\ \partial_t f_2 &= (-\beta_0 + \rho\beta_1) f_2 + \beta_2 f_1^2 - \beta_3 |f_2|^2 f_2 - \beta_3' |f_1|^2 f_2 \\ &\quad - \frac{1}{2}\nabla f_1 + \gamma_2 \nabla\nabla^* f_2 - \gamma_3 f_1^* \nabla f_2 - \gamma_4 \nabla^*(f_1 f_2)\,, \qquad \text{(II.11b)}\end{aligned}$$

where again $\nabla := \partial_x + \mathrm{i}\partial_y$ and the star denotes complex conjugation. In contrast to the previous section II.3.2a, the coupling coefficients are now left general and reflect the microscopic details of the underlying system. The dynamics of the density is again determined by the continuity equation $\partial_t \rho = -\Re[\nabla^* f_1]$. In order to reproduce a bifurcation from a disordered state to a nematic state at a critical

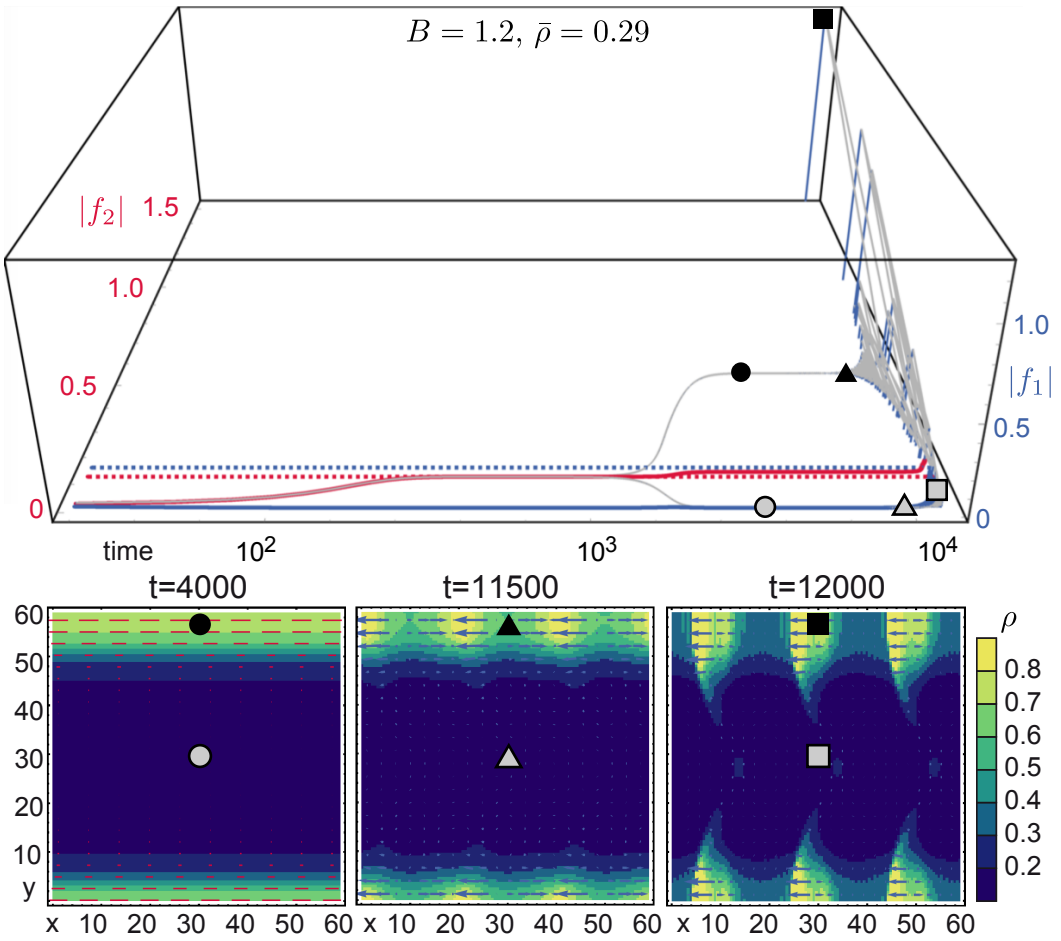

Figure II.7 Numeric solutions of the kinetic Boltzmann equation in Fourier space suggest that higher order fields become relevant at the dynamic pattern transition. Here, we solved the kinetic Boltzmann equation in Fourier space (II.4) with a truncation at $k_c = 12$. Gray solid lines in the top graph depict the dynamics of two exemplary lattice points indicated in the snapshots below. Starting at a disordered state with small density fluctuations, the system first approaches a homogeneous state where the average nematic order (solid red line) approaches the value of the homogeneous steady solution (red dashed line). For larger times, the local nematic order between the two points spread and high density bands of nematic order form. In the nematic band (black circle, simulation snapshot at $t = 4000$), nematic order rapidly grows and even exceeds the nematic-polar order transition (blue dashed line) predicted in II.3.1a. Indeed, we observe a polar instability in the band (black triangle, simulation snapshot at $t = 11500$) followed by growth of the average polar order (solid blue line). Upon the formation of polar wave patterns (black square, simulation snapshot at $t = 12000$) the order fields grow without bound, likely since higher order fields truncated in our implementation become relevant.

density ρ_2^c, we demand β_0 and β_1 to be positive. This directly yields $\rho_2^c = \beta_0/\beta_1$. Likewise, to suppress a direct bifurcation from disorder to polar order, α_0 and α_1 are chosen to be positive as well. As discussed in the previous section, polar order can still grow when the term quadratic in the order fields ($\alpha_2 f_1 f_2$) dominates the linear decay. To assure saturation for f_1 and f_2, the coefficients for the highest order terms, i.e. α_3, β_3, and β_3', are chosen to be positive.

We argue that a polar bias, which mingles polar and nematic collisions, leads to an enhanced coupling between fields of nematic symmetry (i.e. f_{2k}, $k \geq 1$) and polar symmetry (i.e. f_{2k-1}, $k \geq 1$). In equations (II.11), this coupling is reflected in the term $\alpha_2 f_1 f_2$ for the dynamics of the polar order field f_1. To systematically study the effect of a varying coupling strength, we fixed all coefficients in equations (II.11) except for α_2. For simplicity, all other coefficients were fixed to the values given by (II.10) with $\rho = 0.16$ and $\sigma = 0.2$, as derived from the kinetic Boltzmann equation for a purely nematic system close above the transition to nematic order. Based on a linear stability analysis, we then calculated the phase diagram of equations (II.11) as a function of the average density $\bar{\rho}$ and the coupling strength α_2 (Figure II.8(a)). Here, we varied α_2 from the value determined by (II.10) for $\rho = 0.16$ and $\sigma = 0.2$ to higher values.[4]

Our linear stability analysis (fig. II.8(a)) shows that above ρ_2^c, equations (II.11) possess steady homogeneous solutions with purely nematic order (red and orange) as well as steady homogeneous solutions with polar order (green). For large coupling strengths α_2 or large $\bar{\rho}$, there are no physical solutions; more specifically, in all steady state solutions, the polar order exceeds the density (white region). To investigate pattern formation, we study the linear stability of homogeneous states against wave-like perturbations of the form (II.7). As in section II.3.1a, we focus on perturbations along and perpendicular to the respective order. Remarkably, for moderate coupling strengths and close to the transition density, we recover a phase diagram that qualitatively resembles the one of the kinetic Boltzmann equation discussed in section II.3.1a (fig. II.4). In particular, our phase diagram suggests a direct transition from a phase of nematic band patterns to a phase of traveling wave patterns.

To elucidate the dynamics of the order fields f_1 and f_2 for different points in this phase diagram, we numerically solved equations (II.11) together with the continuity equation employing `XMDS2` software. All simulations shown in figures figures II.8–II.10 start at a disordered state with small random fluctuations in the density end assume periodic boundary conditions. In agreement with our linear stability analysis, we find nematic band patterns for low α_2 and close to the transition density

4 We comment that with the definition (II.10), α_2 in fact *decreases* for increasing polar bias. However, since in this section we want to study reduced equations for f_1 and f_2, we argue that an increasing α_2 could reflect higher order terms that are relevant for the nematic polar order transition as discussed in II.3.2a.

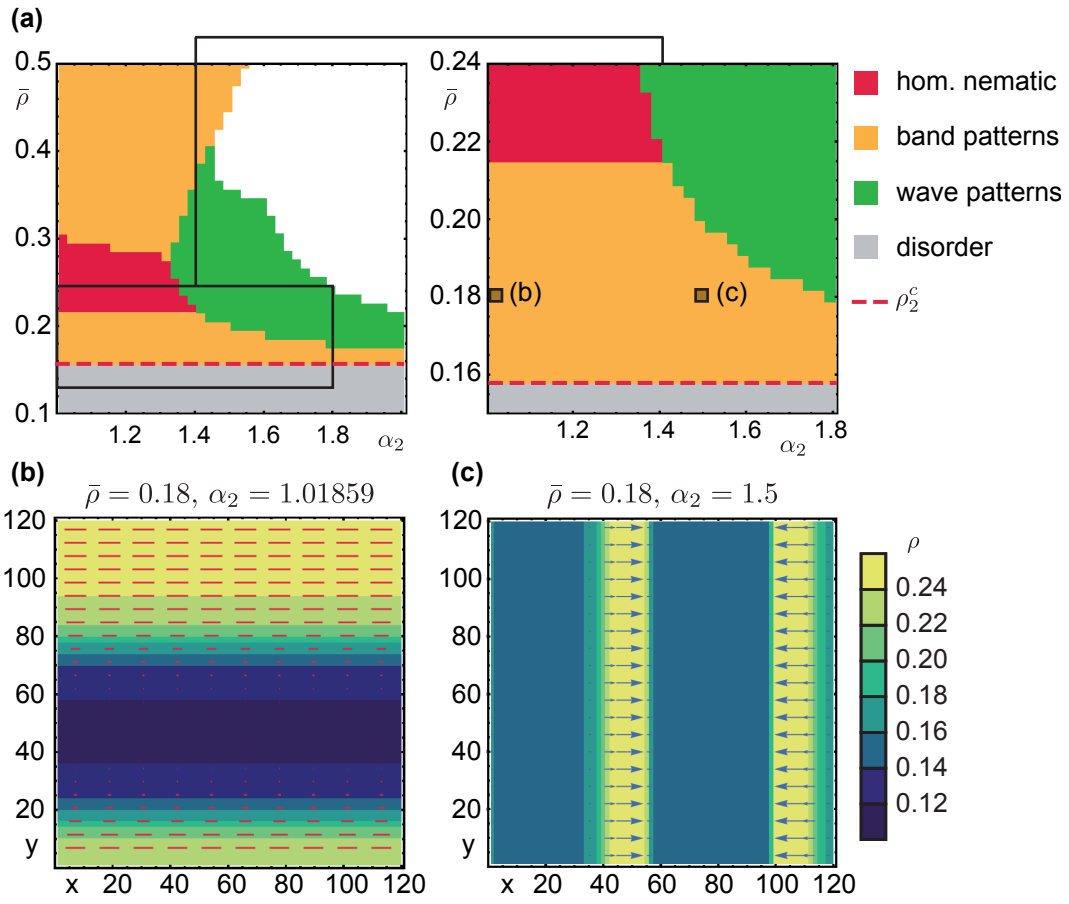

Figure II.8 Varying the coupling strength α_2 between polar and nematic order qualitatively reproduces the phase diagram of the original kinetic Boltzmann equation for a mixed collision rule. **(a)** Phase diagram of the hyrodynamic equations (II.11) in terms of the average density $\bar{\rho}$ and the coupling strength between polar and nematic order, α_2. Close to the transition density to nematic order, ρ_2^c, the phase diagram qualitatively resembles the phase diagram of the kinetic Boltzmann equation with small polar bias (fig. II.4(a)). **(b)** and **(c)** show representative snaphots of our numeric simulation results of equations (II.11). While for a coupling strength α_2 that repesents the fully nematic collision rule, we find nematic bands (b), an increased coupling leads to polar patterns such as crossing polar waves (c). Red bars in (b) and blue arrows in (c) indicate the orientation and strength of respectively nematic and polar local order.

(fig. II.8(b)). For larger α_2 and for densities between the onset of nematic order and polar order, the system also forms nematic bands first. However, after some time these bands show a polar instability along the extension of the band, which leads to a decay of the bands into polar patterns reminiscent to the dynamics in the kinetic Boltzmann approach discussed in II.3.1b. We observe that this polar instability can lead to different polar wave patterns. Depending of the initial conditions and the system size, we observe the formation of multiple counter-directional waves (fig. II.8(c)), formation of multiple waves where one propagation direction eventually dominates (fig. II.9), and even cycling and coexistence of polar wave patterns and nematic lanes (fig. II.10). In particular, the last scenario is found for very large system sizes. We hypothesize, that whereas in the first scenarios traveling wave patterns are stabilised by the periodic boundary conditions, larger systems sizes yield bending instabilities and result in more irregular patterns. Indeed, when gradually increasing the system size, we find that the polar instability in the initially nematic bands leads to wave patterns with an increasingly perturbed wave front. For very large system sizes, the waves eventually break and lead to more irregular patterns. Here, nematic bands and polar waves coexist and the systems show regions of an alternating dominance of nematic and polar symmetry (fig. II.10). We mention that the lengthscales of patterns in our hydrodynamic approach are much smaller than in our kinetic Boltzmann approach, consistent with previous studies (see section II.2, [22]).

Our observations are in very well agreement with the phenomenology observed in [3]. In particular, our coexistence regime features complex dynamics including bending nematic lanes that serve as scaffold for polar wave patterns which in turn can decay again into lanes. Our numerical solutions of the hydrodynamic equations (II.11) suggest that while a dynamic transition from nematic bands to polar waves is generic in the coexistence regime, the initial conditions and especially the system size are important for the final state of the system. Based on this finding, we hypothesize that for larger systems also the kinetic Boltzmann equation might approach states of more irregular dynamics similar to those observed for our hydrodynamic equations (fig. II.10) as well as in [3].

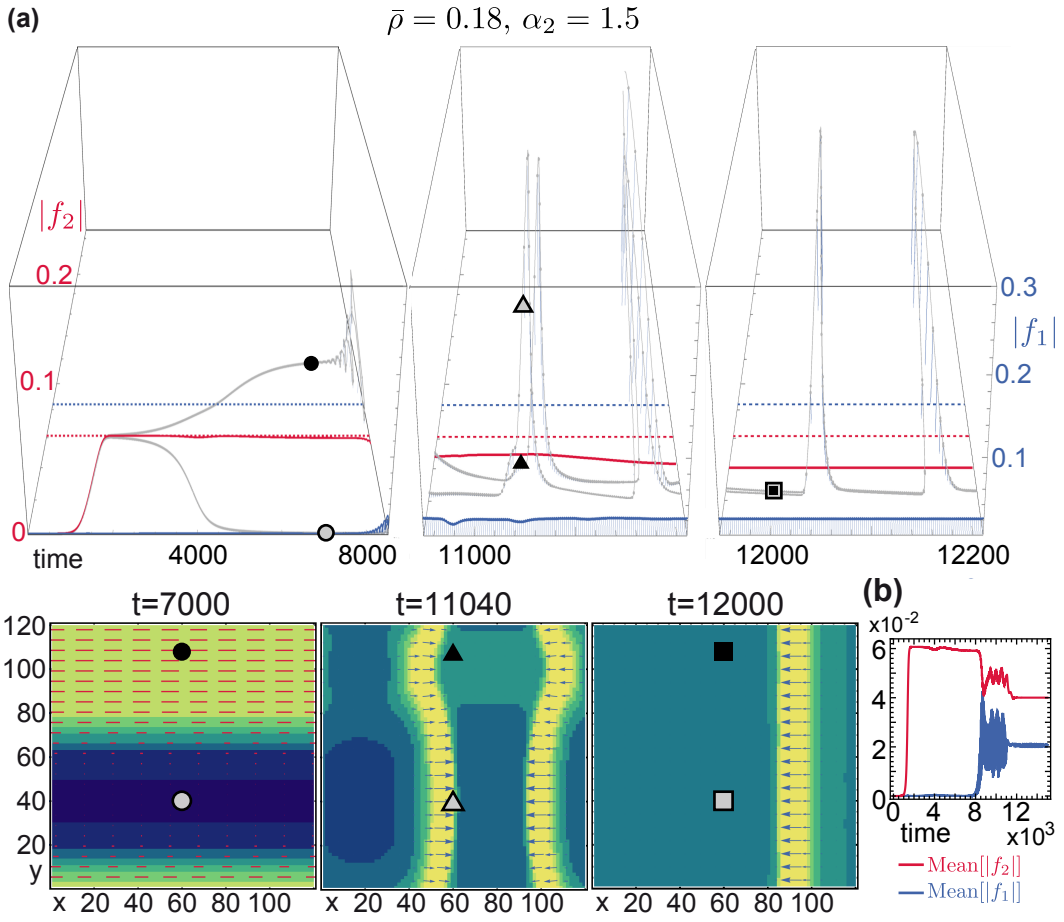

Figure II.9 For a moderate coupling strength α_2, nematic band patterns can induce a polar instability in nematic bands. **(a)** The two grey lines in the top graph indicate the dynamics of two representative points in space marked in the simulation snapshots below (the time axis was split into three parts to show a better time resolution). Initially, the average nematic order (red solid line) approaches the homogeneous steady state solution (red dashed line). After some time ($t \approx 2500$) nematic bands start to form and the nematic order in the band grows (black circle $t = 7000$) whereas the nematic order in the disordered surrounding phase approaches zero (gray circle). In particular, the nematic order in the band exceeds the nematic-polar phase transition observed in (fig. II.8(a)). Accordingly, the band undergoes a polar instability which leads to the formation of two counter-directional traveling waves ($t = 11040$). The local polar order is nonzero for both points whenever a polar wave crosses them. Eventually, one wave dominates and we find a stable traveling wave solution ($t = 12000$). The shown simulation differs from Fig. II.8(c) in terms of different random initial conditions. The color code is as in fig. II.8. **(b)** Mean nematic (red) and polar (blue) order for the simulation shown in (a). After a polar instability in the nematic band ($t \approx 8000$), the systems forms counter-directional traveling waves which are accompanied by oscillations in the mean nematic and polar orders. For larger times, one direction dominates and the mean polar and nematic order saturate.

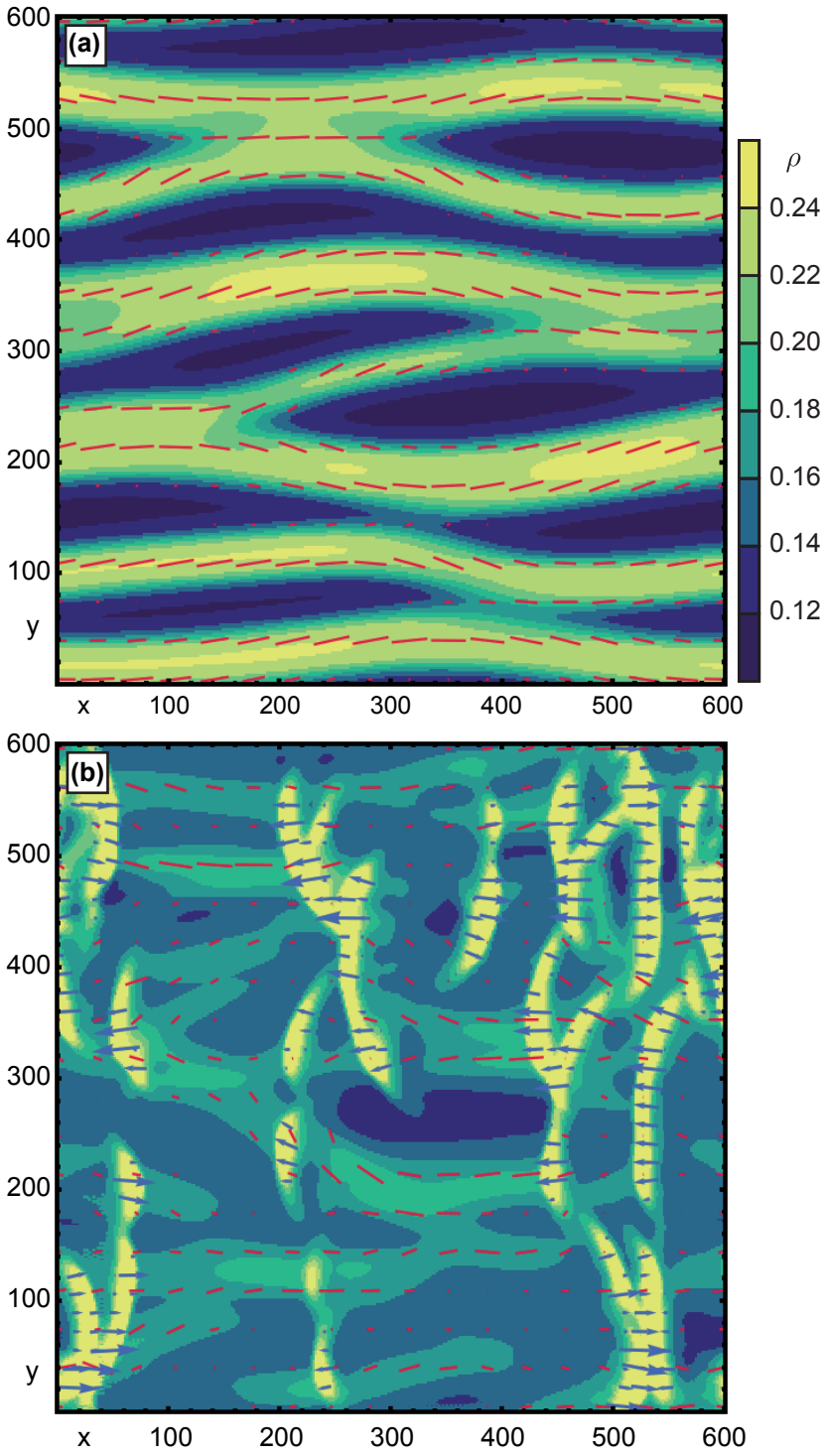

Figure II.10 Dynamic coexistence of local nematic bands and polar wave patterns for moderate coupling strength ($\alpha_2 = 1.5$, $\bar{\rho} = 0.18$).**(a)** Snapshot of nematic band patterns shortly before a local polar instability. **(b)** For later times, polar instabilities lead to the formation of traveling wave patterns with complex dynamics. In particular, we observe the coexistence of local nematic and polar ordered regions which interact, decay and rearrange dynamically. Red bars indicate the orientation and strength of local nematic order, blue arrows denote the strength and direction of polar order (for a clearer view only red bars for nematic order are shown in (a)).

II.3.3 Conclusion

In summary, we first studied a system of self-propelled particles with mixed collision symmetry based on a kinetic Boltzmann equation. We find that already a small polar bias in a (binary) nematic collision rule leads to a direct transition from nematic to polar order beyond a critical density. In addition to the previously studied nematic bands and traveling waves for respectively small and large polar bias, we identify a parameter regime of moderate polar bias and density where nematic patterns can induce a transition to polar order. This dynamic transition can lead to different final states such as polar waves, dynamically rearranging bands or coexisting patterns with nematic and polar symmetry. In the case of coexistence, the system locally switches between nematic band patterns and polar waves.

Our findings shed new light on traditional symmetry assumptions in active matter theories. Our combined linear stability analyses and numerical simulations suggest that the symmetry of patterns can depend on the dynamics of the system due to a mutual feeback between pattern formation and (local) symmetry breaking. Here, an initial Turing instability of the homogeneous nematic state first leads to a redistribution of the density. Since the density acts as bifurcation parameter for the system's symmetry, this redistribution can drive certain regions beyond a bifurcation where the symmetry of the system's dynamics changes from nematic to polar. This creates a polar instability in the nematic bands followed by the formation of polar patterns.

Based on this notion of local instabilities, we studied hydrodynamic equations for propelled particles with a variable coupling strength between polar and nematic order fields. By means of linear stability analyses and numerical simulations, we show that a linear instability of the local steady state is indeed sufficient to reproduce dynamic pattern transitions as observed in our kinetic Boltzmann approach. While numerical solutions of the kinetic Boltzmann equation for large systems are costly, simulations of the reduced hydrodynic equations for large systems reveal very rich dynamics reminiscent to the one recently observed in [3]. In a regime of moderate coupling between polar and nematic order fields, our hydrodynamic equations display complex dynamics where nematic lanes can bend, merge, and serve as scaffold for polar patterns, which also splay, rotate and interact with lanes as well as with other waves. In the future, we plan to study the role of the single terms in our hydrodynamic equations particularly with respect to band formation, band destabilization and saturation. This should yield a more complete description of the nonlinear dynamics in phase space in which attractors and orbits can be identified.

Based on our analyses, a kinetic Boltzmann approach as well as the proposed hydrodynamic equations (II.11) are sufficient to study dynamic transitions between patterns of polar and nematic symmetry reminiscent to the experiments and numerical simulations in [3]. Further controlled experiments and simulations in the

style of [3] could test our prediction that the pattern forming mechanism is based on a local destabilization of polar order.

More generally, our study supports the notion that the dynamics of the system can be rationalized based on the local stability of steady states, as recently also proposed in the context of reaction-diffusion systems [23]. In particular, the local steady states and their stability depend on the respective local density. Thus, convection together with global density conservation intrinsically couple different local steady states and lead to an interesting feedback between particle redistribution and symmetry breaking. We hypothesize that this mechanism is not limited to a system of propelled particles with mixed collision symmetry as studied here but could be a more general principle whenever a bifurcation parameter (such as density) is dynamically redistributed during pattern formation. From a broader perspective of biological active matter systems, this could apply whenever individuals dynamically change their properties (velocity, collision behavior, etc.) as a response to interactions with other individuals. Prominent examples of such feedback between collective effects and the individuals' properties are found in quorum sensing in bacteria [147–149], collective sensing [150, 151], as well as collective learning [151–153].

II.4 Conclusion and outlook

In this chapter, we discussed the collective behavior in systems of self-propelled entities, often referred to as active matter systems [35]. Active matter systems are wide-spread in biological systems, where the consumption of ambient energy in the form of nucleoside triphosphate (NTP) or nutrients enables directed motion [36, 154]. As discussed in the introduction of this chapter II.1, collective behavior in active biological systems can be found on different lengthscales ranging from the subcellular level [2, 90], to cell colonies [87–89], to systems of larger organisms such as groups of animals [84, 155, 156]. Theoretical approaches to active systems have mostly focused on the emergence of macroscopic order as well as on pattern formation [35, 37]. Employing symmetry arguments [109–114] and simplifying interaction assumptions [99, 100, 121, 124], theories were able to create a common and useful basis to understand active systems in terms of statistical physics concepts such as phase transitions and symmetry breaking. Several theoretical predictions, such as a order transition and pattern formation as a function of the average density [99, 100, 123], as well as large number fluctuations [110, 112] were confirmed and further studied by experiments [34, 90, 93, 117, 157]. In turn, controlled experiments have revealed interesting phenomena such as chemical turbulence [117, 158, 159] or vortex patterns [2, 160–163], which have helped to generalize and further refine theoretical approaches [22, 115, 119, 162]. Identifying controllable active systems in biology and finding a suitable theoretical description in the framework of active matter theory has thus proven an especially successful approach in advancing our understanding of active systems.

In this spirit, the first project of this chapter (section II.2) was motivated by recent observations in controlled reconstitution experiments with the bacterial cell division protein FtsZ [2]. In the presence of ATP, GTP and anchor proteins, FtsZ assembles into membrane-bound polymers that undergo effective motion along their backbone based on a treadmilling mechanism. Due to their intrinsic curvature, the polymers effectively propagate along curved (chiral) paths. Depending on the used anchor proteins, the polymers can eventually form dense ring patterns or dynamic bundles. The effective propulsion of the polymers motivated us to consider this system in the context of active matter theories. Employing Brownian dynamics simulations and a kinetic Boltzmann approach, we studied a system of active entities that are propelled (clockwise) on circular paths and that can only interact by steric repulsion consistent with experimental observations [2]. We find that the collective behavior of these entities leads to a phase of vortex patterns for intermediate densities and noise levels, which–in our Brownian dynamics simulations–resemble the ring patterns observed in [2]. Our theoretical prediction of this vortex phase as a function of FtsZ density was recently confirmed by further *in vitro* experiments by Ramirez et al. [34]. Our study thus strongly suggests

that the *in vitro* FtsZ system can be understood in the context of more general active matter theories. Furthermore, our work has helped to establish the *in vitro* FtsZ system as a convenient model system to study intracellular patter formation. From a theoretical perspective, the experimentally motivated inclusion of *curved* motion in our approaches has turned out to provide an interesting link between traditional active matter theories and the theory of diffusively coupled oscillators. More specifically, the hydrodynamic equations derived in our study combine previous active matter continuum equations [109, 123] with the prominent Ginzburg-Landau equation [33].

Our study suggests several interesting questions for future experimental as well as theoretical research. For instance, our results indicate a critical role of polymer length and curvature for the structure of vortex patterns and the presence of closed ring patterns. Furthermore, our hydrodynamic approach points towards more irregular patterns such as turbulence. We think that especially the first prediction could be investigated in controlled FtsZ reconstitution experiments, e.g. by manipulating the FtsZ polymer length.

While several biological examples for active systems [2, 90, 162] appear to be approachable in the classical framework of active matter theory [35, 37], other biological active system clearly elude many of the simplifying assumptions in theoretical approaches especially with respect to simplified interaction rules. This is especially true for systems of larger active organisms such as insects, birds, or mammals, where interactions between individuals are complex and collective effects can lead to several novel phenomena such as collective learning etc. [151]. But even in comparatively controllable systems, such as in *in vitro* experiments, interactions between the constituting individuals can be beyond simple symmetry assumptions as typically considered in active matter theories.

In particular, recent *in vitro* experiments with actomyosin assays [3] give an example where the dynamics of patterns cannot be merely understood in terms of standard symmetry assumptions and symmetry breaking mechanisms studied in the traditional active matter context [37]. By varying the polyethylene glycol (PEG) concentration in a reconstituted actomyosin motility assay, Huber et al. [3] were able to tune the interactions between actin filaments which are propelled on a myosin carpet. Based on binary collision statistics, they argue that the PEG concentration changes the symmetry in actin interactions. In the case of a predominantly polar or nematic interaction symmetry, they observe respectively polar traveling wave patterns or nematic lanes consistent with classical conceptions of symmetry breaking and pattern formation in active matter (see section II.1). However, their experiments also reveal a novel state of coexisiting nematic and polar patterns which can interact, perturb and stabilize each other (also see fig. II.1(g)). In this state, the authors concluded that the symmetry of patterns is itself a dynamic property of the system. The authors complemented their experiments by Brownian

dynamics simulation, which reproduce this coexistence phase for a mixed interaction symmetry (also see fig. II.1(h)). The observed coexistence phase sheds new light on conventional symmetry breaking mechanisms in active matter theories [35], where the microscopic properties and interaction symmetries of the active entities typically lead to either polar or nematic order and patterns. The study by Huber et al [3] is thus at the interface of traditional conceptions of active matter, which show phases of either polar or nematic patterns, and more complex active system, where the individuals' properties can dynamically evolve with pattern formation.

Motivated by [3], the second project of this chapter dealt with systems of propelled particles with a mixed collision symmetry on the basis of a kinetic Boltzmann approach (section II.3). For predominantly nematic or polar collision symmetries, we recovered the well-studied scenarios of nematic or polar patterns, respectively, consistent with previous theoretical studies [127]. Remarkably, for intermediate interaction symmetries, we found dynamic transitions between patterns of different symmetries reminiscent to the dynamics observed in [3]. We complemented this approach by a hydrodynamic description, where for a moderate coupling strength between polar and nematic symmetries we again find dynamic transitions between polar and nematic patterns. For large systems, we observed a coexistence state, where polar and nematic patterns interact, perturb and stabilize each other, similar to the observations in [3]. Besides the reproduction of the pattern phenomenology observed in [3], our study yields insights into the underlying mechanism of dynamic pattern transitions. In particular, our results strongly suggest that these pattern transitions can be understood in terms of the linear stability of local steady states, as it has also been proposed recently in the context of reaction-diffusion systems [23]. More specifically, the formation of density patterns can drive different regions in the system into phases of different symmetries (i.e. polar and nematic). Accordingly, respectively polar and nematic order can locally build up and dynamically interact with each other through the convective transport of active particles. This theoretical prediction should be testable by controlled *in vitro* experiments as well as simulations by manipulating local densities and thereby possibly controlling local phase transitions.

We hypothesize that dynamic transitions between patterns of different symmetries are not particular to our system of mixed collision symmetries, but might be present in various other (active) systems, as well. Especially, we expect dynamic transitions whenever spatial patterns lead to a redistribution of parameters that are critical for pattern selection (such as the density in our case). From a broader perspective of biological active matter systems, this could apply whenever individuals can dynamically change their properties (velocity, collision behavior, etc.) as a response to interactions with other individuals. Prominent examples include quorum sensing in bacteria [147–149], collective sensing [150, 151], and collective learning [151–153]. While all of these systems are known to exhibit

remarkable collective behavior, the possible *mutual* feedback between collective pattern formation and the properties of an individual has remained largely unadressed. We hypothesize that such mutual feedback could be a more general mechanism underlying interesting dynamics including dynamic pattern transitions as observed in our study.

III Collective behavior in ecological systems

III.1 Collective effects in microbial games

Ecosystems are a prominent example of nonequlibrium systems, where interactions between individual organisms can lead to intriguing and vital collective phenomena. Such collective phenomena can range from the formation of complex architectures in coral reefs [164, 165], to the collective productivity in vegetation [166, 167], and can also be found on much smaller scales such as in microbial communities [168–171]. Especially microbes, including bacteria, are instructive to study collective behavior, since they can be grown in controlled environments in the laboratory and their short division time makes the long-term dynamics of the system accessible [38]. Controlled laboratory experiments have revealed various collective effects based on the microbes' interactions. Examples include the formation of fruiting bodies [172](fig. III.1(a)), condensation [39, 173] and ridge architectures [174, 175] in biofilms (fig. III.1(b)), and patch formation in cooperatively growing microbial populations [176](fig. III.1(c)).

Many of these collective phenomena have been interpreted on the basis of relatively simple interaction motifs of microbial cooperation [38, 177]. Cooperation typically means that a microbe provides a public good, which is then shared in the community. Natural examples for public goods are exopolysaccharides, extracellular enzymes, quorum-sensing molecules, extracellular DNA, and antibiotics [178].

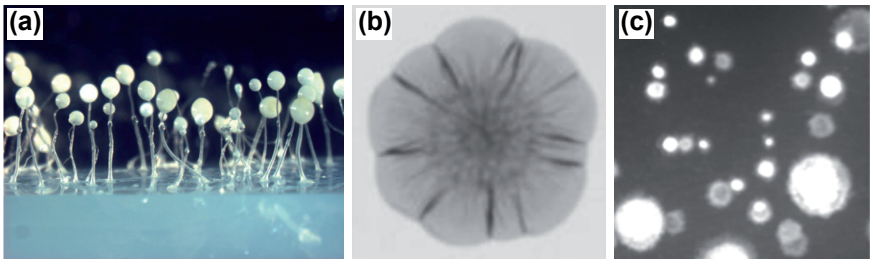

Figure III.1 Examples of collective behavior in microbial systems, adapted from respective publications. **(a)** *Dictyostelium discoideum* fruiting bodies on an agar plate [172]. **(b)** Complex ridge architecture in a biofilm of *Vibrio cholerae* [174]. **(c)** Self-organized patchiness in *Bacillus subtilis* [176].

Already for a population of a single species, cooperative growth can lead to interesting collective effects such as the prominent *Allee effect* [179, 180]. Here, a large enough population can provide sufficient public good to enable collective population growth, whereas a small population would go extinct (strong Allee effect). The Allee effect is exemplified by *Bacillus subtilis*, which is able to digest starch by secretion of the enzyme amylase [181]. Since amylase is secreted from the cell, the breakdown of starch–and thereby population growth–is cooperative. In a spatially extended system, this cooperative growth can result in the survival of Bacillus subtilis patches, which would go extinct in a well-mixed environment [176](fig. III.1(c)). For systems of two (or more) microbial species, cooperation is often understood in the language of the *prisoner's dilemma* [182, 183]. While both species benefit from the public good, only one of them takes the metabolic cost of producing it. The species that provides the public good is therefore commonly referred to as *cooperator*, and the second, 'selfish' species is called *defector* (or *cheater*). Without any further support of the cooperators, cheaters will outgrow the cooperators because they save the metabolic cost of producing the public good. Without cooperators, however, cheaters will be eventually doomed to die, since they rely on the public good. Various theoretical approaches based on concepts from game theory and evolutionary dynamics have helped to gain insights into this *cooperation dilemma* and have proposed ways to rescue cooperators [184, 185]. Theoretical and experimental studies suggested solutions to the cooperation dilemma such as repeated interactions [184, 186, 187], punishment [184, 188], demographic fluctuations [189], and spatial heterogeneity [39, 173, 190, 191]. Besides the prisoner's dilemma, microbial interactions have also been assigned to similar other classes of game strategies [177, 183]. One example is the so-called *snowdrift game*, found in the budding yeast *Saccharomyces cerevisiae* [192], where cooperators and defectors preferentially coexist. For the snowdrift game, theoretical studies suggest that–unlike in the prisoner's dilemma–spatial structure does not neccessarily promote cooperators [193].

All these experiments suggest, that even relatively simple microbial systems can yield interesting insights into the evolutionary strategies in ecological networks. Here, recent experiments on soil bacteria in the group of Jeff Gore have yielded important insights into interactions of microbes and their role in microbial ecosystems [41, 194, 195]. In particular, Friedman et al. [194] studied the pairwise competition of various soil bacteria and observed stable coexistence or dominance of one of the two species. The authors studied the role of pairwise interactions for more complex ecosystems by mixing three different species of soil bacteria and comparing the results with the outcomes of their pairwise competition experiments. They found that their pairwise competition experiments could predict the outcomes in three-species competitions with an accuracy of $\sim 90\%$. In a further study, Ratzke and Gore [41] focused on the nature of the underlying interactions between soil bacteria and found that soil

bacteria can interact by modifying and reacting to the pH in their environment. More specifically, population growth modulates the pH, but the pH also affects microbial growth. The authors identified different scenarios where microbes can either modify the pH in a way that is beneficial or detrimental for their growth. In pairwise competition experiments, the pH-mediated interactions between different species led to interesting effects such as bistability, oscillatory growth dynamics and stabilization of one species by the other. A particularly stunning scenario occurs, when a microbe modifies the pH in way which is detrimental for its own growth. For a severe pH change, this can even lead to population extinction.

The observation of self-inflicted death motivated a more detailed study on the growth dynamics in soil bacteria, which is discussed in section III.2. The presented study was initiated during my three-month research stay in the group of Jeff Gore at MIT, Cambridge, USA in the fall of 2016. During this time, I conducted a variety of growth experiments in well-mixed cultures of different soil bacteria. Section III.2 focuses on a detailed analysis of the growth dynamics of the soil bacterium *Paenibacillus sp.* (most similar to Paenibacillus tundrae), which acidifies its environment and thereby causes its own population death. We show that this negative feedback between population growth and a pH change leads to a non-monotonous growth curve, which can be manipulated by changing the buffer concentration and thereby hampering the pH change. To study long-term effects, we performed daily dilutions over the course of 11 days and revealed oscillatory dynamics of the population size and the acidification time. We further describe how self-inflicted death, which we also refer to as *ecological suicide*, can be prevented by adding substances such as alcohol, salt, or antibiotics, that are usually considered harmful for bacteria. Last but not least, we show that ecological suicide is not particular to *Paenibacillus sp.*, but can be found in various other soil bacteria (about 20% of the tested species), emphasizing the general relevance of our study.

III.2 Publication

Ecological suicide in microbes

by

C. Ratzke[1,*], J. Denk[2,*], J. Gore[1]

[1] Physics of Living Systems, Department of Physics, Massachusetts Institute of Technology, Cambridge, MA, USA

[2] Arnold Sommerfeld Center for Theoretical Physics (ASC) and Center for NanoScience (CeNS), Department of Physics, Ludwig-Maximilians-Universität München, Theresienstrasse 37, D-80333 München, Germany

[*] These authors contributed equally

Reprinted on pages 161–187

Published in **Nature Ecology and Evolution, 2 (2018) 867**,
DOI: 10.1038/s41559-018-0535-1,
The supplemental material is reprinted on pages 188–211.

Ecological suicide in microbes

Christoph Ratzke*[1†], Jonas Denk*[2] and Jeff Gore[1†]

[1] Physics of Living Systems, Department of Physics, Massachusetts Institute of Technology, Cambridge, MA, USA

[2] Arnold-Sommerfeld-Center for Theoretical Physics and Center for NanoScience, Ludwig-Maximilians-Universität München, Theresienstraße 37, D-80333 München, Germany

*equal contribution

[†] correspondence should be sent to: cratzke@mit.edu or gore@mit.edu

Abstract:

The growth and survival of organisms often depend on interactions between them. In many cases, these interactions are positive and caused by a cooperative modification of the environment. Examples are the cooperative breakdown of complex nutrients in microbes or the construction of elaborate architectures in social insects, where the individual profits from the collective actions of her peers. However, organisms can similarly display negative interactions by changing the environment in ways that are detrimental for them, eg by resource depletion or the production of toxic byproducts. Here we find an extreme type of negative interactions, in which *Paenibacillus sp.* bacteria modify the environmental pH to such a degree that it leads to a rapid extinction of the whole population, a phenomenon we call ecological suicide. Modification of the pH is more pronounced at higher population densities, and thus ecological suicide is more likely with increasing bacterial density. Correspondingly, promoting bacterial growth can drive populations extinct whereas inhibiting bacterial growth by the addition of harmful substances – like antibiotics – can rescue them. Moreover, ecological suicide can cause oscillatory dynamics, even in single-species populations. We find ecological suicide in a wide variety of microbes, suggesting that it could play a significant role in microbial ecology and evolution.

Introduction:

Microbes depend on their environment but also modify it[1–4]. An especially important environmental parameter for microbial growth is the pH, since protein and lipid membrane stability depend strongly on it[5,6]. Microbes have a species-dependent pH optimum at which they grow best[7,8] and environmental pH away from this optimum either inhibits growth or can even cause cell death[9,10]. At the same time, bacteria change the environmental pH by their metabolic activities[9,11]. In this way, microbes can potentially induce pH values that are detrimental for their own growth and thus harm themselves.

Results:

The soil bacterium *Paenibacillus sp. (*most similar to *Paenibacillus tundrae*, for more information about this strain see Supplementary Information) can grow in a medium that contains 1% glucose as the main carbon source, in addition to a small amount of complex nutrients (see Methods for details). In soil the amount of carbohydrates lies in the range from 0.1%[12] to 10%[13], mostly in the form of complex carbohydrates. Starting from neutral pH we measured a strong acidification of the environment to a pH of around 4 during bacterial growth by secreting a variety of organic acids (Fig. 1a, Supplementary Fig. 1b). Upon reaching this low pH, the bacteria suddenly start to die, resulting in a non-monotonic growth curve (Fig. 1a), since *Paenibacillus sp.* cannot survive at low pH values (Supplementary Fig. 1A and Supplementary Fig. 3). Indeed, after 24h of incubation, we find that there are no viable cells in the culture (as measured by colony forming units after 48h incubation on rich medium, which may exclude cells that could grow after more than 48h). We note that the bacterial densities that are reached in this experiments lie within the range that can be found in soil[14,15] and soil has even a slightly lower buffering capacity than our medium

(Supplementary Fig. 2). Moreover, ecological suicide also appears on non-glycolytic substrates (like glycerol) and also complex sugars like starch (Supplementary Fig. 1). We call this rapid population extinction due to environmental modification “ecological suicide” - a phenomenon that has been previously speculated about[16,17].

The correlation between the drop of pH and the onset of death suggests that the bacteria themselves may be responsible for their eventual extinction by lowering the pH into regions in which they cannot survive. To test this idea, we added buffer to the medium to temper the pH change. The buffer indeed slows down the death process (Fig. 1b) and prevents it completely at sufficiently high concentrations (Fig. 1c). Thus, it is the pH change that causes the death of the bacteria and the presence of buffer can hinder ecological suicide. These results show that initially flourishing bacterial populations can corrupt their environment and thus cause their own extinction. The pH change resembles a 'public bad' that is collectively produced and harms all members of the populations. This phenomenology can be recapitulated by a simple mathematical description based on negative feedback of the bacteria and the environmental pH (Supplementary Discussion and Supplementary Fig. 10).

Since bacteria collectively change the pH, higher bacterial densities can deteriorate the environment more strongly and thus expedite ecological suicide. We tested this idea experimentally by measuring the fold growth within 24h for different initial bacterial densities and different buffer concentrations. At low buffer concentrations, the bacteria die by ecological suicide independent of their initial density, whereas at high buffer concentrations they always survive (Fig. 2a). At intermediate buffer concentrations, however, survival becomes density-dependent (Fig. 2a). For high initial cell densities, the bacteria die within 24h, but below a critical initial density, the bacteria grow and survive. The fitness of the bacteria thus decreases dramatically with increasing cell density. This aspect of ecological suicide is thus opposite of

the well-known Allee effect, where fitness increases with population density[18–20]. Although the observed death at high cell densities is reminiscent to death at high densities in common logistic growth models, in our experiments death continues until all cells have died out, whereas in logistic growth the density stabilizes at the carrying capacity.

What does this growth behavior mean for the long-term growth dynamics of a population such as occurs in growth with daily dilution into fresh media? Fig. 2a shows how the bacterial density after one day of growth depends on the initial bacterial density. For intermediate buffering the bacteria die for high initial densities but grow for low initial densities. This may cause oscillatory dynamics, since high bacterial densities cause low densities on the next day and vice versa. Indeed, this intuitive prediction is fully supported by a mathematical description based on negative feedback of the bacteria and the environmental pH alone, which shows a bifurcation of the end-of-the-day bacteria densities upon changing the buffer concentration (see Supplementary Information and Supplementary Fig. 11 and 12). To test this prediction, we cultivated the bacteria in batch culture with a daily dilution of the culture 1/100x into fresh media. As expected from Fig. 2a, for low buffering the bacteria go extinct on the first day and for high buffering they grow up to the same saturated density each day (Fig. 2c, e, Supplementary Fig. 6 and 8a). For intermediate buffering, however, the bacteria show oscillatory dynamics as predicted by our model (Fig. 2d, Supplementary Fig. 8b and 10). The oscillations of the populations are accompanied by oscillations of the time at which the pH drops each day (acidification time, Fig. 2d and Supplementary Fig. 5 and 8b), which again shows the connection between pH change and ecological suicide. Ecological suicide caused by environmental deterioration therefore can drive oscillatory dynamics even in populations consisting of just one species.

We have seen that low bacterial densities lead to less deterioration of the environment and thus a less deadly effect on the bacteria. Therefore, effects that hinder bacterial growth by harming the bacteria may be able to save the population from ecological suicide. A first hint in this direction is given by changing the glucose concentration. While one would naively expect that an increase in glucose concentrations is beneficial, in the presence of ecological suicide, the opposite is the case (Fig 3a). At low glucose concentrations, the bacteria grow to lower densities, which hardly changes the pH and therefore allows the bacteria to survive. At high glucose concentrations, bacterial growth causes environmental acidification and thus ecological suicide. The bacterial population is therefore only able to survive in nutrient-poor conditions. Moreover Fig. 3a shows that ecological suicide can be observed even at rather low nutrient concentrations of around 0.2% glucose.

To explore the idea that environments that are usually considered poor can instead save the bacterial population, we measured the growth and survival of bacteria grown in the presence of the antibiotic kanamycin, ethanol, and salt. Although these substances are quite different, they all inhibit bacterial growth and lead to similar profiles of population survival as a function of the concentration of the inhibiting substance (Fig. 3 b-d). In the absence of the harmful substances, the bacteria lower the pH to the point of extinction. At high concentrations, the harmful substances kill the bacteria. However, at intermediate concentrations, the bacteria can grow and survive. This leads to the paradoxical situation that substances that are normally used to kill bacteria in medicine (antibiotics) or food preservation (salt, ethanol) are able to save bacteria and allow their growth. The interplay between the harming substance and the ecological suicide results in a U-shaped dose response curve of the harming substance, which is called hormesis in toxicology[21].

The effect of ecological suicide is surprising and has paradoxical consequences. However, the question arises: How common is ecological suicide in bacteria? To investigate this question, we incubated 119 bacterial soil isolates[22] from a broader taxonomic range (Supplementary Fig. 9) in the presence of glucose as a carbon source and urea as a nitrogen source. Glucose can be converted to organic acids and acidify the medium[23], whereas urea can be converted by many bacteria into ammonia and alkalize the environment[24]. From these 119 strains, the 22 strongest pH modifiers (either in acidic or alkaline directions) were tested for the presence of ecological suicide by measuring the fold growth in 24h at low and high buffer concentrations (Fig. 4a). Indeed, around 25% of the strains suffered ecological suicide and were unable to survive at low buffer concentrations yet could be saved by more buffering (Fig. 4b). Another 20% grew better at high than low buffer, suggesting a self-inhibiting but non-deadly effect of the pH. Finally, one species even changed the pH in ways that supported its own growth (an effect discussed in more detail in a separate manuscript[9]). These results show that ecological suicide is not an exotic effect but appears rather often and its occurrence in nature should be investigated in the future.

Discussion:

We demonstrated that microbes are able to cause their own extinction by deteriorating the environment, a process we call ecological suicide. Several cases are described where microbial populations experience a slow decline after reaching saturation[25,26]. However, this decline is usually very slow compared to the growth rate and does not cause sudden population extinction. In ecological suicide, however, the population does not even reach saturation; instead, the bacteria switch immediately from a growth into a death phase (Fig. 1a). A notable exception are quorum sensing deficient mutants of several *Burkholderia species* that show a type of ecological suicide[27], whereas in the wildtype strains quorum

sensing mediates a change of metabolism that avoids ecological suicide. This shows that bacteria can possess mechanisms that actively counteract ecological suicide[27–29].

A phenomenon similar but not identical to ecological suicide is population overshoot, which is often connected to overexploitation of natural resources and has been proposed in several macro-organisms[30–32], but it is mostly discussed in humans that over-exploit the environment[33–35]. Several ancient civilizations are suspected to have collapsed by overexploitation of natural resources[36–38].Upon overshoot, a population exceeds the long-term carrying capacity of its ecosystem, followed by a drop of the population below the carrying capacity which usually does not lead to extinction of the population but is followed by recovery at a lower density[30,35]. However, in our case of ecological suicide, the carrying capacity of the ecosystem is changed to zero – the bacteria produce a deadly environment and go extinct without recovery, which marks ecological suicide as an extreme version of population overshoot.

In daily dilutions, ecological suicide can result in oscillatory behavior. Oscillations in ecology have been intensely studied, often as a consequence of species interactions[39,40]; in our system the second species is replaced by the pH value, resulting in a situation where interactions between one species and its environment drive the oscillations. In a similar way modifying and reacting to the environment have recently been described to cause metabolic oscillations in yeast[41], expanding waves in microbial biofilms[42] or by toxin production or resource competition[43,44].

In view of the high frequency of ecological suicide that we observed in natural isolates of soil bacteria, this effect may have a broad impact on microbial ecosystems in terms of microbial interactions and biodiversity[9] and its occurrence and ecological meaning in nature have to be investigated in the future. Moreover, ecological suicide can happen on different carbon sources, at lowered temperature of 22°C – although sufficiently low temperatures may stop

ecological suicide - and even complex sugars and thus under conditions that more resemble those in soil (Supplementary Fig. 1). In our case, the ecological suicide was mediated by the pH, but changing any environmental parameter, like oxygen levels or metabolite concentrations in self-harming ways may cause similar outcomes.

Our findings raise the question of how such self-inflicted death of microbes can exist and evolution did not select against them. We speculate that although ecological suicide is detrimental for the population it may be evolutionary beneficial for the individual bacterium. A fast metabolism of glucose may harm and even kill the population but benefits the individual compared to an individual that takes the burden of slower glucose metabolism to save the population. The phenomena of ecological suicide could therefore be an end product of evolutionary suicide[45]. Future work will explore the evolutionary origin of ecological suicide as well as the consequences of this phenomenon for the ecology and evolution of microbes.

Methods:

All chemicals were purchased from Sigma Aldrich, St. Louis, USA , if not stated otherwise.

Buffer:

For pre-cultures of the bacteria the basic buffer recipe was 10g/L yeast extract (Becton Dickinson, Franklin Lakes, USA) and 10g/L soytone (Becton Dickinson, Franklin Lakes, USA). We refer to that buffer as 1xNutrient medium (also 1xNu). The initial pH was 7 and 100mM phosphate were added. For the washing steps and the experiments itself the medium contained 1g/L yeast extract and 1g/L soytone, 0.1mM $CaCl_2$, 2mM $MgCl_2$, 4mg/L $NiSO_4$, 50mg/L $MnCl_2$ and 1x Trace Element Mix (Teknova, Hollister, USA). We refer to that buffer as base buffer. It was supplemented with phosphate buffer and/or glucose as outlined in the single experiments. The usual concentration was 10g/L glucose, deviations from that are described for the single experiments below. All media were filter sterilized.

Estimation of Colony Forming Units (CFU):

To estimate the number of living bacteria in the different experiments we used colony counting. At the end of every growth cycle a dilution row of the bacteria was made by diluting them once 1/100x and 6 times 1/10x in phosphate buffered saline (PBS, Corning, New York, USA). With a 96-well pipettor (Viaflo 96, Integra Biosciences, Hudson, USA) 10µL of every well for every dilution step were transferred to an agar plate (Tryptic Soy Broth (Teknova, Hollister, USA), 2.5% Agar (Becton Dickinson, Franklin Lakes, USA) with 150mm diameter. The droplets were allowed to dry in and the plates were incubated at 30°C for 1-2 days until

clear colonies were visible. The different dilution steps ensured that a dilution could be found that allowed for the counting of colonies.

pH measurements:

To measure the pH directly in the bacterial growth culture at the end of each growth cycle a pH microelectrode (N6000BNC, SI Analytics, Weilheim, Germany) was used. The grown up bacterial cultures were transferred into 96-well PCR plates (VWR, Radnor, USA) that allowed to measure pH values in less than 200µL.

Bacterial culture:

All cultures were incubated at 30°C. The pre-cultures were done in 5mL medium in 50mL culture tubes (Falcon/Becton Dickinson, Franklin Lakes, USA) over night in 1xNu described above with additional 100mM Phosphate. The shaking speed was 250rpm on a New Brunswick Innova 2100 shaker (Eppendorf, Hauppauge, USA), the lids of the falcons tubes were only slightly screwed on to allow gas exchange. Except for the 24 h experiment with hourly measurements, which were done in 50mL culture tubes (Falcon/Becton Dickinson, Franklin Lakes, USA), the experiments were all done in 500µl 96-deepwell plates (Deepwell Plate 96/500 µL, Eppendorf, Hauppauge, USA) covered with two sterile AearaSeal adhesive sealing films (Excell Scientific, Victorville, USA), the plates were shaken at 1350rpm on Heidolph platform shakers (Titramax 100, Heidolph North America, Elk Grove Village, USA). The culture volume was 200µl if not stated otherwise. To avoid evaporation the shakers were covered with a custom made polyacryl box (Wetinator 2000) with small water reservoirs placed within.

Pre-culture and preparation of bacteria**:**

For these experiments *Paenibacillus sp.* (Ps) was used, a bacterium that can acidify the environment but cannot tolerate low pH values. The bacterium was grown at 30°C. The preculture of Ps was done in 5mL 1xNu, pH 7 with 100mM phosphate for around 14h. Ps was diluted 1/100x into the same medium and grown to an OD/cm of 2. The bacterial solution was washed two times with base with 10mM Phosphate, pH 7. The bacteria were resuspended in the same base and the OD/cm adjusted to 2. The buffer concentration of the base was chosen as detailed in the experiments below.

24h experiment with hourly measurement of cell density and pH (Fig. 1):

Tubes were prepared by adding 10ml base with 10g/l glucose and different phosphate concentrations of 10, 14 and 100mM. The bacteria were added by 1/100x dilution. The tubes were incubated at 30°C, 1350rpm shaking. Every hour 200µL were taken from each tube, the CFU was estimated and the pH measured. For every measurement 3 technical replicates were done.

Density dependence of growth (Fig. 2a):

96-deepwell plates were prepared by adding 200µL base with 10g/l glucose and different Phosphate concentrations ranging from 10 to 100mM (see main text). To obtain different initial densities of bacteria, the bacteria were added by different dilutions ranging from 1/10x to $(1/4)^5$/10x dilution. The 96-deepwell plates were incubated at 30°C, 1350rpm shaking. At

the beginning of the experiment as well as after 24h, the CFU was estimated. After 24h the pH was measured. For every condition there are two biological replicates as well as two technical replicates.

Growth under daily dilution (Fig. 2B-d):

96-deepwell plates were prepared as for the 'density dependence of growth' experiment. The bacteria were added by 1/100x dilution. The 96-deepwell plates were incubated at 30°C, 1350rpm shaking. At the beginning of the experiment as well as after 24h, the CFU was estimated. After 24h the pH was measured. Every 24h the CFU estimated and the pH were measured and the bacteria were diluted 1/100x into fresh medium. To study the dynamics of bacterial growth and the pH, at the beginning of each day, the bacteria were also diluted 1/100x into a 96-well plate (96 Well Clear Flat Bottom TC-Treated Culture Microplate, 353072, Falcon, Corning, USA) with the same medium in each well as for the 500µl 96-deepwell plate. In addition, every well was supplemented by fluorescent nanobeads (1/100x dilution), which we fabricated as detailed below. In parallel to the incubation of the 500µl 96-deepwell plate, this 96-well plate was then observed in a Tecan infinite 200 Pro (Tecan, Männedorf, Switzerland) at 30°C, 182rpm , 4mm amplitude. Here, the OD was measured via absorbance and the fluorescence of the nanobeads was measured by exciting fluorescein (excitation wavelength 450nm, emission wavelength 516nm) and TFPP (excitation wavelength 582nm, emission wavelength 658nm). Measuring the OD of the bacteria and the fluorescence of the nanobeads every 15min in the course of one day enabled us to track the change of the pH. Although the OD and fluorescence were measured in the parallel growing 96-well plate, we argue that they (at least qualitatively) capture the dynamics in the 96-deepwell plate, which is

underlined by the fact that the measured acidification time and bacterial density oscillate synchronous (Fig. 2d). Parallel to the oscillations in the CFU observed in the 96-deepwell plates, the fluorescence measurements in the 96-well plates display oscillations in the timepoint, the pH drops, i.e. the timepoints of the fluorescence intensity's turning points (see Fig.2d, Fig. S2).For every buffer condition there were 4 biological replicates in the 96- well and 96-deepwell plates.

Fabrication of fluorescent nanobeads:

To study the change of pH during our daily dilution experiments, we fabricated fluorescent nanobeads following a protocol established previously[46]. These nanobeads contain fluorescein, whose fluorescence intensity depends on the pH[47] , and a highly photostable fluorinated porphyrin (TFPP), which acts as a red-emitting reference dye. Since the fluorescence intensity of TFPP is independent of pH it serves as internal standard to make the result independent of the overall nanobead concentration. Thus the ratio of the fluorescein and TFPP fluorescence signals is a function only of the pH value (Supplementary Fig. 4).

Effect of harmful conditions on bacterial survival (Fig. 3):

The pre-culture was done overnight in 1xNu, pH7 with 100mM Phosphate. After 15h the bacteria were diluted 1/100x into the same medium. Upon reaching OD/cm 2 the bacteria were washed two times with base buffer and the OD/cm adjusted to 2. The bacteria were diluted 1/100x into 96-deepwell plates (Eppendorf, Hauppauge, USA) containing base medium, pH 7 with 10g/L glucose and different amounts of Kanamycin, NaCl or Ethanol. For

Fig. 3a the glucose concentration was varied. The bacteria were incubated for 24h at 30°C, 1350rpm on a Heidolph platform shakers (Titramax 100, Heidolph North America, Elkove Village, USA) as described above. The live cell density was estimated via colony counting upon start of the experiment and after 24h. The pH was measured after 24h with a pH microelectrode as described above.

Frequency of ecological suicide (Fig. 4):

For this experiment 21 different soil bacteria were used, which were identified out of 119 soil bacteria to yield the highest change in pH. The 119 bacterial strains were isolated from a single grain of soil collected in September, 2015 in Cambridge, Mass., U.S.A. The grain weighed ~1 mg and was handled using sterile technique. The grain was washed in phosphate-buffered saline (PBS) and serial dilutions of the supernatant were plated on nutrient agar (0.3% yeast extract, 0.5% peptone, 1.5% bacto agar) and incubated for 48hrs at room temperature. Isolated colonies were sampled and cultured at room temperature in 5 mL nutrient broth (0.3% yeast extract, 0.5% peptone) for 48hrs. To ensure purity, the liquid cultures of the isolates were diluted in PBS and plated on nutrient agar. Single colonies picked from these plates were once again grown in nutrient broth for 48hrs at room temperature and the resulting stocks were stored in 20% glycerol at -80 C. The 16S rRNA gene was sequenced via Sanger sequencing of DNA extracted from glycerol stocks carried out at GENEWIZ (South Plainfield, New Jersey, U.S.A.). Sequencing was performed in both directions using the company's proprietary universal 16S rRNA primers, yielding assembled sequences ~1100nt in usable length. Some of those strains have been in more detail investigated in[24].

In order to identify the 21 species causing the strongest pH change, precultures of the 119 soil bacteria were done in 200µL 1xNu, pH 7 with 100mM phosphate for 14h at room temperature, 800rpm shaking. The precultures were then diluted 1/100x into the same medium and grown for 6hrs, which approximately corresponded to a growth to an OD/cm of 2 for the precultures of Ps used in the Ps experiments detailed above. The bacteria were then diluted 1/100x into fresh medium and grown for 24hrs at room temperature, 800rpm shaking. After 24hrs, the bacterial density (CFU/ml) and pH of all cultures were measured and the 21 bacteria with the highest change in pH were selected.

For these 21 species, precultures were done in 5mL 1xNu, pH 7 with 100mM phosphate for 14hrs. The cultures were diluted 1/100x into the same medium and grown to an OD/cm of approximately 2. The bacteria were resuspended in the same base and the OD/cm adjusted to 2. To categorize the species according to 'suicidal', 'self-inhibiting', 'self-supporting' and 'neutral' each species was grown in the same base once with high buffer concentration (100mM phosphate) and once with low buffer concentration (10mM phosphate). At the beginning and after 24hrs, the CFU was estimated. The pH was measured after 24hrs with a pH microelectrode as described above.

Data availability:

All data generated or analysed during this study are included in this published article (and its supplementary information files)

References:

1. Celiker, H. & Gore, J. Cellular cooperation: insights from microbes. *Trends Cell Biol.* **23,** 9–15 (2013).
2. Ratzke, C. & Gore, J. Self-organized patchiness facilitates survival in a cooperatively growing Bacillus subtilis population. *Nat. Microbiol.* **1,** 16022 (2016).
3. Drescher, K., Nadell, C. D., Stone, H. A., Wingreen, N. S. & Bassler, B. L. Solutions to the Public Goods Dilemma in Bacterial Biofilms. *Curr. Biol.* **24,** 50–55 (2014).
4. Celiker, H. & Gore, J. Competition between species can stabilize public-goods cooperation within a species. *Mol. Syst. Biol.* **8,** 621 (2012).
5. Anderson, D. E., Becktel, W. J. & Dahlquist, F. W. pH-induced denaturation of proteins: a single salt bridge contributes 3-5 kcal/mol to the free energy of folding of T4 lysozyme. *Biochemistry (Mosc.)* **29,** 2403–2408 (1990).
6. Träuble, H., Teubner, M., Woolley, P. & Eibl, H. Electrostatic interactions at charged lipid membranes. *Biophys. Chem.* **4,** 319–342 (1976).
7. Jones, R. T. *et al.* A comprehensive survey of soil acidobacterial diversity using pyrosequencing and clone library analyses. *ISME J.* **3,** 442–453 (2009).
8. Rousk, J., Brookes, P. C. & Bååth, E. Contrasting Soil pH Effects on Fungal and Bacterial Growth Suggest Functional Redundancy in Carbon Mineralization. *Appl. Environ. Microbiol.* **75,** 1589–1596 (2009).
9. Ratzke, C. & Gore, J. Modifying And Reacting To The Environmental pH Drives Bacterial Interactions. *bioRxiv* 136838 (2017).
10. Russell, J. B. & Dombrowski, D. B. Effect of pH on the efficiency of growth by pure cultures of rumen bacteria in continuous culture. *Appl. Environ. Microbiol.* **39,** 604–610 (1980).

11. Raven, J. A. & Smith, F. A. The evolution of chemiosmotic energy coupling. *J. Theor. Biol.* **57,** 301–312 (1976).
12. Safařík, I. V. O. & Šantrůčková, H. Direct determination of total soil carbohydrate content. *Plant Soil* **143,** 109–114 (1992).
13. Mehta, N. C., Dubach, P. & Deuel, H. Carbohydrates in the Soil. in *Advances in Carbohydrate Chemistry* (ed. Wolfrom, M. L.) **16,** 335–355 (Academic Press, 1962).
14. Li, C. H., Ma, B. L. & Zhang, T. Q. Soil bulk density effects on soil microbial populations and enzyme activities during the growth of maize (Zea mays L.) planted in large pots under field exposure. *Can. J. Soil Sci.* **82,** 147–154 (2002).
15. Raynaud, X. & Nunan, N. Spatial Ecology of Bacteria at the Microscale in Soil. *PLOS ONE* **9,** e87217 (2014).
16. Seviour, R. & Nielsen, P. H. *Microbial Ecology of Activated Sludge*. (IWA Publishing, 2010).
17. Seviour, E. M. *et al.* Studies on filamentous bacteria from australian activated sludge plants. *Water Res.* **28,** 2335–2342 (1994).
18. Allee, W. C. E. al. *Principles of Animal Ecology*. (W. B. Saunders, 1965).
19. Courchamp, F., Clutton-Brock, T. & Grenfell, B. Inverse density dependence and the Allee effect. *Trends Ecol. Evol.* **14,** 405–410 (1999).
20. Stephens, P. A., Sutherland, W. J. & Freckleton, R. P. What Is the Allee Effect? *Oikos* **87,** 185–190 (1999).
21. Stebbing, A. R. D. Hormesis — The stimulation of growth by low levels of inhibitors. *Sci. Total Environ.* **22,** 213–234 (1982).

22. Higgins, L. M., Friedman, J., Shen, H. & Gore, J. Co-occurring soil bacteria exhibit a robust competitive hierarchy and lack of non-transitive interactions. *bioRxiv* 175737 (2017). doi:10.1101/175737
23. Paczia, N. *et al.* Extensive exometabolome analysis reveals extended overflow metabolism in various microorganisms. *Microb. Cell Factories* **11,** 122 (2012).
24. Fujita, Y., Ferris, F. G., Lawson, R. D., Colwell, F. S. & Smith, R. W. Subscribed Content Calcium Carbonate Precipitation by Ureolytic Subsurface Bacteria. *Geomicrobiol. J.* **17,** 305–318 (2000).
25. Finkel, S. E. Long-term survival during stationary phase: evolution and the GASP phenotype. *Nat. Rev. Microbiol.* **4,** 113–120 (2006).
26. Burtner, C. R., Murakami, C. J., Kennedy, B. K. & Kaeberlein, M. A molecular mechanism of chronological aging in yeast. *Cell Cycle* **8,** 1256–1270 (2009).
27. Goo, E. *et al.* Bacterial quorum sensing, cooperativity, and anticipation of stationary-phase stress. *Proc. Natl. Acad. Sci.* **109,** 19775–19780 (2012).
28. An, J. H., Goo, E., Kim, H., Seo, Y.-S. & Hwang, I. Bacterial quorum sensing and metabolic slowing in a cooperative population. *Proc. Natl. Acad. Sci.* **111,** 14912–14917 (2014).
29. Cotter, P. D. & Hill, C. Surviving the Acid Test: Responses of Gram-Positive Bacteria to Low pH. *Microbiol. Mol. Biol. Rev.* **67,** 429–453 (2003).
30. Klein, D. R. The Introduction, Increase, and Crash of Reindeer on St. Matthew Island. *J. Wildl. Manag.* **32,** 350–367 (1968).
31. Scheffer, V. B. The rise and fall of a reindeer herd. *Sci. Mon.* **73,** 356–362 (1951).
32. Hindell, M. A. Some Life-History Parameters of a Declining Population of Southern Elephant Seals, Mirounga leonina. *J. Anim. Ecol.* **60,** 119–134 (1991).

33. Wackernagel, M. *et al.* Tracking the ecological overshoot of the human economy. *Proc. Natl. Acad. Sci.* **99,** 9266–9271 (2002).
34. Malthus, T. R. *An Essay on the Principle of Population, as it Affects the Future Improvement of Society: With Remarks on the Speculations of Mr. Godwin, Mr. Condorcet, and Other Writers*. (1798).
35. Meadows, D., Randers, J. & Meadows, D. *Limits to Growth: The 30-Year Update*. (Chelsea Green Publishing, 2004).
36. Diamond, J. *Collapse: How Societies Choose to Fail or Succeed*. (Penguin, 2005).
37. Tainter, J. A. Archaeology of Overshoot and Collapse. *Annu. Rev. Anthropol.* **35,** 59–74 (2006).
38. Shennan, S. *et al.* Regional population collapse followed initial agriculture booms in mid-Holocene Europe. *Nat. Commun.* **4,** 2486 (2013).
39. Fussmann, G. F., Ellner, S. P., Shertzer, K. W. & Jr, N. G. H. Crossing the Hopf Bifurcation in a Live Predator-Prey System. *Science* **290,** 1358–1360 (2000).
40. Yurtsev, E. A., Conwill, A. & Gore, J. Oscillatory dynamics in a bacterial cross-protection mutualism. *Proc. Natl. Acad. Sci.* **113,** 6236–6241 (2016).
41. Tu, B. P., Kudlicki, A., Rowicka, M. & McKnight, S. L. Logic of the Yeast Metabolic Cycle: Temporal Compartmentalization of Cellular Processes. *Science* **310,** 1152–1158 (2005).
42. Liu, J. *et al.* Coupling between distant biofilms and emergence of nutrient time-sharing. *Science* eaah4204 (2017).
43. Collos, Y. *et al.* Phased Oscillations in Cell Numbers and Nitrate in Batch Cultures of Alexandrium Tamarense (dinophyceae)1. *J. Phycol.* **47,** 1057–1062 (2011).

44. Cornejo, O. E., Rozen, D. E., May, R. M. & Levin, B. R. Oscillations in continuous culture populations of Streptococcus pneumoniae: population dynamics and the evolution of clonal suicide. *Proc. R. Soc. Lond. B Biol. Sci.* **276,** 999–1008 (2009).
45. Parvinen, K. Evolutionary suicide. *Acta Biotheor.* **53,** 241–264 (2005).
46. Wang, X., Meier, R. J. & Wolfbeis, O. S. Fluorescent pH-Sensitive Nanoparticles in an Agarose Matrix for Imaging of Bacterial Growth and Metabolism. *Angew. Chem. Int. Ed.* **52,** 406–409 (2013).
47. Rein, J. *et al.* Fluorescence measurements of serotonin-induced V-ATPase-dependent pH changes at the luminal surface in salivary glands of the blowfly *Calliphora vicina*. *J. Exp. Biol.* **209,** 1716–1724 (2006).

Acknowledgements:

We thank Loggan Higgins for providing us with the collection of bacterial soil isolates. J.D. is supported by a DFG fellowship through the Graduate School of Quantitative Biosciences Munich (QBM). We thank all members of the Gore lab for reading and discussing the manuscript. This work was funded by an Allen Distinguished Investigator Award, Simons Foundation and a NIH R01 grant.

Author contributions:

C.R. and J.D. contributed equally to this work. C.R., J.D. and J.G. designed the research. J.D. and C.R. and J.G. carried out the experiments and performed the mathematical analysis. C.R., J.D. and J.G discussed and interpreted the results, and wrote the manuscript.

Author Information:

The authors declare no competing financial interests. Correspondence and requests should be sent to cratzke@mit.edu or gore@mit.edu.

Figures and Legends:

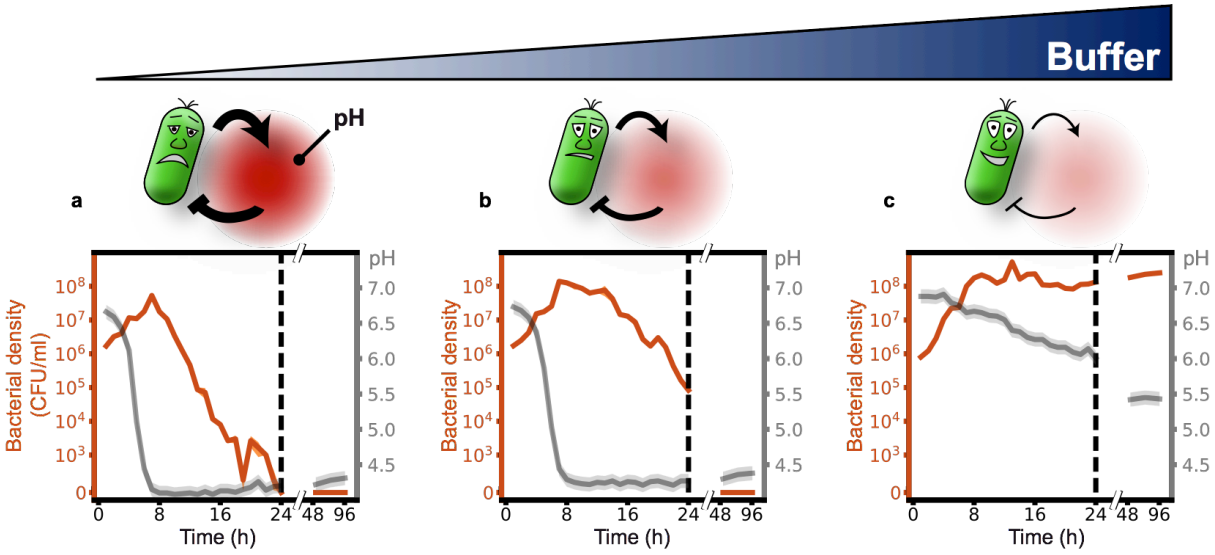

Fig. 1: Microbial acidification can cause ecological suicide. *Paenibacillus sp.* was grown in well-mixed batch culture in media containing 1% glucose as main carbon source and minor amounts of complex nutrients (see methods). **(a)** At low buffer concentrations (10mM phosphate) initially growing bacteria change the pH of the medium so drastically that they cause their own extinction. **(b-c)** Adding increasing amounts of buffer (14 and 100mM phosphate) tempers the acidification, and finally allows for survival of the bacteria. Mean bacterial density (CFU/ml) and SEM are shown for three technical replicates in orange (solid line and shaded region, respectively). pH is shown in gray (solid line); the shaded region depicts the estimated measurement accuracy.

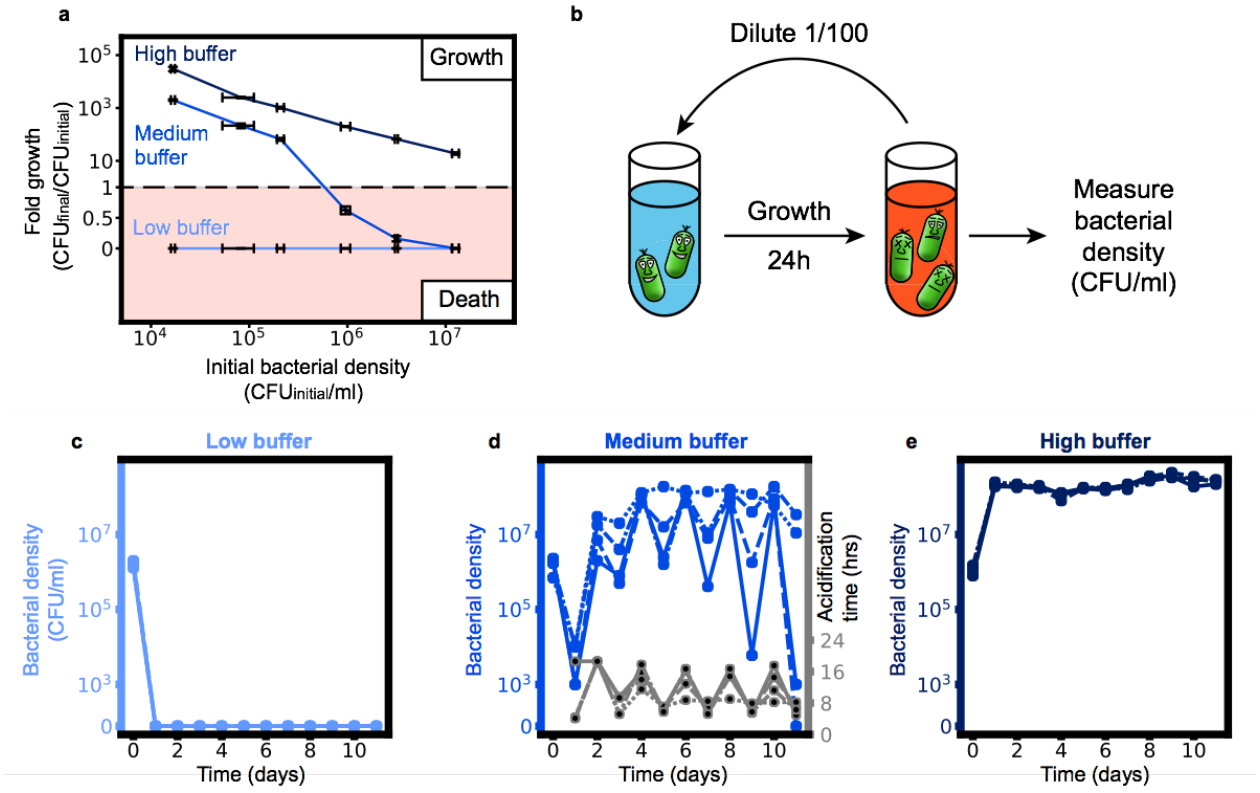

Fig. 2: Ecological suicide can cause oscillations in the population size over time. (a) At low buffer concentration (10mM phosphate) the bacteria commit ecologic suicide and at high buffer concentration (100mM phosphate) the bacteria grow, in both cases independent of their initial density. However, in moderate buffer concentration (26mM phosphate) the bacteria die at high starting densities and grow at low starting densities. The fold growth at high buffer concentration decreases for increasing initial bacterial densities since the final bacterial density equals the carrying capacity and is thus constant. Mean (solid lines) and SEM (error bars) are shown for four replicates. **(b)** To explore long time growth dynamics the bacteria were grown in a daily dilution scheme with 24h of incubation in well mixed conditions followed by a 1/100x dilution into fresh media. **(c and e)**. At low (10mM phosphate) and high (100mM phosphate) buffer conditions the bacteria either die on the first day or grow to saturation every day. **(d)** However, at medium buffer conditions we measure oscillatory dynamics of the

bacterial density. This is accompanied by oscillations in the time the bacteria need to acidify the environment (acidification time, Supplementary Fig. 8). The exact type of oscillatory dynamics depends on the slope and shape of the curve in **(a)**, as discussed in more detail in the supplement. The four blue lines in **(c-e)** (solid, dashed, dotted, dashed-dotted) show different replicates. The strong differences between the replicates highlight the sensitivity of these oscillations to experimental conditions and that they do likely not show a limit cycle oscillation.

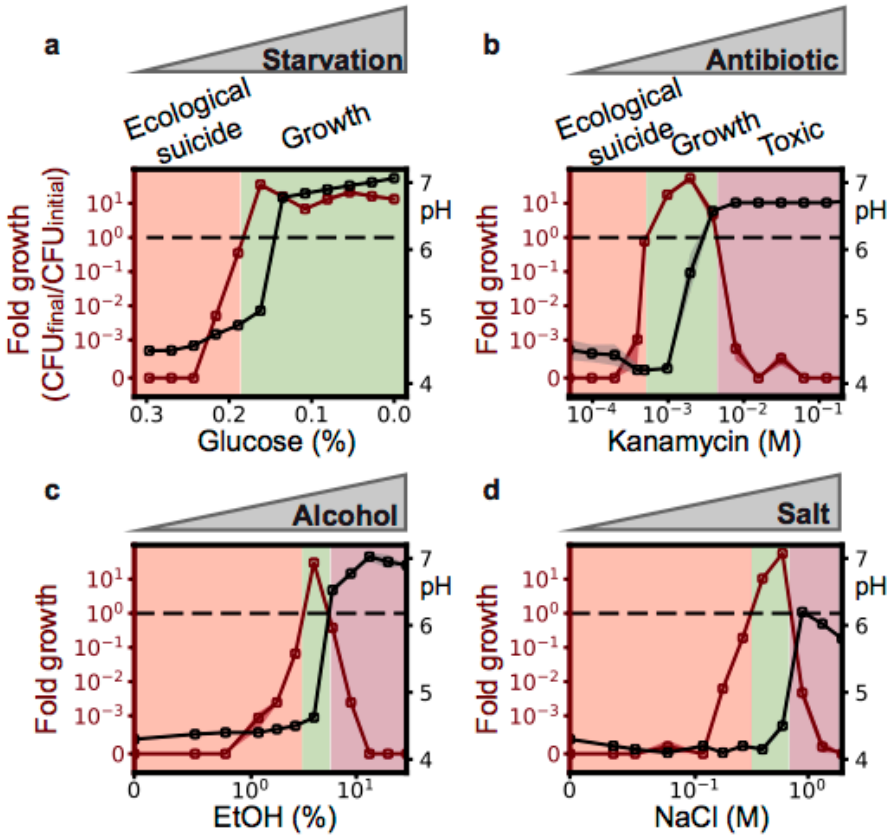

Fig. 3: Inhibiting growth of the bacteria can save the population. (a) Reducing sugar concentration prevents ecological suicide. At moderate concentrations, the addition of bactericidal substances like antibiotics **(b)**, alcohol **(c)** or high amounts of sodium chloride **(d)** can save the population from ecological suicide. Open circles and shaded regions depict respectively mean and SEM of four replicates (orange: fold growth, gray: pH). All values are final values of 24h.

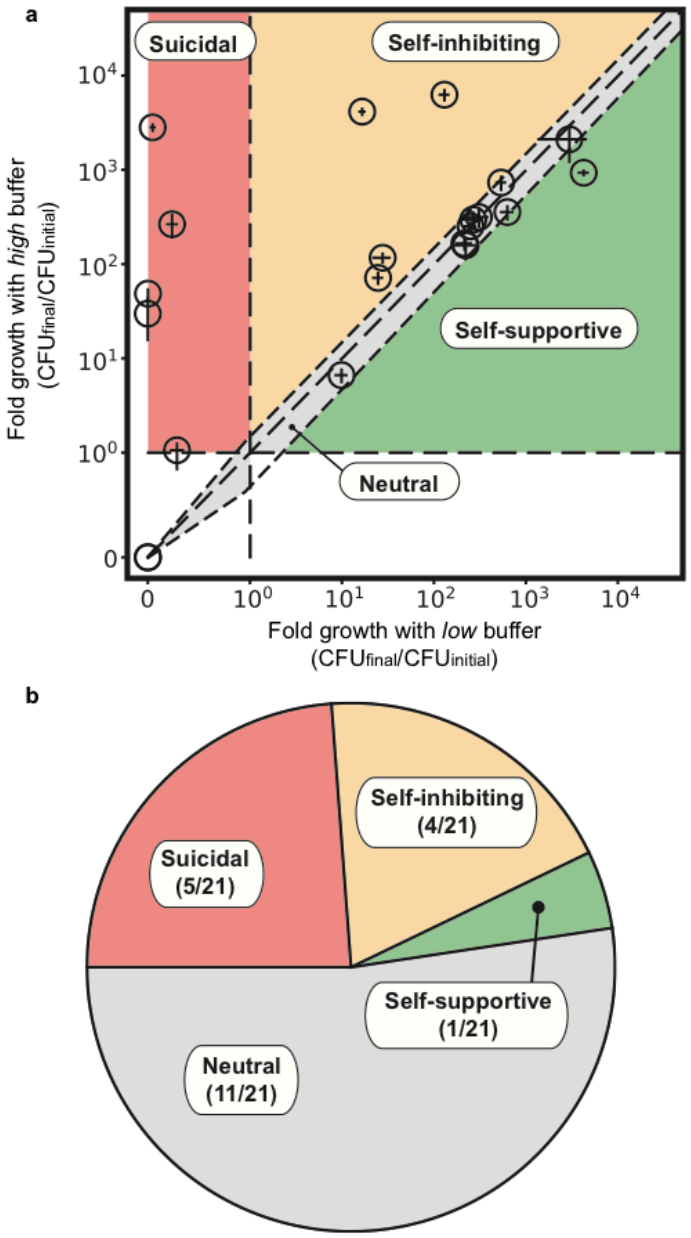

Fig. 4: Ecological suicide is a common phenomenon in microbes. 21 bacteria that strongly modified the pH were tested for ecological suicide by growing them on a medium containing 1% glucose and 0.8% urea at low buffer (10mM Phosphate) and high buffer (100mM Phosphate) conditions. Bacteria that die at low buffer but grow at high buffer concentrations were counted as ecological suicide (suicidal, 5). Bacteria that grow slower at low buffer than high buffer conditions are called self-inhibiting (4). Bacteria that grow in similar ways at low and high buffer (growth in one buffer condition is between equal and 1.5 fold relative to growth in the other condition) were called neutral (11) and bacteria that grow better with low than with high buffer are called self-supportive (1). The circles mark the mean of eight replicates for each individual bacterium; The lengths of the bars denote the SEM in x and y direction respectively.

Supplementary Materials for

Ecological suicide in microbes

Christoph Ratzke*[1†], Jonas Denk*[2] and Jeff Gore[1†]

[1] **Physics of Living Systems, Department of Physics, Massachusetts Institute of Technology, Cambridge, MA, USA**

[2] **Arnold-Sommerfeld-Center for Theoretical Physics and Center for NanoScience, Ludwig-Maximilians-Universität München, Theresienstraße 37, D-80333 München, Germany**

*equal contribution

[†] correspondence should be sent to: cratzke@mit.edu or gore@mit.edu

In these Supplementary notes we further elaborate our dynamical analysis of ecological suicide in microbes. We first discuss the dependence of the fluorescence intensity of our fabricated nanobeads (see Methods) on the pH. Then, we present time resolved measurements of the optical density and the fluorescence intensity of these nanobeads throughout our daily dilution experiments.

To test our conceptual understanding of ecological suicide in Paenibacillus sp. (Ps), we present a mathematical description based on our experimental observations. We show that the proposed mathematical equations capture the complete phenomenology of ecological suicide in Ps, including non-monotonic growth dynamics and oscillatory behavior in daily dilutions.

Paenibacillus sp. isolation and phylogeny:

The Paenibacillus sp. was isolated from a grain of soil collected in Cambridge, MA, USA and was part of a soil species collection that will be described in more detail elsewhere (Logan Higgins et al, in prep). The 16S rRNA of this strain was sequenced and is most closely related to Paenibacillus tundrae A10b[1] according to RDB/SeqMatch tool[2] with a similarity score of 0.995 and a S_{ab} score of 0.975. For a characterization of all 21 species shown in Fig.4, please refer to Fig. S9. Also here we used the to RDB/SeqMatch tool and assigned the used bacteria to their closest related bacteria based in the maximal similarity score and S_{ab}. For a characterization of all 21 species shown in Fig.4, please refer to Supplementary Fig. 9. Also here we used the to RDB/SeqMatch tool and assigned the used bacteria to their closest related bacteria based in the maximal similarity score and S_{ab}.

Paenibacillus sp. growth at different pH values and its production of organic acids

Paenibacillus sp. was pre-cultured in tryptic soy broth. The next day it was diluted into 1xNu with 100mM Phosphate pH7 and grown to OD2. After washing three times in Base medium with 10mM

Phosphate the bacteria were adjusted to an OD of 2 and diluted 1/100x into Base medium with 100mM Phosphate with the pH ranging from 3 to 7. The CFU was measured at the beginning and after 24hours to obtaine a fold growth of the bacteria. As can be seen in Fig. S1A Paenibacillus sp. cannot grow at low pH values. This is in line with Fig. 1 where upon reaching a pH of around 5 the bacteria start to die and again shows that it is the pH that drive the ecological suicide.

To better understand how Paenibacillus sp. changes the pH of the medium we grew it in M9 buffer with 2% Glucose as only carbon source. After 24hours the spent medium was analyzed with mass spectrometry. As can be seen in Fig. S1B a variety of organic acids could either be found to increase in concentration or to become detectable at all.

The proton concentration in a buffer system is given by:

$$\mathrm{H} = \frac{\mathrm{K_d HA}}{\mathrm{A}}$$

with H as proton concentration, K_d as the dissociation constant and A as the base concentration. This can be converted by canceling out the volume into

$$\mathrm{H} = \frac{\mathrm{K_d n_{HA}}}{\mathrm{n_A}}$$

Upon adding a small amount hydrochloric acid n_{HCl} this acid reacts with the acid and base present such that:

$$\mathrm{H_{new}} = \frac{\mathrm{K_d}(\mathrm{n_{HA}} + \mathrm{n_{HCl}})}{\mathrm{n_A} - \mathrm{n_{HCl}}}$$

from which the buffer capacity will be obtained as

$$\frac{-\log(\mathrm{H_{new}})+\log(\mathrm{H_{old}})}{\Delta \mathrm{n_{HCl}}}.$$

Thus, the buffer capacity is independent from the volume (and thus the soil can be diluted with water without affecting the buffer capacity) but just depends on the total amount of buffer, therefore the initial volume/mass for all samples was 5mL/5g.

Dependence of the nanobeads' fluorescence intensity on the pH:

To study the dynamics of the pH, we fabricated fluorescent nanobeads (see methods) which show a pH-dependent fluorescence intensity[3]. These nanobeads contain fluorescein, whose fluorescence intensity depends on the pH, and a highly photostable fluorinated porphyrin (TFPP), which acts as a red-emitting pH independent reference dye. Since the fluorescence intensity of TFPP is independent of pH it serves as internal standard to make the result independent of the overall nanobead concentration. Thus, the ratio of the fluorescein and TFPP fluorescence signals is a function only of the pH value. Since in our 24-hours experiments the pH varied between 4 and 7, we measured the fluorescence intensity ratio of the nanobeads for different pH values in this range. The fluorescence intensity ratio increases monotonic for increasing pH. Moreover, the slope of the intensity ratio decreases for decreasing pH and the intensity seems to saturate for low pH (Fig. S4).

Dynamic measurements of the optical density and pH**:**

As detailed in the main text (Fig. 2c-e), our daily dilution experiments show oscillatory behavior of the bacterial density, which was measured at the end of each day. In contrast, we could not observe significant oscillations in the pH at the end of each day, i.e. for a certain buffer concentration, the pH after one day was approximately constant (Fig. S5).

This suggests that from the pH values at the end of each day it is not possible to infer the (oscillating) behavior of the bacterial density. Therefore, we also studied the dynamics of the pH during the course of each day during our daily dilution experiment. To this end, we prepared parallel experiments with the same buffer conditions and initial bacterial dilutions as for the daily dilution experiments (see Methods). In contrast to the daily dilution experiments, to these parallel experiments we also added fluorescent nanobeads and measured the optical density and fluorescence intensity of the nanobeads (see Methods). Whereas for the bacterial density (CFU/ml) at the end of each day we counted the living bacteria, the optical density provides a measurement for the total amount of bacteria (dead and alive). As detailed above (Fig. S4), the fluorescence intensity ratio of the nanobeads provides a measure for the pH.

For very low buffer concentrations (10mM phosphate), our daily dilution experiments (Fig. 2 left) display ecological suicide during the first day already. Consistently, in the corresponding parallel experiment with fluorescent nanobeads we find an early and strong decrease of the fluorescence intensity ratio after four hours of the first day already, indicating a strong decrease in pH (Fig. S6). This drop in pH is accompanied by a rapid increase of the optical density. On the second day (and all following days), the optical density mostly stays constant for the entire day. This strongly suggests that the bacteria have died on the first day already, which is underlined by finding no viable cells via plating on rich medium agar (Fig. 2c). In all measurements of the nanobeads' intensity ratio, we find an initial rapid increase. We argue that this initial increase is due to the initial increase in temperature during the initial heating of the PlateReader to 30°C. When suspended in pure base (without bacteria) we indeed observed an increase of the fluorescence signal of the nanobeads for increasing temperature (Fig. S7).

For high buffer concentrations, the optical density and the nanobeads' fluorescence intensity show a similar respective increase or decrease on each day (Fig. S8 a,c). This is consistent with the daily saturation of the bacterial density observed in our daily dilution experiments (Fig. 2e). As mentioned above, for intermediate buffer concentrations we could observe oscillations in the bacterial density but not in the pH at the end of each day (Fig. S5). However, our parallel experiments with fluorescent nanobeads reveal oscillatory behavior of the time the fluorescence intensity–and thus also the pH– drops (acidification time, which is

defined as the turning point of the resulting S-shaped fluorescence ratio curve). A late drop of the fluorescence is accompanied with a high final bacterial density in the daily dilution experiment and an early drop with a low final bacterial density. Hence, for intermediate buffer concentration the acidification time in our parallel experiment oscillates with the bacterial density in the daily dilution experiment (Fig. S8).

Mathematical approach to ecological suicide**:**

As detailed in the main text, our conceptual understanding of ecological suicide is based on the following principles: bacterial growth leads to a change in their environment (pH) in a way that eventually harms themselves and leads to their own death. Hence, bacteria experience a negative feedback mediated by the surrounding pH. It is important to note that we do not seek a complete description of ecological suicide including all the molecular details, but rather want to test our conceptual understanding (negative feedback) on a phenomenological level. Here, we show that from a mathematical perspective, ecological suicide is a very generic phenomenon, which can be captured by a minimal extension of previous mathematical descriptions of bacterial growth[5]. Bacteria have an optimal pH value where they grow best[8,9]. Deviations from this value deteriorate their growth and can even cause their extinction. To account for this pH dependence of bacterial growth, we propose the following dynamics for the bacterial density n :

$$\frac{dn}{dt} = \alpha\, n\left(1 - \frac{n}{\kappa}\right) \Gamma[p], \qquad (1)$$

where α and κ are the growth rate and the carrying capacity, respectively, and the function $\Gamma[p]$ depends on the proton concentration p and represents the effect of the proton concentration (pH) on the bacterial growth. For a constant $\Gamma[p]$, this equation is the well-studied logistic growth with growth rate $\alpha\Gamma$ and carrying capacity κ. One ad hoc choice to account for a pH dependence of the bacterial growth is to assume that the deterioration of bacterial growth with changing proton concentration follows a Gaussian. Here, we define

$$\Gamma[p] = 1 - \frac{1-\exp\left[\frac{(p-p_{opt})^2}{2\sigma^2}\right]}{1-\exp\left[\frac{(p^c)^2}{2\sigma^2}\right]}, \quad (2)$$

where p_{opt} denotes the optimal proton concentration and p^c denotes some critical proton concentration deviation beyond which bacteria start to die. All of these proton concentrations are not in physical units but instead are meant to capture the dynamics of the proton concentration. σ determines how far from the optimal proton concentration the species can grow / survive. Based on the strong correlation between the increase in the optical density and the fluorescence intensity ratio (Fig. S6 and S8), we assume that the change in pH—and thus the proton concentration—is directly related to the growth of the bacteria. A naive assumption would therefore be that the change in proton concentration is simply proportional to the change in bacterial density and is completely determined by equation (1). However, note that in this case the system reduces to a system of only one dynamic variable (the bacterial density n), which would not be able to reproduce non-monotonic growth[39] as observed in our experiments (Fig. 1). There are many ways to implement a negative feedback of the proton concentration on the bacterial density capable of reproducing non-monotonic behavior as observed in our experiments[4,5]. The goal of our mathematical description is not to account for the molecular details of the process, which would involve the complex (and largely unexplored) metabolism of the particular bacteria under consideration (in our case Paenibacillus sp.). In contrast, our goal is to develop a simple mathematical model that delivers intuition about the dynamics of ecological suicide in Paenibacillus sp. and test its consequences especially in the light of the experimental findings like non-montonous growth and oscillations.

Fig. 1c displays a decrease of the pH even after saturation of the bacterial density and thereby suggests, that the proton concentration also couples to the bacterial density itself. Since, in principle, the proton concentration could depend on both the change of the bacterial density and the bacterial density itself, we make the following approach for the dynamics of p:

$$\frac{dp}{dt} = \beta_1 \left(\frac{dn}{dt}\right) \Theta\left[\frac{dn}{dt}\right] + \beta_2 n, \quad (3)$$

where β_1 and β_2 are (real, positive) coupling parameters. $\Theta[\cdot]$ denotes the Heaviside step function, which is one for a positive argument and zero otherwise and accounts for our assumption that bacteria increase the proton concentration during their growth, but do not affect the pH when they die. Whereas high β_1 and β_2 will yield a fast increase in the proton concentration with bacterial growth and total density respectively, for very low β_1 and β_2 the proton concentration will hardly change. We therefore assume a decrease of and to emulate an increase in buffer concentration in our experiments. This model is thus an extension of the simpler model used in[10]. Measuring time, bacterial density and proton concentration in units of $1/\alpha$ and κ, and p_{opt}, respectively, the only independent parameters are the rescaled coefficients coupling p to $\frac{dn}{dt}$ and n given by $\beta_1' = \frac{\beta_1 \kappa}{p_{opt}}$ and $\beta_2' = \frac{\beta_2 \kappa}{\alpha\, p_{opt}}$, respectively, the rescaled critical proton concentration deviation $\frac{p^c}{p_{opt}}$, and the rescaled spread $\frac{\sigma}{p_{opt}}$. Fig. S10 a-c show the dynamics of the bacterial density and the proton concentration as a function of time for a certain time interval $\frac{24}{\alpha}$, which is proposed to simulate daily growth. In all simulations we chose the same values $\frac{p^c}{p_{opt}} = 0.6$ and $\frac{\sigma^2}{p_{opt}^2} = 1.0$, assumed the initial proton concentration to be optimal and only varied the coupling coefficients β_1' and β_2'. For convenience, the proton concentration is plotted as $-\log(p)$, which is up to some scaling the corresponding pH of the system. Similar to our experimental observations for increasing the buffer concentration (compare to Fig.1 a-c), decreasing the coupling of the proton concentration to the bacterial density (by lowering β_1' and β_2') shows a transition from a rapid decline of the bacterial density for strong coupling to saturation of the bacterial density at the carrying capacity for weak coupling (Fig. S10 a-c). Note, that due to the continuous description, the bacterial density cannot reach zero (extinction) but only approaches zero for infinite times. However, from our daily dilution experiments (Fig. 1c) we can estimate the carrying capacity with approximately 10^8 cells; hence bacterial densities below $\kappa/10^8$ would correspond to less than one cell. We therefore assume that bacterial densities below $\kappa/10^8$ correspond to extinction in our experiments and manually set the bacterial density to zero, if it is lower than $\kappa/10^8$. Starting at different initial conditions, the fold growth of the bacteria is decreasing for increasing initial concentrations (Fig. S10 d), as observed in our experiments (Fig. 2a). Similarly, there is a critical maximal initial density above which the bacteria start to die out (the fold growth drops

below 1). Eqs.(1)-(3) were solved for different initial bacterial densities and proton concentrations as well as different rescaled coupling coefficients and using NDsolve[] in Wolfram Mathematica 11. Similar to our experiments, this reciprocal dependence of the initial to the final density leads to interesting behavior when simulated in a "daily dilution" simulation: Here, we numerically integrated equations (1) to (3) for times up to $t = 24/\alpha$, which in line with our above simulations represents one day of our experiments. To account for the 1/100x daily dilution, the final bacterial concentration is multiplied by a factor of 1/100 and then taken as the initial bacterial density of the subsequent simulation. Note, that this procedure can be understood as a discrete map for the bacterial density, where - apart from the dilution factor of 1/100 - the mapping is given by the relation of the bacterial density at $t = 24/\alpha$ and $t = 0$ as given in Fig. S6d. Discrete maps show a rich phenomenology ranging from stable fixed points and limit cycles to chaos and can be very sensitive to the form of the mapping function[6]. Similarly, we expect that changing the form of the mapping function (Fig. S10 d) by changing the coupling constants β_1' and β_2' is critical for the long-term behavior in our daily dilution simulations. In view of the similar shapes of this mapping (Fig. S10 d) and the well-studied logistic map[7] we speculate that for a very shallow shape–as it occurs for weak coupling (small β_1' and β_2')–the discrete map approaches a stable fixed point, whereas for a steep (negative) slope due to strong coupling (large β_1' and β_2') the bacterial density will diverge until it eventually takes values below $\kappa/10^8$ (extinction). For intermediate slopes, i.e. for intermediate β_1' and β_2', the daily dilution simulations may show oscillations between multiple values (Fig. S10 g). Fig. S11 shows respective bifurcation diagrams of our daily dilution simulations when varying the coupling constants β_1' and β_2' continuously. These bifurcation diagrams display bifurcations from one stable fixed point to oscillations between two values of the bacterial density. Also our experiments suggest bifurcations between a fixed final bacterial density and oscillations between multiple values (Fig. S12). Due to the sensitivity of logistic maps against a change in the mapping function and due to natural noise in our experiments, we note however that a quantitative categorization of the oscillations observed in our experiments (Fig. 2d) in terms of limit cycles of the underlying discrete map (Fig. 2a) may not be feasible and is beyond the scope of this work.

In our daily dilution simulations, for very strong coupling of the proton concentration to the bacterial density (β_1'=3, $\beta_2' = 1$), the bacterial density dramatically decreases on the first

"simulation day" already (Fig. S10 f). Due to our continuous description, the bacterial density does not reach zero. However, note that the bacterial density drops below $\kappa/10^8$, which corresponds to extinction as detailed above (to account for this extinction, we therefore manually set the density to zero). For medium coupling ($\beta_1' = 0.3,\ \beta_2' = 0.1$), we find oscillations in the final bacterial density (Fig. S10 g), reminiscent to our daily dilution experiments with intermediate buffer concentration (Fig. 2d). Furthermore, we find, that the acidification time (the time of the turning point in the proton concentration) oscillates with the bacterial density. For weak coupling ($\beta_1' = 0.06,\ \beta_2' = 0.02$), the bacterial density saturates at the carrying capacity after the first day already and all subsequent "simulation days" (Fig. S10 h), as observed in our experiments with high buffer concentration (Fig. 2e). The phenomenological agreement between our mathematical description and our experiments strongly suggests, that the coupling of the bacterial density and the environment (here the pH) and the resulting non-monotonic growth dynamics are key aspects in understanding the phenomenon of ecological suicide.

References:

1. Nelson, D. M., Glawe, A. J., Labeda, D. P., Cann, I. K. O. & Mackie, R. I. Paenibacillus tundrae sp. nov. and Paenibacillus xylanexedens sp. nov., psychrotolerant, xylan-degrading bacteria from Alaskan tundra. Int. J. Syst. Evol. Microbiol. **59,** 1708–1714 (2009).

2. Cole, J. R. et al. Ribosomal Database Project: data and tools for high throughput rRNA analysis. Nucleic Acids Res. **42,** D633–D642 (2014).

3. Wang, X., Meier, R. J. & Wolfbeis, O. S. Fluorescent pH-Sensitive Nanoparticles in an Agarose Matrix for Imaging of Bacterial Growth and Metabolism. Angew. Chem. Int. Ed. **52,** 406–409 (2013).

4. Strogatz, S. H. Nonlinear Dynamics and Chaos: With Applications to Physics, Biology, Chemistry, and Engineering. (Westview Press, 2014).

5. May, R. M., Conway, G. R., Hassell, M. P. & Southwood, T. R. E. Time Delays, Density-Dependence and Single-Species Oscillations. J. Anim. Ecol. **43,** 747–770 (1974).

6. Hilborn, R. C. Chaos and Nonlinear Dynamics: An Introduction for Scientists and Engineers. (Oxford University Press, 2000).

7. May, R. M. & others. Simple mathematical models with very complicated dynamics. Nature **261,** 459–467 (1976).

8. Saitou, N. & Nei, M. The neighbor-joining method: a new method for reconstructing phylogenetic trees. Mol. Biol. Evol. **4,** 406–425 (1987).

9. Basan, M. et al. Overflow metabolism in Escherichia coli results from efficient proteome allocation. Nature **528,** 99 (2015).

Supplemental Figures:

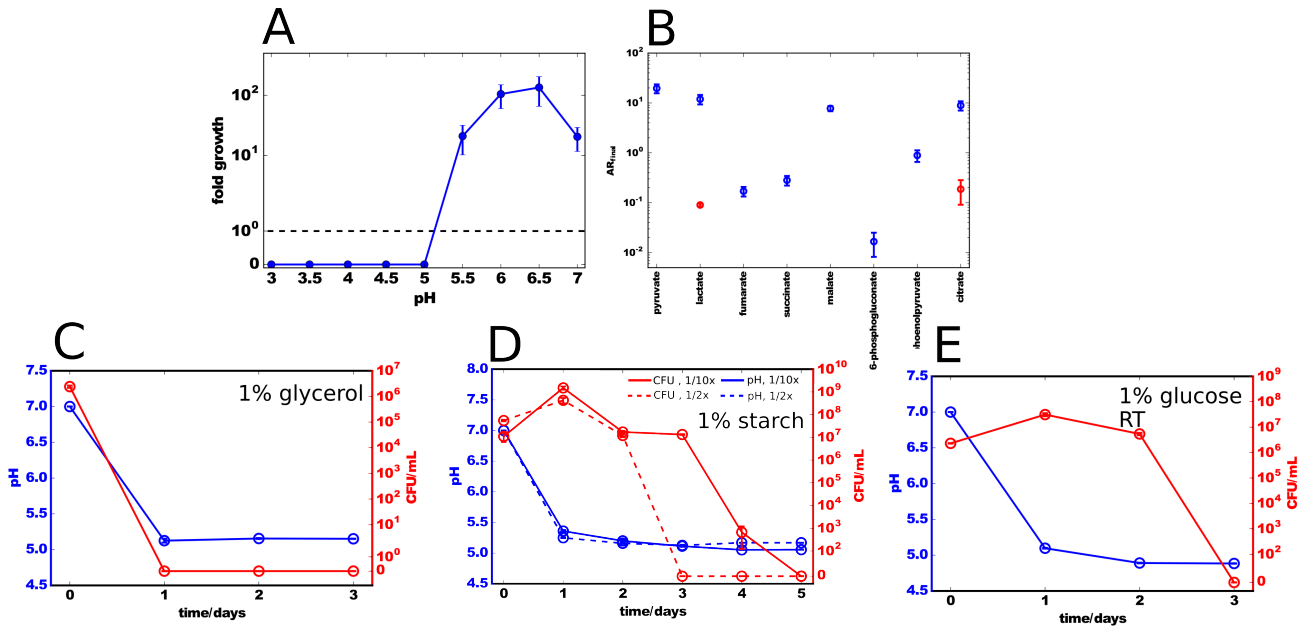

Supplementary Figure 1: Growth of Paenibacillus sp. at different pH values, secretion of organic acids and ecological suicide under different conditions. (A) The CFU were measured at the beginning and end of 24 hours of growth. The fold growth is the ratio of final/initial CFU. At low pH values the bacteria die. The horizontal dashed line marks a fold growth of 1 - eg the cell number did not change over 24 hours. The errorbars are SEM from three replicates. (B) Paenibacillus sp. was grown in M9 media with 2% glucose as the only carbon source. Mass spectrometry of the supernatant indicated that a variety of organic acids were produced by the bacteria. Pyruvate and lactate could be detected in the original media (red circles) but increased in concentration upon bacterial growth. Several other organic acids could not be detected in the original media but accumulated upon bacterial growth. Organic acid secretion can possibly be a result of a type of overflow metabolism[9]. AR is the area ratio of the area under the curve for the detected substance divided by the area under the curve of an internal standard (isotope labeled amino acid). Ecological suicide is observed on 1% glycerol (C), on the complex carbohydrate starch (D), and at room temperature, ~22°C (E). For (C) and (E) the experiment was performed similar to the experiments probing the ecological suicide on glucose and as described in the Methods, but with glycerol or at room temperature instead. For (D) Paenibacillus was grown in 0.5x Nutrient with 1% starch

overnight and directly diluted 1/2x or 1/10x into the same medium with additional 1g/L NH_4Cl. The bacteria were grown at 30°C. The plots show mean and SEM of three replicates each.

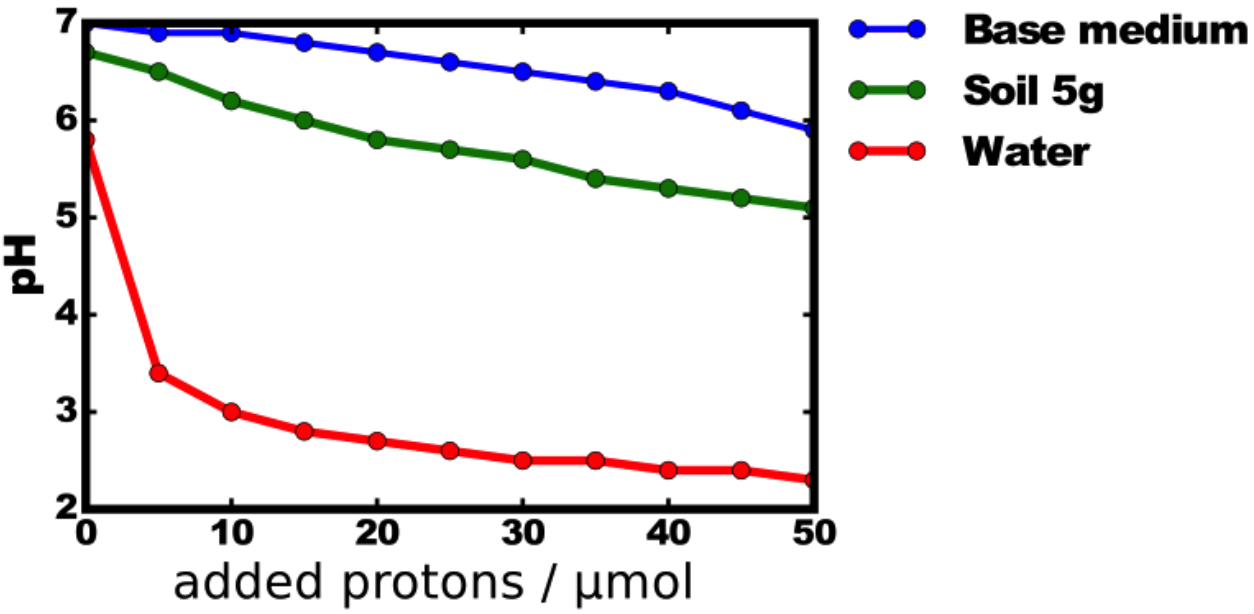

Supplementary Figure 2: Buffer capacity of base medium with 10mM Phosphate is higher than that of the soil the microbes were isolated from. 5g (wet weight) soil from the same location the microbes of this study were isolated from was dispersed in 15mL water. The pH of this dispersion was measured while hydrochloric acid was added. The obtained titration curve was compared with that of 5mL Base medium and pure water. As can be seen our medium is slightly stronger buffered than the soil.

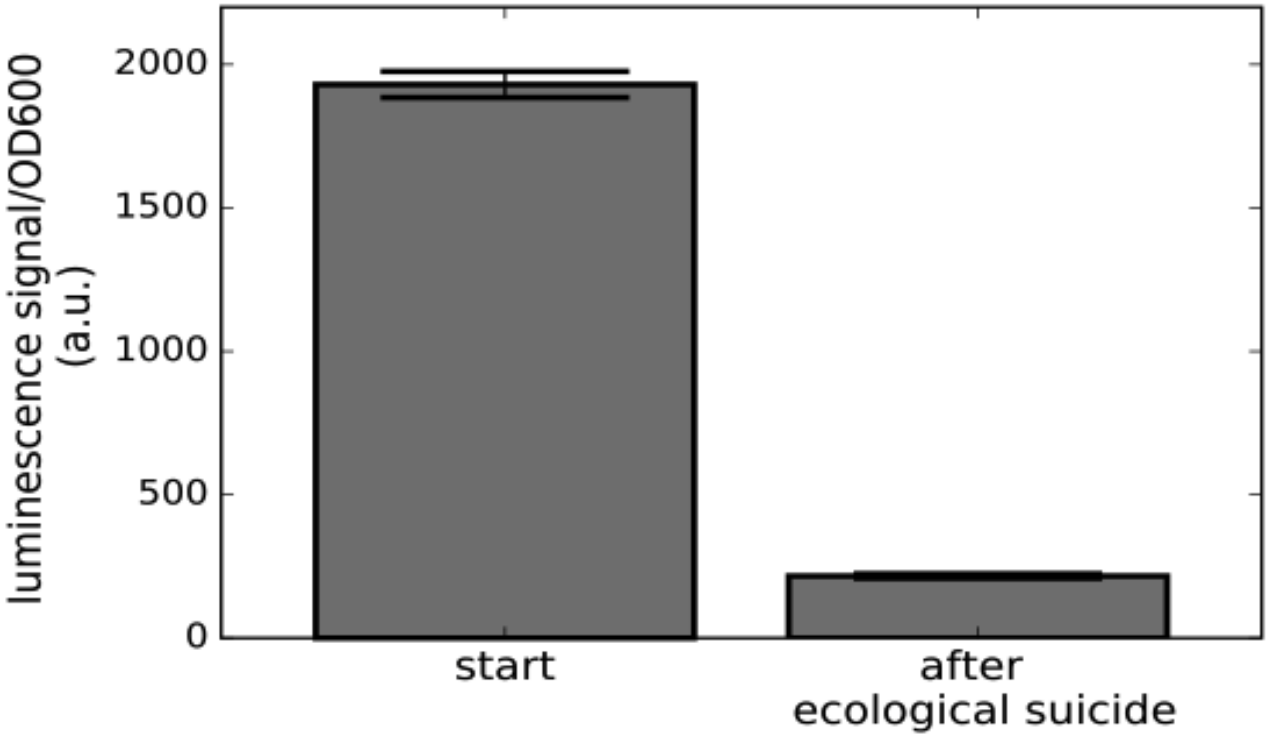

Supplementary Figure 3: Cell viability assay confirms loss of viability upon ecological suicide. The BacTiter-Glo (Promega, Madison, USA) assay was used that measured the cellular ATP content as a indicator for cell viability. As all cell viability assays also this one has the disadvantage that cellular ATP levels to not have to be directly linked to cell viability. However, upon ecological suicide a drop of cellular ATP levels of around 90% could be observed. The final values were taken after 24hours in Base medium with 10mM Phosphate and 10g/L glucose. Bars show mean of 4 replicates and error bars show SEM.

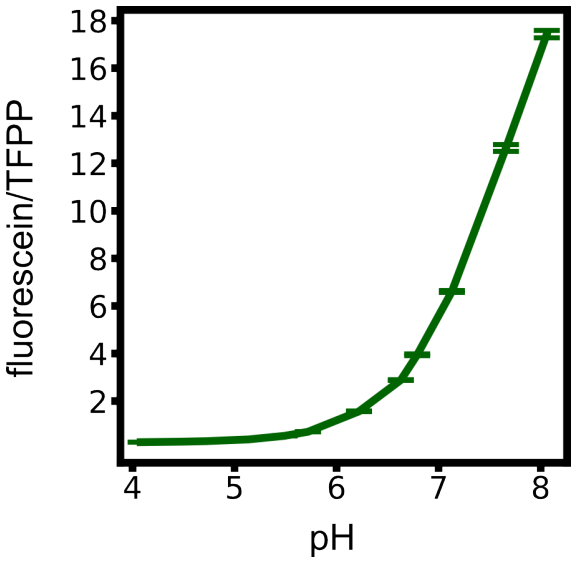

Supplementary Figure 4: The nanobeads' fluorescence ratio of fluorescein and TFPP depends on the pH. Rescaling the fluorescein signal with the TFPP signal shows a monotonic increase as a function of the pH. The fluorescence of the nanobeads was measured in base medium with adjusted pH values as shown on the x-axis**.** Errorbars show the SEM of 8 independent replicates.

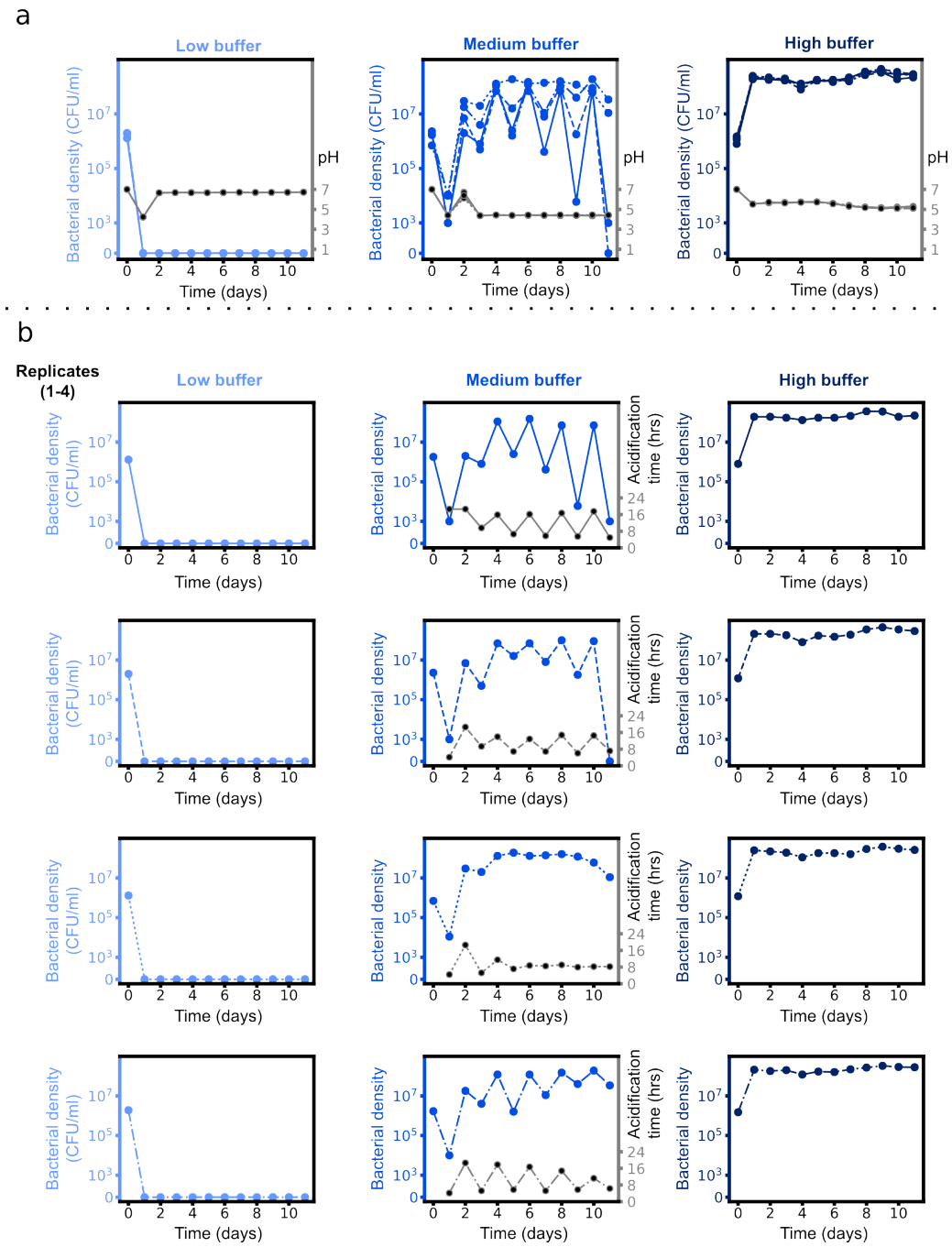

Supplementary Figure 5: Population oscillations. (a) Independent of the initial bacterial density, the daily final pH saturates at the same values. The four blue lines in (c-e) (solid, dashed, dotted, dashed-dotted) show the respective replica also shown in Fig. 2c-e. Instead of the acidification time we plot here the respective daily final pH values in grey (replicates are hardly distinguishable and the daily final pH of the replica are nearly identical). (b) Replicates of Fig. 2 c,d,e as separate plots.

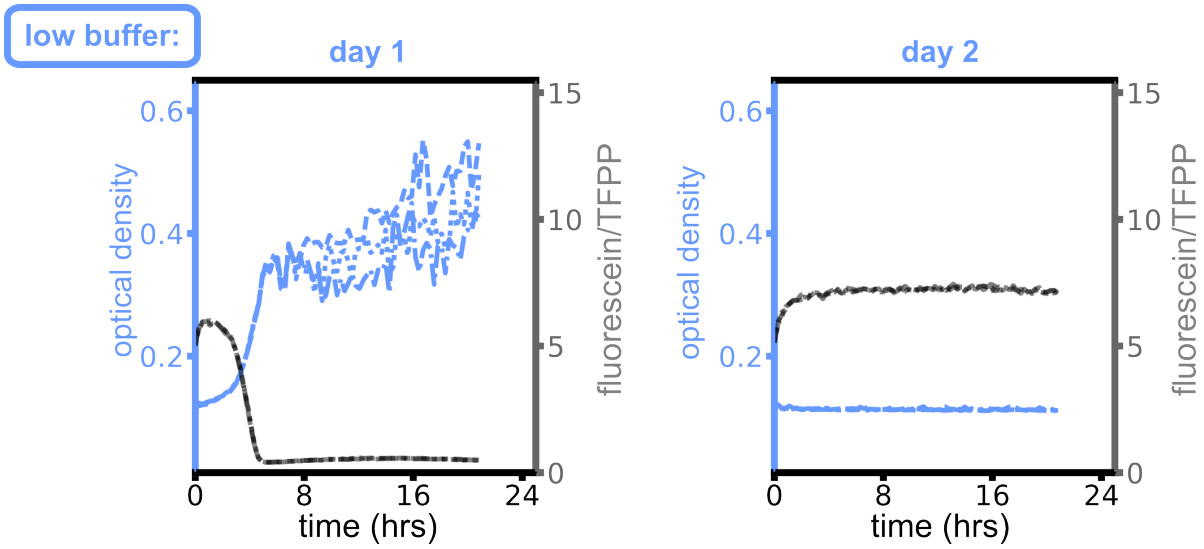

Supplementary Figure 6: For low buffer concentrations (10mM phosphate), an early pH drop leads to ecological suicide. The three sample curves (dashed, dotted, dotted-dashed) correspond to the samples of the daily dilution experiment in Fig. 2 of the main text for the first two days. The fluorescence intensity of fluorescein/TFPP drops after four hours already, eventually leading to ecological suicide on the first day. There was no background correction for the OD values which explains the nonzero OD on day 2.

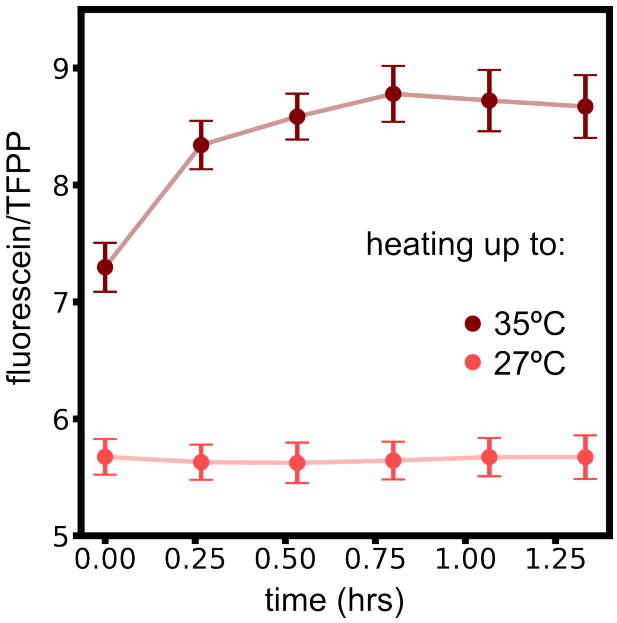

Supplementary Figure 7: The fluorescence intensity ratio of the nanobeads is temperature dependent. The temperature dependence rationalizes the initial increase of the fluorescence intensity ratio in Supplementary Fig. 6 and 8. The fluorescence of the nanobeads was measured over time in base buffer at pH 7. First the nanobeads were incubated at 27°C until a stable value could be obtained. Afterwards the temperature was increased to 35°C and the measurement continued. The increase in temperature is followed by a increase in the fluorescence ratio, which shows that the signal is temperature dependent. Mean and SEM of 10 replicates are shown.

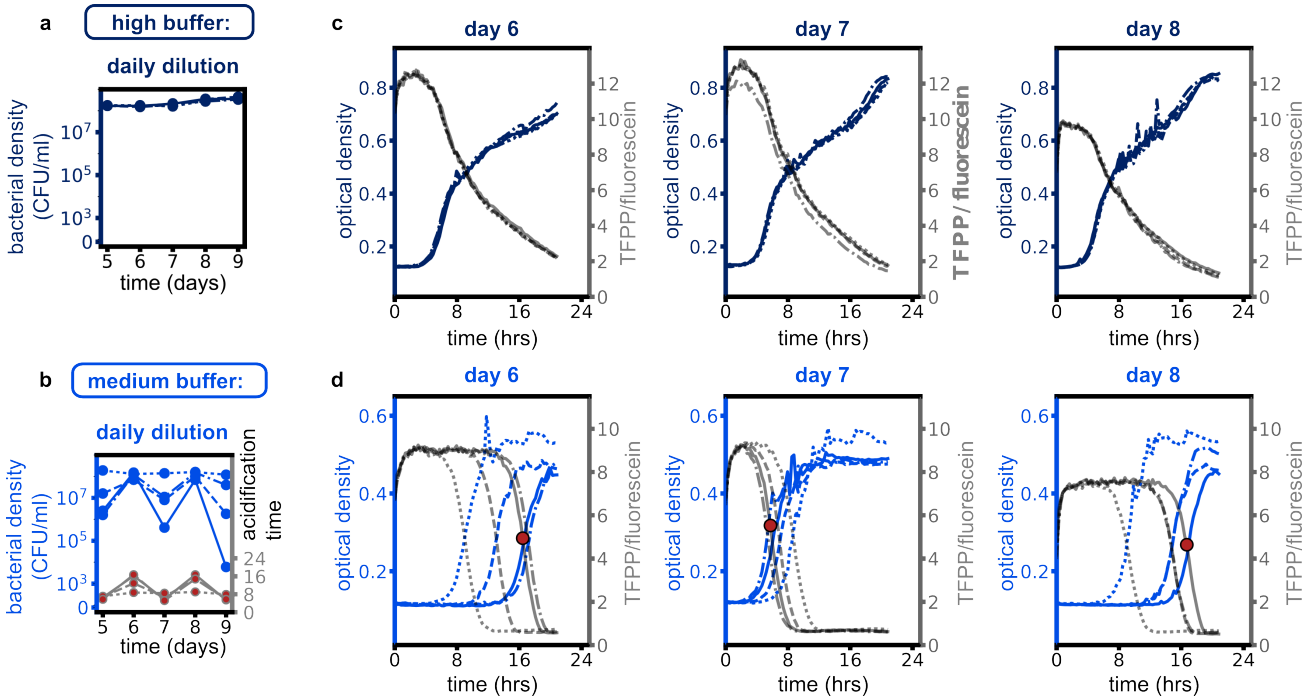

Supplementary Figure 8: The acidification time oscillates with the bacterial density. (a-b) The daily dilution experiments for high (100mM phosphate) and medium (26mM phosphate) buffer concentrations show daily saturation and oscillatory behavior of the bacterial density, respectively. **(c)** For high buffer concentrations, the fluorescence intensity and the optical density in the parallel experiments with fluorescent nanobeads show similar dynamics each day. **(d)** In contrast, for medium buffer concentrations the corresponding parallel experiments with fluorescent nanobeads reveal oscillations in the acidification time (red circle, shown for one sample represented by the solid line). The four different replica (solid, dotted, dashed, dotted-dashed) of these parallel experiments correspond to the respective replica shown in Fig. 2c-e.

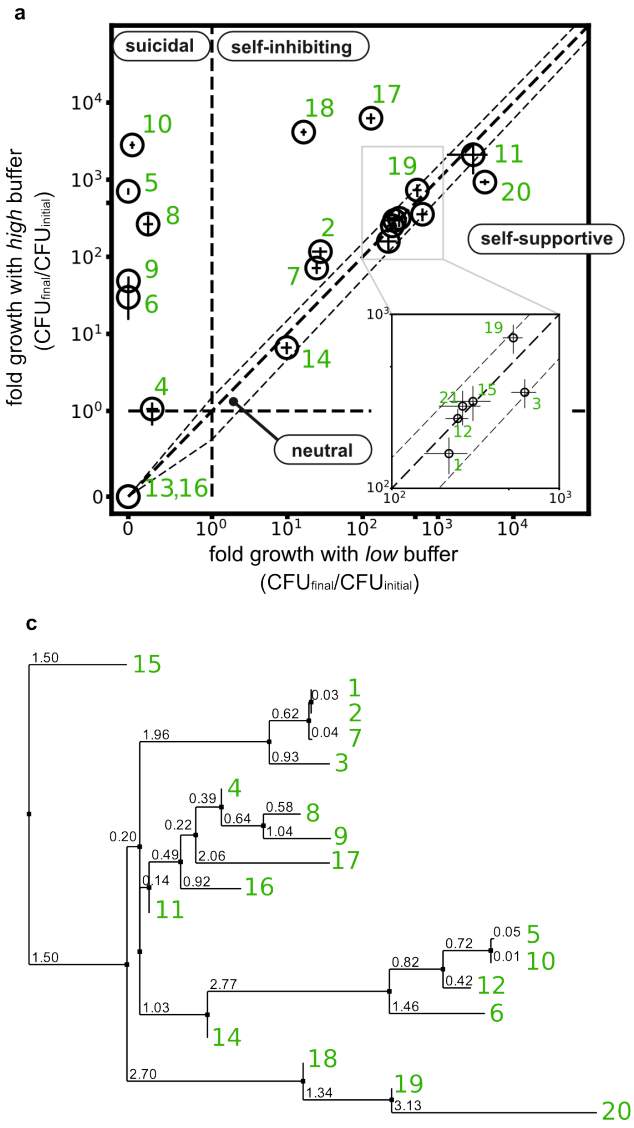

1	Bacillus cereus, Bacillus anthracis, Bacillus thuringiensis, Bacillus thuringiensis serovar fukuokaensis
2	Bacillus cereus, Bacillus anthracis, Bacillus thuringiensis, Bacillus thuringiensis serovar fukuokaensis
3	Bacillus cereus, Bacillus thuringiensis, Bacillus toyonensis, Bacillus thuringiensis serovar colmeri
4	Bacillus firmus
5	Paenibacillus barcinonensis
6	Paenibacillus illinoisensis
7	Bacillus cereus, Bacillus anthracis, Bacillus thuringiensis, Bacillus thuringiensis serovar fukuokaensis
8	Bacillus benzoevorans, Bacillus nealsonii
9	Bacillus benzoevorans, Bacillus nealsonii
10	Paenibacillus amylolyticus
11	Bacillus aestuarii, Bacillus fumarioli, Bacillus drentensis, Bacillus vireti, Bacillus novalis, Bacillus soli, Bacillus senegalensis, Bacillus arbutinivorans, bacterium Ellin505
12	Paenibacillus amylolyticus
14	Rummeliibacillus pycnus
15	Bacillus tequilensis
16	Bacillus bataviensis, Bacillus arbutinivorans, Bacillus niacini, Bacillus bataviensis, Sporosarcina globispora
17	Bacillus megaterium, Bacillus subtilis
18	Arthrobacter aurescens, Arthrobacter nitroguajacolicus
19	Arthrobacter globiformis, Arthrobacter sulfonivorans, Arthrobacter scleromae
20	Arthrobacter ramosus

Supplementary Figure 9: Relatedness of the used soil bacteria used to study the frequency of ecological suicide (Fig. 4 in main text) (a) Categorization of the studied soil species as in Fig.4. The green numbers assign the individual species to their position in the phylogenetic tree (c). (b) Identification of the used species based on their 16s rRNA sequence according to RDB/SeqMatch tool [2]. The right column lists all respective related bacteria with maximal similarity score and S_ab score. (Sequencing of species 13 and 21 failed.) (c) Phylogenetic tree which shows the relatedness of the used bacteria. Green numbers stand for the species used in (a) and assigned in (b), black numbers show genetic distance. The similarity matrix was calculated from the percentage identity (PID) between the sequences after multiple sequence alignment. The tree was build by neighbor joining method[8].

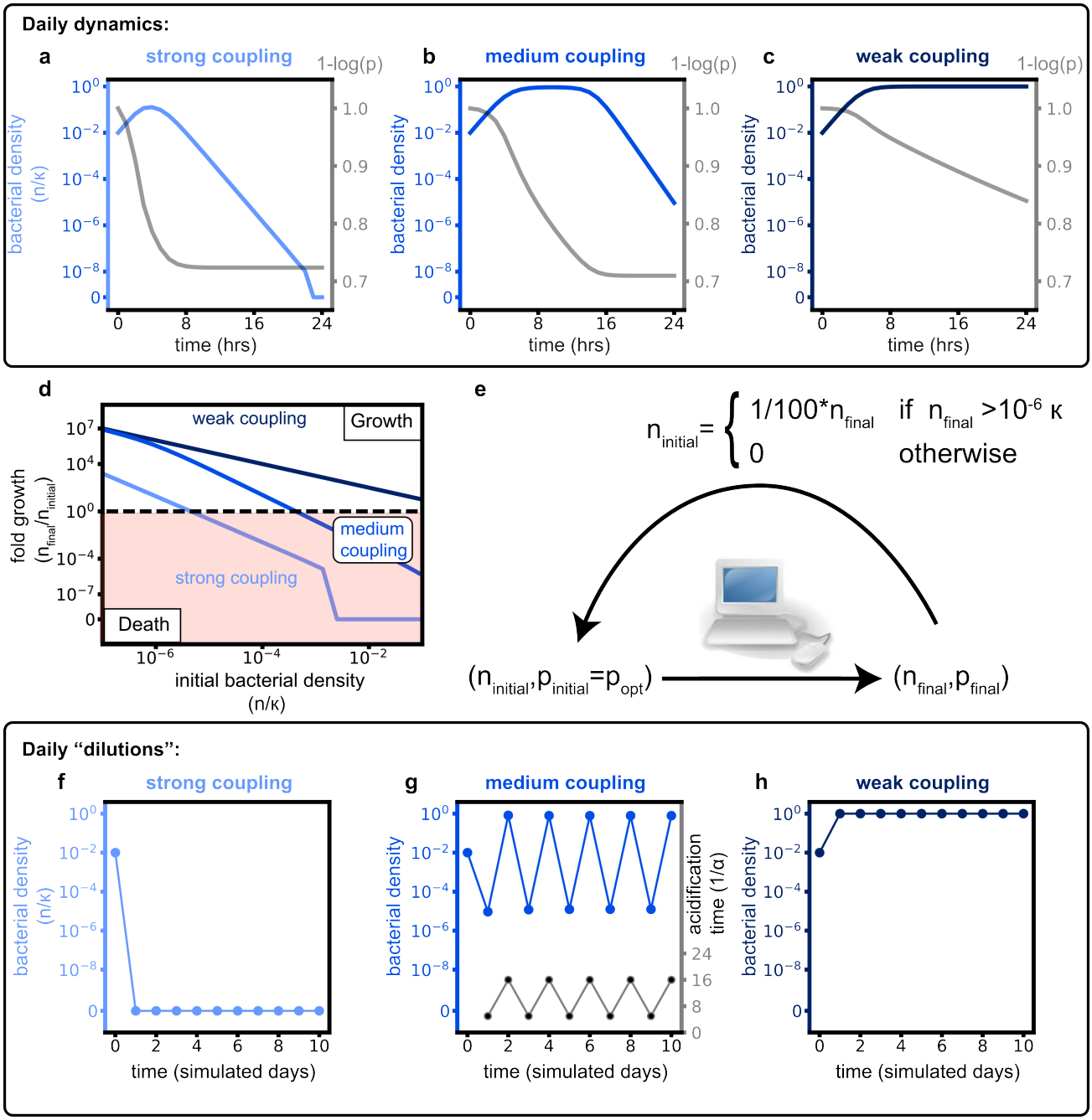

Supplementary Figure 10: Negative feedback of the pH on the bacterial density suffices to recapitulate the phenomenology of ecological suicide as observed experimentally. a-c, Based on eq. (1)-(3), strong ($\beta_1' = 3, \beta_2' = 1$), medium ($\beta_1' = 0.3, \beta_2' = 0.1$), and weak ($\beta_1' = 0.06, \beta_2' = 0.02$) coupling has a similar effect on the growth dynamics as low, medium and high buffer concentrations in our experiments (Fig. 2c-e). **d,** The fold bacterial growth decreases for increasing initial concentration. When simulated in a "daily dilution" scheme. If

the cell number that is 'diluted' at the end of the day dropped below one cell – this is possible since the variables are continuous in differential equitations -the bacterial density was set to zero. **e**, this reciprocal dependence leads to similar scenarios, **f-h,** as observed experimentally (Fig. 2, c-e).

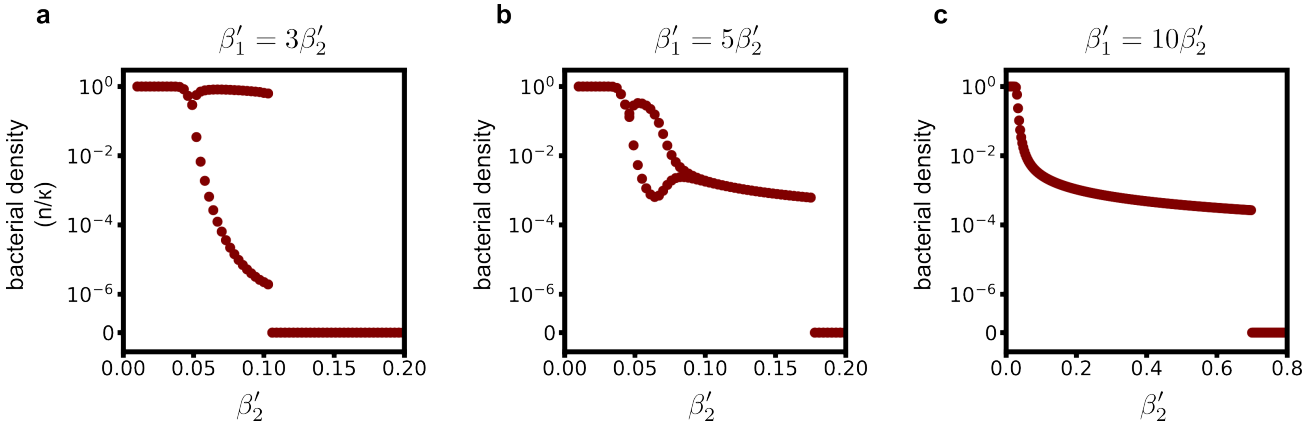

Supplementary Figure 11: Varying the coupling constants and shows bifurcations from one fixed point to oscillations between two points. The bifurcation diagrams show the values of the bacterial density at the end of the last two days after 'daily dilution' simulations corresponding to 60 days. **a,** For comparable coupling constants (here: , as used in Fig. S6), the discrete mapping of 'daily dilution' simulations displays a bifurcation from one stable fixed point (saturation) to oscillations between two points. When a 1/100 dilution would cross the cutoff of (i.e. if after any of the 60 simulation days)**,** the bacterial density was manually set to zero. **b,** For an intermediate ratio , the amplitude of oscillations first increases and then decreases again for increasing . **c**, For high enough (here:) the coupling to the change of bacterial density is dominant and the system saturates at low final densities, but shows no oscillations (recall that strong enough coupling to the bacterial density itself is crucial in our equations (3) to generate oscillations). In b, and c, the bacterial density drops below the extinction cutoff after the first first day already when is too high.

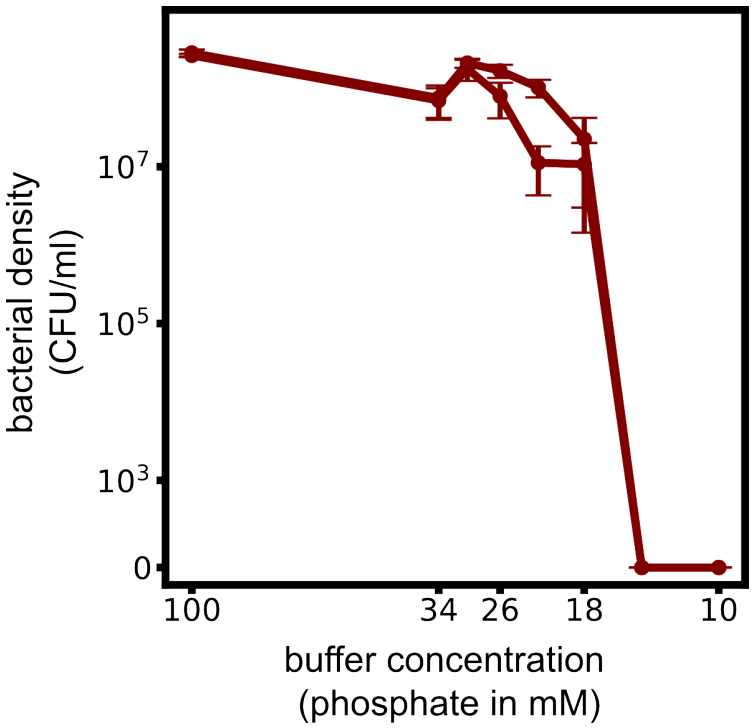

Supplementary Figure 12: Experiments suggest a bifurcation between stable bacterial density at the end of each day and oscillations. The 'bifurcation diagram' shows the mean amplitude of the final bacterial density on the last day (day 11) and the second last day (day 10) for different buffer concentrations. The mean and SEM of the 4 replicates also used in Fig.2 are shown.

III.3 Conclusion and Outlook

In this last chapter of my thesis, I discussed collective behavior in well-mixed growth experiments with soil bacteria. In particular, we found that the soil bacteria *Paenibacillus sp.* collectively modifies the environmental pH in a way that it is bad for its own growth and eventually leads to population death. In time-resolved measurements of the population size and the pH, we observed an initial population growth accompanied by a severe acidification in the medium, which is followed by a strong decline of the population size until extinction (ecological suicide). In the context of evolutionary game theory, this non-monotonous growth curve emphasizes the important role of the environment as an additional player in the microbial ecosystem. Ecological suicide is thus a particularly stunning form of a (negative) feedback between population growth and a change of the population's environment.

Moreover, we found that ecological suicide can in many ways be viewed as a mirror image of the prominent Allee effect [179, 180]. For low initial population sizes, the bacteria managed to grow to a higher population size after one day, whereas for high initial population sizes, the cooperative suicide led to a rapid population decline and eventual extinction. We hypothesize that ecological suicide can have similarly far-reaching consequences as the extensively studied Allee effect. One of these consequences was already revealed by adding substances such as alcohol, salt, and antibiotics, that are usually considered harmful for bacteria. We found that by inhibiting bacterial growth, these substance could hamper the detrimental change in pH and even prevent ecological suicide. Other consequences of ecological suicide could be the formation of patterns in a spatially extended system, as previously observed for the Allee effect [176].

By growing 21 species at low and high buffer concentrations, we identified five further soil bacteria that commit ecological suicide and further four species that change the pH in a self-inhibiting way. This indicates, that self-inflicted death is not limited to *Paenibacillus sp.*, but may be wide-spread in microbes. Yet, the role of ecological suicide in ecosystems and their evolution is elusive. The fact that the studied bacteria all live in the same soil habitat (to be precise, they were all isolated from a spoon of soil in Cambridge, USA [195]), points towards a relevant role of 'suicidal' bacteria in ecological systems. Recent experiments with pairwise competitions [41] already indicate that self-inhibiting growth can have a stabilizing effect. We speculate that a stabilizing effect by ecological suicide might hint towards another example in nature where a diverse ecosystem that contains also less fit species might be more stable and productive than a less diverse ecosystem lacking such species ("diversity-stability debate" [196, 197]).

Bibliography

[1] J. Lutkenhaus. Assembly Dynamics of the Bacterial MinCDE System and Spatial Regulation of the Z Ring. *Annual Review of Biochemistry* **76**(1), 539–562, 2007.

[2] M. Loose and T. J. Mitchison. The bacterial cell division proteins FtsA and FtsZ self-organize into dynamic cytoskeletal patterns. *Nature Cell Biology* **16**, 2013.

[3] L. Huber, R. Suzuki, T. Krüger, E. Frey and A. R. Bausch. Emergence of coexisting ordered states in active matter systems. *Science*, 2018.

[4] K. C. Huang, Y. Meir and N. S. Wingreen. Dynamic structures in Escherichia coli: spontaneous formation of MinE rings and MinD polar zones. *Proceedings of the National Academy of Sciences of the United States of America* **100**(22), 12724–8, 2003.

[5] J. Halatek and E. Frey. Highly Canalized MinD Transfer and MinE Sequestration Explain the Origin of Robust MinCDE-Protein Dynamics. *Cell Reports* **1**(6), 741–752, 2012.

[6] M. Loose, E. Fischer-Friedrich, J. Ries, K. Kruse and P. Schwille. Spatial Regulators for Bacterial Cell Division Self-Organize into Surface Waves in Vitro. *Science* **320**(5877), 789–792, 2008.

[7] K.-T. Park, W. Wu, K. P. Battaile, S. Lovell, T. Holyoak and J. Lutkenhaus. The Min Oscillator Uses MinD-Dependent Conformational Changes in MinE to Spatially Regulate Cytokinesis. *Cell* **146**(3), 396–407, 2011.

[8] G. Bange and I. Sinning. SIMIBI twins in protein targeting and localization. *Nature structural & molecular biology* **20**(7), 776–80, 2013.

[9] A. G. Murzin. Metamorphic Proteins. *Science* **320**(5884), 1725–1726, 2008.

[10] M. Ingerson-Mahar and Z. Gitai. A growing family: the expanding universe of the bacterial cytoskeleton. *FEMS Microbiology Reviews* **36**(1), 256–266, 2012.

[11] D. W. Adams and J. Errington. Bacterial cell division: assembly, maintenance and disassembly of the Z ring. *Nature Reviews Microbiology* **7**, 2009.

[12] L. Rothfield, A. Taghbalout and Y.-L. Shih. Spatial control of bacterial division-site placement. *Nature Reviews Microbiology* **3**, 2005.

[13] J. Lutkenhaus. The ParA/MinD family puts things in their place. *Trends in Microbiology* **20**(9), 411–418, 2012.

[14] D. Fange and J. Elf. Noise-induced min phenotypes in E. coli. *PLoS Computational Biology* **2**(6), 0637–0648, 2006.

[15] M. Loose, E. Fischer-Friedrich, C. Herold, K. Kruse and P. Schwille. Min protein patterns emerge from rapid rebinding and membrane interaction of MinE. *Nature structural & molecular biology* **18**(5), 577–83, 2011.

[16] K. Zieske and P. Schwille. Reconstitution of self-organizing protein gradients as spatial cues in cell-free systems. *eLife* **3**, e03949, 2014.

[17] S. H. Ayed, A. D. Cloutier, L. J. Mcleod, A. C. Y. Foo, A. M. Damry and K. Goto. Dissecting the role of conformational change and membrane binding by the bacterial cell division regulator MinE in the stimulation of MinD ATPase activity. 2017.

[18] K.-t. Park, M. T. Villar, A. Artigues and J. Lutkenhaus. MinE conformational dynamics regulate membrane binding , MinD interaction , and Min oscillation. 2017.

[19] D. D. Leipe, Y. I. Wolf, E. V. Koonin and L. Aravind. Classification and evolution of P-loop GTPases and related ATPases. *Journal of Molecular Biology* **317**(1), 41–72, 2002.

[20] Y.-G. Chang *et al.* A Protein Fold Switch Joins the Circadian Oscillator to Clock Output in Cyanobacteria. *Science (New York, N.Y.)* **349**(6245), 324–328, 2015.

[21] A. G. Vecchiarelli, M. Li, M. Mizuuchi and K. Mizuuchi. Differential affinities of MinD and MinE to anionic phospholipid influence Min patterning dynamics in vitro. *Molecular microbiology* **93**(3), 453–63, 2014.

[22] J. Denk, L. Huber, E. Reithmann and E. Frey. Active Curved Polymers Form Vortex Patterns on Membranes. *Phys. Rev. Lett.* **116**, 178301, 2016.

[23] J. Halatek and E. Frey. Rethinking pattern formation in reaction–diffusion systems. *Nature Physics* **14**(5), 507–514, 2018.

[24] M. Cross and H. Greenside. *Pattern Formation and Dynamics in Nonequilibrium Systems*. Cambridge University Press, 2009.

[25] M. C. Cross and P. C. Hohenberg. Pattern formation outside of equilibrium. *Rev. Mod. Phys.* **65**, 851–1112, 1993.

[26] J. Halatek and E. Frey. Effective 2D model does not account for geometry sensing by self-organized proteins patterns. *Proceedings of the National Academy of Sciences* **111**(18), E1817–E1817, 2014.

[27] S. Jakubith, H. H. Rotermund, W. Engel, A. von Oertzen and G. Ertl. Spatiotemporal concentration patterns in a surface reaction: Propagating and standing waves, rotating spirals, and turbulence. *Phys. Rev. Lett.* **65**, 3013–3016, 1990.

[28] M. Kim. Controlling Chemical Turbulence by Global Delayed Feedback: Pattern Formation in Catalytic CO Oxidation on Pt(110). *Science* **292**(5520), 1357–1360, 2001.

[29] Z. Li, M. J. Trimble, Y. V. Brun and G. J. Jensen. The structure of FtsZ filaments in vivo suggests a force-generating role in cell division. *The EMBO Journal* **26**(22), 4694–4708.

[30] E. L. Meier and E. D. Goley. Form and function of the bacterial cytokinetic ring. *Current Opinion in Cell Biology* **26** Cell architecture, 19–27, 2014.

[31] M. A. Oliva, S. C. Cordell and J. Löwe. Structural insights into FtsZ protofilament formation. *Nature Structural & Amp; Molecular Biology* **11**, 1243 EP, 2004.

[32] H. P. Erickson, D. E. Anderson and M. Osawa. FtsZ in Bacterial Cytokinesis: Cytoskeleton and Force Generator All in One. *Microbiology and Molecular Biology Reviews* **74**(4), 504–528, 2010.

[33] V. García-Morales and K. Krischer. The complex Ginzburg-Landau equation: an introduction. *Contemporary Physics* **53**(2), 79–95, 2012.

[34] D. A. Ramirez-Diaz, D. A. García-Soriano, A. Raso, J. Mücksch, M. Feingold, G. Rivas and P. Schwille. Treadmilling analysis reveals new insights into dynamic FtsZ ring architecture. *PLOS Biology* **16**(5), e2004845–, 2018.

[35] S. Ramaswamy. The Mechanics and Statistics of Active Matter. *Annual Review of Condensed Matter Physics* **1**, 323–345, 2010.

[36] T. Vicsek and A. Zafeiris. Collective motion. *Physics Reports* **517**(3) Collective motion, 71–140, 2012.

[37] M. C. Marchetti, J.-F. Joanny, S. Ramaswamy, T. B. Liverpool, J. Prost, M. Rao and R. Aditi Simha. Soft Active Matter. *ArXiv e-prints*, 2012.

[38] H. Celiker and J. Gore. Cellular cooperation: insights from microbes. *Trends in Cell Biology* **23**(1), 9–15, 2013.

[39] K. Drescher, C. D. Nadell, H. A. Stone, N. S. Wingreen and B. L. Bassler. Solutions to the Public Goods Dilemma in Bacterial Biofilms. *Current Biology* **24**(1), 50–55, 2014.

[40] H. Celiker and J. Gore. Competition between species can stabilize public-goods cooperation within a species. *Molecular Systems Biology* **8**, 621, 2012.

[41] C. Ratzke and J. Gore. Modifying and reacting to the environmental pH can drive bacterial interactions. *PLOS Biology* **16**(3), 1–20, 2018.

[42] J. Raven and F. Smith. The evolution of chemiosmotic energy coupling. *Journal of Theoretical Biology* **57**(2), 301–312, 1976.

[43] W. B. Schofield, H. C. Lim and C. Jacobs-Wagner. Cell cycle coordination and regulation of bacterial chromosome segregation dynamics by polarly localized proteins. *The EMBO Journal* **29**(18), 3068–3081, 2010.

[44] X. Wang, P. M. Llopis and D. Z. Rudner. Organization and segregation of bacterial chromosomes. *Nature reviews. Genetics* **14**(3), 10.1038/nrg3375, 2013.

[45] V. W. Rowlett and W. Margolin. The bacterial Min system. *Current Biology* **23**(13), R553–R556, 2013.

[46] H. Shi, B. P. Bratton, Z. Gitai and K. C. Huang. How to Build a Bacterial Cell: MreB as the Foreman of *E. coli* Construction. *Cell* **172**(6), 1294–1305, 2018.

[47] K. M. Schoenemann and W. Margolin. Bacterial Division: FtsZ Treadmills to Build a Beautiful Wall. *Current Biology* **27**(8), R301–R303, 2017.

[48] D. M. Raskin and P. A. J. de Boer. Rapid pole-to-pole oscillation of a protein required for directing division to the middle of Escherichia coli. *Proceedings of the National Academy of Sciences* **96**(9), 4971–4976, 1999.

[49] Z. Hu and J. Lutkenhaus. Topological Regulation of Cell Division in *E. coli*. *Molecular Cell* **7**(6), 1337–1343, 2001.

[50] A. W. Bisson-Filho *et al.* Treadmilling by FtsZ filaments drives peptidoglycan synthesis and bacterial cell division. *Science* **355**(6326), 739–743, 2017.

[51] X. Yang, Z. Lyu, A. Miguel, R. McQuillen, K. C. Huang and J. Xiao. GTPase activity–coupled treadmilling of the bacterial tubulin FtsZ organizes septal cell wall synthesis. *Science* **355**(6326), 744–747, 2017.

[52] C. A. Hale, H. Meinhardt and P. A. de Boer. Dynamic localization cycle of the cell division regulator MinE in Escherichia coli. *The EMBO Journal* **20**(7), 1563–1572, 2001.

[53] M. Zheng, Y.-L. Chiang, H.-L. Lee, L.-R. Kong, S.-T. D. Hsu, I.-S. Hwang, L. I. Rothfield and Y.-L. Shih. Self-Assembly of MinE on the Membrane Underlies Formation of the MinE Ring to Sustain Function of the Escherichia coli Min System. *Journal of Biological Chemistry* **289**(31), 21252–21266, 2014.

[54] F. Wu, B. G. C. van Schie, J. E. Keymer and C. Dekker. Symmetry and scale orient Min protein patterns in shaped bacterial sculptures. *Nature Nanotechnology* **10**, 2015.

[55] F. Wu, J. Halatek, M. Reiter, E. Kingma, E. Frey and C. Dekker. Multistability and dynamic transitions of intracellular Min protein patterns. *Molecular Systems Biology* **12**(6), 873, 2016.

[56] A. G. Vecchiarelli, M. Li, M. Mizuuchi, L. C. Hwang, Y. Seol, K. C. Neuman and K. Mizuuchi. Membrane-bound MinDE complex acts as a toggle switch that drives Min oscillation coupled to cytoplasmic depletion of MinD. *Proceedings of the National Academy of Sciences* **113**(11), E1479–E1488, 2016.

[57] J. Denk, S. Kretschmer, J. Halatek, C. Hartl, P. Schwille and E. Frey. MinE conformational switching confers robustness on self-organized Min protein patterns. *Proceedings of the National Academy of Sciences*, 2018.

[58] S. Kretschmer, K. Zieske and P. Schwille. Large-scale modulation of reconstituted Min protein patterns and gradients by defined mutations in MinE's membrane targeting sequence. **12**, 2017.

[59] J. Schweizer, M. Loose, M. Bonny, K. Kruse, I. Mönch and P. Schwille. Geometry sensing by self-organized protein patterns. *Proceedings of the National Academy of Sciences of the United States of America* **109**(38), 15283–8, 2012.

[60] K. Zieske and P. Schwille. Reconstitution of Pole-to-Pole Oscillations of Min Proteins in Microengineered Polydimethylsiloxane Compartments. *Angewandte Chemie International Edition* **52**(1), 459–462.

[61] S. Kretschmer and P. Schwille. Pattern formation on membranes and its role in bacterial cell division. *Current Opinion in Cell Biology* **38**, 52–59, 2016.

[62] Z. Hu, E. P. Gogol and J. Lutkenhaus. Dynamic assembly of MinD on phospholipid vesicles regulated by ATP and MinE. *Proceedings of the National Academy of Sciences* **99**(10), 6761–6766, 2002.

[63] L. L. Lackner, D. M. Raskin and P. a. J. de Boer. ATP-Dependent Interactions between Escherichia coli Min Proteins and the Phospholipid Membrane In Vitro. *Journal of Bacteriology* **185**(3), 735–749, 2003.

[64] H. Meinhardt and P. A. J. de Boer. Pattern formation in Escherichia coli: A model for the pole-to-pole oscillations of Min proteins and the localization of the division site. *Proceedings of the National Academy of Sciences of the United States of America* **98**(25), 14202–14207, 2001.

[65] K. Kruse. A Dynamic Model for Determining the Middle of *Escherichia coli*. *Biophysical Journal* **82**(2), 618–627, 2002.

[66] M. Howard, A. D. Rutenberg and S. de Vet. Dynamic Compartmentalization of Bacteria: Accurate Division in E. Coli. *Phys. Rev. Lett.* **87**, 278102, 2001.

[67] E. Frey, J. Halatek, S. Kretschmer and P. Schwille. Protein Pattern Formation. *ArXiv e-prints*, 2018.

[68] Y. Caspi and C. Dekker. Mapping out Min protein patterns in fully confined fluidic chambers. *eLife* **5**, e19271, 2016.

[69] R. Imbihl and G. Ertl. Oscillatory Kinetics in Heterogeneous Catalysis. *Chemical Reviews* **95**(3), 697–733, 1995.

[70] S. Kretschmer and P. Schwille. Pattern formation on membranes and its role in bacterial cell division. *Current Opinion in Cell Biology* **38** Cell architecture, 52–59, 2016.

[71] M. Bonny, E. Fischer-Friedrich, M. Loose, P. Schwille and K. Kruse. Membrane binding of MinE allows for a comprehensive description of Min-protein pattern formation. *PLoS computational biology* **9**(12), e1003347, 2013.

[72] G. Eigenberger. Kinetic instabilities in heterogeneously catalyzed reactions – II: Oscillatory instabilities with langmuir-type kinetics. *Chemical Engineering Science* **33**(9), 1263–1268, 1978.

[73] M. Loose, E. Fischer-Friedrich, C. Herold, K. Kruse and P. Schwille. Min protein patterns emerge from rapid rebinding and membrane interaction of MinE. *Nature Structural &Amp; Molecular Biology* **18**, 2011.

[74] W. R. Inc. *Mathematica, Version 11.3*. Champaign, IL, 2018.

[75] G. van Rossum. *Python tutorial*. Tech. rep. CS-R9526. Amsterdam: Centrum voor Wiskunde en Informatica (CWI), May 1995.

[76] A. Schuster. On the investigation of hidden periodicities with application to a supposed 26 day period of meteorological phenomena. *Terrestrial Magnetism* **3**(1), 13–41, March 1898.

[77] S. C. Goodchild, P. M. G. Curmi and L. J. Brown. Structural gymnastics of multifunctional metamorphic proteins. *Biophysical Reviews* **3**(3), 143, 2011.

[78] A. D. Bershadsky and M. M. Kozlov. Crawling cell locomotion revisited. *Proceedings of the National Academy of Sciences of the United States of America* **108**(51), 20275–20276, 2011.

[79] C. P. Brangwynne, G. H. Koenderink, F. C. MacKintosh and D. A. Weitz. Intracellular transport by active diffusion. *Trends in Cell Biology* **19**(9), 423–427, 2009.

[80] C. P. Brangwynne. Soft active aggregates: mechanics, dynamics and self-assembly of liquid-like intracellular protein bodies. *Soft Matter* **7**, 3052–3059, 2011.

[81] T. H. Tan, M. Malik-Garbi, E. Abu-Shah, J. Li, A. Sharma, F. C. MacKintosh, K. Keren, C. F. Schmidt and N. Fakhri. Self-organized stress patterns drive state transitions in actin cortices. *Science Advances* **4**(6), 2018.

[82] G. Salbreux, G. Charras and E. Paluch. Actin cortex mechanics and cellular morphogenesis. *Trends in Cell Biology* **22**(10), 536–545, 2012.

[83] A. Dajkovic and J. Lutkenhaus. Z Ring as Executor of Bacterial Cell Division. *Journal of Molecular Microbiology and Biotechnology* **11**(3-5), 140–151, 2006.

[84] G. Ariel and A. Ayali. Locust Collective Motion and Its Modeling. *PLOS Computational Biology* **11**(12), 1–25, 2015.

[85] J. Buhl, D. J. T. Sumpter, I. D. Couzin, J. J. Hale, E. Despland, E. R. Miller and S. J. Simpson. From Disorder to Order in Marching Locusts. *Science* **312**(5778), 1402–1406, 2006.

[86] M. L. Anstey, S. M. Rogers, S. R. Ott, M. Burrows and S. J. Simpson. Serotonin Mediates Behavioral Gregarization Underlying Swarm Formation in Desert Locusts. *Science* **323**(5914), 627–630, 2009.

[87] S. Thutupalli, M. Sun, F. Bunyak, K. Palaniappan and J. W. Shaevitz. Directional reversals enable Myxococcus xanthus cells to produce collective one-dimensional streams during fruiting-body formation. *Journal of the Royal Society Interface* **12**(109), 20150049, 2015.

[88] C. Dombrowski, L. Cisneros, S. Chatkaew, R. E. Goldstein and J. O. Kessler. Self-Concentration and Large-Scale Coherence in Bacterial Dynamics. *Phys. Rev. Lett.* **93**, 098103, 2004.

[89] T. B. Saw, A. Doostmohammadi, V. Nier, L. Kocgozlu, S. Thampi, Y. Toyama, P. Marcq, C. T. Lim, J. M. Yeomans and B. Ladoux. Topological defects in epithelia govern cell death and extrusion. *Nature* **544**, 212, 2017.

[90] V. Schaller, C. Weber, C. Semmrich, E. Frey and A. R. Bausch. Polar pattern of driven filaments. *Nature* **467**, 73–7, 2010.

[91] T. M. Butt, T. F. Mufti, A. Humayun, P. B. Rosenthal, S. Khan, S. Khan and J. E. Molloy. Myosin Motors Drive Long Range Alignment of Actin Filaments. *Journal of Biological Chemistry* **285**(7), 4964–4974, 2010.

[92] M. Ibele, T. Mallouk and A. Sen. Schooling Behavior of Light-Powered Autonomous Micromotors in Water. *Angewandte Chemie International Edition* **48**(18), 3308–3312.

[93] A. Bricard, J.-B. Caussin, N. Desreumaux, O. Dauchot and D. Bartolo. Emergence of macroscopic directed motion in populations of motile colloids. *Nature* **503**, 2013.

[94] D. L. Blair, T. Neicu and A. Kudrolli. Vortices in vibrated granular rods. *PRE* **67**(3), 031303, 031303, 2003.

[95] A. Kudrolli, G. Lumay, D. Volfson and L. S. Tsimring. Swarming and Swirling in Self-Propelled Polar Granular Rods. *Physical Review Letters* **100**(5), 058001, 058001, 2008.

[96] A. Kudrolli. Concentration Dependent Diffusion of Self-Propelled Rods. *Phys. Rev. Lett.* **104**, 088001, 2010.

[97] J. Deseigne, S. Léonard, O. Dauchot and H. Chaté. Vibrated polar disks: spontaneous motion, binary collisions, and collective dynamics. *Soft Matter* **8**, 5629–5639, 2012.

[98] J. Deseigne, O. Dauchot and H. Chaté. Collective Motion of Vibrated Polar Disks. *Phys. Rev. Lett.* **105**, 098001, 2010.

[99] H. Chaté, F. Ginelli, G. Grégoire and F. Raynaud. Collective motion of self-propelled particles interacting without cohesion. *Phys. Rev. E* **77**, 046113, 2008.

[100] T. Vicsek, A. Czirók, E. Ben-Jacob, I. Cohen and O. Shochet. Novel Type of Phase Transition in a System of Self-Driven Particles. *Phys. Rev. Lett.* **75**(6), 1995.

[101] H. Chaté, F. Ginelli and R. Montagne. Simple Model for Active Nematics: Quasi-Long-Range Order and Giant Fluctuations. *Phys. Rev. Lett.* **96**, 180602, 2006.

[102] F. Ginelli, F. Peruani, M. Bär and H. Chaté. Large-Scale Collective Properties of Self-Propelled Rods. *Physical Review Letters* **104**(18), 184502, 184502, 2010.

[103] G. Grégoire and H. Chaté. Onset of Collective and Cohesive Motion. *Phys. Rev. Lett.* **92**, 025702, 2004.

[104] G. Baglietto and E. V. Albano. Finite-size scaling analysis and dynamic study of the critical behavior of a model for the collective displacement of self-driven individuals. *Phys. Rev. E* **78**, 021125, 2008.

[105] F. Peruani, A. Deutsch and M. Bär. Nonequilibrium clustering of self-propelled rods. *Phys. Rev. E* **74**, 030904, 2006.

[106] D. Grossman, I. S. Aranson and E. B. Jacob. Emergence of agent swarm migration and vortex formation through inelastic collisions. *New Journal of Physics* **10**(2), 023036, 2008.

[107] C. A. Weber, T. Hanke, J. Deseigne, S. Léonard, O. Dauchot, E. Frey and H. Chaté. Long-Range Ordering of Vibrated Polar Disks. *Physical Review Letters* **110**(20), 208001, 208001, 2013.

[108] Y. Yang, V. Marceau and G. Gompper. Swarm behavior of self-propelled rods and swimming flagella. *Phys. Rev. E* **82**, 031904, 2010.

[109] J. Toner and Y. Tu. Long-Range Order in a Two-Dimensional Dynamical XY Model: How Birds Fly Together. *Phys. Rev. Lett.* **75**, 4326–4329, 1995.

[110] J. Toner and Y. Tu. Flocks, herds, and schools: A quantitative theory of flocking. *Phys. Rev. E* **58**, 4828–4858, 1998.

[111] R. Simha and S. Ramaswamy. Statistical hydrodynamics of ordered suspensions of self-propelled particles: waves, giant number fluctuations and instabilities. *Physica A: Statistical Mechanics and its Applications* **306**, 262–269, 2002.

[112] R. Aditi Simha and S. Ramaswamy. Hydrodynamic Fluctuations and Instabilities in Ordered Suspensions of Self-Propelled Particles. *Phys. Rev. Lett.* **89**, 058101, 2002.

[113] S. Ramaswamy, R. A. Simha and J. Toner. Active nematics on a substrate: Giant number fluctuations and long-time tails. *EPL (Europhysics Letters)* **62**(2), 196, 2003.

[114] K. Kruse, J. F. Joanny, F. Jülicher, J. Prost and K. Sekimoto. Generic theory of active polar gels: a paradigm for cytoskeletal dynamics. *The European Physical Journal E* **16**(1), 5–16, 2005.

[115] J. Dunkel, S. Heidenreich, K. Drescher, H. H. Wensink, M. Bär and R. E. Goldstein. Fluid Dynamics of Bacterial Turbulence. *Phys. Rev. Lett.* **110**, 228102, 2013.

[116] V. Bratanov, F. Jenko and E. Frey. New class of turbulence in active fluids. *Proceedings of the National Academy of Sciences* **112**(49), 15048–15053, 2015.

[117] P. Guillamat, J. Ignés-Mullol and F. Sagués. Taming active turbulence with patterned soft interfaces. *Nature Communications* **8**(1), 564, 2017.

[118] T. B. Liverpool and M. C. Marchetti. Instabilities of Isotropic Solutions of Active Polar Filaments. *Phys. Rev. Lett.* **90**, 138102, 2003.

[119] I. S. Aranson and L. S. Tsimring. Pattern formation of microtubules and motors: Inelastic interaction of polar rods. *Phys. Rev. E* **71**, 050901, 2005.

[120] I. S. Aranson and L. S. Tsimring. Theory of self-assembly of microtubules and motors. *Phys. Rev. E* **74**, 031915, 2006.

[121] A. Baskaran and M. C. Marchetti. Enhanced Diffusion and Ordering of Self-Propelled Rods. *Phys. Rev. Lett.* **101**, 268101, 2008.

[122] A. Baskaran and M. C. Marchetti. Hydrodynamics of self-propelled hard rods. *Phys. Rev. E* **77**, 011920, 2008.

[123] E. Bertin, M. Droz and G. Grégoire. Boltzmann and hydrodynamic description for self-propelled particles. *Phys. Rev. E* **74**, 022101, 2006.

[124] E. Bertin, M. Droz and G. Grégoire. Hydrodynamic equations for self-propelled particles: microscopic derivation and stability analysis. *Journal of Physics A: Mathematical and Theoretical* **42**(44), 445001, 2009.

[125] T. Ihle. Kinetic theory of flocking: Derivation of hydrodynamic equations. *Phys. Rev. E* **83**, 030901, 2011.

[126] F. Thüroff, C. A. Weber and E. Frey. Numerical Treatment of the Boltzmann Equation for Self-Propelled Particle Systems. *Phys. Rev. X* **4**, 041030, 2014.

[127] A. Peshkov, E. Bertin, F. Ginelli and H. Chaté. Boltzmann-Ginzburg-Landau approach for continuous descriptions of generic Vicsek-like models. *The European Physical Journal Special Topics* **223**(7), 1315–1344, 2014.

[128] A. Peshkov, I. S. Aranson, E. Bertin, H. Chaté and F. Ginelli. Nonlinear Field Equations for Aligning Self-Propelled Rods. *Phys. Rev. Lett.* **109**, 268701, 2012.

[129] A. Peshkov, S. Ngo, E. Bertin, H. Chaté and F. Ginelli. Continuous Theory of Active Matter Systems with Metric-Free Interactions. *Phys. Rev. Lett.* **109**, 098101, 2012.

[130] E. Bertin, H. Chaté, F. Ginelli, S. Mishra, A. Peshkov and S. Ramaswamy. Mesoscopic theory for fluctuating active nematics. *New Journal of Physics* **15**(8), 085032, 2013.

[131] B. Mahault, X.-c. Jiang, E. Bertin, Y.-q. Ma, A. Patelli, X.-q. Shi and H. Chaté. Self-Propelled Particles with Velocity Reversals and Ferromagnetic Alignment: Active Matter Class with Second-Order Transition to Quasi-Long-Range Polar Order. *Phys. Rev. Lett.* **120**, 258002, 2018.

[132] A. M. Menzel. Collective motion of binary self-propelled particle mixtures. *Phys. Rev. E* **85**, 021912, 2012.

[133] R. Großmann, P. Romanczuk, M. Bär and L. Schimansky-Geier. Pattern formation in active particle systems due to competing alignment interactions. *The European Physical Journal Special Topics* **224**(7), 1325–1347, 2015.

[134] S. Ngo, F. Ginelli and H. Chaté. Competing ferromagnetic and nematic alignment in self-propelled polar particles. *Phys. Rev. E* **86**, 050101, 2012.

[135] M. Housman, S. L. Milam, D. A. Moore, M. Osawa and H. P. Erickson. FtsZ Protofilament Curvature Is the Opposite of Tubulin Rings. *Biochemistry* **55**(29), 4085–4091, 2016.

[136] M. Osawa, D. E. Anderson and H. P. Erickson. Curved FtsZ protofilaments generate bending forces on liposome membranes. *The EMBO Journal* **28**(22), 3476–3484, 2009.

[137] J. Buhl, D. J. T. Sumpter, I. D. Couzin, J. J. Hale, E. Despland, E. R. Miller and S. J. Simpson. From Disorder to Order in Marching Locusts. *Science* **312**(5778), 1402–1406, 2006.

[138] F. Thüroff, C. A. Weber and E. Frey. Critical Assessment of the Boltzmann Approach to Active Systems. *Phys. Rev. Lett.* **111**, 190601, 2013.

[139] R. Suzuki, C. A. Weber, E. Frey and A. R. Bausch. Polar Pattern Formation in Driven Filament Systems Require Non-Binary Particle Collisions. *Nature physics* **11**(10), 839–843, 2015.

[140] H. Chaté, F. Ginelli and R. Montagne. Simple Model for Active Nematics: Quasi-Long-Range Order and Giant Fluctuations. *Phys. Rev. Lett.* **96**, 180602, 2006.

[141] S. Ngo, A. Peshkov, I. S. Aranson, E. Bertin, F. Ginelli and H. Chaté. Large-Scale Chaos and Fluctuations in Active Nematics. *Phys. Rev. Lett.* **113**, 038302, 2014.

[142] A. Czirók, H. E. Stanley and T. Vicsek. Spontaneously ordered motion of self-propelled particles. *Journal of Physics A: Mathematical and General* **30**(5), 1375, 1997.

[143] I. S. Aranson and L. S. Tsimring. Pattern formation of microtubules and motors: Inelastic interaction of polar rods. *Phys. Rev. E* **71**, 050901, 2005.

[144] G. R. Dennis, J. J. Hope and M. T. Johnsson. XMDS2: Fast, scalable simulation of coupled stochastic partial differential equations. *Computer Physics Communications* **184**(1), 201–208, 2013.

[145] J. Toner, Y. Tu and S. Ramaswamy. Hydrodynamics and phases of flocks. *Annals of Physics* **318**(1), 170–244, 2005.

[146] R. Aditi Simha and S. Ramaswamy. Hydrodynamic Fluctuations and Instabilities in Ordered Suspensions of Self-Propelled Particles. *Phys. Rev. Lett.* **89**, 058101, 2002.

[147] M. B. Miller and B. L. Bassler. Quorum Sensing in Bacteria. *Annual Review of Microbiology* **55**(1) PMID: 11544353, 165–199, 2001.

[148] B. K. Hammer and B. L. Bassler. Quorum sensing controls biofilm formation in Vibrio cholerae. *Molecular Microbiology* **50**(1), 101–104, 2003.

[149] M. Rein, N. Heinß, F. Schmid and T. Speck. Collective Behavior of Quorum-Sensing Run-and-Tumble Particles under Confinement. *Phys. Rev. Lett.* **116**, 058102, 2016.

[150] B. A. Camley. Collective gradient sensing and chemotaxis: modeling and recent developments. *Journal of Physics: Condensed Matter* **30**(22), 223001, 2018.

[151] A. M. Berdahl, A. B. Kao, A. Flack, P. A. H. Westley, E. A. Codling, I. D. Couzin, A. I. Dell and D. Biro. Collective animal navigation and migratory culture: from theoretical models to empirical evidence. *Philosophical Transactions of the Royal Society of London B: Biological Sciences* **373**(1746), 2018.

[152] G. Palmer and S. Yaida. Optimizing collective fieldtaxis of swarming agents through reinforcement learning. *ArXiv e-prints*, 2017.

[153] A. B. Kao, N. Miller, C. Torney, A. Hartnett and I. D. Couzin. Collective Learning and Optimal Consensus Decisions in Social Animal Groups. *PLOS Computational Biology* **10**(8), e1003762–, 2014.

[154] G. Popkin. The physics of life. *Nature* **529**(7584), 16–18, 2016.

[155] M. Nagy, I. D. Couzin, W. Fiedler, M. Wikelski and A. Flack. Synchronization, coordination and collective sensing during thermalling flight of freely migrating white storks. *Philosophical Transactions of the Royal Society of London B: Biological Sciences* **373**(1746), 2018.

[156] C. J. Torney, J. G. C. Hopcraft, T. A. Morrison, I. D. Couzin and S. A. Levin. From single steps to mass migration: the problem of scale in the movement ecology of the Serengeti wildebeest. *Philosophical Transactions of the Royal Society of London B: Biological Sciences* **373**(1746), 2018.

[157] V. Narayan, S. Ramaswamy and N. Menon. Long-Lived Giant Number Fluctuations in a Swarming Granular Nematic. *Science* **317**, 105–, 2007.

[158] J. A. Shapiro. Thinking about bacterial populations as multicellular organisms. *Annual Review of Microbiology* **52**(1) PMID: 9891794, 81–104, 1998.

[159] L. H. Cisneros, R. Cortez, C. Dombrowski, R. E. Goldstein and J. O. Kessler. *Fluid dynamics of self-propelled microorganisms, from individuals to concentrated populations*. Ed. by G. K. Taylor, M. S. Triantafyllou and C. Tropea. Springer Berlin Heidelberg, Berlin, Heidelberg, 2010. Pp. 99–115.

[160] T. Surrey, F. Nédélec, S. Leibler and E. Karsenti. Physical Properties Determining Self-Organization of Motors and Microtubules. *Science* **292**(5519), 1167–1171, 2001.

[161] H. Wioland, F. G. Woodhouse, J. Dunkel, J. O. Kessler and R. E. Goldstein. Confinement Stabilizes a Bacterial Suspension into a Spiral Vortex. *ArXiv e-prints*, 2013.

[162] Y. Sumino, K. H. Nagai, Y. Shitaka, D. Tanaka, K. Yoshikawa, H. Chaté and K. Oiwa. Large-scale vortex lattice emerging from collectively moving microtubules. *Nature* **483**, 2012.

[163] C. Chen, S. Liu, X.-q. Shi, H. Chaté and Y. Wu. Weak synchronization and large-scale collective oscillation in dense bacterial suspensions. *Nature* **542**, 2017.

[164] J. H. Connell. Diversity in Tropical Rain Forests and Coral Reefs. *Science* **199**(4335), 1302–1310, 1978.

[165] J. Bascompte and P. Jordano. Plant-Animal Mutualistic Networks: The Architecture of Biodiversity. *Annual Review of Ecology, Evolution, and Systematics* **38**(1), 567–593, 2007.

[166] D. Tilman, P. B. Reich and F. Isbell. Biodiversity impacts ecosystem productivity as much as resources, disturbance, or herbivory. *Proceedings of the National Academy of Sciences* **109**(26), 10394–10397, 2012.

[167] E. Meron. From Patterns to Function in Living Systems: Dryland Ecosystems as a Case Study. *Annual Review of Condensed Matter Physics* **9**(1), 79–103, 2018.

[168] D. C. Savage. Microbial Ecology of the Gastrointestinal Tract. *Annual Review of Microbiology* **31**(1), 107–133, 1977.

[169] G. J. Velicer. Social strife in the microbial world. *Trends in Microbiology* **11**(7), 330–337, 2003.

[170] H.-C. Flemming, J. Wingender, U. Szewzyk, P. Steinberg, S. A. Rice and S. Kjelleberg. Biofilms: an emergent form of bacterial life. *Nature Reviews Microbiology* **14**, 2016.

[171] T. Gregor, K. Fujimoto, N. Masaki and S. Sawai. The Onset of Collective Behavior in Social Amoebae. *Science* **328**(5981), 1021–1025, 2010.

[172] J. E. Strassmann and D. C. Queller. Evolution of cooperation and control of cheating in a social microbe. *Proceedings of the National Academy of Sciences* **108**(Supplement 2), 10855–10862, 2011.

[173] C. D. Nadell, K. Drescher and K. R. Foster. Spatial structure, cooperation and competition in biofilms. *Nature Reviews Microbiology* **14**, 2016.

[174] J. Yan, C. D. Nadell, H. A. Stone, N. S. Wingreen and B. L. Bassler. Extracellular-matrix-mediated osmotic pressure drives Vibrio cholerae biofilm expansion and cheater exclusion. *Nature Communications* **8**(1), 327, 2017.

[175] L. Chai, H. Vlamakis and R. Kolter. Extracellular signal regulation of cell differentiation in biofilms. *MRS Bulletin* **36**(5), 374–379, 2011.

[176] C. Ratzke and J. Gore. Self-organized patchiness facilitates survival in a cooperatively growing Bacillus subtilis population. *Nature Microbiology* **1**, 2016.

[177] J. A. Damore and J. Gore. Understanding microbial cooperation. *Journal of Theoretical Biology* **299**, 31–41, 2012.

[178] S. A. West, S. P. Diggle, A. Buckling, A. Gardner and A. S. Griffin. The Social Lives of Microbes. *Annual Review of Ecology, Evolution, and Systematics* **38**(1), 53–77, 2007.

[179] W. C. Allee. *Principles of animal ecology*. Philadelphia, Saunders Co., 1949. P. 860.

[180] F. Courchamp, T. Clutton-Brock and B. Grenfell. Inverse density dependence and the Allee effect. *Trends in Ecology & Evolution* **14**(10), 405–410, 1999.

[181] Z. Konsula and M. Liakopoulou-Kyriakides. Hydrolysis of starches by the action of an α-amylase from Bacillus subtilis. *Process Biochemistry* **39**(11), 1745–1749, 2004.

[182] R. Axelrod and W. Hamilton. The evolution of cooperation. *Science* **211**(4489), 1390–1396, 1981.

[183] E. Frey. Evolutionary Game Theory: Theoretical Concepts and Applications to Microbial Communities. *Physica A: Statistical Mechanics and its Applications*(20), 4265–4298, 2010.

[184] R. Axelrod and R. Axelrod. *The Evolution of Cooperation*. Basic books. Basic Books, 1984.

[185] M. A. Nowak. Five rules for the evolution of cooperation. *Science (New York, N.y.)* **314**(5805), 1560–1563, 2006.

[186] R. Trivers. *The Evolution of Reciprocal Altruism*. Vol. 46. Mar. 1971. Pp. 35–57.

[187] J. Andreoni and J. H. Miller. Rational Cooperation in the Finitely Repeated Prisoner's Dilemma: Experimental Evidence. *The Economic Journal* **103**(418), 570–585, 1993.

[188] T. H. Clutton-Brock and G. A. Parker. Punishment in animal societies. *Nature* **373**, 1995.

[189] J. Cremer, A. Melbinger and E. Frey. Growth dynamics and the evolution of cooperation in microbial populations. *Scientific Reports* **2**, 2012.

[190] M. Perc, J. Gómez-Gardeñses, A. Szolnoki, L. M. Floría and Y. Moreno. Evolutionary dynamics of group interactions on structured populations: a review. *Journal of The Royal Society Interface* **10**(80), 2013.

[191] J. S. Chuang, O. Rivoire and S. Leibler. Simpson's Paradox in a Synthetic Microbial System. *Science* **323**(5911), 272–275, 2009.

[192] J. Gore, H. Youk and A. van Oudenaarden. Snowdrift game dynamics and facultative cheating in yeast. *Nature* **459**, 2009.

[193] C. Hauert and M. Doebeli. Spatial structure often inhibits the evolution of cooperation in the snowdrift game. *Nature* **428**, 2004.

[194] J. Friedman, L. M. Higgins and J. Gore. Community structure follows simple assembly rules in microbial microcosms. *Nature Ecology &Amp; Evolution* **1**, 2017.

[195] L. M. Higgins, J. Friedman, H. Shen and J. Gore. Co-occurring soil bacteria exhibit a robust competitive hierarchy and lack of non-transitive interactions. *bioRxiv*, 2017.

[196] K. S. McCann. The diversity–stability debate. *Nature* **405**, 2000.

[197] A. R. Ives and S. R. Carpenter. Stability and Diversity of Ecosystems. *Science* **317**(5834), 58–62, 2007.

Acknowledgements

I would like to thank all the people who supported me during my doctoral studies. First of all, I would like to express my deepest gratitude to Erwin Frey for supervising me and giving me the opportunity to be part of his group. I have been appreciating your extensive knowledge, your experience, and your frank style in many discussions that have helped me to discover these interesting questions I have been working on and to better understand the big pictures behind them. I thank you for making it possible for me to participate in the scientific life, whether it be by connecting me with other researchers to discuss our scientific results, by giving me the opportunity to present our results at numerous conferences and meetings. Especially, I would like to thank you for supporting my research stay in Boston, from which I greatly benefited both scientifically and personally in several aspects. During my time in your group, I have been enjoying the freedom to follow all of my scientific interests and always enjoyed the insightful discussions with you.

A special thanks also goes to Jeff Gore for supporting me during my research stay at MIT and for giving me the opportunity to perform experiments in his laboratory. I would like to thank the whole Physics of Living Systems group at MIT that has made my stay in Boston to a most joyful experience. In particular, I would like to thank Christoph Ratzke, who not only gave me the best introduction to performing lab experiments, but has also become a valuable friend and discussion partner during my time in Boston.

I am very glad that I had the chance to be a member of the graduate school "Quantitative Biosciences Munich" (QBM). The graduate school QBM offered me financial support, for which I would like to express my gratitude.

I always had great pleasure being part of the LS Frey group. Thank you to everyone in the group for creating a fun and stimulating environment, that made work so much more enjoyable. I would like to thank in particular my office colleague Marianne Bauer, Lorenz Huber, Emanuel Reithmann, Felix Kempf, Silke Bergeler, Jacob Halatek, Fridtjof Brauns, Isabella Graf, Timo Krüger, Laeskir Hassan, and Johannes Knebel for both many interesting discussions and, most importantly, for having a great time! For proof-reading my thesis I want to thank Silke Bergeler, Lorenz Huber, Fridtjof Brauns, and Timo Krüger.

Last but not least, I would like to express a cordial thanks to my family. To my parents Christine and Hans as well as my brother Wilfried for their constant support and encouragement over all these years.